e^+e^- PHYSICS WITH THE JADE DETECTOR AT PETRA

B. NAROSKA

Deutsches Elektronen-Synchrotron DESY, Notkestr. 85, 2000 Hamburg 52, FRG

NORTH-HOLLAND – AMSTERDAM

PHYSICS REPORTS (Review Section of Physics Letters) 148, Nos. 2 & 3 (1987) 67–215. North-Holland, Amsterdam

e^+e^- PHYSICS WITH THE JADE DETECTOR AT PETRA

B. NAROSKA

Deutsches Elektronen-Synchrotron DESY, Notkestr. 85, 2000 Hamburg 52, FRG

Received 26 September 1986

Contents:

Single orders for this issue

PHYSICS REPORTS (Review Section of Physics Letters) 148, Nos. 2 & 3 (1987) 67–215.

Copies of this issue may be obtained at the price given below. All orders should be sent directly to the Publisher. Orders must be accompanied by check.

Single issue price Dfl. 105.00, postage included.

Introduction

The JADE detector has been operated at the e^+e^- storage ring PETRA [3] situated at DESY, Hamburg (Germany) since 1979 and will continue taking data until the end of PETRA operations for physics, anticipated for the fall of 1986. The storage ring provides four intersection regions for experiments, the other detectors running in parallel were CELLO, MARK J, PLUTO and TASSO [2].

The JADE detector was built and operated by an international collaboration [1] formed by the following institutions: DESY (Hamburg, Germany), the Universities of Hamburg and Heidelberg (Germany), the Universities of Lancaster and Manchester (England), the Rutherford Appleton Laboratory (Chilton, England) and the University of Tokyo (Japan). The collaboration was later joined by the University of Maryland (College Park, USA).

In the course of the six years of running the maximum centre-of-mass energy of PETRA was increased from ~30 to 46.78 GeV, an energy which will be unsurpassed in e^+e^- storage rings until TRISTAN in Japan or SLC in the USA come into operation. JADE has taken data in the energy range $12 \leq \sqrt{s} \leq 46.78$ GeV. The centre-of-mass energy as a function of time is shown schematically in fig. 1.1 and the integrated luminosity as a function of energy in fig. 1.2. The total integrated luminosity accumulated by the end of 1985[1] was larger than 130 pb^{-1}.

The JADE detector was designed as a multi-purpose detector capable of measuring a large variety of e^+e^- interactions resulting in leptonic and hadronic final states. At present it is believed that all such processes – and also all other conceivable high energy processes – can in principle be described by the standard model, minimal $SU(2) \times U(1) \times SU(3)_{colour}$. Experimental results from e^+e^- interactions have – among others – contributed significantly in establishing the validity of the standard model as an effective theory, which future theories must contain as a limit.

[1]The running energy in 1986 was $\sqrt{s} = 35$ GeV; 80 pb^{-1} were accumulated in total.

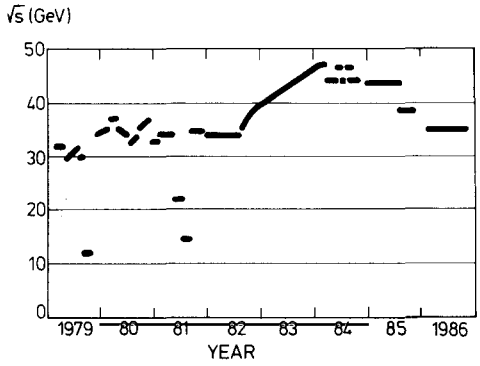

Fig. 1.1. The centre-of-mass energy of PETRA from 1979 until 1985.

Many of the JADE results benefit from a number of important properties of the detector: The pictorial qualities of the jet-chamber and its good double-track resolution result in a high efficiency for track reconstruction, even in complicated events. The homogeneity of the lead-glass shower detector combined with its high granularity and resolution give an efficient recognition of showering particles, which is almost unambiguous in simple events and still satisfactory in complicated hadronic events. The low noise level allows detection of showers of energies as low as 100 MeV. The multilayer muon filter allows muon recognition even in a hadronic jet. The detector can be triggered efficiently by a calorimetric trigger derived from the signals of the lead-glass arrays. The jet-chamber is in addition capable of giving a very efficient track-trigger due to the large number of points measured on a track.

An important feature of the JADE detector is the large coverage of solid angle by the major detector components: the jet-chamber, the lead-glass arrays and the muon filter each cover more than 90% of the full solid angle.

The purpose of this report is to survey the work of the JADE collaboration during the first six years of data taking and summarize the main results. It continues the series of summary reports on experimental e^+e^- results from DESY, which includes reports about PLUTO (data from DORIS and PETRA) [23], MARK J [39] and a global review about all five PETRA experiments including data taken before the middle of 1983 [2]. The report is not exhaustive, some investigations or results will be

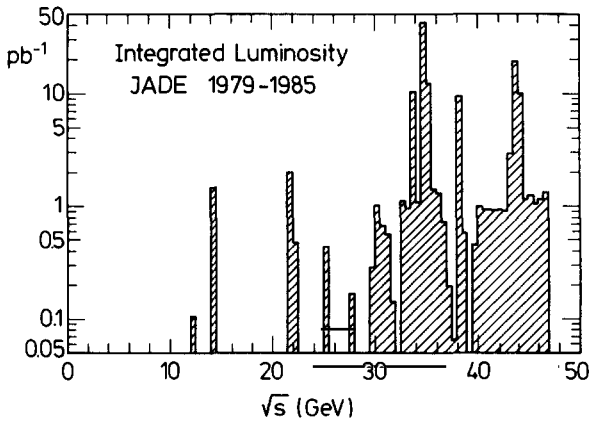

Fig. 1.2. The integrated luminosity collected by the JADE experiment as a function of the centre-of-mass energy.

mentioned only briefly or even be omitted. One field in particular has been omitted, namely the analysis of two-photon scattering, $e^+e^- \to e^+e^- + X$ [4].

The report is arranged as follows: In chapter 1 a summary of the detector components and their main characteristics is given, together with a description of the trigger and the data acquisition system.
In chapter 2 results on the leptonic reactions $e^+e^- \to e^+e^-$, $e^+e^- \to \mu^+\mu^-$ and $e^+e^- \to \tau^+\tau^-$ are surveyed and confronted with QED and the Glashow–Salam–Weinberg electroweak predictions. Section 2.5 is devoted to tests of higher order QED processes.
Chapter 3 describes the determination of the τ decay branching ratios.
The precise measurement of the total hadronic cross-section and its comparison with the prediction of the standard model is described in chapter 4.
Tests of perturbative QCD, investigations about the fragmentation process and tests of fragmentation models are the subject of chapter 5.
The analysis of inclusive particle production in multi-hadronic events is described in chapter 6.
The physics of the heavy c- and b-quarks is discussed in chapter 7. Analysis of the production and decay of charged and neutral D^* is followed by inclusive lepton studies.
Finally, in chapter 8, the searches for new particles and the limits that were set on their masses are summarized.

1. The JADE detector

A perspective view of the JADE detector in fig. 1.3 gives an impression of how the detector parts are arranged around the intersection point of the PETRA beams. A cross-section of the detector in a vertical plane including the PETRA beam-line is shown in fig. 1.4 and a cross-section perpendicular to the beam direction in fig. 1.10. The central part of the detector is a pictorial drift-chamber, the "jet-chamber", which is placed in a homogeneous axial magnetic field of 4.8 kG. The magnet coil is a solenoid of 3.5 m length and of 2 m diameter. Between jet-chamber and coil there are 42 scintillation counters which are used for triggering and for time-of-flight measurement. Outside the magnet coil a fine grain lead-glass detector gives electron/photon recognition. The outermost part of the detector is a rectangular muon filter consisting of layers of planar drift-chambers alternating with absorber. An on-line luminosity measurement is provided by two electromagnetic shower counters in the extreme forward directions, which are also used as tagging devices in two-photon reactions.

Recently, two additional chambers were installed. A vertex-chamber close to the interaction point gives seven precise points on a track. It replaced the beam-pipe scintillation counters which had been used for monitoring of background. Outside the jet-chamber a z-chamber was installed to give a precise measurement of the longitudinal coordinate z. The data described here do not include information from these two devices.

In this chapter a brief description of the detector parts and typical parameters will be given, followed by a short summary of the trigger and the data acquisition system.

1.1. The jet-chamber

The central track detector of JADE, the jet-chamber [5], is a cylindrical drift-chamber of 2.4 m length and of 1.6 m diameter. It is physically subdivided into 24 segments in the azimuthal direction. Each segment contains 4 drift-cells (fig. 1.5) with 16 anode wires in a cell. The drift-cells form three

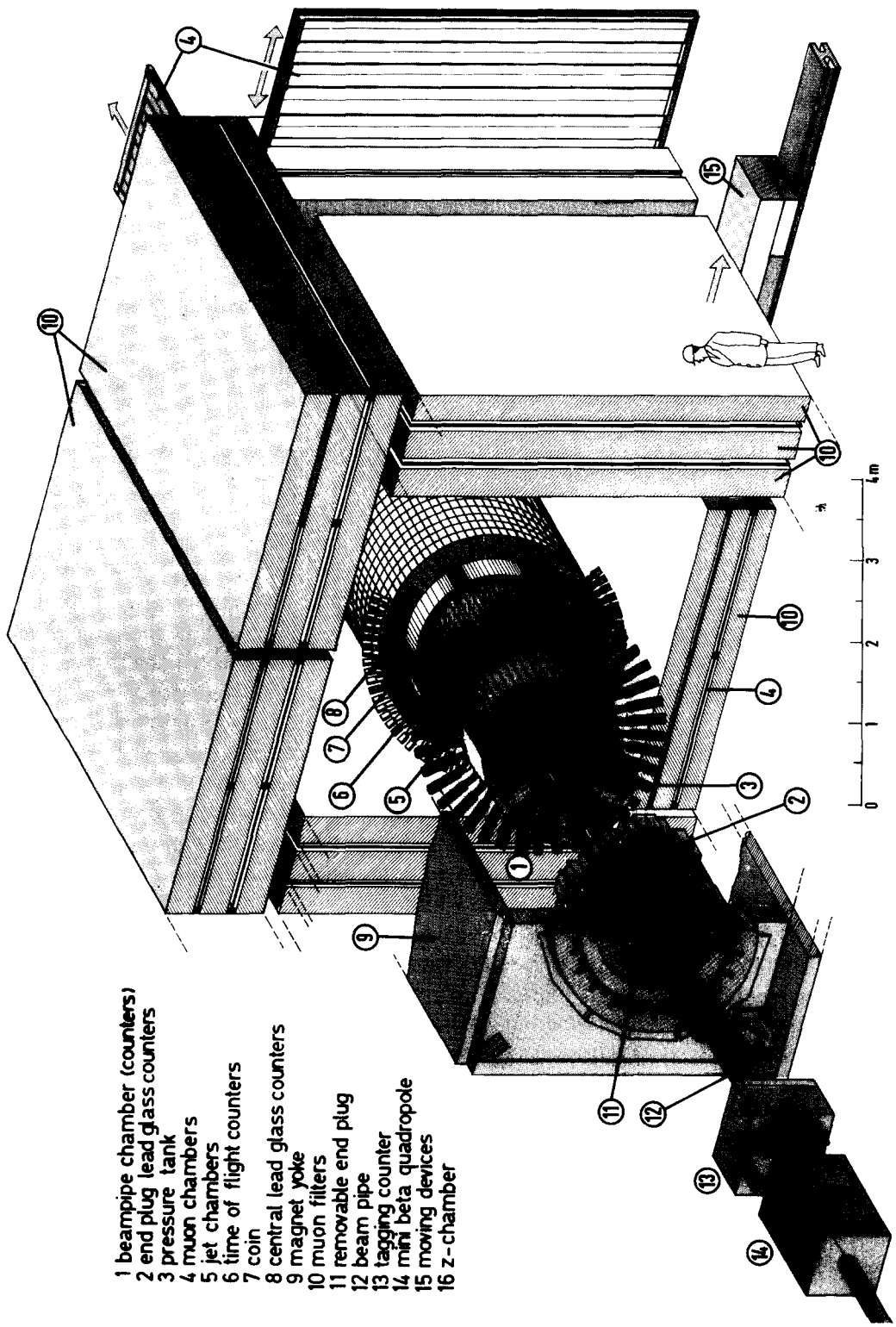

Fig. 1.3. Perspective view of the JADE detector.

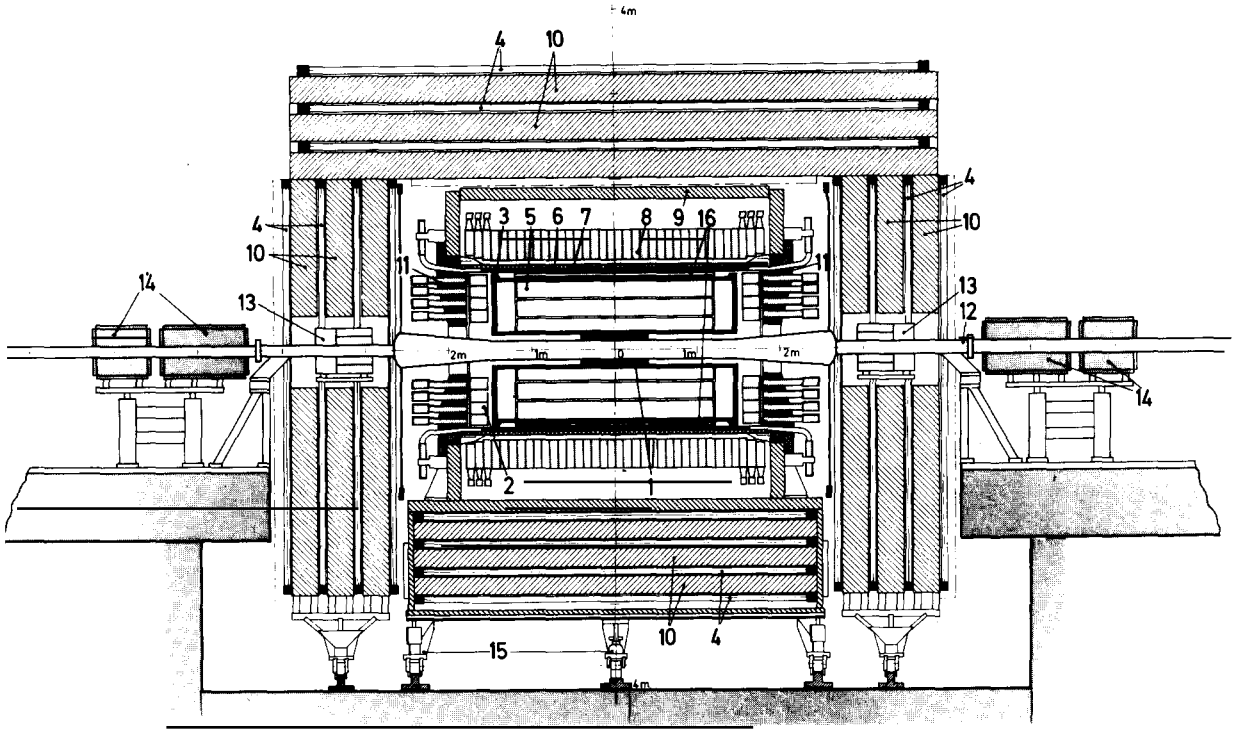

Fig. 1.4. The JADE detector: Vertical section along the beam pipe. (See fig. 1.3 for explanation.)

rings, rings 1 and 2 have 24 cells each and ring 3 has 48 cells. The anode wires are staggered by ± 150 μm in order to solve left–right ambiguities. The equipotential planes of the drift-field are parallel to the plane of the anode wires. Due to the magnetic field, which is orthogonal to the drift-field, the drift-trajectories are tilted by ~18.5°, the so-called Lorentz angle. The gas used is a mixture of argon, methane and isobutane (0.887:0.085:0.028). The detector is run at a pressure of ~4 atm to minimize the influence of diffusion on the spatial resolution. The drift-velocity is roughly 5 cm/μs.

For particles coming from the interaction point of the electron and positron beams (the "vertex region") which have directions between 34° and 146° with respect to the beam-line, a maximum of 48 points can be measured. For 97% of 4π at least 8 points are on a track. The measured points are space points, consisting of a precise measurement in the plane perpendicular to the beam, the $r\varphi$-plane, which is given by the drift-time and the radial wire position, and the longitudinal z-coordinate, which is determined by charge division.

1.1.1. Calibration and pattern recognition

The calibration of the jet-chamber is performed with data, from Bhabha events, two-muon events and from multitrack events. The most important constants which have to be determined are: the drift-velocity, which was allowed to have different values on the two sides of the drift-cells (192 constants); 1536 time-off sets, one for each wire; 384 position constants, four numbers per drift-cell, and 3 Lorentz angles, one for each ring. Gravitational forces acting on the wires are taken into account. Special corrections are determined for coordinates in the region very close to the drift wires, where the

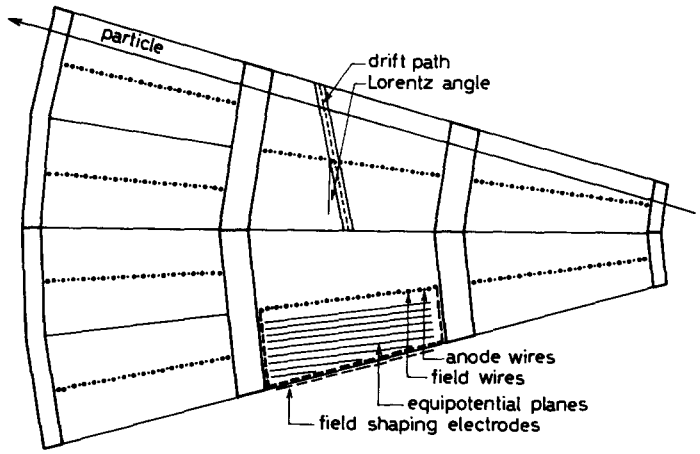

Fig. 1.5. Cross-section through two of the 24 sectors of the jet-chamber.

electric field is cylindrical and varies strongly. Tracks traversing the cell at an angle with respect to the wire plane also necessitated a special correction.

The constants were determined for each gas filling[1] or whenever a change in running conditions was made. The point-resolution obtained in the $r\varphi$-plane is $\sim 180\,\mu m$ and the momentum resolution $\Delta p/p^2 \sim 2\%$ (see fig. 1.6) in the high momentum limit. This can be compared to a momentum resolution of $\Delta p/p^2 \sim 1.5\%$ expected for the quoted point resolution.

The z-coordinate was obtained by charge division, i.e. by the difference of the pulse amplitudes measured on either side of the wire relative to their sum. The calibration was performed using data, four constants were determined for each wire. Systematic distortions of the amplitudes, for example due to cross-talk between wires, due to superposition of pulses close in time, etc. were corrected for. The resolution obtained in z is $\sim 16\,mm$.

The pattern recognition of tracks [6] is performed in the $r\varphi$-plane because there the resolution is a factor 100 better than in the rz-plane. First, triplets of points on adjacent wires which lie on a straight line are searched for; these triplets are then connected to form track-elements, still within a cell. Track-elements in different cells are combined starting in the outermost ring and going inwards. A fit is made to the measured points by a parabola or, below 500 MeV, by a circle. Finally, all points in the vicinity of this fitted trajectory are re-examined and added to the track if they agree with it. For the points selected in this way a straight line fit is attempted in the rz-plane which is repeated after eliminating badly fitting measurements. For special purposes this fitting procedure can be refined, e.g. by adding vertex constraints or by performing a three-dimensional helix fit.

Due to the jet-chamber being operated at 4 atm – which necessitates a pressure vessel – the amount of material to be traversed before the first sense wire is $\sim 16\%$ of a radiation length.

1.1.2. dE/dx measurement and resolution

The specific ionisation loss of a particle in the gas of the jet-chamber is measured by the sum of the pulseheights recorded on both ends of the signal wires. Ideally 48 hits are available on a track, but in practice the number is reduced by demanding good separation from other hits. The raw amplitudes

[1] The gas in the jet-chamber was renewed in shut-down times of PETRA, typically three times per year. During data taking periods the gas was only circulated.

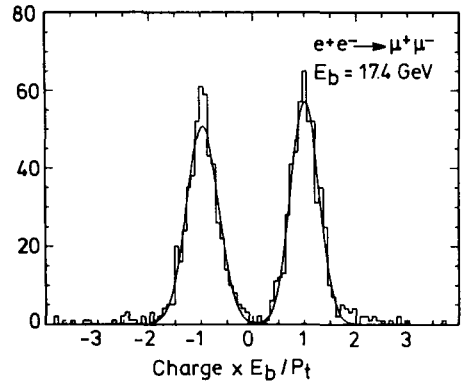

Fig. 1.6. Momentum resolution: Charge $\times E_{beam}/p_t$ for muon pairs at $E_{beam} \sim 17$ GeV. The histogram represents the data. The curves are fitted Gaussians yielding resolutions of $\Delta p_t/p_t^2 = 1.8\%$ and 1.6%.

have to be corrected for individual gas amplification and electronic gain, different path-lengths of the tracks in the drift-space, for electron attachment and saturation effects. Some of these corrections are time-dependent, because they depend on the age of the gas filling.

To diminish fluctuations due to the Landau tail of the pulseheight distribution only the lowest 70% of all pulseheight measurements were used and averaged (method of "truncated mean"). In addition the lowest 5% were rejected. The truncated mean $\langle dE/dx \rangle$ for the tracks in a sample of multihadronic events is shown in fig. 1.7. Bands can be recognised for pions, kaons and protons.

The resolution achieved for Bhabha electrons is $\sigma = 6.5\%$ for an average of 42 hits per track (fig. 1.8). This resolution is close to the theoretical expectation of 5%.

In multihadronic events the number of useful samplings is in general smaller. Demanding at least 33 hits (38 hits on average) a resolution of $\sigma \sim 8\%$ is obtained for minimum ionising pions (fig. 1.8).

For each particle a probability is calculated for it being an electron, a pion, a K or a proton. This is done by comparing the measured momentum and $\langle dE/dx \rangle$ with the predicted curves and computing a

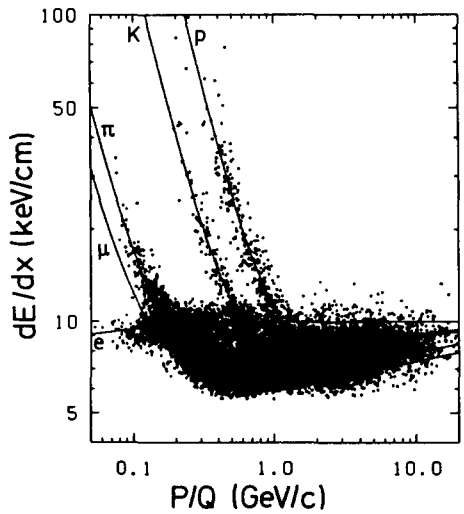

Fig. 1.7. $\langle dE/dx \rangle$ (truncated mean) as a function of momentum. The bands correspond to electrons (e), pions (π), kaons (K) and protons (p).

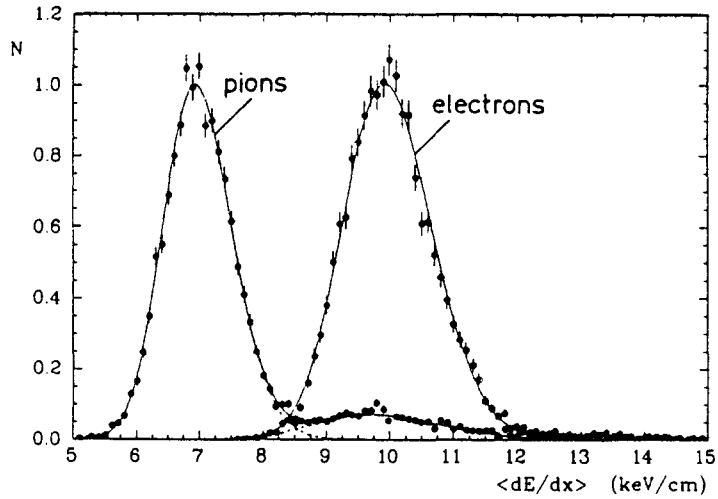

Fig. 1.8. $\langle dE/dx \rangle$ distribution for tracks from multihadronic events of momenta $0.4 \leq p \leq 0.6$ GeV – mainly pions, the tail is due to electrons and kaons – and for electrons from Bhabha scattering.

χ^2 taking into account the measurement errors. Cuts in the probability are applied according to the analysis requirements.

1.2. Scintillation counters

The jet-chamber is surrounded by 42 scintillation counters, 3.2 m long, which are read out at each end by photomultipliers. The two signals are used in coincidence to suppress photomultiplier noise. The counters were used for triggering and for time-of-flight measurement (they are named "TOF" counters). The thresholds were kept as low as permitted by the trigger rate in order to be sensitive to fractionally charged particles; it corresponded roughly to 0.1–0.5 of a minimum ionising particle. The time resolution obtained was ~300–400 ps. In fig. 1.9 the time difference for coplanar pairs of minimum ionising particles is shown; a clear separation of beam–beam events from cosmic ray muons which traverse the detector in $6\,\text{ns}/\sin\theta$ (θ is the polar angle) is visible.

In the forward direction between the end caps of the lead-glass and the muon filter there are two rectangular scintillator hodoscopes of 8 counters each; the useable region covers roughly $0.8 \lesssim |\cos\theta| \lesssim 0.94$. They were installed specially to detect muon pairs at these low angles.

1.3. The lead-glass detector

The lead-glass detector is arranged in 3 parts: the largest part is a cylindrical array surrounding the magnet coil; it consists of 2520 blocks arranged in 30 rings of 84 blocks each. The blocks (Schott SF5) are wedge shaped, the inner surface is $85 \times 102\,\text{mm}^2$, the thickness is 300 mm corresponding to 12.5 radiation lengths. They are read out by photomultipliers (Hamamatsu R594-02), connected with the lead-glass blocks by short light-guides.

In 1983, for running at the highest PETRA energies, the middle part of the cylinder (20%) was replaced by blocks of SF6, which have 15.7 radiation lengths but are identical in shape.

The other two parts of the detector are supported by flat iron endcaps which close the cylinder and

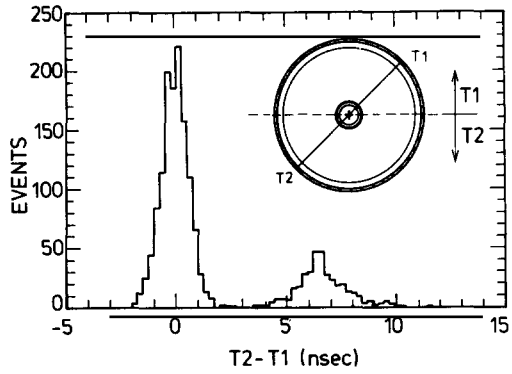

Fig. 1.9. Difference of arrival time at the TOF counters for coplanar track pairs.

are part of the magnet return iron. The lead-glass blocks are inside the iron, the light is transported to the photomultipliers outside by light-guides embedded in the iron. The block-size is $140 \times 140 \times 230\,\text{mm}^3$ corresponding to a depth of 9.6 radiation lengths. The total acceptance of all three hodoscopes is 90% of 4π.

The initial individual calibration of the counters was done with electrons of 6 GeV. During operation in PETRA Bhabha events were used for calibration. The gain of the photomultipliers was monitored by Xe-spark lamps, connected to the counters by quartz optical fibers. The variation in gain was typically 1–2% in half a year.

The energy resolution is a function of the polar angle; for average angles (~40° with respect to the beam-line), Bhabha events between 7 and 17 GeV have a resolution of $\sigma_E/E = 4\%/\sqrt{E} + 1.5\%$, where E is measured in GeV. The angular resolution is $\sigma_\theta = 0.6°$ and $\sigma_\varphi = 0.7°$.

The detection of showering particles, electrons and photons, was based on "energy clusters" in the lead-glass arrays. These were defined by adjacent counters which had registered pulses above a fixed threshold (~45 MeV). The energy sum of all counters belonging to one cluster was defined as the cluster energy. If a track was pointing towards the cluster its momentum was compared with the cluster energy, and if the cluster energy was more than 60–70% of the momentum, the track was called an electron. This simple definition was useful in low multiplicity events, e.g. for all leptonic reactions described in chapter 2. In hadronic events problems due to overlapping tracks necessitated tighter selection criteria, which will be described in chapter 6.

1.4. The muon filter

The outermost detector part is the muon filter, which is a segmented system with five layers of absorber and drift-chambers covering 92% of the solid angle [7]. The main absorber components are the lead-glass shower counters, the iron return yoke and three layers of iron loaded concrete with a density of $\sim 5.2\,\text{g/cm}^3$. The concrete surrounds the otherwise cylindrical detector like a rectangular box. The minimum thickness perpendicular to the beam is 6.4 absorption lengths; the minimum momentum necessary for a muon to traverse the muon filter is roughly 1.4 GeV.

Between the absorber segments and on the outside there are 618 single wire drift-chambers (see fig. 1.10). Particles emanating from the interaction region in the central part ($|\cos\theta| \lesssim 0.6$) traverse 5 layers of chambers, the innermost of which is a completely overlapping double layer. In the endwalls the innermost layer of muon chambers is missing, so that only four layers are available.

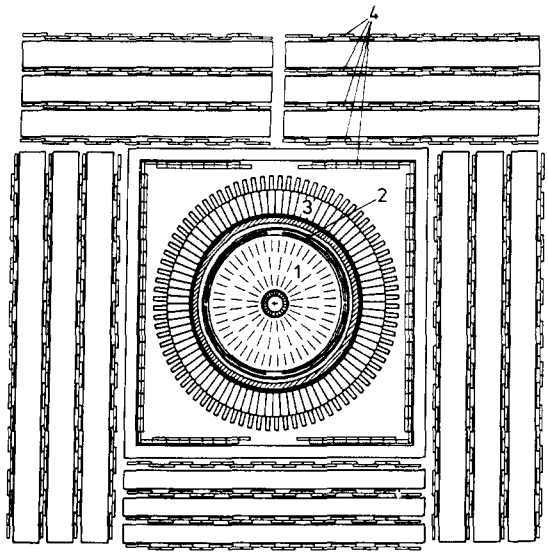

Fig. 1.10. Cross-section of the JADE detector perpendicular to the beam direction (1 = jet-chamber, 2 = TOF counters, 3 = lead-glass barrel, 4 = drift-chambers in muon filter).

The sensitive volume of one drift-chamber has a cross-section of $305 \times 20\,mm^2$ and a length of up to 5 m. The chambers are filled with argon–ethane (90:10). The drift-velocity is 40.7 mm/μs. The average track detection efficiency per chamber is better than 98%. The space resolution in the drift direction obtained for $e^+e^- \rightarrow \mu^+\mu^-$ events was 5 mm in the barrel part and 10 mm in the endwalls. This precision is of the same order as the extrapolation uncertainties of the jet-chamber tracks.

For the identification of muons all tracks found in the jet-chamber are extrapolated into the muon chambers, taking into account multiple scattering and bending in the field and return yokes. Hits in the muon chambers are associated if they lie within a certain minimum distance from the extrapolated track in the drift direction [7].

1.5. Trigger and data taking

The beam crossing rate at PETRA is ~250 kHz. The trigger system was designed to give a trigger rate manageable by the on-line data acquisition system (a few events per second) and to reduce the amount of data to be handled off-line. Apart from the rate considerations the design of the trigger system of the JADE experiment aimed at high efficiency in particular for e^+e^- annihilation events.

High efficiency was achieved by a few standard trigger conditions for the main known types of annihilation events. In addition several triggers were run in parallel to provide redundancy and flexibility in adjusting to background conditions. They were also intended to detect unexpected processes of various topologies and events from two-photon collisions.

Trigger actions

The trigger was based on signals from scintillation and lead-glass counters and on output signals from hard-wired track finding logics for the jet-chamber and for the muon filter. The trigger decision was carried out in three steps which were determined by the times when the signals from the different detector components were available for pattern checks. At a time T1, ~400 ns after the beam-crossing

time T0, the signals from photomultiplier read-out (scintillation and lead-glass counters) were available. At this stage an event could be rejected, accepted, or the decision could be postponed. If an event was rejected at T1 the system was reset without dead-time.

At time T2 ~ 2 μs after T0 the signals from the jet-chamber were available and could be used for further trigger decisions. In the first years of operation the rejection of an event at T2 caused the loss of the next bunch-crossing because of the necessary reset-time of the analog read-out of the jet-chamber electronics. From 1982 onwards this reset-timing was changed such that also a T2-reject caused no extra dead-time.

The trigger decision could be postponed even further until T3 ~ 5 μs after T0 when the signals from the muon chambers were available. A T3-reject always caused the loss of an extra bunch-crossing.

The digitisation of most detector signals was started at T0, but was aborted at a reject condition. If an event was accepted at any of the stages T1–T3 an interrupt signal was sent to the NORD-10 computer and the digitised detector signals were read out via CAMAC.

Energy triggers

From the signals of the lead-glass system calorimetric triggers were obtained by analog summing of the signals from the whole lead-glass system or parts of it. The standard energy-triggers used the following signal sums:

E_{tot}, the total sum of all signals;

E_{BAR}, the sum of the barrel part ($|\cos\theta| \lesssim 0.82$);

E_{EC}^{+} and E_{EC}^{-}, the sums of the end-caps at $+z$ and $-z$.

The following table shows the standard energy-triggers which led to an accept condition. The equivalent analogue thresholds and the Boolean logics conditions for the discriminator signals are given; the logical AND (OR) being indicated by the $\cdot$ (+) sign, respectively.

Signals	Thresholds[1]	Main use
E_{tot}	4–6 GeV	Hadrons, Bhabha events
E_{BAR}	2–5 GeV	Hadrons, large angle Bhabha events, τ pairs
$E_{EC}^{+} \cdot E_{EC}^{-}$	1 GeV	Hadrons, Bhabha events, 2-photon events
$(E_{EC}^{+} + E_{EC}^{-}) \cdot E_{BAR}$	0.5, 0.5, 1.5 GeV	2-photon events
$E_{EC}^{+} \cdot E_{EC}^{-} \cdot E_{tot}$	0.3, 0.3, 2.5 GeV	2-photon events, hadrons

[1] The thresholds were adjusted to the beam energy and according to background conditions.

Track triggers

Bunch-crossings which did not generate an "accept"-pattern in the energy triggers could still be accepted by track triggers, if the signals of the lead-glass and the scintillation counters met one of the rather loose T1-postpone conditions.

The lead-glass signals used in these pre-triggers had much lower thresholds than the signals for the energy triggers discussed in the previous section. The most important of these were the barrel-group (abbr. BG) signals. They were formed by the analog sum of the signals from all lead-glass blocks behind a TOF counter and its two neighbours and used in coincidences "TBG" with these.

The track-trigger logics of the jet-chamber only used the one-bit information whether at least one hit had occurred on a wire within the maximum drift-time, but had no access to drift-times or signal amplitudes, i.e. z values. A track condition was set up in the following way: In one cell or two adjacent cells of each ring of the jet-chamber a minimum number of wires must have registered a hit. The cells in

the three rings were combined in appropriate patterns. For background suppression the track logics required also a coincident signal from one of the 3–4 TOF counters behind the hit jet-chamber segments.

There were two sets of track signals: Ordinary tracks with full efficiency above 100 MeV; and fast tracks with full efficiency above 1 GeV. With additional logics two found tracks were classified as coplanar within a given angle, i.e. the tracks were emerging in nearly opposite directions in the $r\varphi$-plane. The track triggers together with their adjoined T1-postpone triggers are shown in the next table:

Postpone condition	Tracks	Main use
2 TOF · E_{tot} (>1.5 GeV)	2 ordin.	Hadrons, τ pairs
2 TOF · $(E^{+}_{EC} + E^{-}_{EC})$ (>1 GeV)	2 ordin.	2-photon events, hadrons
2 TBG · ≤6 TOF	2 ordin.	2-photon events, τ pairs
2 $TOF_{copl\pm30°}$ · ≤4 TOF	2 fast coplanar ±34°	μ, τ pairs, 2-photon events
2 $TOF_{copl\pm13°}$ · ≤6 TOF	2 fast coplanar ±20°	μ, τ pairs, 2-photon events
2 $TBG_{copl\pm21°}$	2 fast coplanar ±34°	μ, τ pairs, 2-photon events
1 TBG · E_{BAR} (>1.5 GeV)	1 fast	Hadrons, τ pairs, 2-photon

For some T1-postpone triggers an upper limit for the number of TOF signals was set (indicated by the ≤ symbol in the table) to reject background triggers.

A special trigger for low-θ μ-pair events used coincidences of opposite forward scintillation counters as T1-postpone conditions and asked for a track signal from the endwalls of the muon filter. For events caused by two-photon collisions a number of special triggers was installed. Since the physics will not be covered by this report they are not listed, however.

Data taking

The steps of the data flow for the JADE experiment are shown in fig. 1.11. The computer for data taking and on-line monitoring was a NORD-10/S coupled with a NORD-50 by Norsk Data. The read-out used a GEC Elliot system crate with a NORD-10 interface developed at CERN. 40 Camac

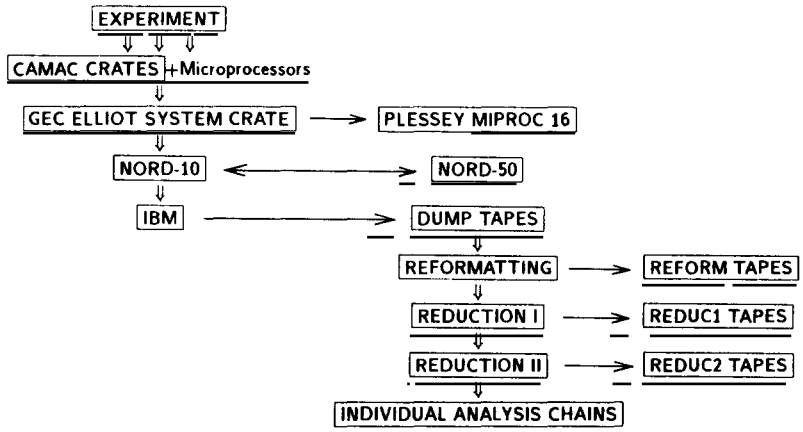

Fig. 1.11. Schematic data flow in the JADE experiment.

crates were used and read out by a direct memory access (DMA) data transfer. A (short) event of 3000 words needed approximately 25 ms read-out time.

Parallel to the read-out the jet-chamber data were analysed in a fast microprocessor, the Miproc 16 by Plessey. It imposed tighter cuts on track triggers than the hard wired logics and rejected events with an origin clearly outside the interaction point of the beams.

The data acquisition system is described in more detail in [8]. The data from Camac were written into a NORD-10 buffer which could also be read by the NORD-50, which performed event checking, accumulated histograms and performed on-line filtering [9]. Results of the NORD-50 analysis were appended to the data which were then transferred by a direct link to the computing centre of DESY. After reformatting, the data were passed through filtering programs before they were used for analysis and final calibrations.

2. Tests of QED and electroweak theories in leptonic interactions

Purely leptonic processes, such as $e^+e^- \to e^+e^-$, $\mu^+\mu^-$, $\tau^+\tau^-$ and $\gamma\gamma$ have been extensively studied at e^+e^- colliders of lower energies, for example DORIS and SPEAR. These processes can be described by QED and quantitative comparisons showed the theory to be valid within the experimental accuracy [23]. At higher energies such as became available at PETRA, deviations from pure QED were predicted by electroweak theories which give a unified description of electromagnetic and weak interactions. The standard model by Glashow, Salam and Weinberg [10], minimal $SU(2) \times U(1)$, predicted that the interference of the photon with the neutral weak intermediate boson would lead to a charge asymmetry of the order of 10% for fermion pairs at $s \approx 1000\,\mathrm{GeV}^2$. Establishing the asymmetry first for $e^+e^- \to \mu^+\mu^-$, then also for $e^+e^- \to \tau^+\tau^-$ and for the heavy quarks c and b was one of the major results achieved in the JADE experiment as well as in the other experiments at PETRA and later on at PEP.

This chapter will be concerned with leptonic processes. After a summary of the cross-sections from QED and the Glashow–Salam–Weinberg (GSW) model the discussion of the data will start with Bhabha scattering and $e^+e^- \to \gamma\gamma$. Electroweak effects are small for them, thus they serve as tests for QED. Afterwards we turn to the discussion of $e^+e^- \to \mu^+\mu^-$ and $e^+e^- \to \tau^+\tau^-$ and the extraction of electroweak parameters. The chapter will be concluded by tests of higher order QED.

2.1. Cross-sections

In QED the processes $e^+e^- \to e^+e^-$, $\mu^+\mu^-$, $\tau^+\tau^-$ and $\gamma\gamma$ are described by the diagrams in fig. 2.1 and the differential cross-sections are in lowest order given by:

$$e^+e^- \to e^+e^-: \qquad \frac{d\sigma}{d\Omega} = \frac{\alpha^2}{4s}\left(\frac{3+x^2}{1-x}\right)^2 \tag{2.1}$$

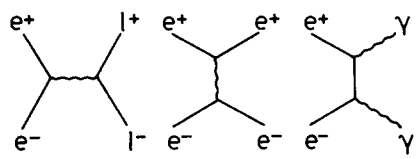

Fig. 2.1. Diagrams contributing to $e^+e^- \to \ell^+\ell^-$ (ℓ = e, μ or τ) and $e^+e^- \to \gamma\gamma$ to order α^2.

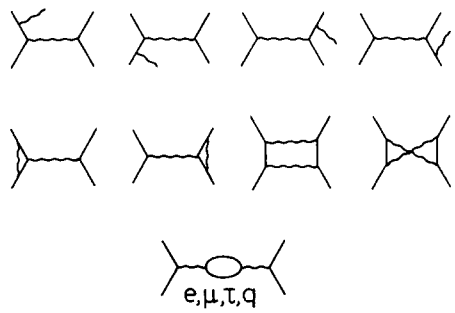

Fig. 2.2. α^3 contributions to $e^+e^- \to \mu^+\mu^-$ and $\tau^+\tau^-$. The vertex correction, two-photon exchange and vacuum polarization contribute to α^3 only by interference with the diagram of lowest order.

$$e^+e^- \to \mu^+\mu^-,\ \tau^+\tau^-: \qquad \frac{d\sigma}{d\Omega} = \frac{\alpha^2}{4s}(1+x^2) \tag{2.2}$$

$$e^+e^- \to \gamma\gamma: \qquad \frac{d\sigma}{d\Omega} = \frac{\alpha^2}{s}\left(\frac{1+x^2}{1-x^2}\right) \tag{2.3}$$

where α is the fine structure constant and $x = \cos\theta$; θ is the scattering angle. These expressions are valid for the limit of vanishing masses. For the correct description of the data it is in general necessary to include contributions of higher order, in general the next to leading order α^3 is sufficient. As an example the diagrams contributing to muon pair production up to order α^3 are shown in fig. 2.2. They include emission of photons in the initial and final state and interference of the box diagram, vertex correction and vacuum polarization diagrams with the diagrams of lowest order. The corrections have been calculated and they depend on the detector acceptance. Therefore the data are corrected for these radiative effects and can then be compared more easily with data by other experiments and they can be compared with the theoretical predictions of lowest order.

Interference of the photon propagator with the neutral weak current (fig. 2.3) leads to modifications of the cross-sections. A quantitative prediction has been made by the standard model of Glashow, Salam and Weinberg, in which the weak neutral current is mediated by one intermediate boson Z^0. In lowest order the cross-section for $e^+e^- \to \mu^+\mu^-$ and $e^+e^- \to \tau^+\tau^-$ is given by [11]:

$$\frac{d\sigma}{d\Omega} = \frac{\alpha^2}{4s}(C_1(1+\cos^2\theta) + C_2\cos\theta) \tag{2.4}$$

where θ is the polar angle of the lepton,

$$C_1 = 1 + 2v_e v_\ell \chi + (v_e^2 + a_e^2)(v_\ell^2 + a_\ell^2)\chi^2\,,$$

$$C_2 = \ +4a_e a_\ell \chi + 8v_e v_\ell a_e a_\ell \chi^2\,.$$

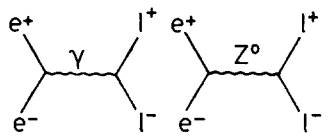

Fig. 2.3. $e^+e^- \to \ell^+\ell^-$ ($\ell = \mu$ or τ) in lowest order in the standard model.

Table 2.1
Weak coupling constants

Particle f	a_f	v_f	$v_f(\sin^2\theta_W = 0.22)$
e, μ, τ	−1	$-1+4\sin^2\theta_W$	−0.12
u, c, t	+1	$+1-(8/3)\sin^2\theta_W$	0.41
d, s, b	−1	$-1+(4/3)\sin^2\theta_W$	−0.71

v_ℓ and a_ℓ denote the vector and axial-vector weak couplings of the leptons ℓ (ℓ = e, μ or τ), their values are given in table 2.1. χ is given by:

$$\chi = \frac{\rho G_F M_Z^2}{8\pi\alpha\sqrt{2}} \frac{s}{s - M_Z^2} . \tag{2.5}$$

Here G_F is the Fermi coupling constant and M_Z the mass of the Z^0. G_F and α have been determined accurately [12] and their errors will be neglected. The mass M_Z of the Z^0 was determined by the experiments at the $p\bar{p}$ collider to be $M_Z = 93 \pm 2$ GeV [13]. ρ is defined as

$$\rho = M_W^2/(M_Z^2 \cos^2\theta_W) \tag{2.6}$$

where θ_W is the weak mixing angle. In the standard model at the Born level ρ is identical to 1, and we shall use this value, which agrees with current measurements [13, 14].

The cross-section (2.4) leads to a deviation of the angular distribution from the distribution predicted by QED. It has become customary to express this deviation by the angular asymmetry which is defined as:

$$A = (N_F - N_B)/(N_F + N_B)$$

where N_F is the differential cross-section integrated over the forward and N_B over the backward region; forward and backward refer to θ being smaller and larger than 90°, respectively. The asymmetry of the differential QED cross-section is zero in lowest order (eq. 2.2); an asymmetry is introduced by α^3 effects, which is however small for the cuts used. In the standard model the asymmetry is:

$$A = \tfrac{3}{8} C_2/C_1 \approx 1.5 \cdot a_e a_\ell \cdot \chi . \tag{2.7}$$

The approximation is valid at energies where the weak amplitude is small compared with the electromagnetic one; it is still good to a one percent accuracy even at the highest PETRA energy. The asymmetry is thus mainly sensitive to the axial-vector weak coupling. A is shown in fig. 2.14 as a function of s; around $s \approx 2000$ GeV^2 it is $\sim -16\%$. Approximately a third of the asymmetry is due to the finite Z-mass in the propagator.

Since several parameters enter the expression for the asymmetry the comparison with the data can be used to extract different parameters depending on the assumptions one is willing to make. If χ is parameterized by G_F, α and ρ as in eq. (2.5), a very precise prediction is obtained for the asymmetry, since the errors of G_F and α are negligible, $\rho = 1$ is assumed and the expression depends only weakly on M_Z. This parameterization will be used for the determination of the coupling parameters v_ℓ and a_ℓ for ℓ = μ or τ (and later also for the c- and b-quarks, sections 7.1 and 7.2.4 respectively).

A second method to compare the data with the predictions was first used in [48]. G_F which is related to the strength of the charged weak current is eliminated in χ by using relation (2.6) and $M_Z^2 = \pi\alpha/(\sqrt{2}G_F \sin^2\theta_W \cos^2\theta_W)$. Then one has:

$$\chi = \frac{1}{16 \sin^2\theta_W \cos^2\theta_W} \frac{s}{s - M_Z^2} . \tag{2.8}$$

This parameterization gives a much stronger dependence on $\sin^2\theta_W$ and M_Z than the one by eq. (2.5). Assuming the standard values for the v_ℓ and a_ℓ one can determine either M_Z or $\sin^2\theta_W$. The predicted asymmetry has a slightly different value with the two parameterizations for the current values of $\sin^2\theta_W$ and M_Z. This difference is resolved if complete electroweak one-loop corrections are applied to the asymmetry which have been calculated in both parameterizations and turn out to be slightly different [49, 50].

For fermions f of charge Q_f the asymmetry (eq. 2.7) is modified into:

$$A \approx -1.5 \frac{a_e a_f}{Q_f} \chi . \tag{2.9}$$

For fractionally charged quarks one therefore expects a larger asymmetry than for muons and taus, for b quarks for example an asymmetry of approximately -0.28 is expected at $\sqrt{s} = 34.6$ GeV.

The total cross-section is obtained by integrating eq. (2.4) and is given by:

$$R = \sigma_{\ell\ell}/\sigma_0 = C_1 \qquad \text{with } \sigma_0 = 4\pi\alpha^2/3s . \tag{2.10}$$

σ_0 is the lowest order total cross-section for lepton pairs produced by e^+e^- annihilation in the s-channel.

For Bhabha scattering the deviation from QED predicted by the standard model with the numerical values as indicated is small due to the t-channel contributions. Even at the highest energy the deviations are below the experimental precision (see fig. 2.8). The differential cross-section in lowest order is given by:

$$\frac{d\sigma}{d\Omega} = \frac{\alpha^2}{8s} [4B_1 + (B_3 + B_2)(1 + x^2) + 2(B_3 - B_2)x] \tag{2.11}$$

where

$$B_1 = \frac{s^2}{t} (1 + (v_e^2 - a_e^2)\chi')^2$$

$$B_2 = (1 + (v_e^2 - a_e^2)\chi)^2$$

$$2B_3 = \left(1 + \frac{s}{t} + (v_e + a_e)^2\left(\frac{s}{t}\chi' + \chi\right)\right)^2 + \left(1 + \frac{s}{t} + (v_e - a_e)^2\left(\frac{s}{t}\chi' + \chi\right)\right)^2 .$$

The momentum transfer t is in the high-energy limit given by $t = -0.5s(1 - \cos\theta)$ and χ' is defined in analogy to χ simply replacing s by t in eq. (2.5).

2.2. Study of $e^+e^- \to e^+e^-$ and $e^+e^- \to \gamma\gamma$

The study of Bhabha scattering and of $e^+e^- \to \gamma\gamma$ is of fundamental importance for any e^+e^--experiment since these reactions provide sensitive tests of QED and furthermore are used as normalisation processes for other reactions. The experimental signature of the two processes is very similar, namely two energetic clusters back to back in the lead-glass detectors; a common event selection was therefore used.

Two clusters of energy deposited in the lead-glass arrays were required, each corresponding to an energy $E > E_{\text{beam}}/3$, where E_{beam} is the beam energy [16, 17]. Furthermore they had to be collinear within 10° assuming that the origin of the particles was the interaction region of the e^+e^--beams. Acollinearity was defined as:

$$\alpha = \pi - \arccos(\boldsymbol{u}_1 \cdot \boldsymbol{u}_2) \tag{2.12}$$

where $\boldsymbol{u}_i$ was the unit vector pointing to the ith cluster.

2.2.1. Luminosity determination

For the determination of the luminosity no attempt was made to separate $e^+e^- \to e^+e^-$ and $e^+e^- \to \gamma\gamma$; the latter process contributes ~12% in the barrel part of the detector but only ~1.7% in the end-caps. Small corrections were applied for background (from $e^+e^- \to$ hadrons, $\tau^+\tau^-$ and $e^+e^-\gamma$) and for detector effects (e.g. dead counters and gaps).

The acceptance was calculated using programs by Berends and Kleiss, which included all diagrams up to order α^3 [18, 20].

The luminosity was determined separately for the barrel part ($|\cos\theta| \leq 0.76$) where an estimated systematic error of 1.5% was achieved (2.5% for the high-energy running at $\sqrt{s} \geq 40$ GeV), and the end-cap region ($0.91 < |\cos\theta| < 0.95$), where the systematic error was estimated to be 2.8%. The main contributions to the systematic errors came from uncertainties in the counter geometry and missing corrections for radiative effects of orders α^4 and higher. The two luminosity values agree well within the errors (see fig. 2.4).

2.2.2. Total cross-section and angular distributions

For the comparison of the Bhabha and $\gamma\gamma$ data to theory the small background which was still contained in the selected data sample was reduced by visually scanning ambiguous events. By this procedure the background from $e^+e^- \to$ hadrons could be reduced to a negligible fraction and that from $e^+e^- \to \tau^+\tau^-$ and $e^+e^-\gamma$ events was reduced to ~0.1% at $\sqrt{s} = 30$ GeV.

The jet-chamber information was used to separate e^+e^- from $\gamma\gamma$ final states. For $\gamma\gamma$ events, at least one energy cluster in the lead-glass had to have no high-energy track pointing towards it. Corrections were then applied for a background from doubly converted $\gamma\gamma$ events in $e^+e^- \to e^+e^-$ and for the loss of them in $e^+e^- \to \gamma\gamma$. The conversion probability in the material of the detector was determined by determining the fraction of $e^+e^- \to \gamma\gamma$ events where one photon had converted. It is ~15% at 90° to the beam direction. Radiative corrections were applied to correct for effects of order α^3 using programs by Berends et al. mentioned above. The total cross sections for $e^+e^- \to e^+e^-$ and $e^+e^- \to \gamma\gamma$ for $|\cos\theta| < 0.76$ normalized to the end-cap luminosity are shown in fig. 2.5 as a function of $\sqrt{s}$. They are compared with lowest order QED and the agreement is excellent.

The angular distributions for $e^+e^- \to e^+e^-$ and $e^+e^- \to \gamma\gamma$ at four centre-of-mass energies are shown

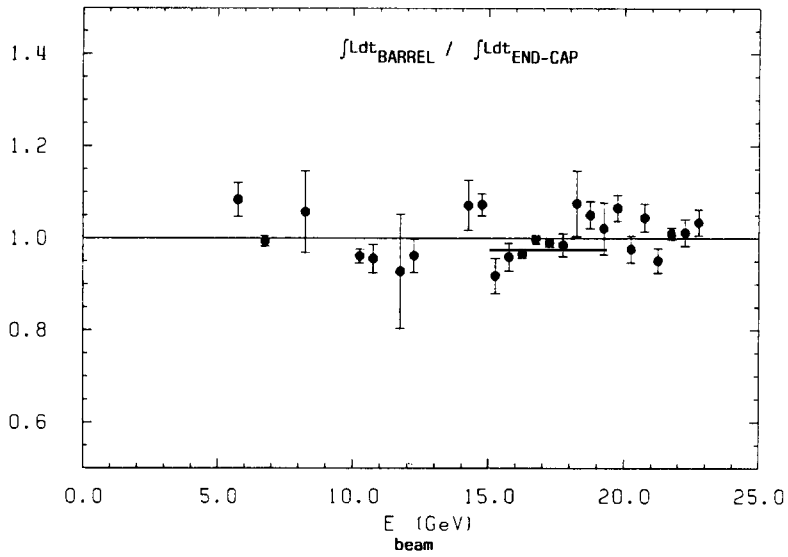

Fig. 2.4. Comparison of the integrated luminosity determined in the barrel and end-cap parts of the detector. The errors are statistical.

in figs. 2.6 and 2.7. To determine the angular distributions for Bhabha scattering, the events were separated into "forward", i.e. the positive electron is scattered at an angle $\theta < 90°$ with respect to the positron beam direction, and "backward", i.e. $\theta > 90°$. The jet-chamber information was used for the charge separation. 8% of the events at $\sqrt{s} = 30$ GeV had the same measured charge, partially due to charge confusion after showering in the material of the detector and partially due to the finite momentum resolution. The same sign events were corrected for statistically in each angular bin. The

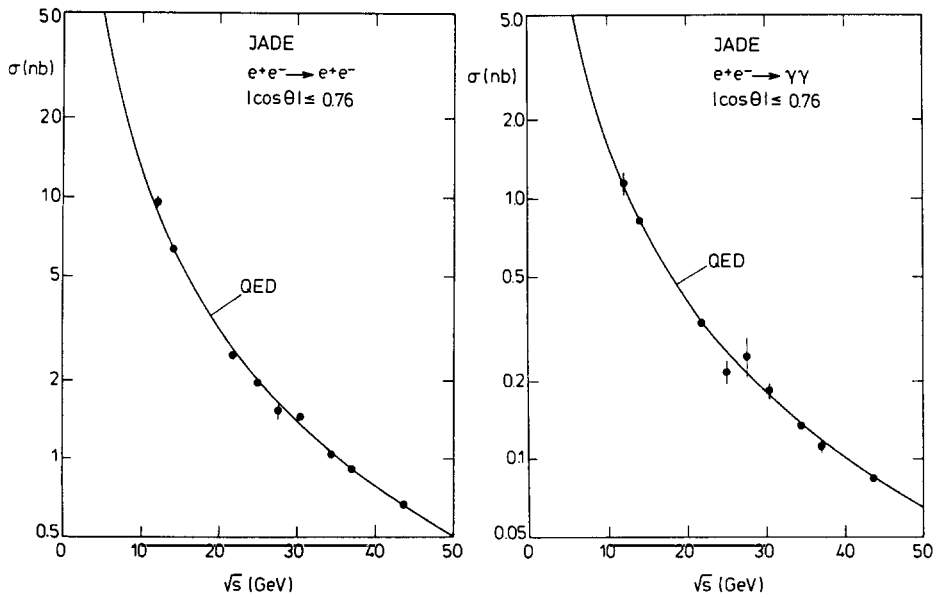

Fig. 2.5. Total cross-section for $|\cos\theta| < 0.76$ as a function of the centre-of-mass energy $\sqrt{s}$ for $e^+e^- \to e^+e^-$ and $e^+e^- \to \gamma\gamma$.

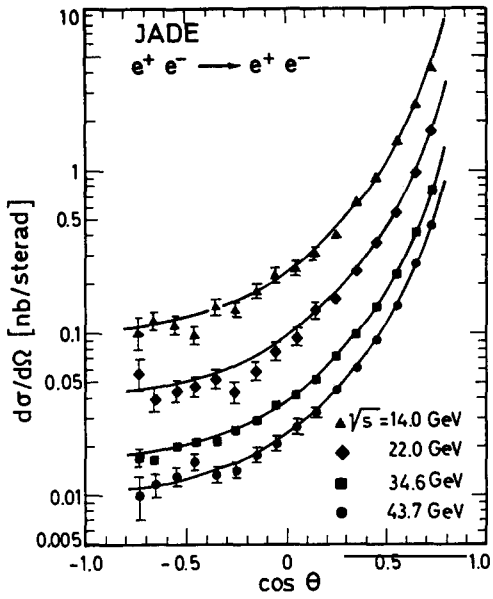

Fig. 2.6. Differential cross-section for $e^+e^- \to e^+e^-$ at four values of the centre-of-mass energy.

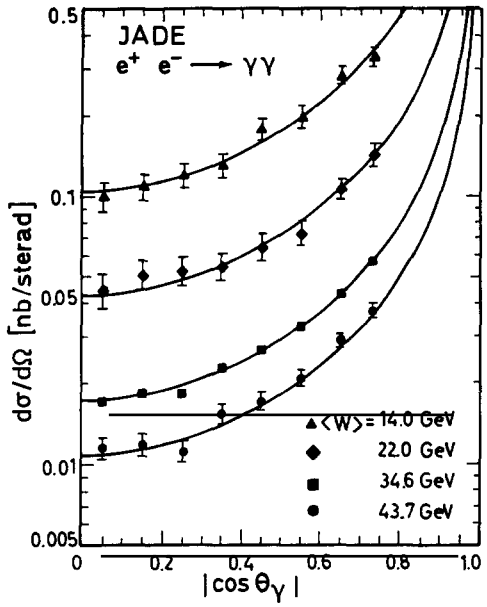

Fig. 2.7. Differential cross-section for $e^+e^- \to \gamma\gamma$ at four values of the centre-of-mass energy.

angular distributions for both processes are well described by the predictions of QED which are also indicated in figs. 2.6 and 2.7.

Deviations from QED are expected for Bhabha scattering due to electroweak interference effects, which are small and can be calculated in the standard model. They will be discussed in more detail in section 2.4. Note that the weak neutral current does not contribute to $e^+e^- \to \gamma\gamma$ in lowest order.

Limits can be derived for a possible break-down of QED at high momentum transfers, which could occur, for example, if the fermions were not point-like. Such a hypothetical break-down of QED can be taken into account by introducing form-factors $F(q^2)$ in the cross-sections. They can be parameterized by introducing a cut-off parameter Λ [23, 21, 22], for $\Lambda \to \infty$ the validity of QED is restored,

$$F(q^2) = 1 \mp \frac{q^2}{q^2 - (\Lambda_\pm^{\mathrm{QED}})^2} \,. \tag{2.13}$$

The form-factors lead to a modification of the angular distribution as well as the total rate for Bhabha scattering. The lower limits at 95% confidence level for the cut-off parameters assuming that Λ is the same in the s- and t-channel are given in table 2.2 and displayed in fig. 2.9. They are of the order of 200 GeV, i.e. QED remains valid at distances of the order of 10^{-16} cm.

For $e^+e^- \to \gamma\gamma$ a deviation from QED could for example be caused by the exchange of a heavy electron; the deviations are proportional to Q^4. The modified cross-section is given by:

$$\frac{\mathrm{d}\sigma}{\mathrm{d}\Omega} = \frac{\alpha^2}{s} \frac{1+x^2}{1-x^2} \left[\pm \frac{s^2}{2\Lambda_\pm^4} (1-x^2) \right].$$

The lower limits on Λ are given in table 2.2. The limits on the mass of a new heavy lepton which can be derived from Λ_+ will be discussed in chapter 8.

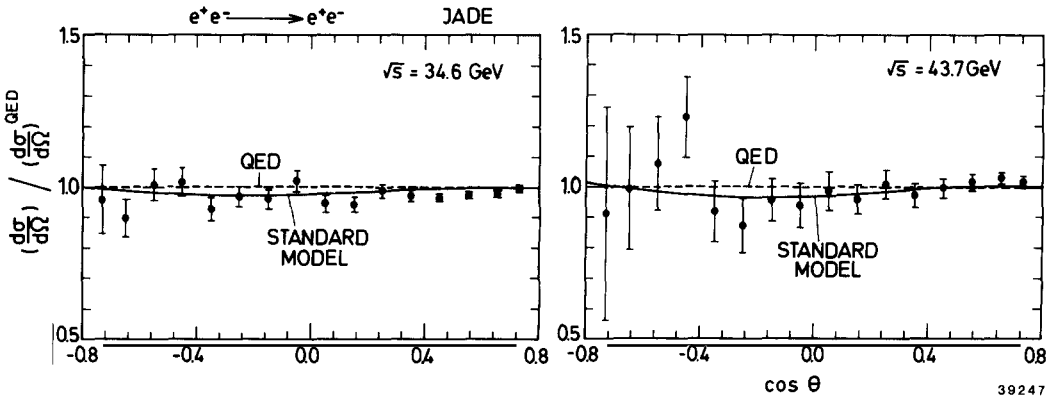

Fig. 2.8. Ratio of the measured angular distribution for $e^+e^- \to e^+e^-$ to the QED expectation for two centre-of-mass energies.

Table 2.2
Lower limits at 95% C.L. for the QED cut-off parameters. For $e^+e^- \to e^+e^-$ and $e^+e^- \to$ hadrons electroweak effects were taken into account

Final state	e^+e^-	$\mu^+\mu^-$	$\tau^+\tau^-$	$\gamma\gamma$	Hadrons
Λ_+	174	230	345	66.3	277
Λ_-	313	245	220	75.3	266

Comparisons of Bhabha scattering to QED and electroweak theories were also done by CELLO [24], MARK J [39], PLUTO [25] and TASSO [26] at PETRA. They came to similar conclusions as described here. HRS and MAC [15] at PEP claim a deviation from QED by two standard deviations in agreement with the standard model.

2.3. *Production of muon and tau pairs*

The charge asymmetry predicted by electroweak theories was first established in $e^+e^- \to \mu^+\mu^-$ at an energy of $s \approx 1000\ \text{GeV}^2$ [27, 28]. Since these early results the statistical error has been reduced and the

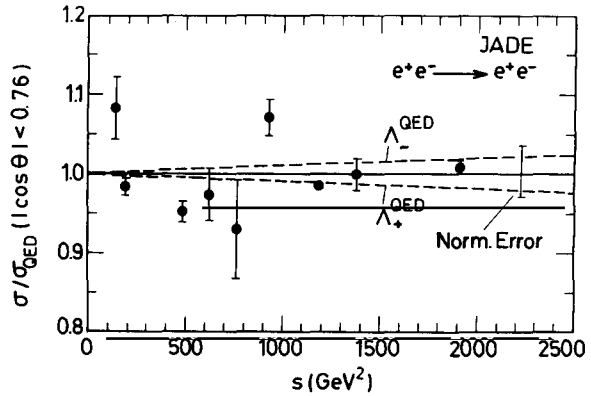

Fig. 2.9. Ratio of the measured total cross-section for $e^+e^- \to e^+e^-$ to the QED expectation for $|\cos\theta| < 0.76$.

range of energy has been extended up to $s \approx 2000\,\mathrm{GeV}^2$. The asymmetry has in addition been established for τ pairs. All data were found to be in agreement with the standard model within the experimental errors [29, 30, 31].

2.3.1. Event selection: $e^+e^- \to \mu^+\mu^-$

The selection of muon pair candidates started by selecting pairs of tracks of momentum $p > E_{\mathrm{beam}}/3$ in a fiducial region of $|\cos\theta| < 0.80$, where θ was the angle between the track and the positron beam direction. For the data around 34 GeV muon pairs were also analysed in the forward direction around $\cos\theta \sim 0.89$. The following cuts were applied:

1. The tracks must be back to back with an acollinearity $\alpha < 0.2$ radians and must come from the interaction region within 3 mm in the $r\varphi$-plane and within 80 mm in the beam direction.

2. The energy deposited in the lead-glass counters had to be compatible with that of a minimum ionising particle. The particle had to be identified as penetrating in the muon filter.

3. A time-of-flight cut was applied to remove cosmic rays.

Remaining background was removed by a visual scan of the events. After this procedure the background from Bhabha events and cosmic rays was negligible except in the data at the highest beam energies, where a background of 3% from cosmic rays remained due to large background in the TOF counters. It was subtracted statistically.

The contribution of muon pairs from two-photon scattering was calculated to be 0.7% using the programs by Vermaseren et al. [32]. Tau pairs, where both taus decayed leptonically into a muon were calculated to constitute 2% of the final sample (for the description of the τ Monte Carlo events see next paragraph). The total detection efficiency was ~65%.

2.3.2. Event selection: $e^+e^- \to \tau^+\tau^-$

Taus decay into leptons or hadrons and are accompanied by one or two neutrinos which carry away a fraction of energy and momentum. The event topology is thus more complicated than for muon pairs and numerous cuts were necessary to select a clean tau sample. The aim of the tau selection was high efficiency, i.e. all decays were selected except those where both taus decayed into electrons or both into muons and neutrinos (for the detailed cuts see [30]). The event selection started from events which had between 2 and 10 tracks of at least 100 MeV coming from the interaction region. The events were required to form two "jets" by the following cuts: the jet-axes, which were given by the vector sum of the momenta of the charged particles in a jet, were required to be separated by at least 100°, that is the jets emanated from the beam roughly back to back. All particles of a jet were required to be in a cone of opening angle 45° around the jet-axis. If there were only two charged particles in the event they were required to have momenta above 1 GeV.

The lead-glass counters were used to remove Bhabha and e^+e^- events from two-photon scattering, and the muon filter was used to remove $\mu^+\mu^-$ events. Multihadronic events were rejected by requiring both jets to have an invariant mass below 3 GeV and one of them below 2 GeV.

The detection efficiency and background contributions were calculated using Monte Carlo techniques. Tau pairs were generated according to the QED or electroweak cross-section and decayed according to the known branching ratios [12]. A full detector simulation was applied to the decay products and the same analysis programs as for the data were applied to the events generated in this way. The efficiency of the event selection was found to be $(41.3 \pm 0.6)\%$ which corresponded to 72% in the analysed angular region of $|\cos\theta| < 0.76$.

In the final sample, which was obtained after a visual scan to eliminate background events, the

remaining background was $(5.7 \pm 0.8)\%$. The largest background contributions came from the processes $e^+e^- \to e^+e^-\tau^+\tau^-$ and $e^+e^- \to$ hadrons. The background from other two-photon reactions was small. The Bhabha background was estimated to be $(0.6 \pm 0.6)\%$.

2.3.3. Results for muon and tau cross-sections

The data for μ and τ pairs were corrected for effects of order α^3 (diagrams in fig. 2.2) using Monte Carlo programs by Berends, Kleiss and Jadach [33] (for τ's a comparison was also made to [34]). QED corrections in the Z^0 amplitudes were not taken into account. Radiative effects increase the total measured cross-section for τ pairs by a factor ~1.3. For muon pairs the correction factor was close to 1 because of the collinearity cut. The radiative effects produced an angular asymmetry, which was determined to be +2.0% for μ pairs and +1.5% for τ pairs. The total cross-sections are shown in figs. 2.10 and 2.11 as a function of s; within errors they agree well with the QED prediction of lowest order which is also shown. Possible deviations were parameterized by form-factors. In contrast to Bhabha scattering, where the form-factors modify the shape of the angular distribution, only the total rate is affected for μ and τ pairs:

$$\sigma = \frac{4\pi\alpha^2}{3s} |F(s)|^2 .$$

F has been defined in eq. (2.13). The lower limits for the cut-off parameters Λ obtained from the measured cross-sections are given in table 2.2. They exceed 200 GeV, implying that QED describes the total cross-sections well up to s values of 2000 GeV^2 and muons and taus still behave as point-like particles.

The radiatively-corrected angular distributions are shown in figs. 2.12 and 2.13. θ is the angle between the positive muon and the positron beam direction for μ pairs. For muon pairs the number of same sign tracks was negligible if a vertex constrained fit was used.

For τ pairs the original flight direction could only be approximately reconstructed. The simulations showed that the best approximation was given by the vector difference of the two jet-axes. In order to

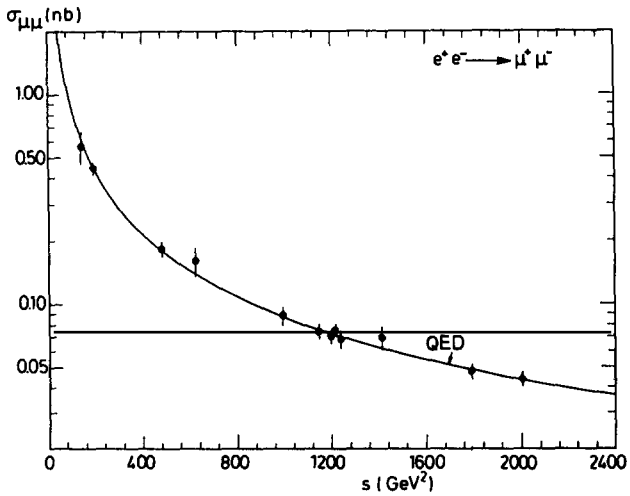

Fig. 2.10. Total cross-section for $e^+e^- \to \mu^+\mu^-$ as a function of s.

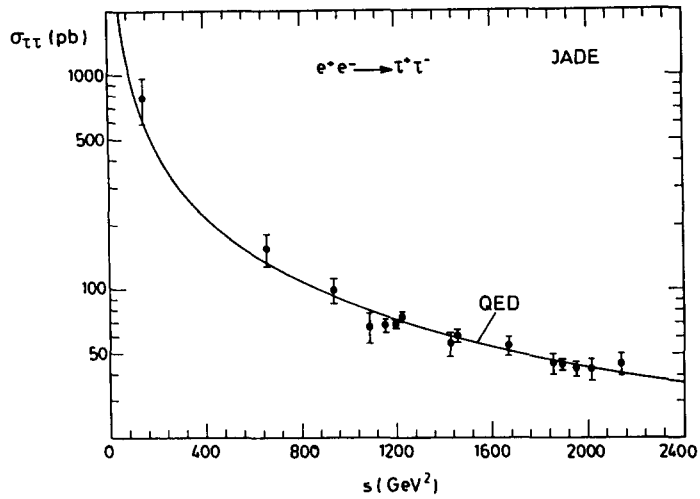

Fig. 2.11. Total cross-section for $e^+e^- \rightarrow \tau^+\tau^-$ as a function of s.

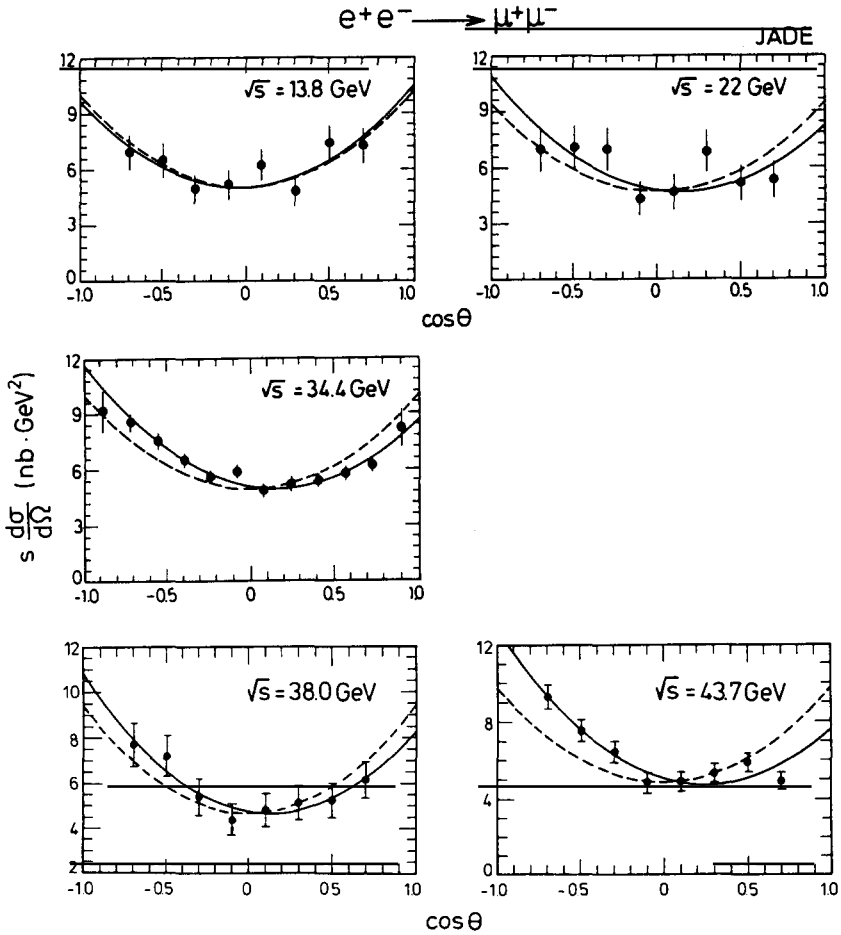

Fig. 2.12. Differential cross-section for $e^+e^- \rightarrow \mu^+\mu^-$ at five values of s; the full curves represent the asymmetric fits while the dashed curves represent the symmetric behaviour expected from QED.

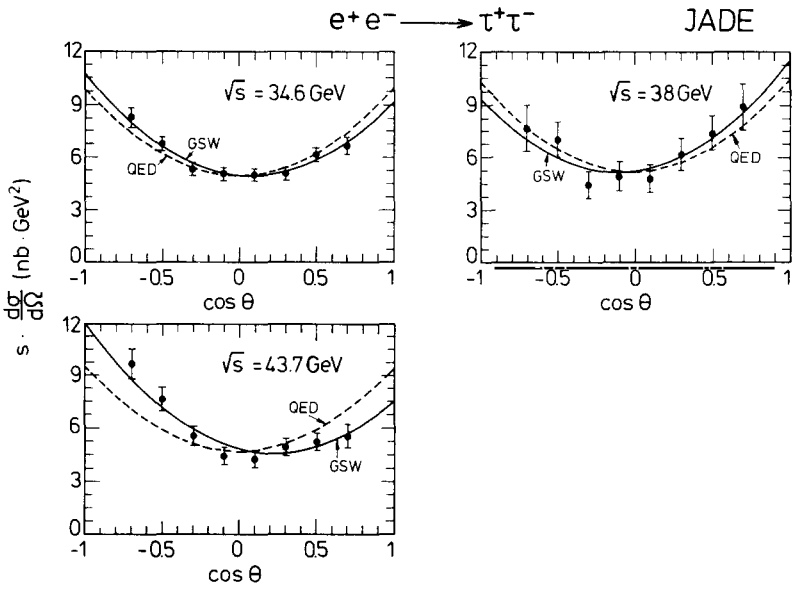

Fig. 2.13. Differential cross-section for $e^+e^- \to \tau^+\tau^-$ at two values of s; the curves are explained in fig. 2.12.

determine uniquely whether a tau pair had been produced in the forward or backward direction one jet was restricted to have only one charged track according to which the event was classified as being forward or backward.

The curves in figs. 2.12 and 2.13 show fits of the angular distribution given in eq. (2.4) to the data where C_1 and C_2 were treated as free parameters. Allowing for a non-zero asymmetry ($C_2 \neq 0$) one obtains the full lines which at high energies describe the data better than the symmetric dashed lines, which represent pure QED.

The resulting fitted asymmetries are given in table 2.3. The first error quoted is statistical, while the second one is the estimated systematic error. The systematic errors have different origins for muons and taus. For muons the main contribution comes from possible errors in the charge determination and an unrecognised Bhabha background. For τ's, the main uncertainties were Bhabha events, two-photon background and uncertainties in the determination of the flight direction of the tau.

The asymmetry values obtained from the JADE data are shown together with measurements by other experiments at PETRA [26, 28, 35–42] and PEP [43–47] as a function of s in fig. 2.14. There is good agreement of the JADE data with others at the same energy. The prediction of the standard

Table 2.3
Asymmetries for $e^+e^- \to \mu^+\mu^-$ and $\tau^+\tau^-$. Where two errors are given, the second one is due to systematics

$e^+e^- \to \mu^+\mu^-$					$e^+e^- \to \tau^+\tau^-$				
s (GeV^2)	$\int L\,dt$ (pb^{-1})	Events	A (%)	$A_{St.M}$ (%)	s (GeV^2)	$\int L\,dt$ (pb^{-1})	Events	A (%)	$A_{St.M}$ (%)
192.0	1.6	458	$+2.7 \pm 4.9$	−1.2	1195.0	62.4	1998	$-6.0 \pm 2.5 \pm 1.0$	−8.8
484.0	2.4	264	-10.6 ± 6.4	−3.2	1444.0	11.8	336	$+7.5 \pm 6.3 \pm 1.0$	−11.1
1181.7	71.2	3400	$-11.1 \pm 1.8 \pm 1.0$	−8.7	1909.7	43.1	913	$-17.0 \pm 3.6 \pm 1.0$	−15.6
1444.0	11.9	422	$-9.7 \pm 5.0 \pm 1.0$	−11.1					
1909.7	43.1	1258	$-19.1 \pm 2.8 \pm 1.0$	−15.6					

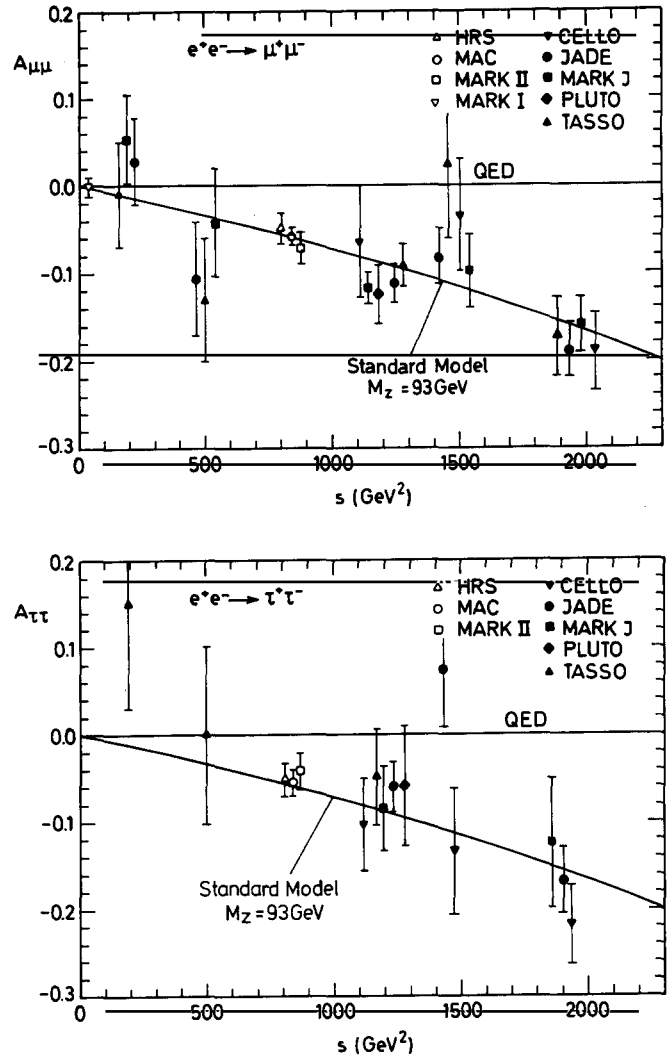

Fig. 2.14. Asymmetry as a function of s for $e^+e^- \rightarrow \mu^+\mu^-$ and $e^+e^- \rightarrow \tau^+\tau^-$.

model in fig. 2.14 was calculated using eqs. (2.7) and (2.8) with $M_Z = 93$ GeV and $\sin^2\theta_W = 0.22$. The data are in agreement with the standard model within two to three standard deviations. A detailed comparison will follow in the next section.

2.4. *Comparison with electroweak theories*

As explained in the previous sections the data are already corrected for α^3 radiative effects which affect the diagrams with a photon propagator (fig. 2.2). Corrections for the Z^0 exchange amplitudes were also applied to the asymmetry. They consist of QED corrections – for example radiation of a photon – and purely weak corrections, the most important one is the self-energy of the Z^0. The corrections have been calculated in both parameterizations of χ [49, 50] and are slightly different. The corrections are negligible for the parameterization of χ by $\sin^2\theta_W$ and M_Z, but change the expected

asymmetry by roughly +0.01 if G_F and $\sin^2\theta_W$ are used. We shall always apply the correction to the theoretical prediction, which is then independent of the parameterization. The electroweak corrections have been calculated within the standard model, i.e. assuming the existence of one Higgs doublet. They depend very weakly on the mass spectrum of all leptons and quarks and also the Z, W and Higgs masses. Recently they have been extended to a model with two Higgs doublets [51]. In such a model the predicted asymmetry is either unaffected or slightly lower in magnitude than the standard asymmetry.

2.4.1. Determination of weak coupling constants

The simplest way to determine the axial–vector coupling constants for muons and taus is to calculate them by comparing eq. (2.7) with the measured asymmetries. The values obtained at three values of s and averaged over all s values are shown in table 2.4. The errors in table 2.4 include the statistical and experimental systematic errors. The error due to the uncertainty in the Z mass is negligible in comparison with the experimental errors. The values of $a_e a_\mu$ agree approximately within one standard deviation with the expectation and those for $a_e a_\tau$ within 1.5–2 standard deviations. Within statistical and systematic errors universality of muons and taus is confirmed.

The constraints on the weak vector couplings come mainly from the total cross-section. Assuming again $M_Z = 93$ GeV and setting $a_e a_\ell = 1$ one obtains, averaging over all energies:

$$v_e v_\mu = 0.07 \pm 0.37, \qquad v_e v_\tau = 0.20 \pm 0.34 .$$

The quoted errors are statistical, a normalisation error of typically 4% leads to a systematic error approximately three times the size of the statistical one. The results depend only weakly on the exact value of $a_e a_\ell$. Both measurements are in agreement with the prediction of the standard model, which is $v_e v_\ell = 0.017$ with $\sin^2\theta_W = 0.217$. The large errors of the vector coupling constants are characteristic for leptonic e^+e^- reactions since the predicted deviation of the total cross-section from QED due to electroweak effects is small; it is approximately 0.8% at $s = 2000\ \text{GeV}^2$, well below the measurement errors, see fig. 2.15.

For Bhabha scattering the prediction of the standard model with $a_e = -1$ and $v_e = -0.13$ is shown in fig. 2.8. The electroweak contributions only lead to a small deviation in the angular distribution with respect to QED. The expected difference at $\cos\theta \sim -0.2$ is approximately 2% at $s = 1195\ \text{GeV}^2$ and 4.4% at $s = 1909.7\ \text{GeV}^2$. The experimental errors are similar at the lower s value and twice as large for the higher value of s. Under the assumption that the weak neutral current is described by the standard model the weak coupling constants for electrons were deduced from a fit of the high energy data to eq. (2.11). They are shown in line 1 of table 2.5 and are close to the expectation.

The experimental results for the axial–vector and vector coupling constants of electrons, muons and taus are consistent with universality. So one can assume universality and perform two-dimensional fits with v_ℓ and a_ℓ as free parameters. Their small correlation will then also be taken into account. The fit

Table 2.4
Measured axial–vector coupling constants

s	1182 GeV^2	1443 GeV^2	1909 GeV^2	Average
$a_e a_\mu$	1.27 ± 0.24	0.88 ± 0.47	1.22 ± 0.20	1.21 ± 0.14
$a_e a_\tau$	0.68 ± 0.30	-0.68 ± 0.57	1.09 ± 0.25	0.76 ± 0.18

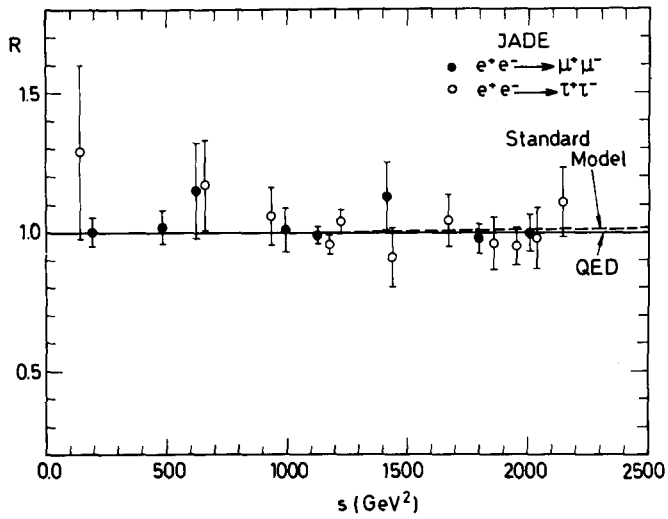

Fig. 2.15. Total cross-section ratio for $e^+e^- \to \mu^+\mu^-$ and $e^+e^- \to \tau^+\tau^-$ compared with the predictions from QED (full line) and standard model (dashed line).

results assuming e–μ or e–τ universality are shown in lines 2 and 3 of table 2.5. Finally a common fit was made of all data, assuming e–μ –τ universality; the results are shown in the last line of table 2.5. The prediction of the standard model for the axial-vector coupling constant is confirmed with an error of 8%.

The weak coupling constants have also been determined in neutrino scattering off electrons, which is also a purely leptonic process [53]. There, two sets of solutions exist, one of which is excluded by the e^+e^- measurements. The remaining solution is [52]:

$$a_e = 2g_A = -0.990 \pm 0.052, \qquad v_e = 2g_V = -0.076 \pm 0.094$$

in good agreement with the e^+e^- values assuming lepton universality.

2.4.2. *Determination of* $\sin^2\theta_W$ *and* M_Z

We have compared the predictions of the standard model for the charge asymmetry A and the normalised cross-section R (eqs. (2.7) and (2.10)) with the measured muon and tau asymmetries and R values using the parameterization of χ as in eq. (2.8) with M_Z and $\sin^2\theta_W$ as free parameters. The contours of 68% and 95% C.L. are shown for μ pairs in fig. 2.16. The limit at 95% C.L. is also shown for a combined fit to μ- and τ-pair data. The contour extends along the prediction of the standard model, its "width" is related to the errors of the measured angular asymmetry and the "length" (and

Table 2.5
Coupling constants from 2-parameter fits and results for $\sin^2\theta_W$

Input	$\lvert a_\ell \rvert$	$\lvert v_\ell \rvert$	$\sin^2\theta_W$
e^+e^-	$0.96^{+0.28}_{-0.53}$	0.30 ± 0.33	0.26 ± 0.10
$\mu^+\mu^-$	1.11 ± 0.11	0.36 ± 0.50	$0.16^{+0.03}_{-0.02}$
$\tau^+\tau^-$	$0.88^{+0.15}_{-0.18}$	0.50 ± 0.31	–
e^+e^-, $\mu^+\mu^-$, $\tau^+\tau^-$	1.02 ± 0.08	$0.35^{+0.14}_{-0.25}$	$0.20^{+0.03}_{-0.02}$

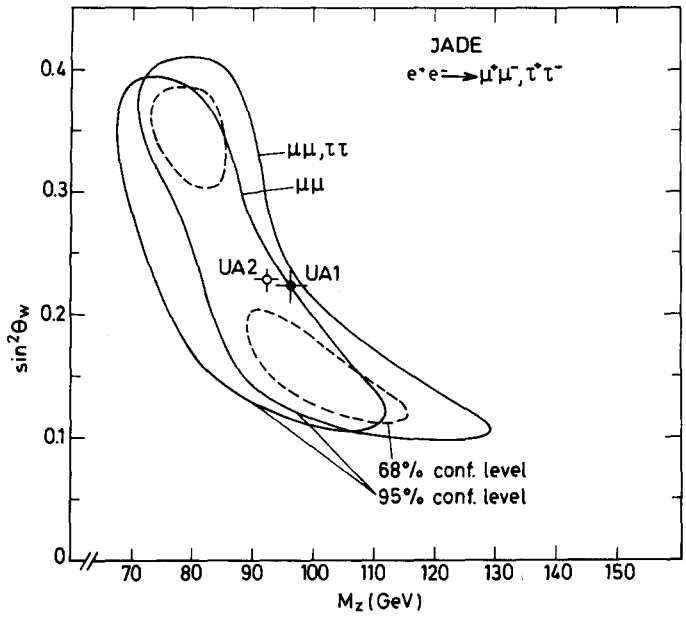

Fig. 2.16. Contours in the $\sin^2\theta_W$, M_Z plane.

also the splitting into two regions) depends strongly on the normalisation error [56]. Due to the shape of this contour a simultaneous precise determination of $\sin^2\theta_W$ and M_Z are not possible. Fixing one of the two parameters leads to the following results for a combined analysis of muons and taus:

$$\sin^2\theta_W = 0.20^{+0.04}_{-0.03} \pm 0.01 \qquad \text{with } M_Z = 93\,\text{GeV fixed}.$$

The second error of $\sin^2\theta_W$ is due to an uncertainty of ± 2 GeV in M_Z. The result changes only slightly when the Bhabha data are also included, while μ pairs alone give a lower value (table 2.5).

Using $\sin^2\theta_W = 0.217$ the mass of the Z is determined to be:

$$M_Z = (91 \pm 4)\,\text{GeV} \qquad \text{for } \mu\mu,\ \tau\tau\,.$$

Muon data alone give 89 ± 5 GeV.

In fig. 2.17 our value of $\sin^2\theta_W$ is compared with other recent values of $\sin^2\theta_W$ determined in other e^+e^- experiments [25, 38, 41] and a combined result from all results from PETRA and PEP [54]. In addition results from neutrino–electron scattering [53], recent results from the $p\bar{p}$ collider [195] and the new precise results from neutrino–nucleon scattering [55] are shown. Agreement within the experimental errors is observed, although all values from e^+e^- annihilation are less than 0.20, while the others are systematically above.

2.5. Tests of QED in processes of order α^3 and α^4

The tests of QED which have been described so far were mainly tests of the cross-sections to lowest order in α and involved contributions from higher orders only as corrections. In this section results on

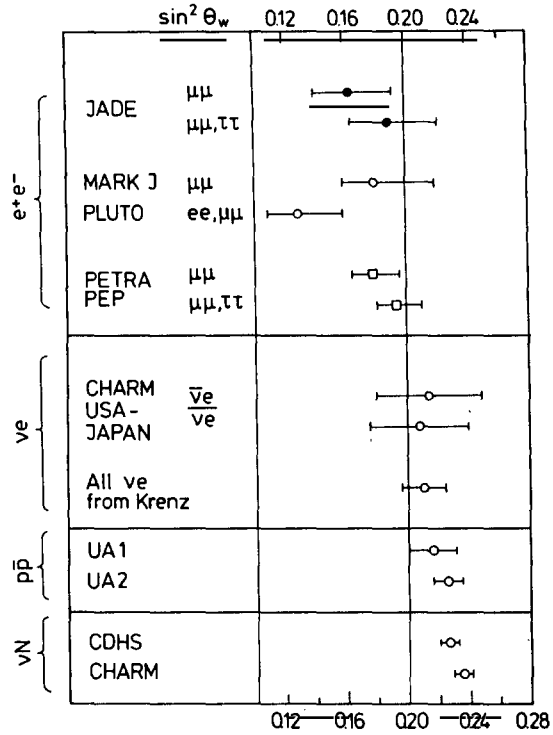

Fig. 2.17. $\sin^2\theta_w$ from recent measurements in different processes. For the references see text. The line at $\sin^2\theta_w = 0.20$ is to guide the eye.

reactions will be discussed which are described by diagrams of order α^3 and α^4. The results serve as tests for QED and for the calculation of the hard radiative corrections.

The processes of order α^3 and α^4 studied by JADE are summarized in table 2.6. The QED calculations up to order α^3 were done using Monte Carlo programs provided by Berends et al. [18, 19, 20]. The calculations for the α^4 processes with two photons were done according to a prescription by Berends et al. [60]. The calculations of the four-lepton final states used the program by Vermaseren [32] and for comparison that by Berends, Daverfeldt and Kleiss [61].

Many experimental distributions were compared with the predictions of QED; agreement between data and theory within statistics was found nearly everywhere. Here we will show a few characteristic distributions which will be accompanied by a brief description of the analysis procedure. The selection cuts are summarized in tables 2.7 and 2.8. More details can be found in [17, 57, 58, 59].

2.5.1. $e^+e^- \to e^+e^-\gamma$, $\gamma\gamma\gamma$, $e^+e^-\gamma\gamma$ *and* $\gamma\gamma\gamma\gamma$

The final states $e^+e^-\gamma$, $\gamma\gamma\gamma$, $e^+e^-\gamma\gamma$ and $\gamma\gamma\gamma\gamma$ were selected by mainly using the lead-glass shower counters. The cuts are listed in table 2.7. Final states with photons only were distinguished from those with electrons and photons by appropriate cuts on the number of "neutral" clusters, i.e. clusters which were not connected with a charged track. The selected events were scanned visually to verify that they corresponded to the desired topology. The number of resulting events are given in table 2.6. Sample distributions of photon energy and polar angle and the invariant mass of electron and photon are shown in figs. 2.18–2.22. The agreement in rate and distributions between data and the order α^3 and α^4 QED calculations which are also shown is in general good.

Table 2.6
Data for leptonic processes of order α^3 and α^4

Final state	$\langle\sqrt{s}\rangle$ (GeV)	$\int L\,dt$ (pb^{-1})	Events	Prediction
$e^+e^-\gamma$	34.4	115.7	3227*	3320 ± 9
(e)eγ	34.4	115.7	3230*	3127.3 ± 4.8
$\gamma\gamma\gamma$	34.4	115.7	246*	235 ± 4
$e^+e^-\gamma\gamma$	34.4	115.7	176	170 ± 5
$\gamma\gamma\gamma\gamma$	34.4	115.7	10	9.0 ± 0.3
$\mu^+\mu^-\gamma$	35.1	99.5	340	332.4 ± 4.2
$\mu^+\mu^-\gamma\gamma$	35.0	80.6	16	11.7
$\tau^+\tau^-\gamma$	36.6	89.0	112*	100 ± 4
$\tau^+\tau^-\gamma\gamma$	36.6	89.0	9.4*	9.7 ± 1.2
$e^+e^-\mu^+\mu^-$	36.4	94.0	8	8.5 ± 0.5
$e^+e^-e^+e^-$	36.4	94.0	13	11.8 ± 0.6
$e^+e^-e^+\mu^-$	36.4	94.0	0	2 ± 0.5

* Corrected for background and efficiency.

In a few distributions deviations between data and QED are found which cannot be explained by detector effects. For example, the sum of the three cluster energies in $e^+e^- \to e^+e^-\gamma$ has a wider distribution than expected, see fig. 2.23. This is due to α^4 effects, in particular emission of two photons one of which is not detected. Using this deviation one can estimate an upper limit on the error of the luminosity measurement due to missing α^4 corrections, it is $<1\%$.

$e^+e^- \to$ (e)eγ: *Two visible clusters*

A special event selection was made for $e^+e^- \to$ (e)eγ where one electron was not registered since it escaped into the beam pipe. The cross-section for such a topology is large due to the t-channel contribution which results in a large forward peak. The QED prediction for these events in the extreme forward direction could not be calculated with the standard QED programs. Instead an approximate procedure was used: radiation of photons or the incoming electrons followed by Compton scattering off

Table 2.7
Cuts for the processes $e^+e^- \to e^+e^-\gamma$, (e)eγ, $\gamma\gamma\gamma$, $e^+e^-\gamma\gamma$ and $\gamma\gamma\gamma\gamma$

Selection by lead-glass clusters of energies $E_1 > E_2 \ldots$.
$\theta_{i,j} \equiv$ angle between clusters i and j.
$E_{\text{rest}} \equiv$ remaining lead-glass energy outside selected clusters.

Final state	Lead-glass cuts	Angle cuts	Neutral clusters
$e^+e^-\gamma$ $\gamma\gamma\gamma$	3 clusters (barrel) $E_1, E_2 > \sqrt{s}/6$; $E_3 > \sqrt{s}/20$ $E_1 + E_2 + E_3 > 0.75\sqrt{s}$	$\theta_{i,j} > 10°$; $i, j = 1, 2, 3$ $\theta_{12} + \theta_{23} + \theta_{31} > 350°$	≤ 1 for $e^+e^-\gamma$ ≥ 2 for $\gamma\gamma\gamma$
(e)eγ	2 clusters (barrel) $E_1, E_2 > \sqrt{s}/8$ $E_1 + E_2 > 0.50\sqrt{s}$ $E_{\text{rest}} < 1$ GeV	$\alpha > 10°$ $\Delta\varphi < 10°$	1
$e^+e^-\gamma\gamma$ $\gamma\gamma\gamma\gamma$	4 clusters (2 in barrel) $E_1, E_2 > \sqrt{s}/8$ $E_3, E_4 > \sqrt{s}/40$ $E_1 + E_2 + E_3 + E_4 > 0.75\sqrt{s}$ $E_{\text{rest}} < 1$ GeV	$\theta_{i,j} > 10°$; $i, j = 1, \ldots, 4$	2 for $e^+e^-\gamma\gamma$ ≥ 3 for $\gamma\gamma\gamma\gamma$

Table 2.8
Cuts for the processes $e^+e^- \to \mu^+\mu^-\gamma$, $\mu^+\mu^-\gamma\gamma$, $\tau^+\tau^-\gamma$ and $\tau^+\tau^-\gamma\gamma$

$\mu^+\mu^-\gamma$ and $\mu^+\mu^-\gamma\gamma$			
Exactly two tracks ($p > 0.06$ GeV) are required which deposit <2.5 GeV in the lead-glass and one (two) photon(s), of energies $E_1 > E_2$. E_{rest} ≡ remaining neutral energy apart from selected photons.			
Final state	Lead-glass cuts	Angle cuts	Other cuts
$\mu^+\mu^-\gamma$	$E_1 > 1$ GeV $E_{rest} < 1$ GeV	$\theta_{\gamma,\mu} > 20°$ Σ (opening angles) > 355°	$E_{vis} > (2/3)\sqrt{s}$ inv. mass ($\mu\mu$) > 1.2 GeV $1/3 \le E_\gamma^{obs}/E_\gamma^{calc} \le 3$
$\mu^+\mu^-\gamma\gamma$	$E_1 > 1$ GeV, $E_2 > 0.5$ GeV all other photons have energy < 0.5 GeV	$\theta_{\gamma,\mu} > 15°$ Σ (opening angles) > 355°	$E_{vis} > 0.25\sqrt{s}$ momentum balance
$\tau^+\tau^-\gamma$ and $\tau^+\tau^-\gamma\gamma$			
Start from τ-pair sample and demand one (two) photon(s) of energies: $E_1 > E_2$. E_{rest} ≡ remaining energy outside selected photons.			
Final state	Lead-glass cuts	Angle cuts	Other cuts
$\tau^+\tau^-\gamma$	$E_1 > 0.5$ GeV $E_{rest} < 1$ GeV	$\theta_{\gamma,\tau} > 30°$ Σ (opening angles) > 350°	Sum of momenta of τ decay products > 1 GeV
$\tau^+\tau^-\gamma\gamma$	$E_1, E_2 > 0.5$ GeV $E_{rest} < 0.5$ GeV	$\theta_{\gamma,\tau} > 30°$ $\theta_{\gamma_1,\gamma_2} > 10°$ Σ (opening angles) > 350°	Sum of momenta of τ decay products > 1 GeV inv. mass ($\gamma\gamma$) > 0.5 GeV

the positrons (or vice versa). The photon spectrum was calculated in the equivalent photon approximation [62]. Another contribution comes from the α^3 reaction $e^+e^- \to \gamma\gamma\gamma$ where one photon escapes into the beam pipe and a second one converts in the material of the detector. It was calculated using the programs by Berends et al. The sum of the two contributions given in table 2.6 is in reasonable agreement with the observation taking into account statistical and the normalisation errors. Distributions of data and predictions are shown in fig. 2.20 and good agreement is observed.

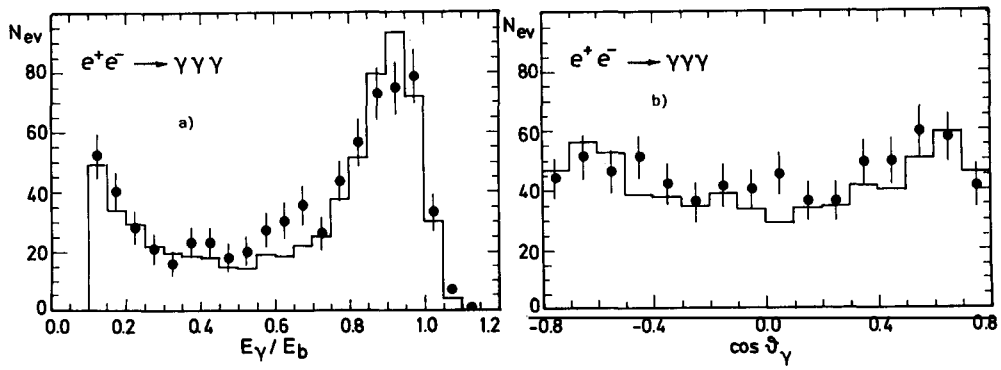

Fig. 2.18. $e^+e^- \to \gamma\gamma\gamma$: a) E_γ/E_{beam} (3 entries/event); b) polar angle of the photon (3 entries/event). The histograms show the predictions of QED to order α^3.

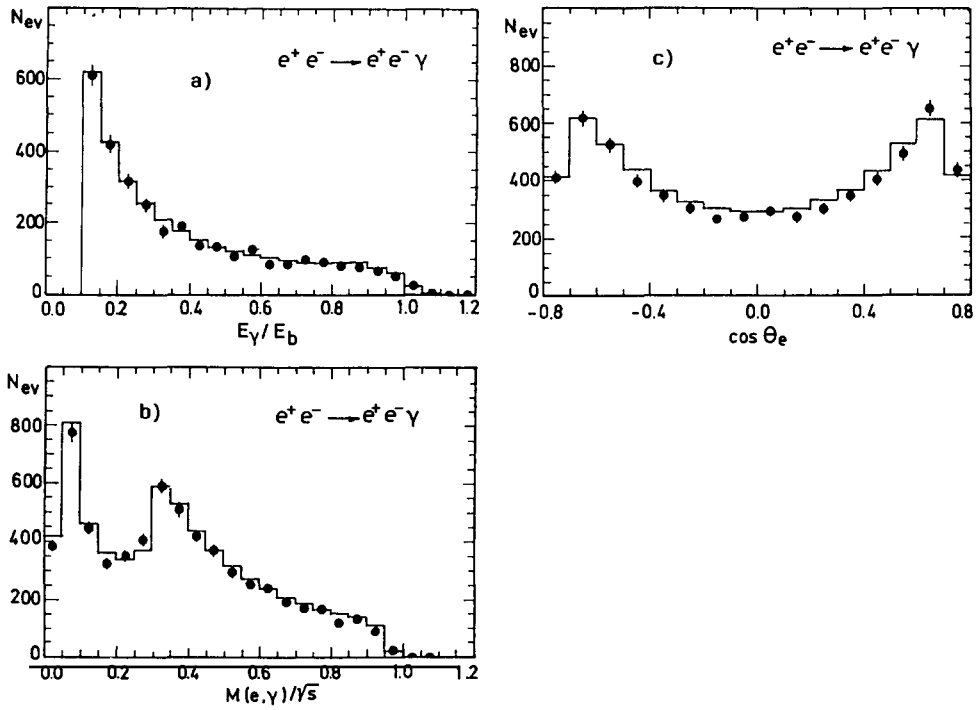

Fig. 2.19. $e^+e^- \to e^+e^-\gamma$: a) E_γ/E_{beam}; b) invariant mass of $M(e\gamma)/\sqrt{s}$ (2 entries/event); c) polar angle of the electron (2 entries/event). The histograms show the predictions of QED to order α^3.

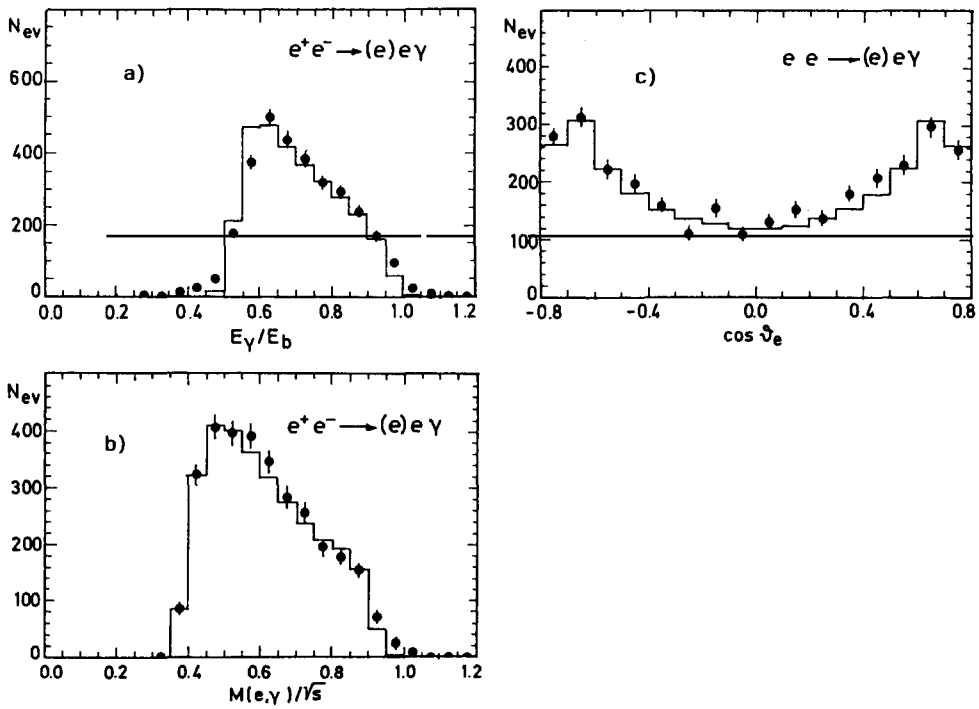

Fig. 2.20. $e^+e^- \to (e)e\gamma$: the distributions described in fig. 2.19 for the case that one electron escapes into the beam pipe.

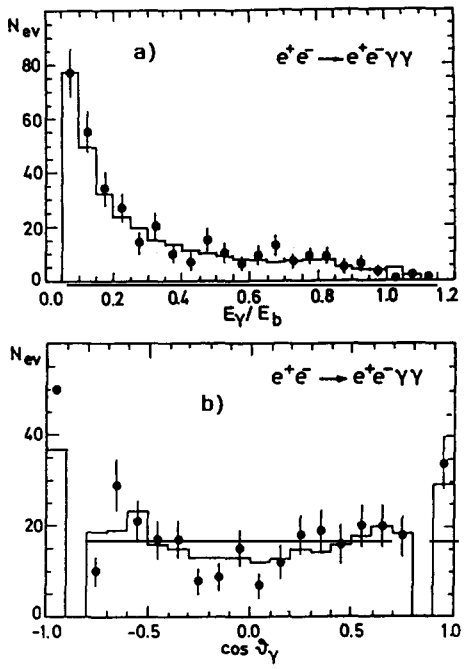

Fig. 2.21. $e^+e^- \to e^+e^-\gamma\gamma$: a) E_γ/E_{beam} (2 entries/event); b) polar angle of the photon (2 entries/event). The histograms show the predictions of QED to order α^4.

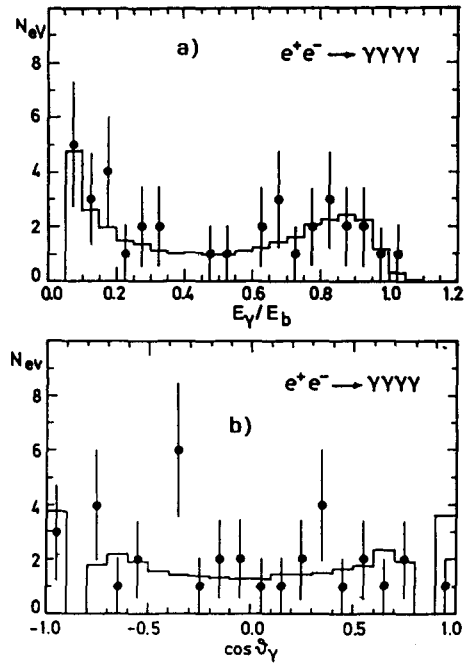

Fig. 2.22. $e^+e^- \to \gamma\gamma\gamma\gamma$: a) E_γ/E_{beam} (4 entries/event); b) polar angle of the photon (4 entries/event). The histograms show the predictions of QED to order α^4.

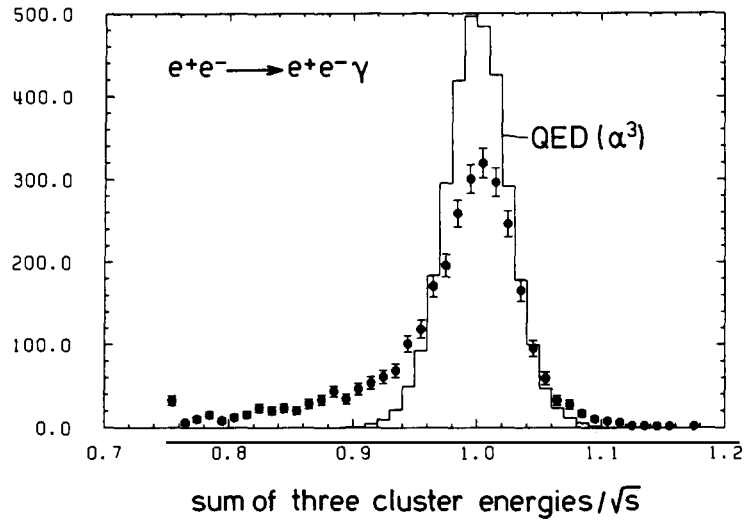

Fig. 2.23. Energy sum of the electron, positron and photon normalised to the centre-of-mass energy. The histogram is the prediction of QED to order α^3.

2.5.2. $e^+e^- \to \mu^+\mu^-\gamma$ and $\mu^+\mu^-\gamma\gamma$

The selection cuts for $\mu^+\mu^-\gamma$ and $\mu^+\mu^-\gamma\gamma$ are given in table 2.8. Two tracks and one or two well-separated photons are required. Cuts on the sum of the opening angles ensured three- or four-body kinematics. A visual scan verified that the events corresponded to the desired pattern. In the scan the tracks were observed to be compatible with being muons although no identification was required. The number of events are given in table 2.6.

The remaining background (mainly $\tau^+\tau^-$ events) was estimated to be <2%. The α^3 simulations for this process reproduce the photon energy and the angular distributions shown in fig. 2.24a and b well.

The angular distribution 2.24b shows a strong negative asymmetry which is due to the interference of amplitudes with initial and final state radiation. The measured asymmetry is $A = -(39 \pm 8)\%$ and from QED one expects $-(34 \pm 0.6)\%$. Taking into account also electroweak interference effects one expects $-(40 \pm 0.6)\%$. The experiment agrees also with this prediction within errors. The contributions from the amplitudes for initial and final state radiation can be varied by cuts on the photon energy. The asymmetry as a function of photon energy is shown in fig. 2.24c. It is also well reproduced by α^3 QED with and without including electroweak interference.

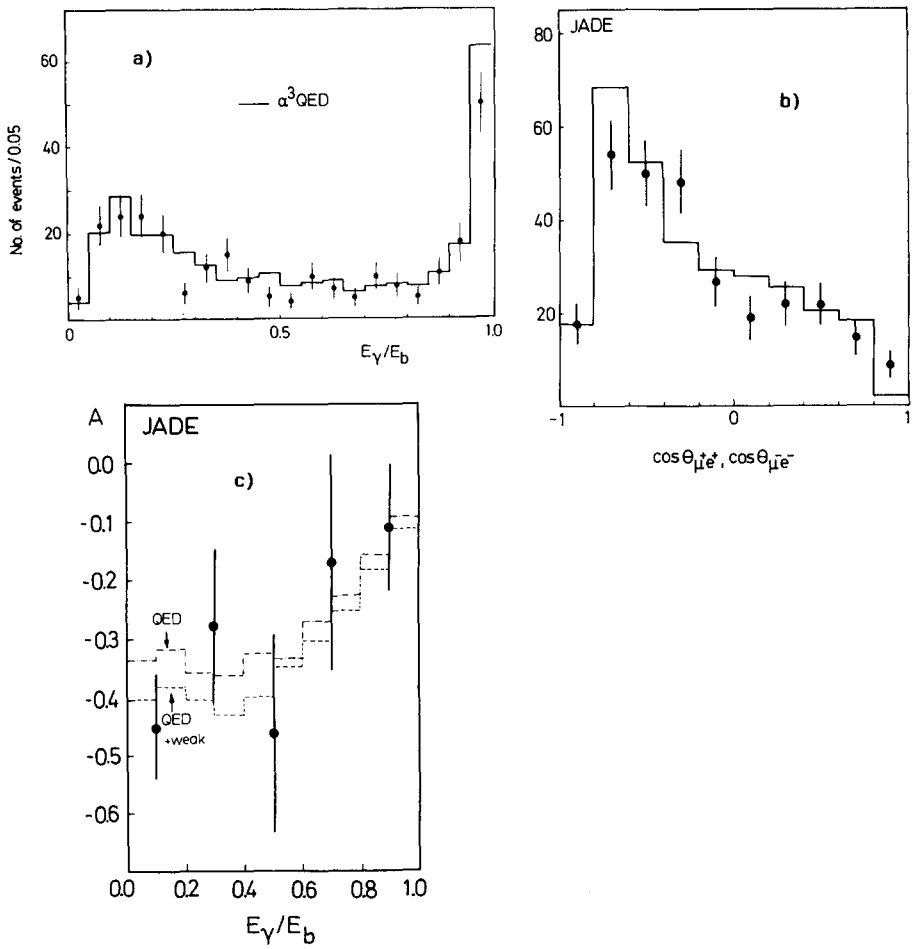

Fig. 2.24. $e^+e^- \to \mu^+\mu^-\gamma$: a) E_γ/E_{beam}; b) polar angle of the μ^+ with respect to the e^+ and of the μ^- with respect to the e^- direction (2 entries/event). The histograms show the predictions of QED to order α^3; c) forward–backward asymmetry as a function of E_γ.

Recently CELLO has observed an excess of events at high $\mu\gamma$ masses [63]. We have applied their cuts to our $\mu^+\mu^-\gamma$ data sample, but we do not observe such an excess: for $M(\mu^+\mu^-) \geq 0.1\sqrt{s}$ and the lower mass solution of $M(\mu\gamma) \geq 0.1\sqrt{s}$ we observe 265 events and expect 269.8. At a mass greater than $0.8\sqrt{s}$ there are 20 events and 21 are expected. Agreement with QED is also observed by the MARK J Collaboration [64].

For the $\mu^+\mu^-\gamma\gamma$ events (selection cuts in table 2.8) one track was demanded to be a muon and they were visually scanned to remove remaining background. After a kinematical fit with four constraints the estimated background was negligible. The distributions of muon and photon energy shown in fig. 2.25 agree well with the calculated α^4 distributions.

2.5.3. $e^+e^- \to \tau^+\tau^-\gamma$ *and* $\tau^+\tau^-\gamma\gamma$

In τ decays there is a high probability of observing photons which come from π^0 decays and tend to be close to the charged decay products. In selecting $\tau^+\tau^-\gamma$ events an isolated photon well-separated from the τ decay products was therefore required. The selection started from the tau sample described in section 2.3.2. The additional cuts applied to the τ data sample in order to select $\tau^+\tau^-\gamma$ events are listed in table 2.8. The events were scanned and remaining background estimated by Monte Carlo methods. The number of events after background subtraction is given in table 2.6. The background from non-radiative events among them was estimated to be 0.5%. Experimental distributions of the photon energy and angle and the τ polar angle are compared with the predicted distributions in fig. 2.26. Good agreement is observed.

The angular distribution of τ's (fig. 2.26c) shows a similar asymmetry as the one from $\mu^+\mu^-\gamma$ events. The measured asymmetry is $A = -(28 \pm 9)\%$, QED predicts -31% and the standard model -36%. Again the data agree with both predictions and cannot distinguish between them.

The distributions of $\tau^+\tau^-\gamma\gamma$ events (event numbers in table 2.6) are shown in fig. 2.27. Agreement with the α^4 predictions is observed.

2.5.4. $e^+e^- \to e^+e^-e^+e^-$ *and* $e^+e^- \to e^+e^-\mu^+\mu^-$

Events with four charged particles were sought, two of which were associated with clusters of energy $E > E_{beam}/3$ in the fiducial region of the lead-glass arrays. The acollinearity between these so-called "tagged electrons" had to be larger than 10° to avoid Bhabha events and less than 170° to ensure a spatial separation. The corresponding momentum transfer is $Q^2 > 9.2\,\mathrm{GeV}^2$.

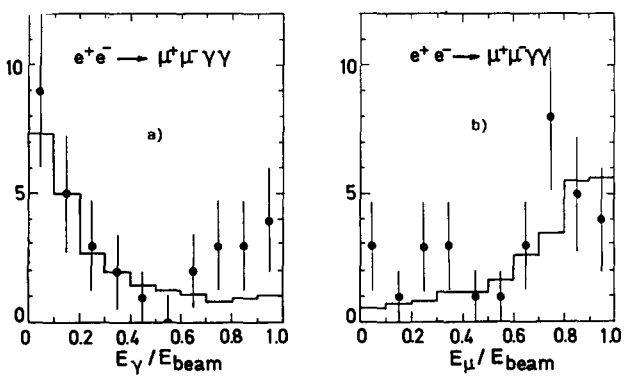

Fig. 2.25. $e^+e^- \to \mu^+\mu^-\gamma\gamma$: a) E_γ/E_{beam} (2 entries/event); b) E_μ/E_{beam} (2 entries/event). The histograms show the predictions of QED to order α^4.

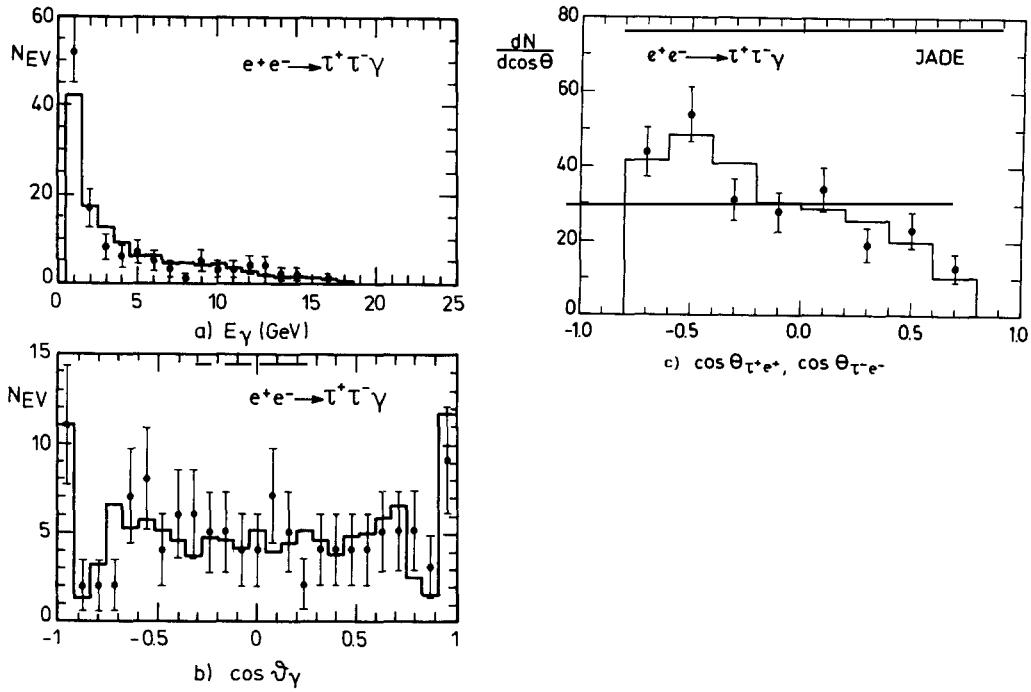

Fig. 2.26. $e^+e^- \to \tau^+\tau^-\gamma$: a) E_γ, b) polar angle of the photon; c) polar angle of the τ^+ with respect to the e^+ and of the τ^- with respect to the e^- direction (2 entries/event).

The requirements on the $\ell^+\ell^-$ candidates were: momenta above 50 MeV and for one track at least 1 GeV, both had to have polar angles above 15°. All tracks should be separated from all others by at least 10°. After these cuts a few events which contained hadrons were removed; then the events were classified as $e^+e^-e^+e^-$ if they contained one identified electron in addition to the tagged electrons and as $e^+e^-\mu^+\mu^-$ if they contained one identified muon. No event was found which contained an electron and a muon.

A kinematical fit with four constraints was performed and events with a bad χ^2 were eliminated. They were probably due to missing neutrinos or radiative photons. 8 $e^+e^-\mu^+\mu^-$ and 13 $e^+e^-e^+e^-$ events were left, of which 0 and 1 respectively had an additional photon of energy above 1 GeV.

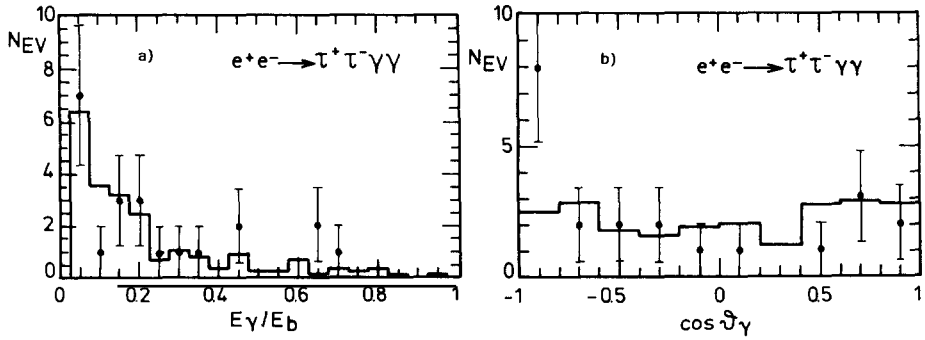

Fig. 2.27. $e^+e^- \to \tau^+\tau^-\gamma\gamma$: a) E_γ/E_{beam} (2 entries/event); b) polar angle of the photons (2 entries/event). The histograms show the predictions of QED to order α^4.

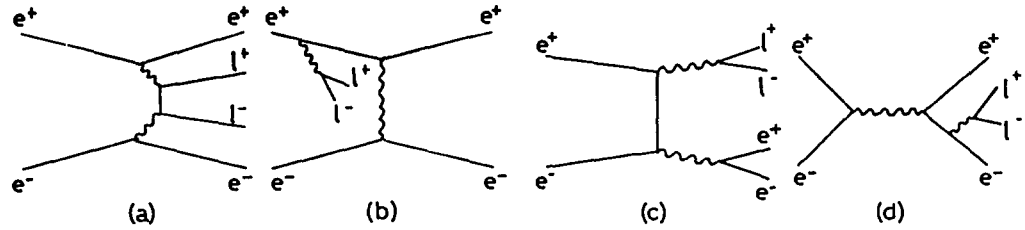

Fig. 2.28. Diagrams contributing to $e^+e^- \to e^+e^-\ell^+\ell^-$: a) multiperipheral, b) bremsstrahlung, c) annihilation and d) conversion diagrams.

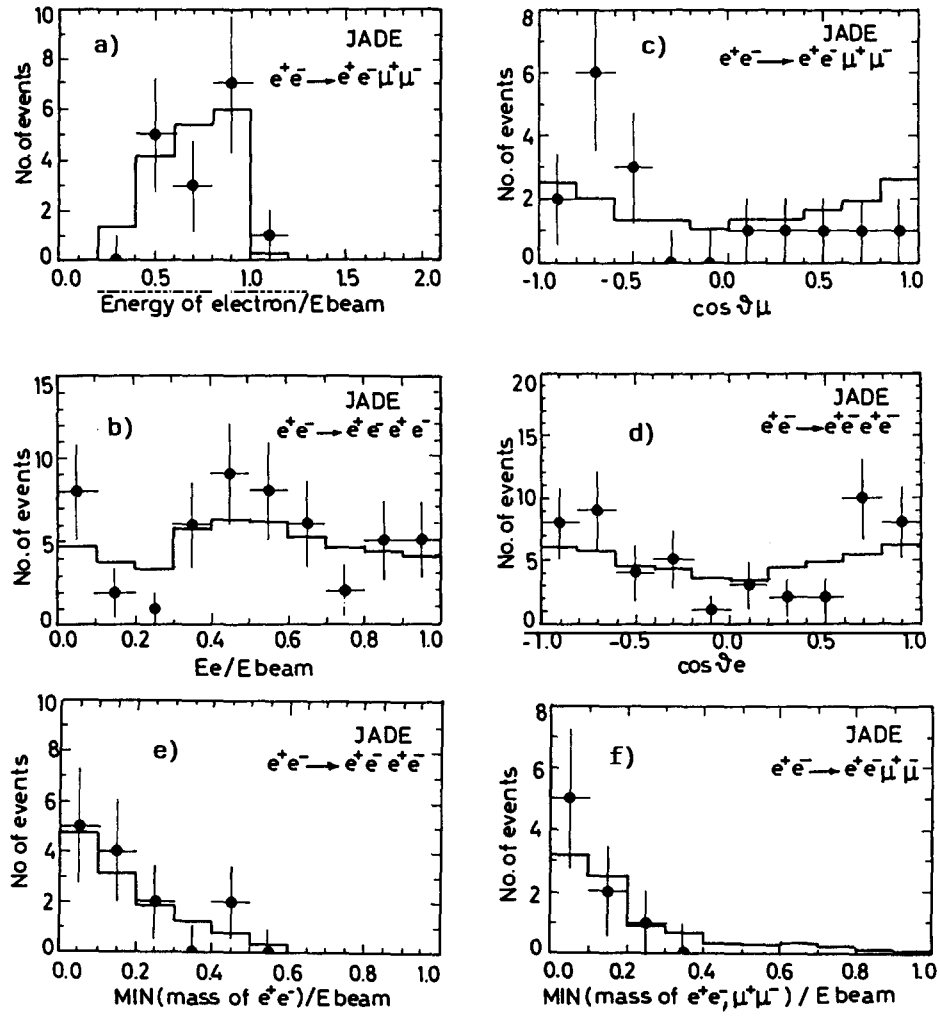

Fig. 2.29. $e^+e^- \to e^+e^-\mu^+\mu^-$ and $e^+e^-e^+e^-$. a, b) E_e/E_{beam}; c) $\cos\theta_\mu$; d) $\cos\theta_e$; e) minimum mass of two electrons for $e^+e^-e^+e^-$; f) minimum of the two-electron and the two-muon masses for $e^+e^-\mu^+\mu^-$. The histograms show the predictions of QED to order α^4.

The Monte Carlo calculations were performed according to Vermaseren et al. [32] including only the multiperipheral and bremsstrahlung diagrams (fig. 2.28a and b). The program by Berends et al. [61] included also contributions from conversion and annihilation diagrams (fig. 2.28c and d). These latter diagrams were found to contribute ~13% to the $e^+e^-\mu^+\mu^-$ final state and 2% to the four-electron final state if all generated particles were required to have polar angles above 10°. Within statistics the two programs gave compatible results. In table 2.6 and fig. 2.29 data are compared with the Vermaseren calculations, the agreement is reasonable in view of the limited statistics.

CELLO [65] has found a small deviation in the final state $e^+e^-\mu^+\mu^-$: The number of events at high invariant muon masses was larger than the expectation. In our event sample we do not observe such an excess, see fig. 2.29f.

3. τ decay branching ratios

Production and decay of the τ lepton have been extensively studied at all e^+e^- storage rings and all measurements so far agree with the predictions of the standard model [66, 67], in which the τ is a sequential lepton belonging to the third family. The tests of the neutral current sector which were performed with the JADE detector were described in chapter 2. Here we shall discuss τ decays, which probe the charged current sector.

The τ is the only known lepton which can decay into hadrons, and thus provides measurements of couplings between a lepton and quarks. Branching ratios for many decay channels of the τ have been measured [164]. For the decays into only one charged particle there is a small difference corresponding to 3 standard deviations between the sum of the measured exclusive one-prong branching ratios and the topological branching ratios [68, 69, 70].[1] Therefore the measurement of the inclusive and exclusive branching ratios with increased precision is of interest. The high energy available at PETRA facilitates such a measurement since it allows a cleaner separation of τ events from hadronic events than was possible at SPEAR and DORIS I energies.

JADE has presented precise measurements of the inclusive branching ratios for one and three charged particles [30] and also of the exclusive ones for $\tau \to e\nu_\tau\nu_e$, $\mu\nu_\tau\nu_\mu$ and $\pi\nu_\tau$ [71]. A data sample of clean τ events obtained with the cuts described in section 2.3.2 was used corresponding to a luminosity of 62.4 pb^{-1} at an average centre-of-mass energy of 34.6 GeV.

3.1. Topological branching ratios

The observed multiplicity distribution of charged tracks in τ decays is shown in the first line of table 3.1, after a correction for background the numbers in the second line were obtained. e^+e^- pairs from photon conversions have been subtracted. Beside the expected events with one, three and five tracks there are non-negligible numbers of decays into an apparently even number of tracks. They result from several sources: a track from a genuine three-track event can be lost because of the finite double track resolution of the inner detector or because it does not satisfy the track selection criteria or because it interacts in the material in front of the jet-chamber. On the other hand an additional track can come from an unrecognized photon conversion or from π^0 Dalitz decay.

These effects were included in the Monte Carlo program, which was then used in an unfolding procedure to fit the decay branching ratios into one, three and five charged tracks. After correcting for

[1] A summary of the situation with respect to the theoretical calculations is given in [70].

Table 3.1
Observed and simulated multiplicities

	Observed multiplicity				
	1	2	3	4	5
Data raw	3374	327	624	23	8
Data corr.	3213.4	287.7	574.2	17.4	5.8
M-C sum	3232.9	256.2	587.9	15.5	6.4
M-C 1	3197.3	150.9	56.5	4.2	0
M-C 3	35.3	104.4	528.0	6.1	1.0
M-C 5	0.3	0.9	3.4	5.2	5.4

the efficiencies, which depend slightly on the multiplicity, the following values were found:

$$BR_1 = (86.1 \pm 0.5 \pm 0.9)\%,$$

$$BR_3 = (13.6 \pm 0.5 \pm 0.8)\%,$$

$$BR_5 = (0.3 \pm 0.1 \pm 0.2)\%.$$

The main contribution to the systematic errors, which is the second error quoted, is due to uncertainties in modelling the detector whereas uncertainties in background and efficiencies only lead to small systematic errors. The systematic error in BR_5, however, is dominated by the uncertainty of the background subtraction.

The multiplicity distributions, generated with these branching ratios are shown in table 3.1 in the lines labelled "M-C" for each generated multiplicity and for the sum. The sum coincides with the corrected data.

The measured values for the topological branching ratios are different from those observed at lower energies [12] but compare well with the values obtained recently by other experiments at PETRA and PEP [35, 40, 67, 68, 72].

3.2. *Measurement of the branching ratios for* $\tau \to e\nu_e\nu_\tau$, $\tau \to \mu\nu_\mu\nu_\tau$ *and* $\tau \to \pi\nu_\tau$

For the determination of the leptonic and the pionic branching ratios τ events with one isolated track were used, which was separated from all other track(s) by at least 100°. A lower momentum cut of 1 GeV was applied on the isolated track, and its polar angle was restricted to $|\cos\theta| < 0.76$ to avoid inefficiencies at the edges of the lead-glass shower counters. It was further required that there be no photon of more than 300 MeV within 30° of the isolated track.

Electrons were identified using the lead-glass arrays. The τ decay into a charged and a neutral π, which overlap in space, is the main background for electrons. It was reduced by requiring good matching between the extrapolated track impact point on the lead-glass counters with the centre-of-gravity of the energy cluster. The cuts were:

e1. $|\Delta\varphi| < 1.5°$ and $|\Delta\theta| < 5°$, where $|\Delta\varphi|$ is the azimuthal difference of the extrapolated track and the energy cluster and $|\Delta\theta|$ the difference in polar angle.

e2. $E_{sh}/p > 0.80$, where E_{sh} is the measured shower energy and p the track momentum.

The distribution of E_{sh}/p is shown in fig. 3.1 for data and simulated electrons from τ decay and also for

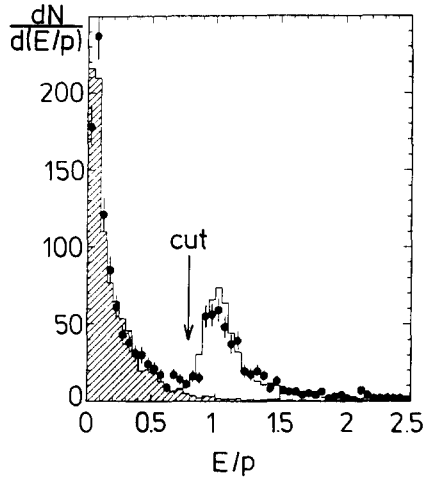

Fig. 3.1. Ratio of lead-glass energy E to track momentum p for the identification of electrons in τ decays. The histogram shows the simulated data, the shaded histogram shows the background.

the background. A total of 523 electrons was found. The electron detection efficiency was estimated to be 90.1%. The probability of misidentification was 7.6%, which was mainly due to semileptonic decays with single or multiple π^0s, where the cluster of the charged hadron overlaps with that of a photon from a π^0 decay.

For the selection of pions and muons a non-showering track of momentum $p > 1.8$ GeV was required which was then classified with the help of the muon filter. The track was required to hit a part of the muon filter where at least two chambers along its path were active. To be called a muon candidate the following requirements had to be met by a track:

m1. The energy deposited in the lead-glass arrays was not greater than 1 GeV.

m2. At least two muon chambers along the extrapolated track path outside the magnet yoke had to have registered a hit.

The number of observed muons was 544, which includes a small background from other τ decays (mainly into single charged pions) of 1.7%. The probability of muon identification was 77.7%.

Pions were required to fulfill:

p1. Not more than one muon chamber along the extrapolated track path was allowed to have registered a hit.

p2. $|\Delta\varphi| < 2°$ and $|\Delta\theta| < 5°$.

p3. $E_{sh}/p < 0.70$.

After these cuts 372 candidates for the decay $\tau \to \pi\nu_\tau$ were found. The probability of π identification was determined to be 61.7% and the misidentification probability to be 14.4%, mainly from the decay $\tau \to \rho\nu_\tau$, and with a small contribution from muons.

The branching ratios were calculated according to:

$$\mathrm{BR}_i = \frac{N_i^c}{N_1^c}\,\frac{\varepsilon_1}{\varepsilon_i}\,\mathrm{BR}_1\,, \tag{3.14}$$

where N_i^c and N_1^c are the corrected number of τ decays into a particle of type i ($i = e, \mu, \pi$) and into one charged particle, ε_i and ε_1 are the corresponding efficiencies of identifying the decay mode including the

efficiency of the selection of τ-pair events and BR_1 is the branching ratio for the τ decay into one charged particle. The use of the above expression, rather than the integrated luminosity and the total cross-section for normalisation, has the advantage that the systematic error is reduced. The uncertainty in the luminosity measurement does not enter the branching ratio determinations and the effect of the errors in the efficiency and background calculation are smaller since only the relative errors are of significance. The effect of the major background contribution, $e^+e^- \to e^+e^-\tau^+\tau^-$, is also reduced since the efficiency depends only slightly on the production mode after the selection cuts.

The number of corrected decays N_i^c (line 2 of table 3.2) was obtained from the number of observed events by subtracting the background due to misidentification of other τ decay modes and the background from other reactions (e.g. two-photon processes, Bhabha scattering, $e^+e^- \to \mu^+\mu^-$) determined using simulated events. A correction for event losses which were not included in the Monte Carlo calculation of the efficiency the largest of which were event losses due to nuclear interactions in front of the jet-chamber. For electrons a loss due to a Bhabha rejection algorithm in an event filter used for part of the data was corrected for. The corrections and the final numbers of events are listed in table 3.2, where also the number of one-prong decays before and after similar corrections are listed. The efficiencies for the various decay channels were calculated using Monte Carlo techniques. The efficiencies with which a track was identified as a lepton or pion including the efficiency for the selection of τ-pair events are also given in table 3.2.

The results for the branching ratios are, using the world average for the one-prong decay of $BR_1 = (86.7 \pm 0.3)\%$ which agrees well with our measurement but has a smaller error [35, 67]:

$$BR_e = (17.0 \pm 0.7 \pm 0.9)\%$$
$$BR_\mu = (18.8 \pm 0.8 \pm 0.7)\%$$
$$BR_\pi = (11.8 \pm 0.6 \pm 1.1)\%$$

where the first error is statistical and the second one systematic. The result for BR_π was corrected for a background from the τ decay into $K\nu_\tau$, using $B(\tau \to K\nu_\tau) = (0.59 \pm 0.18)\%$ [73]. The systematic error results mainly from uncertainties in the efficiency calculation and the Monte Carlo simulation of the detector, and was estimated by varying the appropriate cuts. Other sources of error were the determination of background and event-losses and the scan of the data. The measured branching ratios agree, within the errors, with the values calculated using the total cross-section and integrated luminosity for normalization, which are $(16.1 \pm 0.7 \pm 1.0)\%$, $(17.8 \pm 0.8 \pm 0.8)\%$ and $(11.2 \pm 0.6 \pm 1.2)\%$ respectively. The results are also in agreement with previous measurements performed by other experiments [12, 74].

Table 3.2
Determination of exclusive τ branching ratios

	Electrons	Muons	Pions	1 charged particle
Selected events	523	544	372	3024
Corrected events	515	558	328	3192
Subtracted background from tau decays (%)	7.6	1.7	14.4	-
Subtracted background from other reactions (%)	5.0 ± 2.0	3.5 ± 0.8	7.8 ± 2.2	4.7
Event losses (%)	11.1	7.8	10.3	10.3
Efficiency (%)	28.0	28.8	25.6	34.1
Branching ratio (%)	$17.0 \pm 0.7 \pm 0.9$	$18.8 \pm 0.8 \pm 0.7$	$11.8 \pm 0.6 \pm 1.1$	

The ratio BR_μ/BR_e is calculated to be 0.973 using e–μ universality [75]. The measured value $1.10 \pm 0.07 \pm 0.06$ agrees well with this prediction. Therefore the branching ratios BR_e and BR_μ were determined using e–μ universality as a constraint and the following values were obtained:

$$BR_e = (18.2 \pm 0.8)\%, \qquad BR_\mu = (17.7 \pm 0.7)\% .$$

Using this value of BR_e and the relation to the life-time:

$$BR(\tau \to e\nu_\tau\nu_e) = \tau_\tau \cdot \Gamma(\tau \to e\nu_\tau\nu_e) \qquad \text{with} \qquad \Gamma(\tau \to e\nu_\tau\nu_e) = \frac{G_F^2 m_\tau^5}{192\pi^3}$$

one determines τ_τ to be $(2.90 \pm 0.13) \times 10^{-13}$ sec in good agreement with direct measurements [68, 76].

The decay $\tau \to \pi\nu_\tau$ involves the coupling of the weak axial-vector current to the pion, which has been accurately determined in pion decay measurements. Using the measured pion decay rate [12], the theoretical prediction for the ratio of the branching ratios of taus decaying into pions and into electrons is $(BR_\pi/BR_e)_{th} = 0.607$. The value of $BR_\pi/BR_e = 0.647 \pm 0.039 \pm 0.061$ derived from our results is in good agreement with the prediction. The measured value of BR_π is also in good agreement with the theoretical expectation of $BR_\pi = (10.7 \pm 0.8)\%$, calculated from the measured τ life-time [68].

As a conclusion one can say that the measurements of the topological branching ratios into one and three charged particles and the exclusive ones into electron, muon and pion are in good agreement with new measurements at PEP and from MARK III at SPEAR. Theoretical relations are well fulfilled.

4. Total hadronic cross-section

4.1. Introduction

Hadron production in e^+e^- annihilation is, in the quark parton model, described by pair production of quarks (fig. 4.1a) and their subsequent hadronisation. The total cross-section far above the quark thresholds is given by:

$$R_{had} = \frac{\sigma(e^+e^- \to \text{hadrons})}{\sigma_0} = 3\sum_q Q_q^2 \qquad \text{with} \qquad \sigma_0 = \frac{4\pi\alpha^2}{3s} . \tag{4.15}$$

The sum runs over all known quarks, q = u, d, c, s and b at PETRA energy, and Q_q denotes their electric charge. The factor 3 takes into account colour. In addition, contributions from QCD processes (fig. 4.1b and c) and Z^0 exchange are expected. Taking into account their contributions the cross-section ratio then becomes [77]:

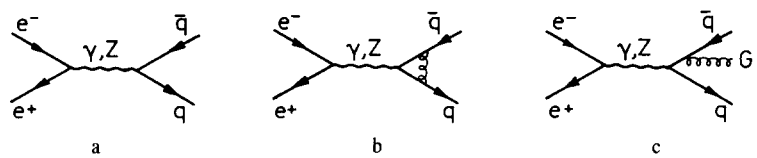

Fig. 4.1. Lowest order diagrams for $e^+e^- \to$ hadrons including Z^0 exchange and QCD contributions.

$$R_{had} = 3\sum_q \left(1 + \frac{\alpha_s}{\pi} r_{tot}\right) C_{VV} + \left(1 + \frac{\alpha_s}{\pi} r'_{tot}\right) C_{AA} \tag{4.16}$$

with

$$C_{VV} = Q_q^2 - 2Q_q v_e v_q \chi + (v_e^2 + a_e^2) v_q^2 \chi^2 \tag{4.17}$$

$$C_{AA} = (v_e^2 + a_e^2) a_q^2 \chi^2 . \tag{4.18}$$

χ was defined in chapter 2, eq. (2.5). The values of weak vector and axial-vector coupling constants v_e, v_q, a_e and a_q predicted by the standard model are given in table 2.1. α is the fine structure constant and α_s is the QCD coupling constant, which is in first order related to the QCD scale parameter Λ by:

$$\alpha_s = \frac{12\pi}{(33 - 2N_f)\ln(s/\Lambda^2)} \tag{4.19}$$

where N_f is the number of flavours. The QCD correction functions r_{tot} and r'_{tot}, the so-called Schwinger terms, depend on $2m_q/\sqrt{s}$. They approach 1 for $m_q/\sqrt{s} \to 0$. In this limit the QCD correction in eq. (4.16) reduces to the well-known $1 + \alpha_s/\pi$. Since the mass of u, d and s quarks was neglected, the c-quark mass was assumed to be 1.5 GeV and that of the b-quark 5 GeV, these QCD corrections are important only for the heavy quarks.

The QCD corrections result in an increase of R_{had} by ~4%, which is almost independent of s. The electroweak correction leads to an energy dependent effect, which, for $\sin^2\theta_W = 0.22$ is approximately +5% at $\sqrt{s} = 45$ GeV, while it is small around $\sqrt{s} = 14$ GeV. In view of the size of these effects the measured total hadronic cross-section will only provide a meaningful tool for a comparison with theory if its errors are small enough. The error of R_{had} is dominated by systematic effects and an effort was made to minimize them. The systematic error achieved is ±3% (3.4%) at $\sqrt{s} \sim 34$ (~43) GeV and is mainly a normalization error. A similar effort has been undertaken by MAC [80]. MAC took data only at one centre-of-mass energy $\sqrt{s} = 29$ GeV and has achieved a normalisation error of 2.4%.

4.2. *Determination of* R_{had}

The experimental evaluation of R_{had} is done using the following expression:

$$R_{had} = \frac{N - N_{BG}}{L\varepsilon(1+\delta)} \cdot \frac{1}{\sigma_0}$$

where N is the number of multihadronic events, N_{BG} the estimated number of background events contained in the sample, L is the integrated luminosity, ε is the acceptance and $1 + \delta$ corrects for contributions from QED diagrams up to order α^3. In the following the determination of the factors and their systematic errors will be discussed.

Selection of multihadronic events

The selection procedure for multihadronic events will be described in some detail, because the multihadronic data sets are not only used to determine R_{had}, but will also be used for studies of QCD

and fragmentation, for investigations on inclusive particle production and for the search of new particles.

The following cuts were applied to select multihadronic events:

1. In order to be accepted an event had to deposit a minimum shower energy either in the barrel part of the lead-glass detector (E_{BAR}), or in each end-cap, E_{EC}. The cuts were:

$\sqrt{s}$ (GeV)	E_{BAR} (GeV)	E_{EC} (GeV)
<16	>1.2	>0.2
16–24	>2.0	>0.2
>24	>3.0	>0.4

2. At least 3 charged particles were reconstructed in the jet-chamber and came from the interaction region, a cylinder of radius 30 mm and a length of 350 mm around the interaction point of the beams.

3. Among the tracks at least one had to be registered with at least 24 points (henceforth called "long" track).

Events passing these cuts were separated into two classes: the first class, which was immediately accepted, contained "safe" events; they had at least 7 long tracks which did not belong to converted photon pairs and came from the vertex region. The second class, which did not fulfill these criteria (roughly 50%), was visually inspected by physicists. The criteria for the visual inspection were:

4. At least 4 charged particles which were not part of e^+e^- pairs came from the interaction volume.

5. Among the tracks at least 3 had to be long.

6. If there were only 4 charged particles in the event, three of them should not be in the opposite hemisphere of the fourth. This requirement rejected τ pairs.

The events of this data sample which is called the "extended multihadronic data set" contains mostly multihadronic events from e^+e^- annihilation and two-photon exchange; in addition there is a background from beam–gas and beam–wall interactions. For the final selection of annihilation events the visible energy E_{vis}, where $E_{vis} = \Sigma\,|p_i|$, and longitudinal momentum imbalance $p_{bal} = \Sigma\, p_i^z / E_{vis}$ were calculated, where the sums include charged and neutral particles. The following final cuts were then applied:

7. $E_{vis} \geq \sqrt{s}/2$.

8. $|p_{bal}| \leq 0.4$.

9. The event vertex in the z-direction should be within 150 mm of the interaction point.

The distributions of some of the variables used for cuts are shown in fig. 4.2 compared with model calculations which are seen to describe the data well.

Determination of background

τ pairs will contribute to the background only if they result in events with more than 4 charged particles. If, however, the event topology is distorted, for example by initial state radiation, a tau might be missed by the scanners. These effects were estimated by Monte Carlo simulation and gave a mean correction to R_{had} of $(2.4 \pm 1.5)\%$, where the error includes the uncertainties introduced by the visual scan.

Two-photon scattering was also estimated by a Monte Carlo simulation [32, 81], where the processes in fig. 4.3 were included. The VDM-like process (fig. 4.3a) leads to a low visible energy because the two scattered electrons usually stay in the beam-pipe; therefore this background was efficiently removed by cut 7. The estimated background at 35 GeV is $(0.5 \pm 0.5)\%$, where the error reflects the uncertainty in

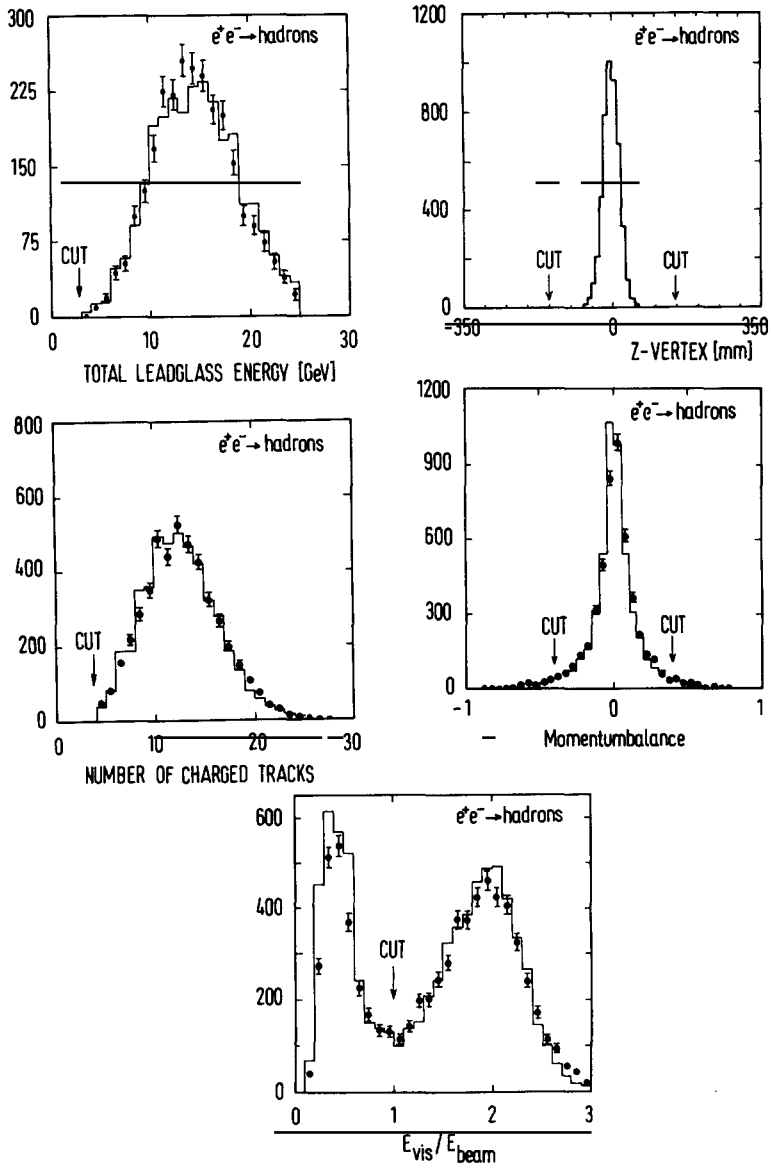

Fig. 4.2. Distributions for the selection of multihadronic events.

the cross-section $\sigma(\gamma\gamma \rightarrow \text{hadrons})$. The contribution from the other diagrams was estimated to be $(0.7 \pm 0.5)\%$. This number was checked by comparing the observed number of events with a high energy electron with the calculation.

Beam-gas interactions, Bhabha scattering and cosmic ray events were removed to a negligible level by the cuts.

The total background from these contributions was $(3.6 \pm 1.6)\%$.

Acceptance and radiative corrections

The acceptance was determined by a Monte Carlo simulation which used the Lund model [91, 92]

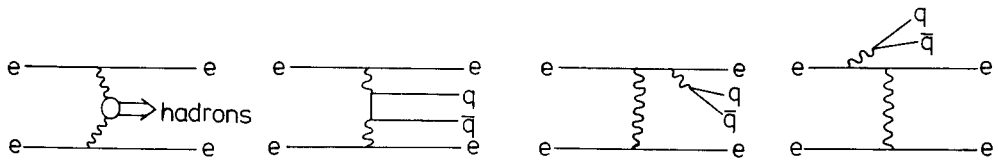

Fig. 4.3. Diagrams for hadron production by two-photon processes.

including radiative corrections [82]. The Lund model was chosen because it was found to give a better description of the data than other fragmentation models (see chapter 5); the most important distribution for the present analysis is the observed multiplicity of charged tracks and neutral kaons. The simulated events were then tracked through the detector taking into account all known detector effects. Afterwards the events were passed through the same selection chain as the real data. The efficiency including radiative corrections was determined to be: $\varepsilon(1+\delta) = 1.03$ at $\sqrt{s} = 35$ GeV and 1.01 at $\sqrt{s} = 14$ GeV.

The systematic error of the acceptance was determined by varying the cuts within reasonable limits. For example, moving the cut on $E_{vis}/\sqrt{s}$ from 1.0 to 1.6 changes R by 0.8%. A total systematic error of 1.5% is attributed to the acceptance calculation; this also includes the error on α_s.

The radiative corrections included diagrams up to order α^3: Initial state radiation, vertex correction and vacuum polarisation from electrons, muons, taus and hadrons were included. The largest uncertainty came from the hadronic vacuum polarisation, which was calculated as a dispersion integral over the total hadronic cross-section. Varying the hadronic cross-section by ±15%, the uncertainty in R_{had} was estimated to be ±0.8%.

Luminosity

The luminosity was determined from Bhabha scattering in the barrel part of the detector as described in section 2.2.1. Its uncertainty relevant for the hadronic cross-section is estimated to be 1.5% mainly due to acceptance and radiative corrections. In addition we attribute a point-to-point error of 1% to it, taking into account possible errors in the background subtraction, energy calibration, etc.

Results

The final R values are listed in table 4.2 and shown in fig. 4.4 as a function of s. The summary of the

Table 4.1
Systematic errors of R (in %)

	$\sqrt{s}$ (GeV)		
Error	≤14	22–37	39–46.8
Background subtraction	1.6	1.6	1.6
Radiative corrections	1.1	0.8	1.2
Luminosity normalisation	1.5	1.5	1.7
Overall normalisation	2.4	2.4	2.6
Detection efficiency	2.5	1.5	2.0
Luminosity point-to-point	1.0	1.0	1.0
Total point-to-point	2.7	1.8	2.2
Total	3.6	3.0	3.4

Table 4.2
R values. The errors include the statistical and point-to-point systematic error

$\sqrt{s}$ (GeV)	Ev.	R	ΔR	$\sqrt{s}$ (GeV)	Ev.	R	ΔR
12.00	219	3.45	0.27	35.01	4162	3.93	0.10
14.04	2649	3.94	0.14	35.45	679	3.93	0.18
22.00	1871	4.11	0.13	36.38	420	3.71	0.21
25.01	290	4.24	0.29	40.32	539	4.05	0.19
27.66	84	3.85	0.48	41.18	437	4.21	0.22
29.93	101	3.55	0.40	42.55	378	4.20	0.22
30.38	642	3.85	0.19	43.53	471	4.00	0.20
31.29	251	3.83	0.28	44.41	417	3.98	0.20
33.89	3785	4.16	0.10	45.59	459	4.40	0.22
34.50	570	3.93	0.20	46.47	330	4.04	0.24

systematic errors is given in table 4.1. The error bars in fig. 4.4 include only the part of the systematic error which can vary from point to point.

The results are in agreement with measurements from MARK J and TASSO in the same energy range [83, 84] and with the result from MAC [80] at $\sqrt{s} = 29$ GeV.

4.3. Comparison with theory

The data were fitted to the prediction by the standard model (eq. 4.16) leaving Λ, $\sin^2\theta_W$ and an overall normalisation factor f as free parameters. The point at 12 GeV was not used in the fit since it could be affected by the b threshold. The best fit yielded:

$$\sin^2\theta_W = 0.23^{+0.03}_{-0.04}$$
$$\alpha_s(34\,\text{GeV}) = 0.19^{+0.06}_{-0.07}$$
$$f = 0.99 \pm 0.02$$

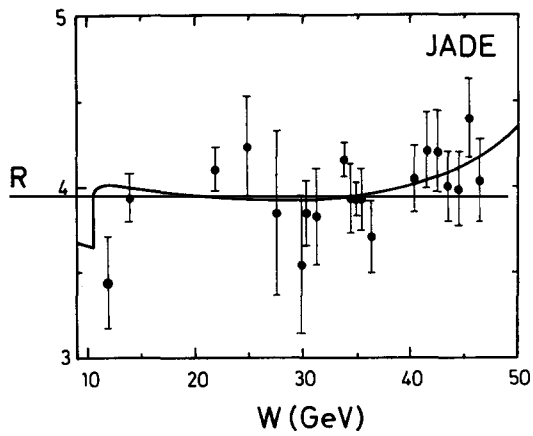

Fig. 4.4. Measured R values, the errors include statistical and point point-to-point systematic errors, an additional normalisation error of 2.4% is not shown. The line is a fit to the data including electroweak and QCD effects to lowest order. The parameters correspond to those given for the best fit in the text.

where f is an overall normalisation factor which was allowed to vary with an error corresponding to the systematic normalisation error. The errors correspond to one standard deviation irrespective of the values of the other parameters. The full line in fig. 4.4 was calculated using these parameters. The χ^2 of the fit is 11.2 for 17 d.o.f. The data are however also compatible with a straight line, the average for $\sqrt{s} > 13$ GeV is then: $R = 4.02 \pm 0.04 \pm 0.10$ with a $\chi^2 = 13.9$ for18 d.o.f.

Limits on the point-like nature of the quarks can be determined by introducing in eq. (4.16) a form-factor $F(s) = 1 \pm s/(s - \Lambda_{\mp}^2)$. The limits found are $\Lambda_+ > 277$ GeV and $\Lambda_- > 266$ GeV at 95% C.L.

5. Tests of QCD and fragmentation

QCD tests in e^+e^- interactions at the high energies available at PETRA were done under various aspects. The initial success of finding evidence for hard gluon radiation [85, 86] was a motivation to study in detail the predictions of perturbative QCD and the properties of gluon initiated jets with the data obtained in the JADE detector.

While cross-sections for $e^+e^- \to q\bar{q}(g)$ can be calculated exactly to second order in perturbation theory no such calculations exist for the hadronisation process. One is forced to resort to model calculations. Optimizing the models and comparing them with the data was expected to shed some light also on the understanding of the underlying physics processes. JADE was the first experiment to establish a difference between the fragmentation of gluons and quarks. Evidence was accumulated that these differences and many properties of the data were described better by a model based on string fragmentation than by models which treated the quarks and gluons as independent.

$O(\alpha_s^2)$ contributions to the hadronic cross-section were found experimentally by establishing the existence of four-jet events. A comparison between the jet multiplicities of the data and the predictions of $O(\alpha_s^2)$ QCD seems to point to an excess of events with four or more jets compared with the predictions.

The determination of the QCD coupling constant α_s was undertaken several times as knowledge about theory and data progressed. The model dependence of the results found stimulated a model independent determination by deriving limits for variables calculable in second order QCD.

A different approach to describe the data was pursued in the so-called QCD shower models which apply perturbative methods not only to the formation of the initial parton state but also to part of the hadronic cascade. Including interference effects between soft gluons this class of models led to a successful description of many properties of the data.

There are many contributions from the JADE group which are addressed to both domains of interest, the validity of perturbative QCD and to the comparison of fragmentation models with the data. These two topics were found to be closely interleaved and it is impossible to understand the QCD analyses without understanding some of the properties of the fragmentation models. Therefore we begin this chapter by describing the most important fragmentation studies and by introducing the models to compare them with. Afterwards the determination of α_s will be described. Finally a comparison of jet multiplicities with the predictions of $O(\alpha_s^2)$ QCD and of a leading log calculation will be made.

5.1. Jet topologies, evidence for three-jet events

Hadronic events at high energies, $\sqrt{s} \sim 30$ GeV, are dominated by two-jet events, which in the quark parton model are due to $e^+e^- \to q\bar{q}$ with subsequent hadronisation of the quarks. Due to the large

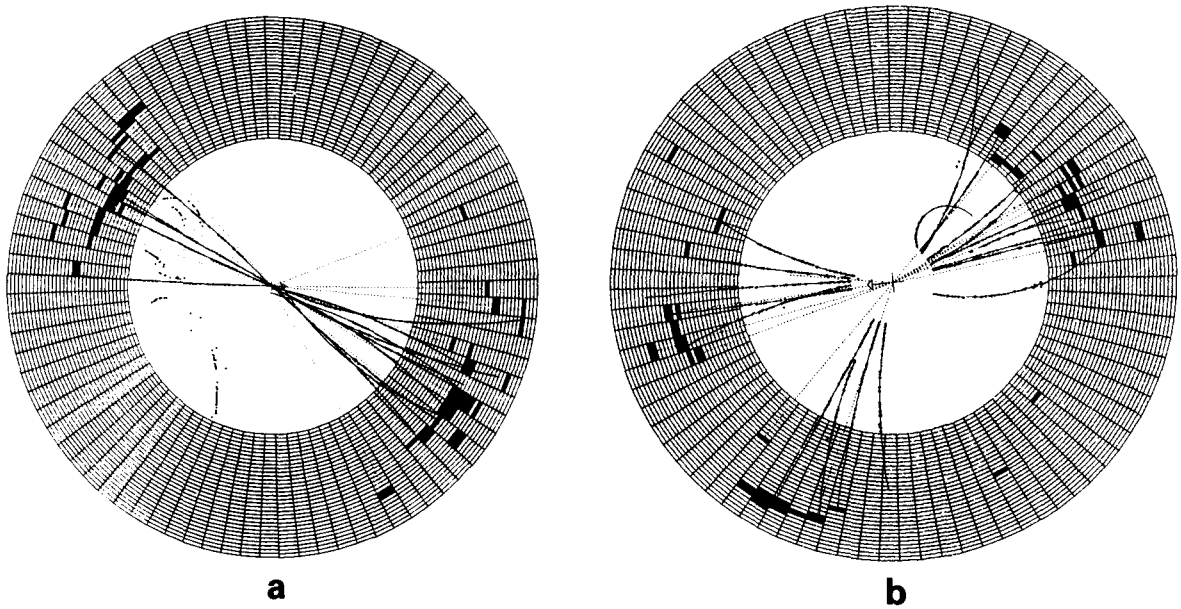

Fig. 5.1. Examples of a two-jet and a three-jet event in the JADE detector.

energy of the primary partons the hadrons are strongly boosted into the parton direction and the two-jet structure can be recognised easily by visual inspection (fig. 5.1a). The transverse momentum of the particles with respect to the jet-axis is limited with an average $\langle p_t \rangle \sim 300$ MeV, the same value as measured at lower energies. A fraction of events shows a different structure, the events are more planar and some have a clear three-jet structure (fig. 5.1b). These features can be quantified for example by the thrust value, defined as

$$T = \max_n \sum_i |\boldsymbol{p}_i \cdot \boldsymbol{n}| \Big/ \sum_i |\boldsymbol{p}_i| \tag{5.20}$$

the $\boldsymbol{p}_i$ are the particle momenta, and the sum runs over charged and neutral particles.[1] $\boldsymbol{n}$ is the vector along the axis with respect to which the expression is maximal. Thrust approaches the value of 1 for two-jet-like events and is 0.5 for spherical events. The thrust distributions for $\sqrt{s} = 14$, 22, 34 and 44 GeV are shown in fig. 5.2. The peaks at large thrust values, which get narrower towards higher energies, correspond to the two-jet-like events. A long tail towards small thrust values exists even at high centre-of-mass energies. It cannot be described by two-jet events with limited transverse momentum but is well reproduced by a model which contains additional gluon emission according to perturbative QCD.

Another way to describe the event shape is a two-dimensional Dalitz plot, the Q-plot. For each event the normalised momentum tensor $T_{\alpha\beta}$ is calculated:

$$T_{\alpha\beta} = \sum p_{i\alpha} p_{i\beta} \Big/ \sum \boldsymbol{p}_i^2 \qquad (\alpha, \beta = x, y, z) .$$

[1] In the JADE experiment the inclusion of neutral particles is possible due to the small grain lead-glass arrays with almost complete angular coverage. Including neutral particles has the advantage that the particle multiplicity is approximately doubled compared to using only charged particles. This in turn facilitates the jet definition.

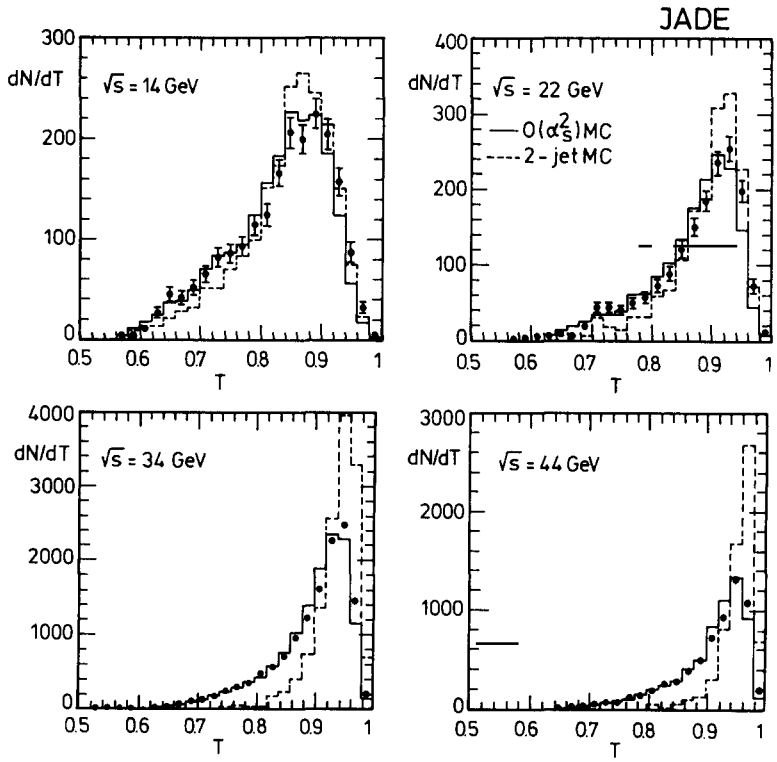

Fig. 5.2. Thrust distributions at four centre-of-mass energies compared with two models: The dotted line was calculated for two-jet events and $\sigma_q = 265$ MeV, the full line is from a model (Lund) which contains gluon emission.

The normalised eigenvalues Q_i of the momentum tensor are obtained by diagonalisation, their sum is normalized to 1 and they are ordered $Q_1 < Q_2 < Q_3$. They correspond to the lengths of the three principal axes $\boldsymbol{n}_1$, $\boldsymbol{n}_2$ and $\boldsymbol{n}_3$ of the momentum ellipsoid. The plane defined by the two largest axes, $\boldsymbol{n}_3$ and $\boldsymbol{n}_2$, is called the event plane. $\boldsymbol{n}_3$ is the axis with respect to which the sum of the squared transverse momenta is minimal, it is called the sphericity axis. Sphericity, another frequently used shape variable, is defined as $S = \frac{3}{2}(Q_1 + Q_2)$.

The distribution of hadronic events in the "Q-plot", a triangle plot of Q_1 versus $(Q_3 - Q_2)/\sqrt{3}$, is shown in fig. 5.3 for the data around 34 GeV. Most events are clustered in the corner of large $Q_3 - Q_2$ and small Q_1, they are two-jet-like events. The events with small Q_1 outside the two-jet corner have a planar structure, they are dominated by three-jet events. Spherical events are found at large values of Q_1.

Evidence for planar events was observed also in other distributions and the predictions of perturbative QCD fitted the data in both event rate and event shape [85]. These observations were also made by other experiments at PETRA [86]. Thus gluon emission was adopted as a working hypothesis and has been confirmed in all subsequent analyses.

5.2. *Fragmentation models*

Before the description of the data analysis is continued, a brief summary of the currently used fragmentation models will be given. They belong to either of two classes: the first class is based on the

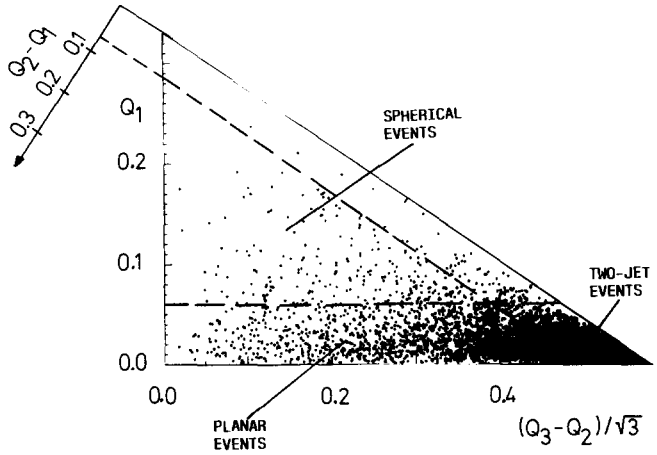

Fig. 5.3. Q-plot for multihadronic events at $\sqrt{s} \sim 34$ GeV.

exact matrix element in first- or second-order perturbative QCD and a phenomenological fragmentation model (the models by Hoyer et al., Ali et al. and by the Lund group). This class of models has been used by the PETRA experiments since the first data were taken and consequently are rather well understood. The second class of models uses perturbative QCD calculations in a leading logarithmic approximation (LLA) to calculate a shower of quarks and gluons (the Gottschalk and Webber models).

5.2.1. Models using a QCD matrix element + phenomenology

In this class of models the process $e^+e^- \rightarrow$ hadrons is visualised as a two-step procedure:

1. e^+e^- annihilation into a few simple final states of quarks and gluons: $e^+e^- \rightarrow q\bar{q}$, $q\bar{q}g$, $q\bar{q}gg$.
2. The transformation of these partons into hadrons: "hadronisation" or "fragmentation".

Step 1, the production of two, three or four partons at high centre-of-mass energy can be calculated exactly in the framework of QCD using perturbative methods. The relative probability of gluon emission is given by α_s, the strong coupling constant. These calculations were initially available to order α_s and included therefore only two- and three-parton events. Subsequently matrix elements to second order were calculated including also four-parton configurations and the virtual corrections. All calculations were however carried out for massless partons.

The transformation of these partons into observable hadrons is performed in a second step based on ideas developed by Field and Feynman [87] for configurations of two partons. The $q\bar{q}$ pairs generated in the e^+e^- collisions are turned into hadrons through an iterative procedure in which pairs of quarks $q'\overline{q'}$, $q''\overline{q''}$, ... etc., are created in the colour field between the primary quark pair. The secondary quark pairs are combined to form mesons or meson resonances, for instance $q'\overline{q''}$. In a last step the unstable resonances decay.

The momentum spectrum of the secondary quark pairs is described by ad hoc functions; the transverse momenta of the secondary hadrons are assumed to have a Gaussian distribution $\exp(-p_t^2/(2\sigma_q^2))$ with width σ_q around the parton direction and the longitudinal momentum distribution is given by a fragmentation function $f(z)$ of the form:

$$f(z) = 1 - a_F + 3a_F(1-z)^2 \qquad \text{with} \qquad z = (E + p_\parallel)_{\text{meson}}/(E + p_\parallel)_{\text{quark}} \tag{5.21}$$

with an adjustable parameter a_F to be determined from the data.

At PETRA energies the production of gluons has to be taken into account and the fragmentation has to be extended to gluons, of which little was known initially. Two methods were followed to achieve this: the models by Hoyer et al. and Ali et al. pursued an approach where the partons fragment independently from each other. The Lund model is in contrast based on a string model, which assumes that colour strings connect the partons and give rise to the hadronisation process (compare fig. 5.4).

Model by Hoyer et al. In the model proposed by Hoyer et al. [88], which was originally formulated in first-order perturbation theory, the partons fragment independently. The quarks fragment as in the Field–Feynman approach with slightly modified fragmentation functions. The gluon turns into a $q\bar{q}$ pair but only one partner of the pair carries the total momentum. At the end of the fragmentation process energy-momentum conservation is enforced by first enforcing local conservation of transverse momentum in each jet so that the original parton direction is conserved. The longitudinal momenta are scaled by a factor which is chosen such that the ratio of the jet-momentum to the momentum of the original parton is the same for all partons and so that also energy is conserved.

Model by Ali et al. In the model by Ali et al. [89] important diagrams of second-order QCD have been included. The gluon also decays into a $q\bar{q}$ pair but in contrast to the Hoyer model, the energies are distributed between the q and the $\bar{q}$ according to the Altarelli–Parisi distribution function [90]. In addition the quarks are assumed to acquire a transverse momentum with respect to the gluon, its distribution is assumed to be Gaussian with the same σ_q as for quarks. Energy-momentum conservation is implemented by first boosting all momenta along the direction of the missing momentum and then rescaling energies by a common factor. In this scheme the relative energies of the partons are approximately conserved while the directions are changed.

Lund model. This model is based on the relativistic massless string model described in [91]. The fragmentation occurs along the colour flux lines which are stretched from quark to antiquark via the gluon(s), which is situated at the kink of a colour string (fig. 5.4). The colour strings are expanding while the partons move away from the origin; the string energy grows proportional to its length until it breaks and secondary quark–antiquark pairs are generated at the break-up points. The secondary quark

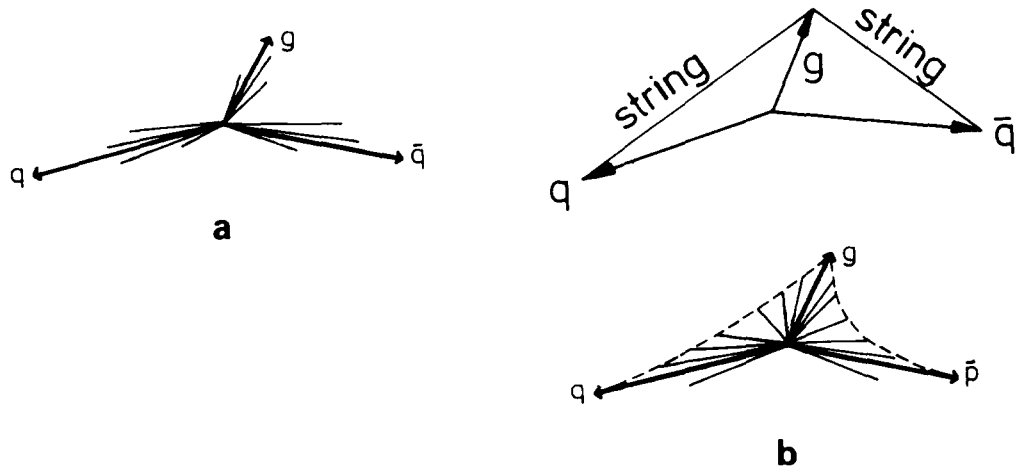

Fig. 5.4. a) Independent fragmentation and b) string fragmentation of three-jet events.

pairs are generated in the centre-of-mass system of the string and after being combined into hadrons they are boosted back into the centre-of-mass system of the event. Thus the final hadron momentum vectors lie on hyperbolae between the quarks and the gluon. Energy and momentum is conserved in every step and does not have to be imposed artificially. For further details see [92, 93].

The way energy-momentum conservation is imposed in the models with independent fragmentation is important and implies a systematic distortion in the event shape reconstructed from the final hadrons compared with the primary partons. These distortions have a significant effect on determining the three-jet rate and thus may bias the determination of α_s as will be seen later [115, 108, 109].

The original versions of these models were provided by the authors. Subsequently T. Sjöstrand provided a program code which included all three possibilities for fragmentation. This led to more flexibility since it was for example possible to combine the different ways of gluon fragmentation with the various schemes of momentum conservation. Two versions of this program were used: Lund version 4.3 and 5.2. Apart from many improvements in details of the fragmentation process, which were implemented in version 5.2, the main change was the inclusion of the full matrix element to second order.

Production of baryons was included in these models; it is realised as the formation of pairs of diquarks, which are combined with quarks to form baryons.

5.2.2. Shower models using leading log approximation in QCD

In the second class of models QCD calculations in leading log approximation (LLA) are used to calculate also part of the hadronisation process in an attempt to minimize the part to be described by empirical models. In this approach a pair of quarks is generated, which initiates a parton shower by radiating gluons (fig. 5.5). These gluons can again split into gluon pairs and, with a smaller probability, into quark pairs. The high virtual mass of the initial partons is lowered in each branching until a cut-off which is close to the real particle masses, is reached. The multitude of coloured quarks and gluons generated in this way is transformed into colourless hadrons by a phenomenological procedure.

QCD shower models were introduced by Fox and Wolfram [94] and subsequently further developed. Two models based on this approach were compared with the data, the model by Gottschalk [95] and the model by Webber and Marchesini [96]. They differ in many details in the cascade process and also in the final hadronisation procedure. The main new ingredient in the Webber model came from calculations which showed that interference effects in the process of multiple gluon emission are important [97]. They can be approximately taken into account by ordering the gluon emission angles: any subsequent angle in the cascade is smaller than the previous one.

5.2.3. The parameters of the models

The models based on a QCD matrix element and phenomenological hadronisation contain many parameters which have to be determined from the data. Typical sets of parameters are shown in table 5.1. The principal parameters relevant for the shape of the events are the QCD coupling constant α_s or the QCD scale parameter Λ, the parameters of the fragmentation function and σ_q. The energy dependence of α_s is described by introducing the scale parameter Λ; the relation between α_s and Λ is given to first- and second-order by eqs. (4.19) and (5.26). In addition there are parameters describing details in the hadronisation process, such as γ_s the relative probability to create $s\bar{s}$ pairs in the fragmentation, $r = PS/(PS + V)$, the fraction of pseudoscalar mesons generated. Their determination will be discussed in the following chapter 6 on inclusive particle production. Other parameters, for example those for the formation of baryons, were left as inserted by the authors.

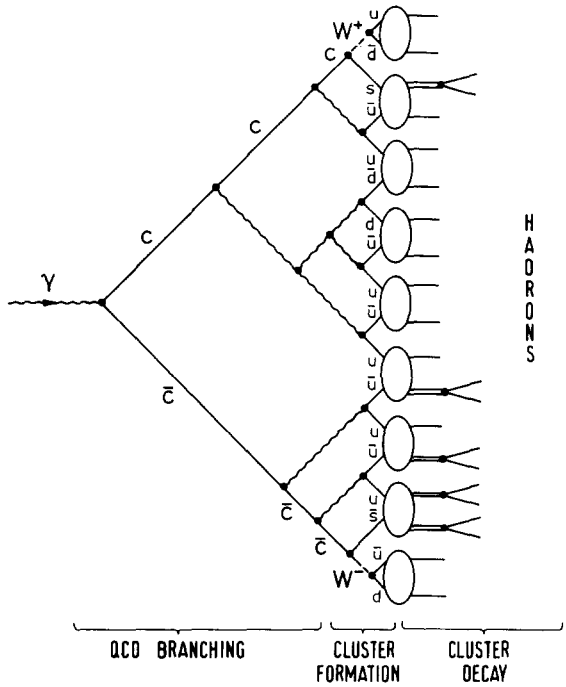

Fig. 5.5. Development of a parton shower in the Webber model.

The functional form of the fragmentation function has been adapted to the improving data several times. The original fragmentation function in the LUND model (version 4.3) was:

$$f(z) = (1+\beta)(1-z)^{\beta}\,; \tag{5.22}$$

β is flavour dependent. For heavy quarks a value substantially smaller than for u and d quarks was chosen, typically $\beta_c = 0.3\beta_u$ and $\beta_b = 0.1\beta_u$. Subsequently different functions were proposed for heavy quarks to conform with the measurements on c- and b-quarks. The function

$$f(z) = (1-z)^{A}\,\frac{1}{z}\exp\left(-B\,\frac{m_{\perp}^2}{z}\right) \tag{5.23}$$

Table 5.1
Typical sets of parameters for the Lund model (FF = fragmentation function) and for QCD shower models

	Lund model	
Parameter	Vers. 4.3	Vers. 5.2
Λ (GeV)	0.3	0.5
σ_q (MeV)	250	265
γ_s	0.3	0.3
r	0.5	0.5, 0.25
FF u, d, s	$\beta \sim 0.5$	$A = 1.0$, $B = 0.6$
FF c, b	β small	$\varepsilon_c = 0.05$, $\varepsilon_b = 0.018$

QCD shower models	
Model	Parameters
Gottschalk	$\Lambda = 0.2$ GeV, $t_0 = 1.5$ GeV^2, $W_{min} = 1.25$ GeV
Webber	$\Lambda = 0.3$ GeV, $Q_g = 0.7$ GeV, Max. clust. mass 3.5 GeV

was proposed by the Lund group [92]. It has only two parameters for all quark flavours, the flavour dependence is introduced through the transverse quark masses $m_\perp = \sqrt{p_t^2 + m_q^2}$. It was optimized by fitting the energy weighted angular correlations (section 5.4.3) and gave good fits of the data for $A = 1.0$ and $B = 0.6$–0.8.

Another widely used function for heavy quarks was proposed by Peterson et al. [100]:

$$f(z) = \frac{1}{z(1 - 1/z - \varepsilon_q/(1-z))^2} \,. \tag{5.24}$$

The parameter ε_q has to be determined separately for c- and b-quarks. ε_c and ε_b in the table were obtained from an analysis of all available data on D* [98] and leptonic b-decays [99].

The LLA shower models both have three important parameters, current values are given in table 5.1. The first one is the QCD scale parameter Λ, which determines the probability of gluon emission but which need not be the same as in the matrix elements in the first model class. The second parameter determines the end of the showering process (t_0 and Q_g in table 5.1) and the third one is necessary for the final decays into observable hadrons (W_{min} in the Gottschalk model and a "maximum cluster mass" in the Webber model).

5.3. *Properties of three-jet events*

5.3.1. *Experimental evidence for a difference between quark- and gluon-jets*

A consequence of the non-Abelian nature of QCD is the self-coupling of the gluon, which leads to the process $g \to gg$. Due to this possibility the hadron-jet originating from a primary gluon is expected to be different from a quark initiated jet; one might expect a higher multiplicity and a softer fragmentation function for gluon initiated jets.

In order to study the properties of gluon-jets and to compare them with quark-jets, planar events were selected from the sample of multihadronic events by applying the cuts in the Q-plot, which are indicated in fig. 5.3: $Q_1 < 0.06$, $Q_2 - Q_1 > 0.07$. In the selected events three jets are defined by maximizing triplicity [101], an extension of thrust to three jets:

$$T_3 = \max \frac{\left|\sum_{i_1} \boldsymbol{p}_{i_1}\right| + \left|\sum_{i_2} \boldsymbol{p}_{i_2}\right| + \left|\sum_{i_3} \boldsymbol{p}_{i_3}\right|}{\sum_{\text{all}} |\boldsymbol{p}_i|} \,,$$

where i_1, i_2 and i_3 run over three non-overlapping sets of particles (charged and neutral). The jet-axis $\boldsymbol{k}_j$ was determined as the vector sum of all particles belonging to a jet. The jet energy was calculated in two ways, once E_j^e was calculated by summing the energies of all particles and alternatively E_j^d was obtained from the angles between the jet-axes:

$$E_j^d = E_{cm} \frac{2 \sin \theta_{kl}}{\sin \theta_{12} + \sin \theta_{23} + \sin \theta_{31}} \qquad j, k, l \text{ cyclic} \,.$$

Both ways to calculate the jet energy are influenced by detector effects in different ways, for instance by

missing particles, neglected mass effects, etc. The results discussed in this chapter did not show a significant sensitivity to which jet energy was used, E_j^e or E_j^d.

Events which contained jets with less than 4 particles or with $E_j^e < 2\,\text{GeV}$ were rejected. The jets were then ordered according to decreasing jet energy: $E_1^d > E_2^d > E_3^d$.

Model events were generated (Lund version 4.3) and the particles were "tracked" through the detector, simulating the detector signals with all resolutions and efficiencies. Then the analysis described above was also carried out for the model events. The parton which was closest in angle to the reconstructed jet-axis was defined to be the source of the jet. The gluon content of the three jets is shown in table 5.2 for two centre-of-mass energies along with the background of $q\bar{q}$ events incorrectly classified as three-jet events. As expected, the jet of lowest energy, jet #3, has the highest probability of being produced by the gluon. For simplicity we shall sometimes call jet #3 the "gluon"-jet and jets 1 and 2 the quark-jets.

The distribution of transverse momentum relative to the jet-axis is shown in fig. 5.6 for the "gluon"-jet (jet #3) and a quark-jet (jet #2). A distinct difference can be seen in the slope of the two distributions the "gluon"-jet falling off more slowly than the quark-jet.

This difference can also be seen by comparing the average transverse momenta of the three jets. The averages are shown as a function of jet energy E_j^e in fig. 5.7. The "gluon"-jet has higher $\langle p_t \rangle$ values than the quark-jets #1 and 2 for a wide range of jet-energies. This difference indeed suggests a broader p_t distribution for gluons. This broadening is also seen in p_t^{out}, the component of p_t perpendicular to the event plane (fig. 5.8). Experimentally the event plane is well defined and p_t^{out} is thus expected to be less affected by fluctuations than p_t. It is also less sensitive to fragmentation effects.

The particle multiplicity $dN/d\theta$ and the energy density $dE/d\theta$, where θ is the angle with respect to the jet-axis, of the gluon-jet were also examined. Figure 5.9 shows the multiplicity distribution as an example. $dN/d\theta$ is found to be larger for the "gluon"-jet at large values of θ than for jets 1 and 2. This can be explained by a softer fragmentation function of the gluon as will be seen presently.

The data for $\langle p_t \rangle$, $\langle p_t^{out} \rangle$, $dN/d\theta$ and $dE/d\theta$ (not shown) were compared with the available fragmentation models (figs. 5.7 and 5.8 give examples). The Hoyer model in which the gluon fragments like a quark cannot explain the p_t behaviour. A wider p_t distribution would have to be introduced for the gluon-jet in order to reproduce the results. An increase of σ_q from ~330 (for quark-jets) to ~500 MeV for the gluon-jet gave a fairly good description of the data. This larger σ_q is however not sufficient to also describe the $dN/d\theta$ behaviour (fig. 5.9). Only if in addition a softer fragmentation function is introduced for the gluon ($a_g = 4$ in the Hoyer fragmentation function instead of $a_q = 0.5$ for quarks) does the model describe the data. The Lund model 4.3 showed the observed effects in p_t and $dN/d\theta$ without further tuning and the agreement of the Lund model with the data is not affected by the inclusion of second-order QCD (version 5.2).

The Gottschalk and the Webber model give as good a description of the $\langle p_t \rangle$ distributions as the Lund model. The Ali model has a tendency into the right direction but cannot describe the magnitude

Table 5.2
Gluon content and $q\bar{q}$ background in three-jet events (calculated with Lund 4.3)

	Gluon content (%)			
$\sqrt{s}$ (GeV)	Jet #1	Jet #2	Jet #3	$q\bar{q}$ background (%)
22	9	20	34	37
33	12	22	51	15

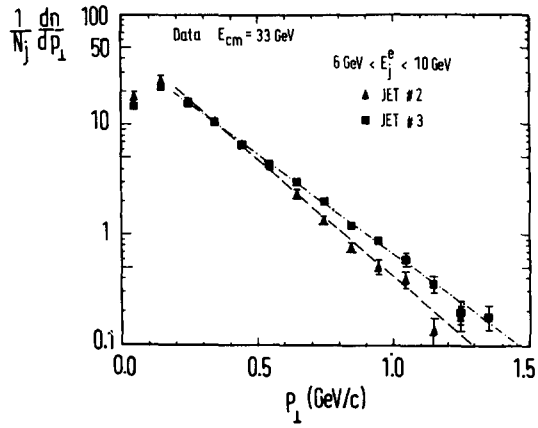

Fig. 5.6. p_t distribution for the "gluon"-jet and for a quark-jet for jet energies between $6 \leq E_j^e \leq 10$ GeV.

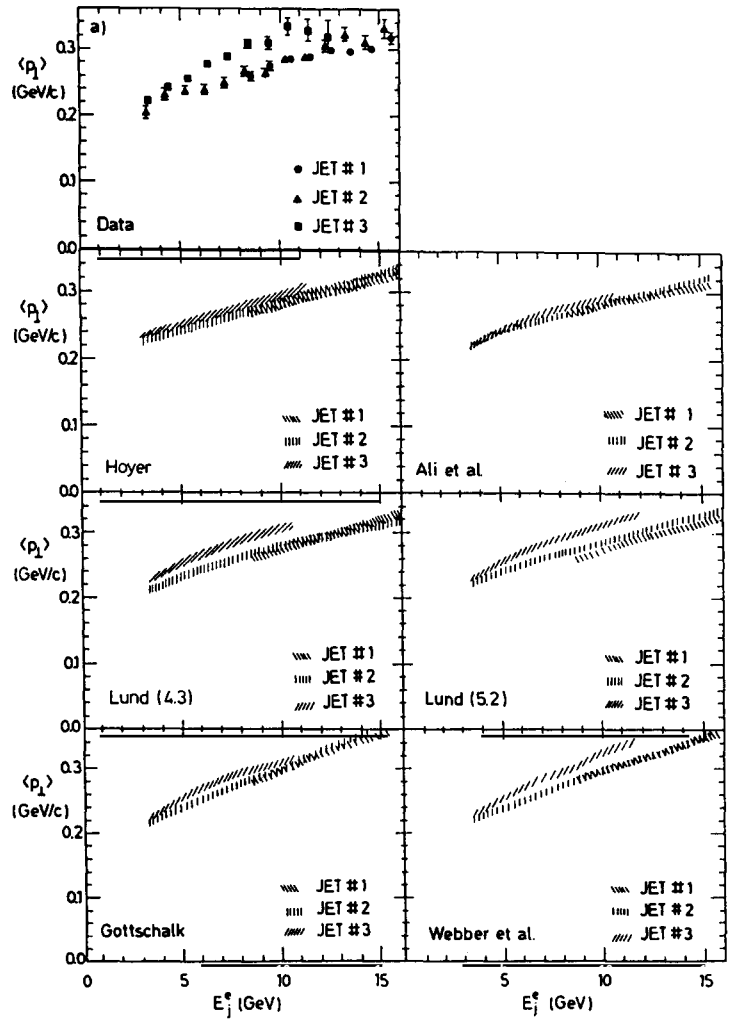

Fig. 5.7. $\langle p_t \rangle$ as function of E_j^e (see text for details).

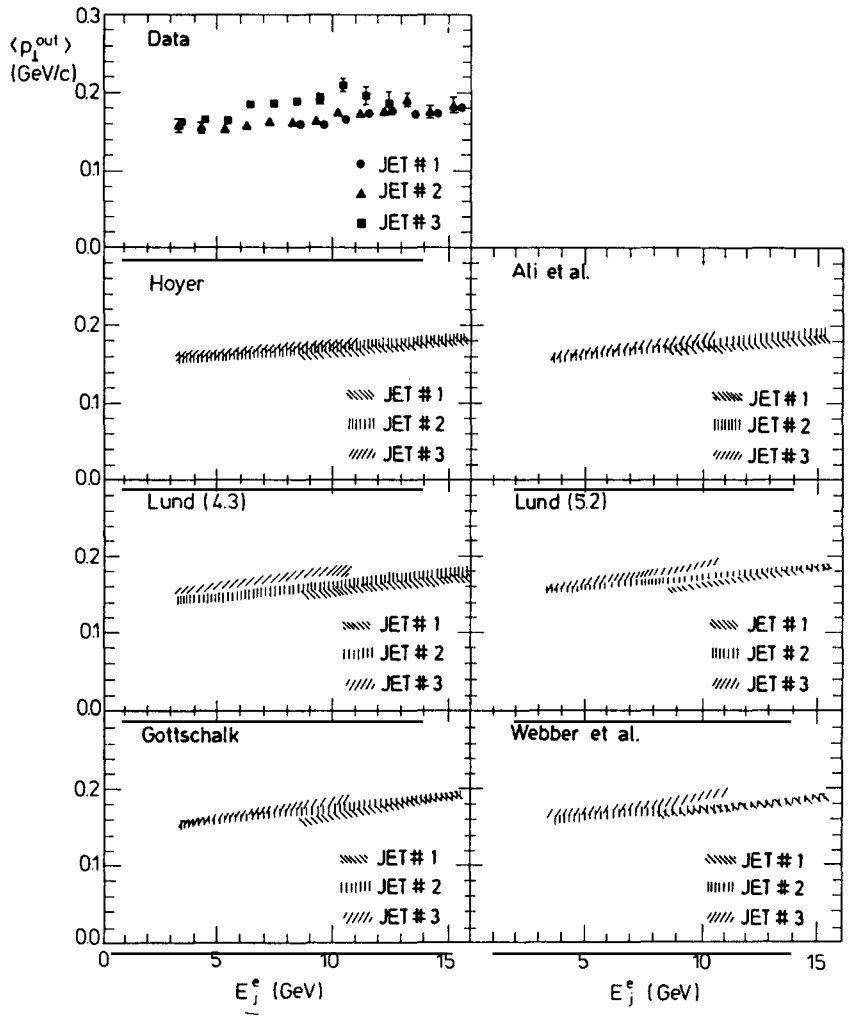

Fig. 5.8. $\langle p_t^{out} \rangle$ as function of E_j^e (see text for details).

of the effect. For the $\langle p_t^{out} \rangle$ distributions and the angular distribution of the particle flux only the Lund and the Webber model show the right behaviour, although the magnitude of the difference in $\langle p_t^{out} \rangle$ seen in the data is not reached in the models.

5.3.2. The "string" effect

In the Lund model the gluon is different from the quarks by construction. The fragmentation of qqg events occurs in the centre-of-mass system of the two colour strings stretched from quark to antiquark via the gluon. The fragmentation products are afterwards boosted into the event centre-of-mass system. A consequence of this procedure (shown by A. Petersen [104]) is a depletion of particles in the angular region between the two quark-jets (see fig. 5.4b). This effect can be observed in the data by plotting the energy and particle flow $dE/d\theta$ and $dN/d\theta$ in the event plane for the whole event (fig. 5.10). θ is counted from jet #1 over jet #2 and 3, back towards jet #1. The data show three maxima corresponding to the average positions of the three jets. The valley between jets 1 and 2 which have the

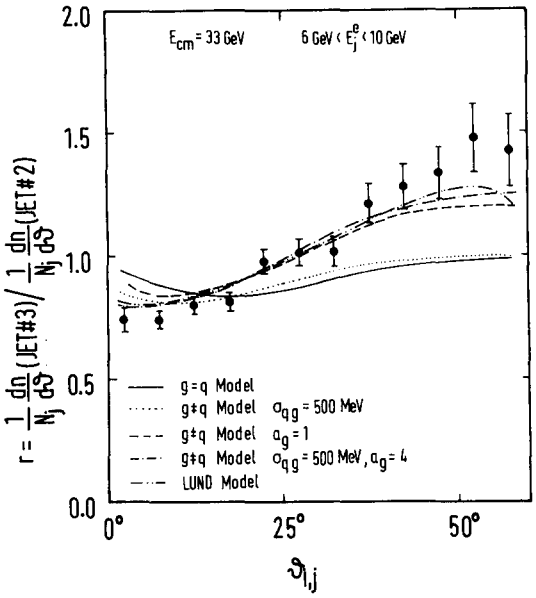

Fig. 5.9. Ratio of particle fluxes $dN/d\theta$ for jet #3 over jet #2 as a function of the angle with the jet-axis.

highest probability to originate from the quarks is deeper than the two valleys between jet 3 – the "gluon-jet" – and jets 1 and 2. The general shape of the distribution is described well by the Hoyer and by the Lund model, but the Hoyer model fails to reproduce the difference in the depth of the valleys which is correctly described by the Lund model.

Since this "string" effect is produced by the Lorentz boost from the centre-of-mass system of the string into that of the event, it can be enhanced by selecting those particles which are more affected by the boost. The relevant quantity for the boost is the transverse mass, $\sqrt{m^2 + (p_t^{out})^2}$. The distribution for particles of $p_t^{out} > 0.3$ GeV in fig. 5.10.Ic indeed shows a deeper valley between jets 1 and 2 than the distribution for all particles. Again the agreement of the data and the Lund model is good.

The data are compared with the model by Ali et al. and with the Lund model 5.2, which includes $O(\alpha_s^2)$ QCD effects, in fig. 5.10.II. The agreement between data and the Lund model is not altered by including second-order QCD. The Ali model fails to describe the depletion of the region between jets 1 and 2. The QCD shower models are examined in fig. 5.10.III. The Gottschalk model does not reproduce the string effect but the Webber model does. Subsequently the equivalence of the soft gluon interference effects, which are approximately included in the Webber model, with the string effect was demonstrated [102].

The sensitivity of the string effect to p_t^{out} and the particle mass can be seen in fig. 5.11 where the ratio of the number of particles in the region between the "gluon" – and a quark-jet (1 and 3) to the number between the two quark-jets 1 and 2 is shown for all particles, for those with $p_t^{out} > 0.3$ GeV and for a kaon enriched data sample. The ratio is larger than 1 and is reproduced well by the Lund and by the Webber model, while no other model shows this effect.

The string effect, described so far, concerns mainly particles of low energy between the jets. But also energetic particles in the centre of the jet are indirectly affected by the string effect as can be seen in fig. 5.12. The average transverse momenta of the particles in the event plane $\langle p_t^{in} \rangle$ are shown as a function of their longitudinal momenta $p_{\parallel}$ parallel to the jet-axis. To $\langle p_t^{in} \rangle$ is attributed a sign which is defined in

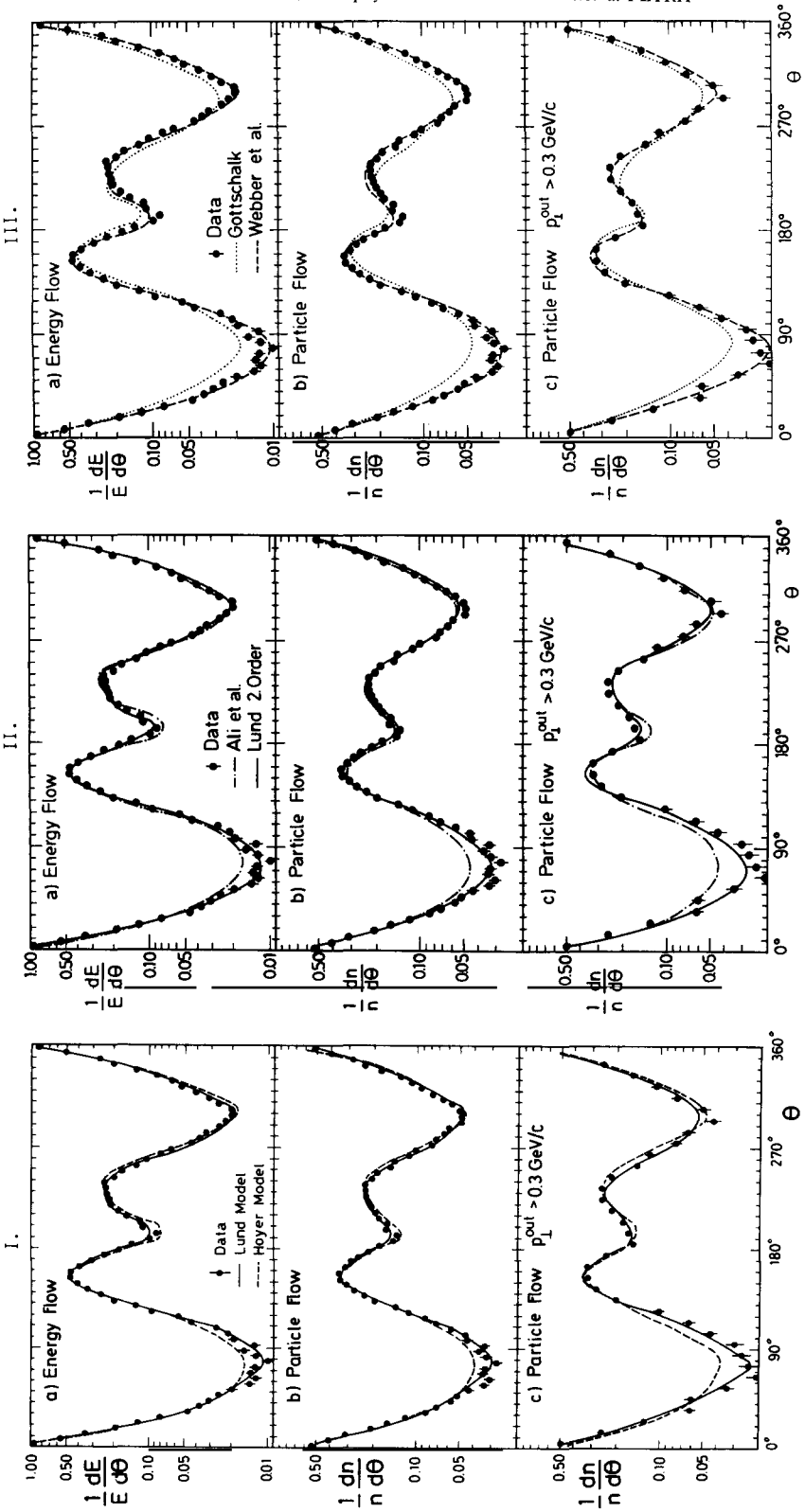

Fig. 5.10. Energy and particle flow in the event plane compared to predictions of the I, Hoyer and Lund (version 4.3) models; II, the Ali and Lund (version 5.2) models; III, the Gottschalk and Webber models (see text for details).

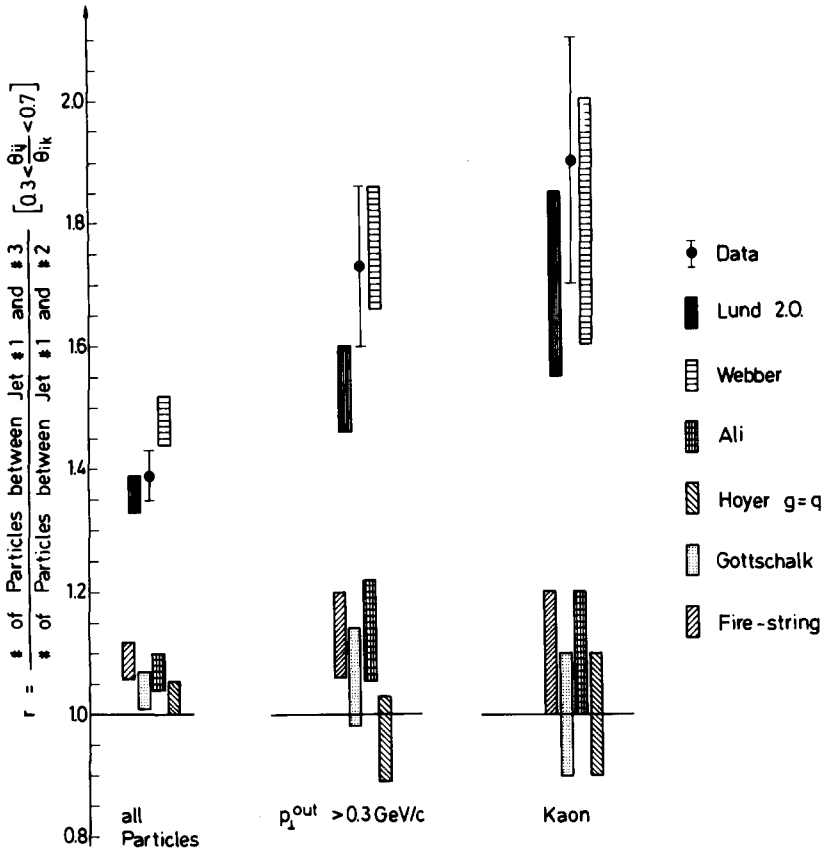

Fig. 5.11. Number of particles in the angular region between jets #1 and 3 compared to the region between jets #1 and 2 for all particles, particles with $p_t^{out} > 0.3$ GeV and for a K enriched sample.

the insert of fig. 5.12. At small $p_{\parallel}$, the data agree with the models reasonably well. But for $p_{\parallel} \gtrsim 5$ GeV $\langle p_t^{in} \rangle$ in jet #1 is positive and in jet #2 negative, that means that the momentum vectors of the two quark-jets point away from the "gluon"-jet. This is also a consequence of the string effect: in the boost after the fragmentation particles with small momenta are more affected than high momentum particles. The direction of the boost is in general quite close to the gluon direction. Therefore the reconstructed jet-axes of the quark-jets, which are calculated using all particles, are shifted towards the gluon. Energetic fragmentation products are therefore preferentially found opposite to the side of the gluon. This effect is again reproduced only by the Lund and by the Webber models, while the independent parton models and the Gottschalk model do not show this behaviour.

The ability of the models to reproduce the differences in the $\langle p_t \rangle$ and $\langle p_t^{out} \rangle$ distributions, the angular distribution of the particle flow in a jet and the string effect, is summarized in table 5.3. The models which best describe these features of the data are the Lund and the Webber model while the Hoyer model is ruled out and the Ali and Gottschalk models take an intermediate position: they give a fair description of the p_t behaviour, but they do not show the string effect.

More details about the analyses can be found in [103] and in [104]. The TPC collaboration has carried out similar investigations and confirmed the string effect at $\sqrt{s} = 29$ GeV and also found that models with independent fragmentation are in many ways not able to describe the data [105]. The

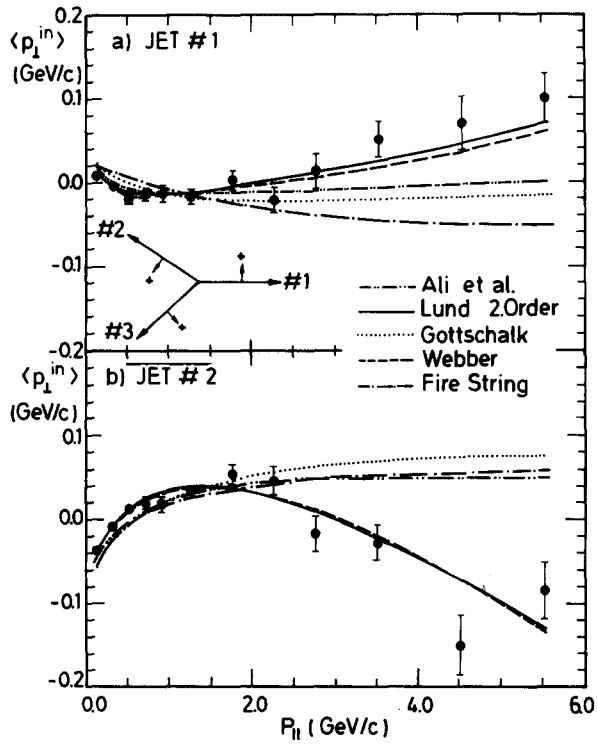

Fig. 5.12. p_t^{in} as a function of longitudinal momentum parallel to the jet-axis for jets #1 and 2.

TASSO collaboration also confirmed the latter point for soft particles between jets [106]; they however found deviations from the Lund model for particles of larger momenta. The discrepancy between data and Lund model was particularly large for events with low planarity $Q_2 - Q_1 < 0.07$, which have been removed by the event selection in the JADE and TPC experiment. These events might be due to events from heavy quarks rather than from three-jet events.

A difference in particle composition which has also been predicted for gluon-jets has not yet been found (see chapter 6).

5.4. *Determination of* α_s

5.4.1. *Introduction*

A determination of the coupling constant of QCD and the scale parameter Λ has been one of the

Table 5.3
Qualitative agreement of models with gluon properties and the string effect, "yes" means good agreement, "appr" trend in the right direction and "no" does not reproduce the data

Distribution	Hoyer	Ali	Lund	Gottschalk	Webber
$\langle p_t \rangle$	no	appr	yes	yes	yes
$\langle p_t^{out} \rangle$	no	no	appr	no	appr
$dN/d\theta$	no	no	yes	no	yes
String	no	no	yes	no	yes

major aims pursued by all PETRA experiments [107, 108–112]. These measurements turned out to be quite involved mainly due to two facts: hadronisation effects were very important [108, 115] and α_s^2 corrections were not negligible (see e.g. table 5.4).

The calculations of the exact matrix element to second order was carried out by three groups with conflicting results: the results of Fabricius, Gutbrod, Kramer, Schierholz and Schmitt (FKSS) [116] or GKS [117] predicted the $O(\alpha_s^2)$ corrections to the three-jet cross-section to be small. The Ellis, Ross and Terrano (ERT) [118] and Vermaseren, Gaemers and Oldham (VGO) groups [119] predicted large corrections and were in agreement with each other. The disagreement between FKSS/GKS and ERT/VGO arose from the three-jet cross-section, while the four-jet cross-section was unambiguous. The two groups used different techniques to deal with the singularities which occur in the amplitudes of the three-jet cross-section for the case that two partons are very close together (collinear singularities) or that one parton is very soft (infrared singularities). In the FKSS/GKS calculation a resolution criterion was introduced and when two partons were found irresolvable they were combined into one. The resolution criterion in the FKSS calculation used the Sterman–Weinberg definition of a jet: two partons which had energies above $\varepsilon\sqrt{s}/2$ were called resolvable if the angle between them was larger than δ. In the GKS calculation two partons were called irresolvable if their invariant mass was below a limit $y_{\min}^{\text{theor}}\sqrt{s}$. ε, δ and $y_{\min}^{\text{theor}}$ are parameters which have to be adjusted.

The ERT and VGO matrix elements in contrast were obtained for "bare" partons. The FKSS/GKS matrix elements were found to agree with ERT/VGO for the limit of infinitely good resolution [117, 120].

Matrix elements from both groups FKSS/GKS and ERT were used for the determination of α_s and the results were found to depend on the matrix element and – for the same matrix element – on the fragmentation model used.

Part of the difference in the results may be explained by the observation of Gottschalk and Shatz [121], who pointed out that approximations made in the FKSS and GKS calculations would lead to an overestimation of α_s by approximately 10%.

In this chapter we will describe in some detail the analysis of the energy–energy correlations between particles and a fragmentation-model independent determination of α_s using the s-dependence of variables which are calculable in QCD. Finally the α_s values from all e^+e^- experiments obtained with similar methods will be compared.

5.4.2. Early determinations of α_s

The first determination of α_s using JADE data was attempted when ~1000 hadronic events had been collected. Fitting the data to the sphericity and Q_1 distributions which were calculated in the Hoyer model using $O(\alpha_s)$ cross-sections resulted in $\sigma_q = 0.34 \pm 0.03$ and $\alpha_s = 0.18 \pm 0.03 \pm 0.03$. Other models gave results compatible within the error [122].

The importance of including the terms of $O(\alpha_s^2)$ was shown in the next analysis [123] which was carried out for three-jet events by comparing the same data with first- and second-order QCD. The $O(\alpha_s^2)$ three-jet cross-sections were taken from FKSS/GKS. The three-jet events were selected by two different cluster methods and the data were corrected not only for detector and radiation effects but also for fragmentation effects using model calculations. The result did not depend strongly on the cluster method used, but the value of α_s was found to decrease by roughly 20% if α_s^2 corrections were taken into account (see table 5.4). The dependence on the fragmentation model was covered by a systematic error of 0.03 at a $y_{\min} = y_{\min}^{\text{theor}} = 0.04$.

5.4.3. Energy–energy correlations

The energy–energy correlation "EEC" (sometimes also called the energy weighted angular correlation) between final state particles have been shown to be calculable in perturbative QCD up to second order [125, 126]. The energy–energy correlations were proposed early on to be used for α_s determinations [124] especially since fragmentation effects were expected to be small in its asymmetry [127].

The EEC is calculated as the energy weighted sum over pairs of particles i and j with an angle θ between them:

$$\frac{d\Sigma}{d\theta}(\theta) = \frac{1}{N}\sum_{k=1}^{N}\sum_{i,j} x_i^k x_j^k \frac{1}{\Delta\theta}\int_{\theta-\Delta\theta/2}^{\theta+\Delta\theta/2} \delta(\theta_{i,j}^k - \theta')\,d\theta'$$

where the x_i are the normalised energies, $x_i = E_i/\sqrt{s}$. The inner sum extends over all particle pairs in an event and the outer sum over all events. The EEC is calculated for a bin around θ of width $\Delta\theta$.

For 2-jet events $d\Sigma/d\theta$ is expected to be symmetric around 90° even including fragmentation effects. Hard gluon emission on the other hand results in a non-vanishing asymmetry defined as:

$$A_{EEC}(\theta) = d\Sigma(\pi-\theta)/d\theta - d\Sigma(\theta)/d\theta\,.$$

The multihadronic data at c.m. energies of 14 GeV, 22 GeV and 34 GeV were analysed. In addition to the standard selection cuts the events were required to be well-contained in the detector and well-balanced in momentum. The reduction of events with hard bremsstrahlung by removing events containing an isolated photon of more than 3 GeV was found to be important, because these radiative events also contribute to the asymmetry A_{EEC}. At $\sqrt{s} = 34$ GeV ~12 700 events were used for the analysis.

The experimental energy correlation function was calculated in bins of $\Delta\theta = 3.6°$ and was corrected for detection efficiencies, resolution effects and for bremsstrahlung of the initial state leptons. The corrections were applied bin by bin in θ and were obtained from the Lund Monte Carlo. Using the Hoyer or Ali Monte Carlo gave only small changes in the correction factors. The asymmetry A_{EEC} was calculated from the uncorrected experimental distributions and corrected afterwards. This procedure had the advantage of partially cancelling corrections. The correction factors for the asymmetry were close to 1 everywhere except at very small and very large values of θ.

The corrected data are shown in figs. 5.13 and 5.14. They were analysed once neglecting the effect of fragmentation and also in the context of fragmentation models. In fig. 5.14 the $O(\alpha_s^2)$ result for A_{EEC} calculated by Ali and Barreiro [126] is also shown. A direct comparison of the data with the QCD results disregarding any fragmentation effects results in $\alpha_s = 0.14 \pm 0.01$, 0.13 ± 0.01 and 0.115 ± 0.005 at the three energies 14, 22 and 34 GeV, where the errors are only statistical. The weak energy dependence of these values confirms the prediction that fragmentation effects are indeed small in the asymmetry of the energy–energy correlation.

The data were also analysed in the framework of fragmentation models in order to check on their ability to describe the EEC and also to determine α_s. In the model calculations detector effects were simulated and they were subjected to the same treatment as the data. The models used were all based on the $O(\alpha_s^2)$ GKS matrix elements but differed in details of gluon fragmentation and momentum conservation.

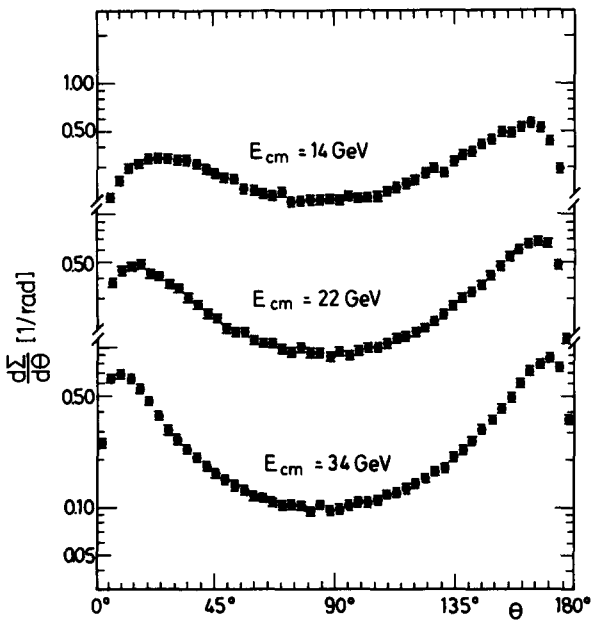

Fig. 5.13. The corrected energy–energy correlation function $d\Sigma/d\theta$ data at $\sqrt{s} = 14$, 22 and 34 GeV.

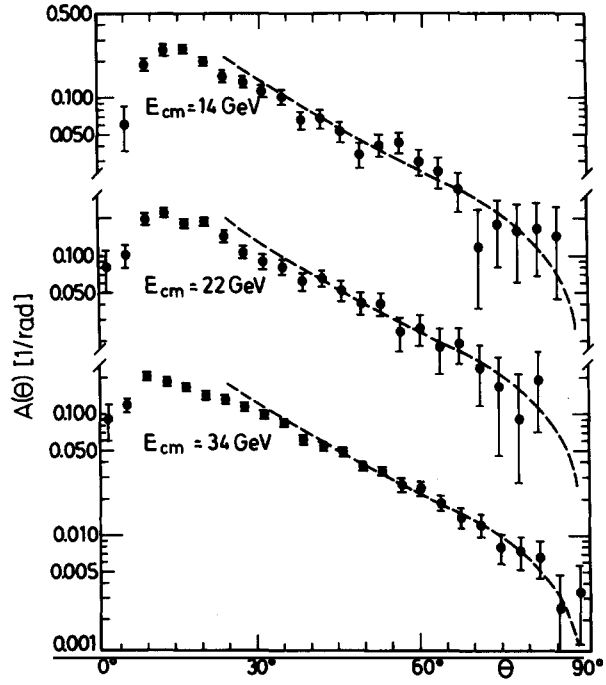

Fig. 5.14. The corrected asymmetries A_{EEC} of the energy–energy correlation at $\sqrt{s} = 14$, 22 and 34 GeV. The curves represent fits to the data using $O(\alpha_s^2)$ QCD calculations by Ali and Barreiro neglecting fragmentation effects [126].

Comparison with the Lund model

The corrected data for the energy–energy correlation and the asymmetry are compared with the Lund model (version 5.2) in fig. 5.15. The asymmetry is well described by the model for $\theta > 36°$ with a $y_{min}^{theor} = 0.02$. In order to describe also the region of small angles well, which is sensitive to fragmentation effects, smaller values of y_{min}^{theor} are necessary. $y_{min}^{theor} = 0.0125$ gives a good fit and does not alter the agreement at higher angles substantially. For such small values of y_{min}^{theor} nearly all events are generated as three- or four-parton events. The value of $\alpha_s = 0.165 \pm 0.01 \pm 0.01$ was determined with $y_{min}^{theor} = 0.0125$, $\sigma_q = 0.220$ GeV, the parameters of the Lund fragmentation function (eq. 5.23) were $A = 1.0$ and $B = 0.70$.

Comparison with models having independent fragmentation of partons

The independent fragmentation models were used in several versions, which differed in the treatment of gluons and in the way energy-momentum conservation was imposed. In general they led to smaller values of α_s than the Lund model, the values ranged between 0.11 and 0.14. At values of $\theta > 36°$ they showed little dependence on fragmentation parameters (fig. 5.16). The region below 36°, where fragmentation effects are most important, could not be described well by any combination of parameters. The agreement between data and model was equally bad for the EEC function itself.

The results for α_s determined by analysing the asymmetry of the energy–energy correlation are summarized in table 5.4 together with the early results. A discussion of the results will follow after the presentation of the model-independent analysis in the next section.

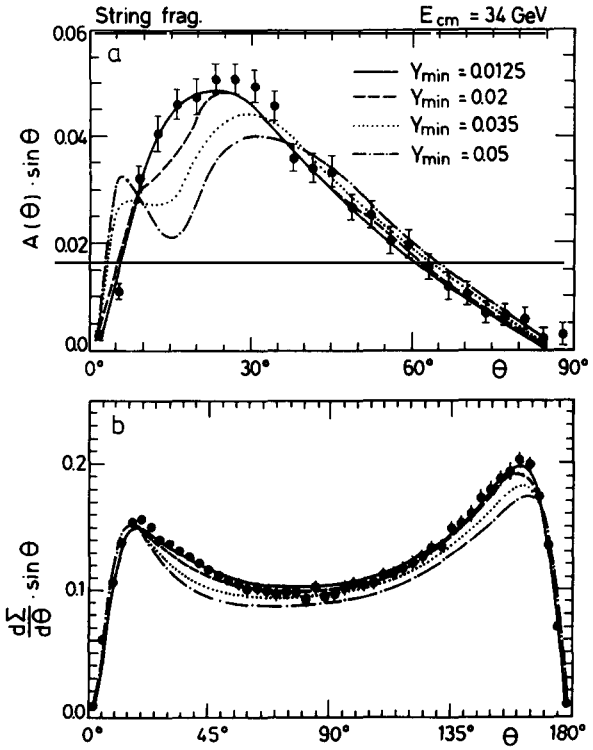

Fig. 5.15. Comparison of the asymmetry $A(\theta)$ of the EEC and the EEC function $d\Sigma/d\theta$ at 34 GeV with QCD results using the string fragmentation model for different y_{min} values. Note that A and $d\Sigma/d\theta$ have been multiplied by $\sin\theta$.

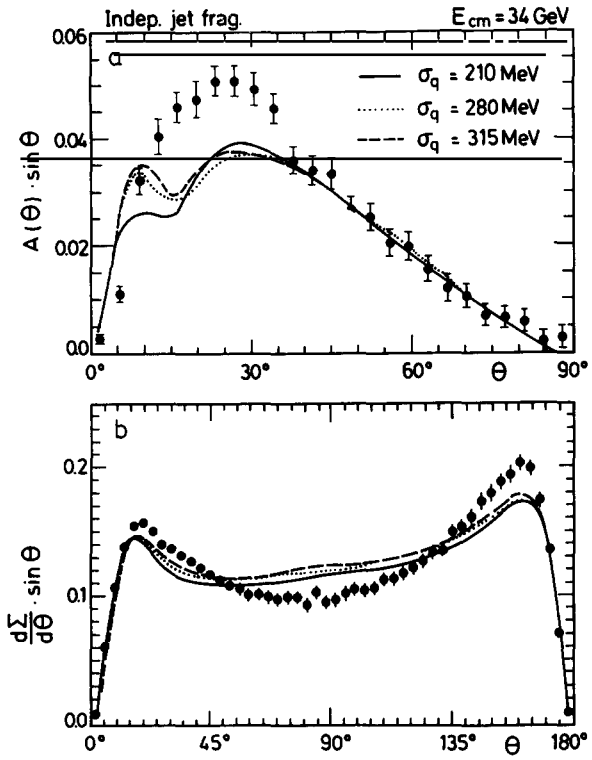

Fig. 5.16. The asymmetry $A(\theta)$ of the EEC and the EEC function $d\Sigma/d\theta$ compared with QCD calculations using independent fragmentation of partons for several values of σ_q. Note that A and $d\Sigma/d\theta$ have been multiplied by $\sin\theta$.

5.4.4. *Limits on α_s from variables calculable in QCD*

In view of the model dependence of α_s determinations within fragmentation models, a different approach was tried [128] to determine α_s, which was called to attention by Field [129]. It had been used previously by the PLUTO Collaboration up to $\sqrt{s} = 30$ GeV [130]. The method is based on jet shape variables which can be calculated in QCD to order α_s^2. The variables studied were:

Table 5.4
Determination of α_s by the JADE Collaboration

$\sqrt{s}$ (GeV)	Events	QCD	Method	Fragm. model	α_s	Year
30	1000	$O(\alpha_s)$	S, Q_1	Hoyer, Lund	$0.18 \pm 0.03 \pm 0.03$	1980
34	4800	$O(\alpha_s)$	$d\sigma/dx$ for	Lund, Ali	$0.20 \pm 0.015 \pm 0.03$	1982
		$O(\alpha_s^2)$ FKSS/GKS	three-jet events	Lund, Ali	$0.16 \pm 0.015 \pm 0.03$	
34	12 700	$O(\alpha_s^2)$ GKS	A_{EEC}	Lund	$0.16 \pm 0.01 \pm 0.01$	1984
				Ali	0.14 ± 0.01	
				Hoyer	0.11 ± 0.01	
		Ali-Barreiro	A_{EEC}	neglected	0.12 ± 0.01	
44	6636		Energy dependence			1986
35	12 700	$O(\alpha_s^2)$ ERT	of $\int_{45}^{90} A_{EEC}\, d\theta$,	-	$0.10 < \alpha_s < 0.15$	
22	1666		$\langle 1-T \rangle$, $\langle M_H^2 \rangle$		at 95% C.L.	
14	2090			$\sim 1/\sqrt{s}$	$0.12 \pm 0.01 \pm 0.01$	

– $\langle 1 - T \rangle$, where T is the event thrust,

– $\int_{45}^{90} A_{EEC}\, d\theta$, the integrated asymmetry of the energy–energy correlation, the integration limits correspond to the region where the influence of fragmentation is small,

– $\langle M_H^2 \rangle$, the average heavy jet mass suggested by Clavelli [132]. M_H is defined in the following way: each event is divided into two hemispheres and the invariant mass is calculated for each hemisphere, M_H and M_L. The hemispheres are chosen such that $M_H^2 + M_L^2$ is minimal.

The distributions of the data in $1 - T$ and M_H^2, normalised to the visible energy E_{vis}, are shown in fig. 5.17 for three centre-of-mass energies. They show a peak which gets narrower and shifts towards lower values of $1 - T$ and M_H^2/E_{vis}^2 with increasing centre-of-mass energy, where fragmentation effects become less important.

The results of the QCD calculation for the mean values $\langle 1 - T \rangle$ and $\langle M_H^2 \rangle$ and for the integral over the asymmetry of the energy–energy correlation can be written as:

$$O = C_1 \alpha_s (1 + C_2 \alpha_s) + F \tag{5.25}$$

where O denotes the variable and the coefficients $C_{1,2}$ were calculated in [131, 132] using the exact ERT matrix element to second order. They are given in table 5.5. F in eq. (5.25) symbolizes non-perturbative effects. It can only be derived from models, thus its magnitude is model-dependent. Its sign is however unique; this was verified with the available models. The sign of F is also given in table 5.5. Neglecting fragmentation effects one will therefore get upper or lower limits on α_s from a measurement of O.

The mean values $\langle 1 - T \rangle$ and $\langle M_H^2 \rangle / E_{vis}^2$ and $\int_{45}^{90} A_{EEC}\, d\theta$ were experimentally determined at five values of centre-of-mass energy. The data have been corrected for initial state radiation as well as detector acceptance and resolution. Inserting these values into eq. (5.25) and solving for α_s with $F = 0$ led to the data points in fig. 5.18. Note the weak energy dependence of $\int_{45}^{90} A_{EEC}\, d\theta$. Since F was determined to be positive for $\langle 1 - T \rangle$ and $\langle M_H^2 \rangle$ an upper limit was derived from the lowest point using the $O(\alpha_s^2)$ expression for α_s

$$\alpha_s = \frac{2\pi}{b_0 \ln(Q^2/\Lambda^2) + (b_1/b_0) \ln \ln(Q^2/\Lambda^2)} \tag{5.26}$$

where $\Lambda = \Lambda_{\overline{MS}}$, $b_0 = (33 - 2N_f)/6$ and $b_1 = (153 - 19N_f)/6$. The number of flavours N_f was set to 5. A lower limit for α_s was derived from $\int_{45}^{90} A_{EEC}\, d\theta$ for which F is negative. The limits are also shown in fig. 5.18. They correspond to:

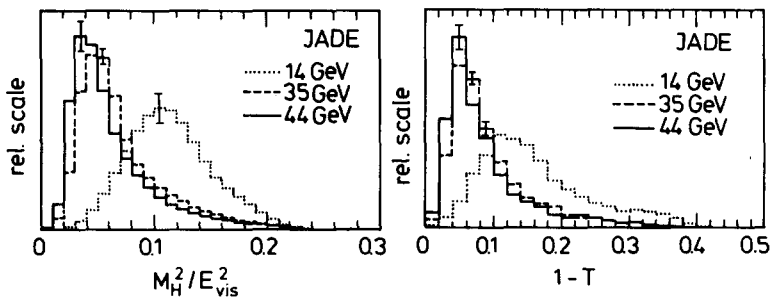

Fig. 5.17. Experimental distributions of $\langle M_H^2 \rangle / E_{vis}^2$ and $1 - T$ for $\sqrt{s} = 14$, 34.6 and 44 GeV.

Table 5.5
Coefficients to be used in eq. (5.25) [131, 132]

O	C_1	C_2	Sign of F
$\langle 1-T\rangle$	0.334	2.88	+
$\int_{45}^{90} A_{EEC}\,d\theta$	0.098	0.923	−
$\langle M_H^2\rangle$	0.334	2.09	+

$25 < \Lambda < 400$ MeV at 95% C.L.

$0.10 < \alpha_s < 0.15$ at $\sqrt{s} = 34.6$ GeV.

The fragmentation effects are expected to decrease with increasing centre-of-mass energies while α_s is almost independent of energy. Therefore better constraints on α_s can be obtained by taking into account the energy dependence of the calculated variables. F was assumed proportional to $1/\sqrt{s}$ which describes the s-dependence of the data well, see fig. 5.19. Therefore $F = k_i/\sqrt{s}$ was inserted in eq. (5.25) and a simultaneous fit was made to the three observables for $\sqrt{s} > 15$ GeV with Λ and k_i, $i = 1, 2, 3$, as free parameters. The result is:

$\Lambda = 70 \pm 30^{+50}_{-30}$ corresponding to

$\alpha_s = 0.12 \pm 0.01 \pm 0.01$ at $\sqrt{s} = 34.6$ GeV.

The first error is in both cases statistical, the second systematic. The systematic error of Λ was estimated by varying the functional form of $F = F(\sqrt{s})$ and by estimating background effects and errors in the correction procedure. The χ^2 of the fit is 14.4 for 8 degrees-of-freedom. The curve representing the best fit is shown in fig. 5.19. Also shown is the contribution from pure QCD determined with $\Lambda = 70$ MeV.

5.4.5. *Comparison of α_s measurements from e^+e^- annihilations*

In view of what has been said in the beginning of this section one has to be careful in comparing α_s values from different groups and one has to take into account the method employed. It has been shown that α_s^2 corrections are not negligible therefore we shall only consider determinations which have used

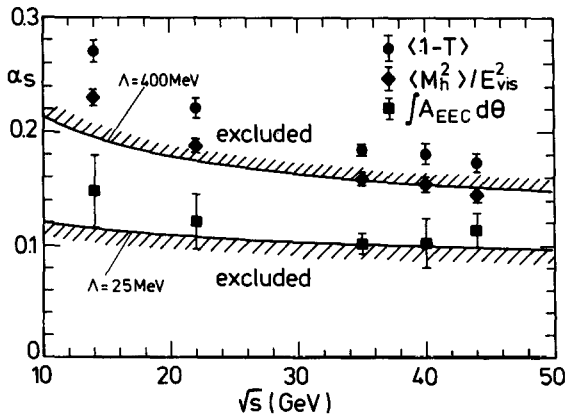

Fig. 5.18. Limits on α_s as a function of $\sqrt{s}$ computed from $\langle 1-T\rangle$, $\langle M_H^2\rangle/E_{vis}^2$ and $\int_{45}^{90} A_{EEC}\,d\theta$.

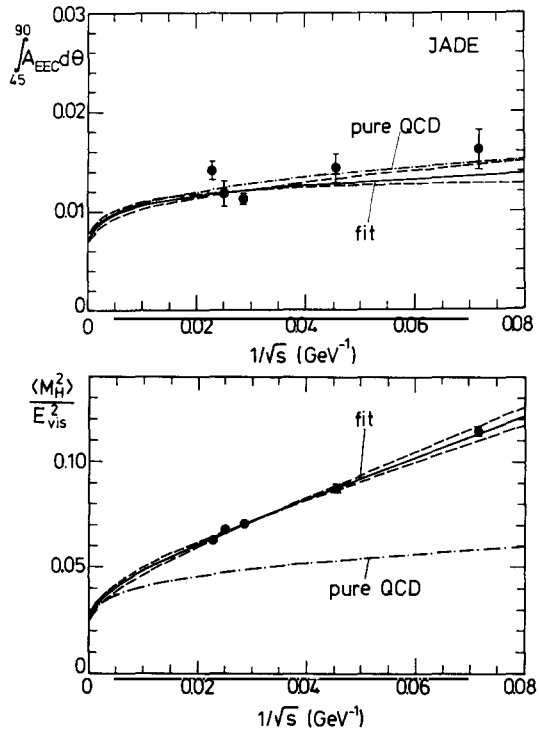

Fig. 5.19. $\int_{45}^{90} A_{EEC}\, d\theta$ and $\langle M_H^2 \rangle / E_{vis}^2$ as functions of $1/\sqrt{s}$. The full line represents the best fit to eq. (5.25) with $F = k_1/\sqrt{s}$ and $\Lambda = 70$ MeV, the dashed lines correspond to fits with $\Lambda = 40$ and 100 MeV. The dash-dotted line represents pure QCD with $\Lambda = 70$ MeV.

$O(\alpha_s^2)$ QCD. Then there are the two different matrix elements and in view of the approximations made in the FKSS/GKS calculations [121] the results should be compared with caution. Finally there exist different methods to determine α_s with a varying degree of model dependence. The experimental distribution least sensitive to fragmentation effects – beside the total hadronic cross-section (chapter 4) – was found to be the asymmetry of the energy–energy correlation. An analysis of the EEC asymmetry has been performed by all experiments working at PETRA and by the MAC Collaboration at PEP. The results from these analyses are listed in table 5.6.

Four groups of results can be distinguished which are shown in fig. 5.20: The smallest values of α_s are those which were derived neglecting fragmentation effects, which is approximately justified for the asymmetry of the EEC in view of its weak dependence on fragmentation effects. The results from this first group of data are in agreement with the model-independent results described in the previous chapter and also with the value obtained by assuming a $1/\sqrt{s}$ behaviour of fragmentation effects.

Among the results including models the values of α_s determined with the Lund model are larger than those with independent fragmentation of partons. This difference is larger when the FKSS/GKS matrix elements are used than with ERT. In fig. 5.20 independent fragmentation is represented by the model by Ali et al., which was used by all groups.

For the same analysis method the agreement between results from different groups is remarkable. Most values of α_s lie between 0.10 and 0.15 corresponding to a $\Lambda \approx 20$ to 300 MeV. The group of results using FKSS/GKS + Lund yields values of ~0.18 which due to missing terms in the matrix element may have to be reconsidered as was mentioned at the beginning of the chapter. Note however that in the α_s

Table 5.6
Comparison of α_s (34 GeV) obtained in e^+e^- annihilations using the asymmetry of the energy–energy correlation calculated in second-order QCD. *The errors are statistical.* The results marked with an * give the results obtained in section 5.4.4. "Neglected" in the column "Fragmentation model" means that the data have been fitted directly to the A_{EEC} calculated in QCD

Data	QCD $O(\alpha_s^2)$	Cut	Fragm. model	α_s	Ref.
JADE	GKS	$y_{min}^{theor} = 0.0125$	Lund	0.165 ± 0.01	[109]
			indep. partons[1]	0.11–0.14	
	$O(\alpha_s^2)$ QCD		neglected	0.115 ± 0.005	
	ERT		–	0.12 ± 0.02*	[128]
	ERT		$\sim 1/\sqrt{s}$	0.12 ± 0.01*	
CELLO	GKS	$y_{min}^{theor} = 0.03$	Lund	0.19 ± 0.02	[108]
			indep. partons	0.12–0.15	
PLUTO	ERT	$\varepsilon = 0.1$, $\delta = 0.4$ rad	Lund	0.145 ± 0.006	[110]
			Ali et al.	0.135 ± 0.006	
	$O(\alpha_s^2)$ QCD		neglected	0.125 ± 0.004	
MARK J	ERT		Lund	0.134 ± 0.005	[111]
			Ali et al.	0.114 ± 0.005	
TASSO	ERT	$\varepsilon = 0.2$, $\delta = 40°$	Lund	0.16 ± 0.012	[112]
			indep. partons	0.12–0.13	
	FKSS (extended)	$\varepsilon = 0.2$, $\delta = 40°$	Lund	0.19 ± 0.01	
			indep. partons	0.11–0.16	
PLUTO + TASSO	ERT		Lund	0.147 ± 0.010	[113]
			Ali et al.	0.142 ± 0.010	
	$O(\alpha_s^2)$ QCD		neglected	0.123 ± 0.004	
MAC	GKS	$y_{min}^{theor} = 0.015$	Lund	0.185 ± 0.013	[114]
			indep. partons	0.105–0.140	
	$O(\alpha_s^2)$ QCD		neglected	0.12 ± 0.006	

[1] "Independent partons" means that the authors have analysed several possibilities for gluon fragmentation and conservation of energy momentum.

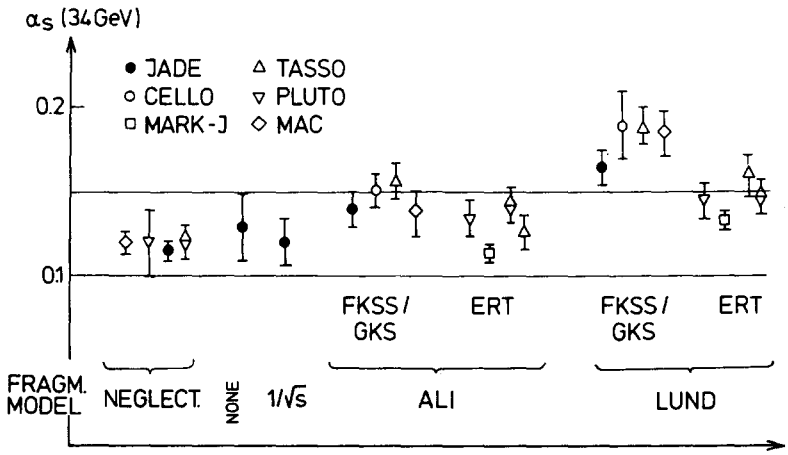

Fig. 5.20. α_s determined from the asymmetry of the energy–energy correlation to $O(\alpha_s^2)$ by e^+e^- experiments. Below the data is indicated which QCD matrix element was used and how fragmentation was treated. "Neglected" under fragmentation means that data were fitted directly to the QCD prediction. The points marked with "none" and $\sim 1/\sqrt{s}$ were obtained by the method described in section 5.4.4. The other data were obtained by using fragmentation models by Ali et al. and the Lund model.

analyses described, the contributions from four-jet events are not accounted for separately. This may result in a systematic effect in α_s due to a deficiency in four-jet events, which was observed in the model calculations using the $O(\alpha_s^2)$ QCD matrix element. This will be discussed in the next section.

The results for Λ obtained from e^+e^- annihilation are in agreement with the results from deep inelastic lepton nucleon scattering, where the values range between $\approx$100 and 300 MeV [133]. The most recent analyses of Y decays gave values around 100 MeV [107].

5.5. *Four-jet events*

5.5.1. *First evidence*

The existence of multijet events and in particular four-jet events is expected from QCD due to diagrams as shown in fig. 5.21. After having collected some 3000 well-contained hadronic events the JADE data showed evidence for the existence of four-jet events [134]. The data were analysed in terms of two quantities sensitive to a four-jet structure, acoplanarity A [135] and tripodity D_3 [136]. Acoplanarity is defined as:

$$A = 4 \min\left\{\sum_i |\boldsymbol{p}_i^{\perp}| \Big/ \sum_i |\boldsymbol{p}_i|\right\}^2 \tag{5.27}$$

where the $\boldsymbol{p}_i$ were the particle momenta and the $\boldsymbol{p}_i^{\perp}$ their components perpendicular to a plane which was oriented such that the expression in parentheses was minimized. Neglecting fragmentation effects, two- and three-parton events have $A = 0$, while four-parton events are in general non-planar and give non-vanishing acoplanarity.

Tripodity is a variable that gives non-zero values only for a particular class of four-jet events, namely those where one jet was oriented opposite to the other three. The reader is referred to [136] and [134] for details about the tripodity analysis. The multihadronic data samples showed deviations from the acoplanarity and tripodity distributions calculated with models containing only two- and three-jet events. Adding 7.2% of four-parton events improved the agreement between data and model prediction. The amount of four-parton events necessary was slightly larger than expected from the calculations by Ali et al. [89].

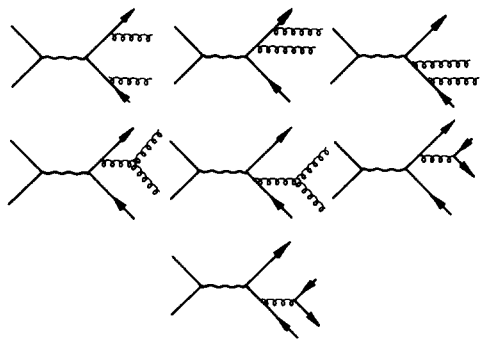

Fig. 5.21. Diagrams for $e^+e^- \to 4$ partons to order α_s^2.

5.5.2. A comparison of jet-multiplicities with $O(\alpha_s^2)$ QCD and a leading log model

Since second-order QCD calculations became available and have been incorporated in the Lund fragmentation program [92] the study of jet multiplicities could be pursued in a more quantitative analysis [137]. Data up to the highest PETRA energies ($\sqrt{s} = 46.7$ GeV) were included and compared with the predictions of the Lund fragmentation program (version 5.2) and with the Webber model. The hadronic data were subjected to the usual cuts to ensure good containment in the detector and to limit missing momentum; in total 2090 events at $\sqrt{s} = 14$ GeV, 1666 events at 22 GeV, 13 617 events at 34 GeV and 6636 events at 44 GeV were used.

The jet-multiplicity was calculated using a cluster method. The normalised invariant mass was calculated for each pair of particles i and j according to:

$$y = \frac{2E_iE_j}{E_{\text{vis}}^2}(1 - \cos\theta_{ij}).$$

If the minimum invariant mass falls below a resolution limit $y_{\min}$ the corresponding pair of particles is replaced by a pseudoparticle, the four-vector of which corresponds to the sum of the two four-vectors. This procedure is repeated until all masses exceed the threshold $y_{\min}$. The multiplicity of remaining pseudoparticles or particle clusters will be called jet-multiplicity. The jet-multiplicity determined in this way can only be expected to correspond to the parton-multiplicity if a reasonable choice of $y_{\min}$ is made. If $y_{\min}$ is chosen too small, the jet-multiplicity is too high compared with the parton-multiplicity. A $y_{\min}$ chosen too large washes out the parton structure. The proportions of two-, three-, four- and five-jet events are shown for $\sqrt{s} = 34$ GeV as a function of $y_{\min}$ in fig. 5.23. The proportions of two- and three-jet events vary slowly with $y_{\min}$ above ~0.03. The four-jet events are observed to fall steeply with $y_{\min}$. The proportions found at $y_{\min} = 0.04$ are listed in table 5.7.

The $O(\alpha_s^2)$ QCD prediction, which is shown in fig. 5.23 for comparison, was calculated with the Lund program which uses the GKS matrix element. The model parameters were chosen close to the values found in the analysis of the energy–energy correlation (section 5.4.3): $y_{\min}^{\text{theor}} = 0.015$, $\Lambda_{\overline{\text{MS}}} = 500$ MeV (corresponding to $\alpha_s = 0.165$ at 34 GeV) and $\sigma_q = 265$ MeV. The two-jet fraction predicted by this model falls below the data, the three-jet rate is predicted slightly too high and the four-jet prediction is too low. The predictions for two- and three-jet events approach the data only at very high values of $y_{\min}$, where the predicted four-jet fraction falls substantially below the data.

The comparison with the leading log calculation (LLA) was done in the Webber model which

Table 5.7
Proportions of n-jet events in % obtained with the cluster algorithm at $y_{\min} = 0.040$ (five-jet events have been combined with four-jet events)

$\sqrt{s} = 34$ GeV	Data	$O(\alpha_s^2)$	LLA
two-jet events	56.1 ± 0.4	53.2 ± 0.3	58.5 ± 0.4
three-jet events	40.2 ± 0.4	44.0 ± 0.3	37.8 ± 0.4
four-jet events	3.75 ± 0.16	2.85 ± 0.12	3.69 ± 0.15
four-/three-jet	0.093 ± 0.004	0.065 ± 0.003	0.098 ± 0.004

[2] The parameters were chosen as in table 5.1. These parameters were optimized in a comparison with distributions of particle multiplicities and momentum distributions.

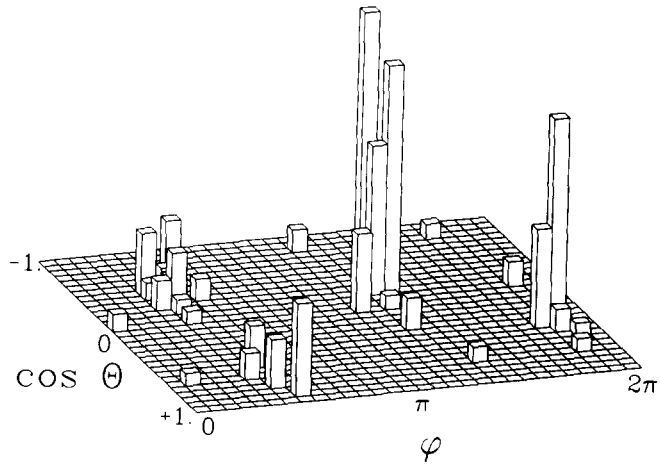

Fig. 5.22. Energy-flow diagram in the $\cos\theta-\varphi$ plane for a four-jet event.

includes interference of soft gluons.[2] The model shows discrepancies in the two- and three-jet fractions, the deficiency in three-jet events in QCD shower models is well known. The observed fraction of four-jet events is nevertheless well reproduced and in particular the ratio of three- to four-jet fraction at $y_{\min} = 0.04$ agrees well with the data as can be seen in table 5.7.

Data and predictions are compared as a function of s in fig. 5.24. The relative variation of the cluster multiplicities with s is well reproduced by both models but the three-jet rate is too high in the Lund

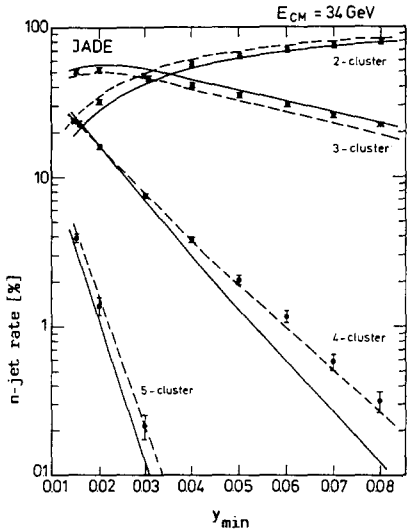

Fig. 5.23. Proportion of n-jet events as a function of $y_{\min}$ for data at $\sqrt{s} = 34$ GeV compared with two models: $O(\alpha_s^2)$ QCD and Lund fragmentation (solid lines) and a leading log model (Webber, broken lines).

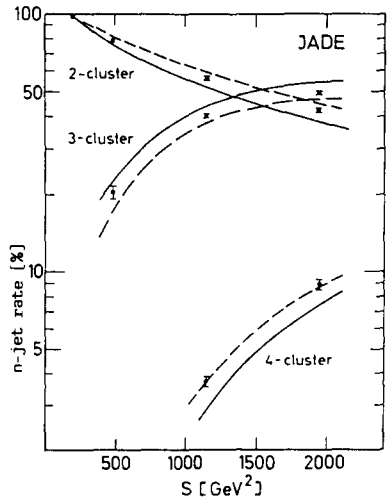

Fig. 5.24. Proportion of n-jet events as a function of s; curves as in fig. 5.23.

model and the four-jet rate too low at all values of s, while in the Webber model the three-jet rate is too low and the four-jet rate fits the data.

The origin of the systematic discrepancy in the Lund model based on second-order QCD was investigated further. The fraction of three- and four-jet events is determined by the value of α_s. The systematic discrepancy between data and predictions over the large range of y_{min} seems to point to a problem in the QCD calculations since there is no way to adjust α_s to decrease the amount of three-jet events and at the same time increase four-jet events. The phenomenological fragmentation part in the model was excluded as the origin of the discrepancy by several investigations. Different cluster algorithms or an event classification by the Q-plot gave similar results as above. A variation of fragmentation parameters only led to an increased four-jet rate if a very soft fragmentation function was introduced for heavy quarks or if σ_q was increased to very large values. Both modifications lead to disagreements with other distributions. These modifications would always increase both the four- and the three-jet rate.

In order to exclude further fragmentation effects as the origin of the observed differences a comparison of the two models was made at the parton level. For this comparison the partons which are generated in the Webber model were combined in a way analogous to the method used in the second-order calculations [117], i.e. two partons were combined if their invariant mass was below y_{min}^{theor}. The fractional multiplicities of these combined parton vectors are shown in fig. 5.25 together with the multiplicity fractions of second-order QCD as a function of the resolution cut y_{min}^{theor}. Similar systematic deviations between the two models as with the inclusion of fragmentation effects are observed.

As mentioned in the beginning of this chapter the approximations made in the GKS matrix element will lead – once corrected – to a reduction of α_s. Such a reduction, although favourable for the three-jet rate will reduce the four-jet fraction further and enlarge the problem described above.

An attempt was made to determine the fraction of missing four-jet events using the acoplanarity distribution. Acoplanarity was defined above; it is by definition sensitive to multijet events which have a spherical structure. The acoplanarity distribution is shown in fig. 5.26 at three values of centre-of-mass energy. The lack of spherical events with large acoplanarities in the $O(\alpha_s^2)$ model can be seen for

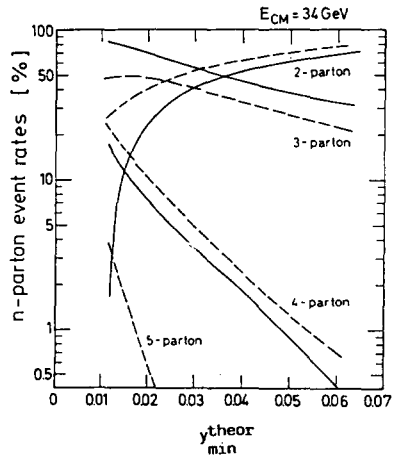

Fig. 5.25. Proportion of n-parton events as a function of y_{min}^{theor}; curves as in fig. 5.23.

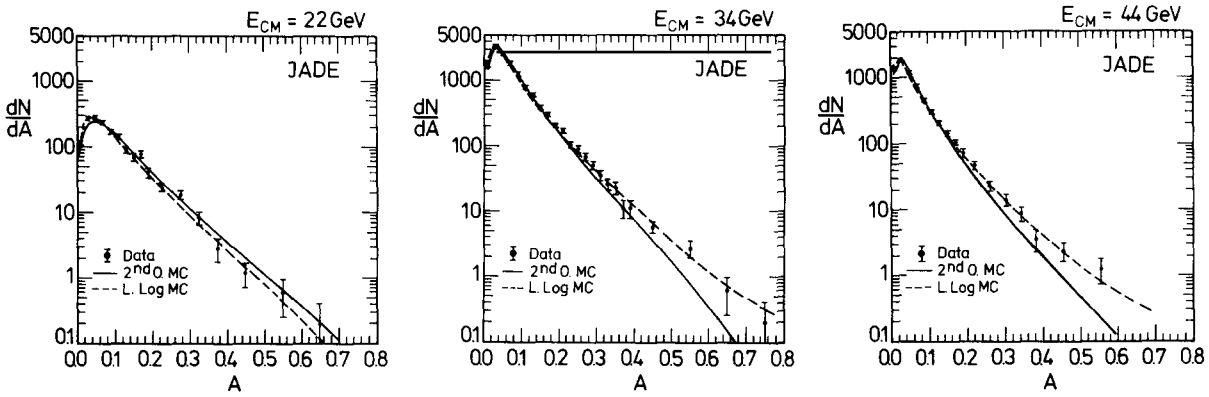

Fig. 5.26. Acoplanarity distributions for multihadronic events at three c.m. energies compared with the Lund and the Webber model.

$\sqrt{s} > 34$ and 44 GeV. The χ^2 of the data with respect to the $O(\alpha_s^2)$ distribution is bad (table 5.8). After increasing artificially the proportion of four-parton events and decreasing the proportion of three-parton events in the event generation a better fit was obtained (table 5.8). Instead of increasing the four-jet fraction by a rather large factor (~1.5) it was found that the addition of a small proportion of five-parton events,[3] of the order of 2%, also produced a similarly good agreement with the data at high acoplanarity values.

The LLA model gives a better description of the data at high values of acoplanarity. By artificially varying the proportions of parton multiplicity it was found that the best fit was obtained by increasing the three-parton fraction, decreasing the two-parton fraction and leaving the fraction of four and five partons unchanged. These results are summarized in table 5.8.

Table 5.8
Fit results for the proportions $R_n(\%)$ of n-parton events obtained by optimizing with respect to the acoplanarity distributions in a $O(\alpha_s^2)$ QCD (Lund) and a LLA model (Webber)

	$\sqrt{s} = 34$ GeV				$\sqrt{s} = 44$ GeV			
Model	R_3	R_4	R_5	χ^2/d.o.f.	R_3	R_4	R_5	χ^2/d.o.f.
$O(\alpha_s^2)$ QCD original	76.7	12.3		63/22	74.3	11.5		6.2/16
$O(\alpha_s^2)$ QCD best fit, $R_5 = 0$	61.5	19.0		25.6/21	52.5	20.3		8.9/15
$O(\alpha_s^2)$ QCD best fit, R_5 fixed	69.0	12.0	2.0	19.5/21	56.5	16.4	1.4	9.6/15
LLA original	47.3	16.2	1.85	30/22	48.1	14.1	1.42	30/16
LLA best fit, R_5 fixed	56.0	16.6	1.85	13.2/21	54.0	14.1	1.42	11.9/15

6. Inclusive particle production

6.1. Introduction

The study of inclusive spectra of hadrons in $e^+e^- \rightarrow h + X$ is mainly used to investigate the process of hadronisation. The choice of particles h which can be studied is limited by the production rates and by

[3] They were taken from the Webber event generator.

the abilities of the detector. In addition to charged particles without further identification, JADE has studied the production of

$$\gamma, \pi^0, K^0, \eta, \rho^0, K^{*\pm}, \Lambda, \Xi^-, D^* .$$

Upper limits on F* production were also determined. The analysis of D*, F* will be discussed together with the analysis of inclusive electrons and muons in the following chapter about properties of heavy quarks. Except for photons, which were identified by the lead-glass detector, all particles were identified by reconstructing their invariant masses.

In the quark parton model the hadrons are formed from the initially created quark pairs in a process which is not well understood in terms of QCD. It is described by phenomenological models as outlined in the previous chapter. A basic assumption in these models is that a particle h created in the fragmentation can be described by a function, which depends on the parent quark and the particle h, but not on the centre-of-mass energy (Feynman scaling). Usually the scaled energy of the particle h, $x_E = 2E_h/\sqrt{s}$ is introduced, where E is the energy of h. The scaled differential cross-section

$$\frac{1}{\beta\sigma_{tot}} \frac{d\sigma^h}{dx_E} ,$$

where σ_{tot} is the total hadronic cross-section is in the quark parton model expected to be independent of s. Scale breaking occurs through threshold effects and due to gluon emission.

We shall mostly use the following expression for the scaled cross-section:

$$\frac{s}{\beta} \frac{d\sigma^h}{dx_E} = \frac{R_{had} 4\pi\alpha^2}{\beta\sigma_{tot}} \frac{d\sigma^h}{dx_E} \tag{6.28}$$

where R_{had} is the ratio of the total measured hadronic cross-section to the cross-section for μ pair production.

Integrating the cross-section yields the average multiplicity of the particle species h:

$$\langle N_h \rangle = \frac{1}{\sigma_{tot}} \int_{\text{threshold}}^{1} \frac{d\sigma^h}{dx} dx .$$

This chapter will be ordered according to the analysis techniques used. The analysis method will be discussed briefly, the inclusive particle spectra and multiplicities will be shown and compared with measurements from other detectors. Parameters of fragmentation models will be determined, namely the probability to create $s\bar{s}$ quarks γ_s and the relative rate of pseudoscalar mesons r will be determined. Baryon number compensation will be studied in the Λ analysis.

6.2. *Multiplicity of charged particles*

The multiplicity of charged particles is a fundamental characteristic of multihadronic events. It was determined for three energies, $\sqrt{s}$ = 12, 30 and 35 GeV, where for the latter ~8200 multihadronic events

were used [138]. Charged tracks with $p_t > 0.05$ GeV relative to the beam direction were counted unless they belonged to an e^+e^- pair. Nuclear interactions in the material in front of the detector were counted as one charged track. Corrections were applied for particles lost in the beam-pipe, for the decay of long-lived particles outside the jet-chamber, for tracks of momenta below the cut, for tracks lost in the reconstruction due to double track resolution, for tracks lost because they were falsely identified as belonging to an e^+e^- pair or a nuclear interaction. A background from unrecognised e^+e^- pairs and τ decays was subtracted and a correction due to initial state radiation was applied. The counting criteria and corrections were verified in a visual scan of the events. The sum of all corrections amounted to approximately one particle per event at 35 GeV and was less at lower energies. The average charged multiplicity obtained in this way is listed in table 6.1. It is not corrected for contributions from Dalitz decays of the π^0, from K^0_S and Λ decays which are counted as two particles and from leptonic decays of heavy quarks. The multiplicity corrected for these effects is given in the footnote of table 6.1 for comparison.

In figs. 6.1 the multiplicity distributions are shown at the three centre-of-mass energies. The data were compared to two model calculations, the Lund model (version 4.3) and the Hoyer model. In these models the multiplicity is mainly sensitive to the fragmentation function and its parameter values and to the relative number of pseudoscalar and vector mesons generated, $r = PS/(V + PS)$. The fragmentation functions used in the two models were given in eqs. (5.21) and (5.22). These functions contain an adjustable parameter, a_F in the case of the Hoyer model and β in the Lund model. The fragmentation functions for the heavy quarks were harder and were kept fixed in the fits.

β and a_F were fitted using the mean values for the multiplicities at the three energies and setting $r = 0.5$. Both parameters β and a_F were found to show a slight energy dependence [138]. Using the optimized values the predicted multiplicity distributions were compared to the measurements in fig. 6.1. Whereas the mean multiplicities are fitted well at all energies by both models, this is not the case for the multiplicity distribution. The independent jet-models have a tendency to give a broader distribution than observed, while the Lund model reproduces the shape well.

The mean values of the multiplicities are shown as a function of $\sqrt{s}$ in fig. 6.2. They are compared with data from other experiments at PETRA and at lower energies. At low energy the data rise like log s, at high energies they rise faster. This is attributed to QCD effects. The s dependence of the mean multiplicity can be fitted by a variety of functional forms containing e.g. terms proportional to $(\ln s)^2$, a

Table 6.1
Average multiplicity per event for several particle types

Particle	Decay	M (MeV)	Meas. width (MeV)	$\langle N \rangle$ at $\sqrt{s} = 34$ GeV
γ				$13.7 \pm 0.4 \pm 0.7$
π^0	$\rightarrow \gamma\gamma$	135 ± 0.5	17.1 ± 0.6	$6.1 \pm 0.1 \pm 0.7$
K^0	$\rightarrow \pi^+\pi^-$	502 ± 0.8	21.8 ± 0.8	$1.5 \pm 0.05 \pm 0.04$
η	$\rightarrow \gamma\gamma$	559 ± 9	51 ± 11	0.64 ± 0.15
ρ^0	$\rightarrow \pi^+\pi^-$			$0.98 \pm 0.09 \pm 0.05$
$K^{*\pm}$	$\rightarrow K^0_S\pi^\pm$			$0.87 \pm 0.16 \pm 0.08$
Λ	$\rightarrow p\pi$	1120 ± 1	9.4 ± 0.7	$0.25 \pm 0.014 \pm 0.03$
Ξ^-	$\rightarrow \Lambda\pi^-$	1325 ± 4		$0.05 \pm 0.01 \pm 0.01$
charged particles				$13.6 \pm 0.3 \pm 0.6$[1]

[1] Includes K^0_S and Λ decay products and leptons from weak quark decays and Dalitz decay. If these contributions are removed $\langle N \rangle_{charged} = 11.8 \pm 0.4 \pm 0.7$ at 34 GeV.

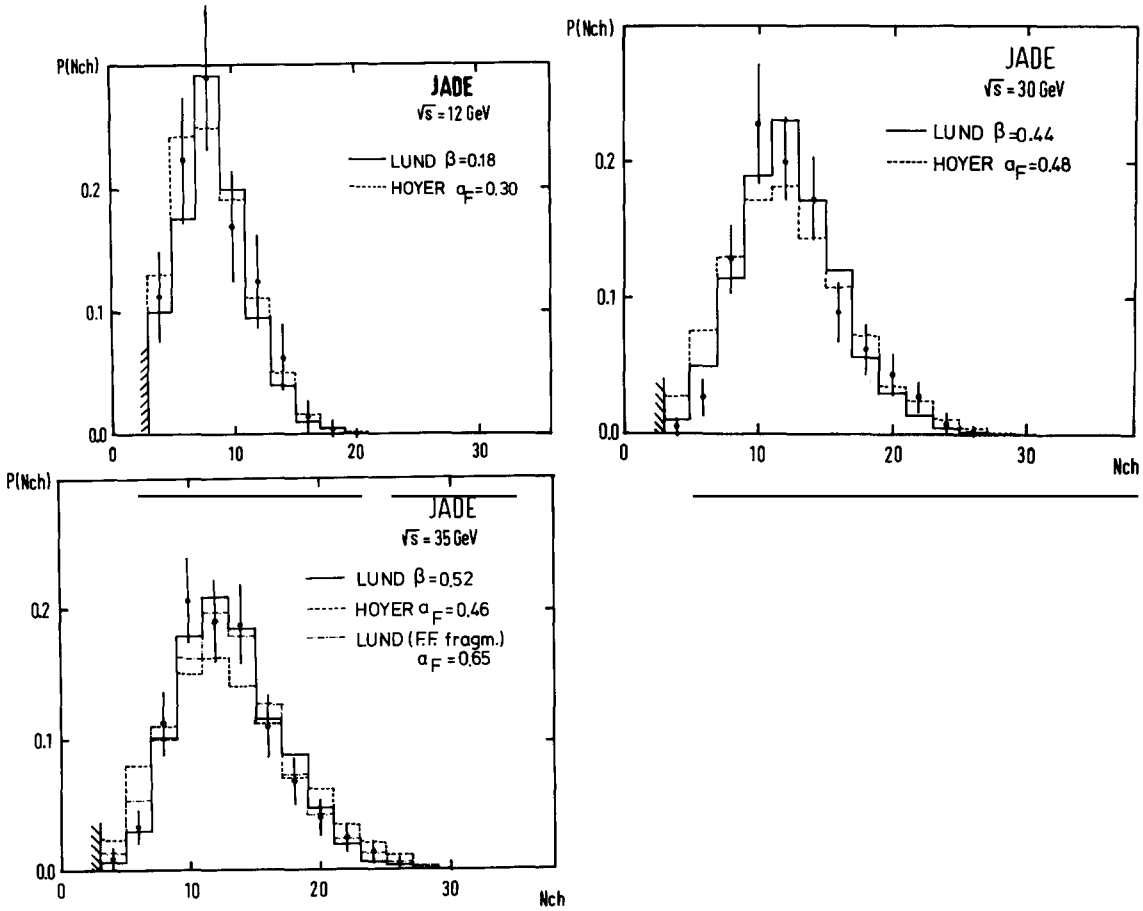

Fig. 6.1. Corrected multiplicity distributions of charged particles at three centre-of-mass energies compared with predictions from a string model (Lund) and a model which has independent fragmentation of partons (Hoyer).

power of s or exponentials of $\sqrt{s}$. The prediction of the Lund model, which also gives a good fit, is shown in fig. 6.2 for comparison.

6.3. Final states with photons

6.3.1. Single photons

The study of neutral particles in the hadronic final state complements the investigations of charged particles, since they are produced in a similar abundance. The fine-grain lead-glass detector enabled the analysis of photons in hadronic events. The data sample used for this and the following sections corresponds to 2968, 2353 and 23 926 hadronic events at $\sqrt{s} = 14$, 22 and 34 GeV respectively. Single photons were reconstructed using the barrel lead-glass array since it has better resolution than the end-caps. The fiducial range was restricted to $|\cos\theta| < 0.76$. In order to reduce background from overlapping clusters due to charged particles or other photons, each cluster was compared to the

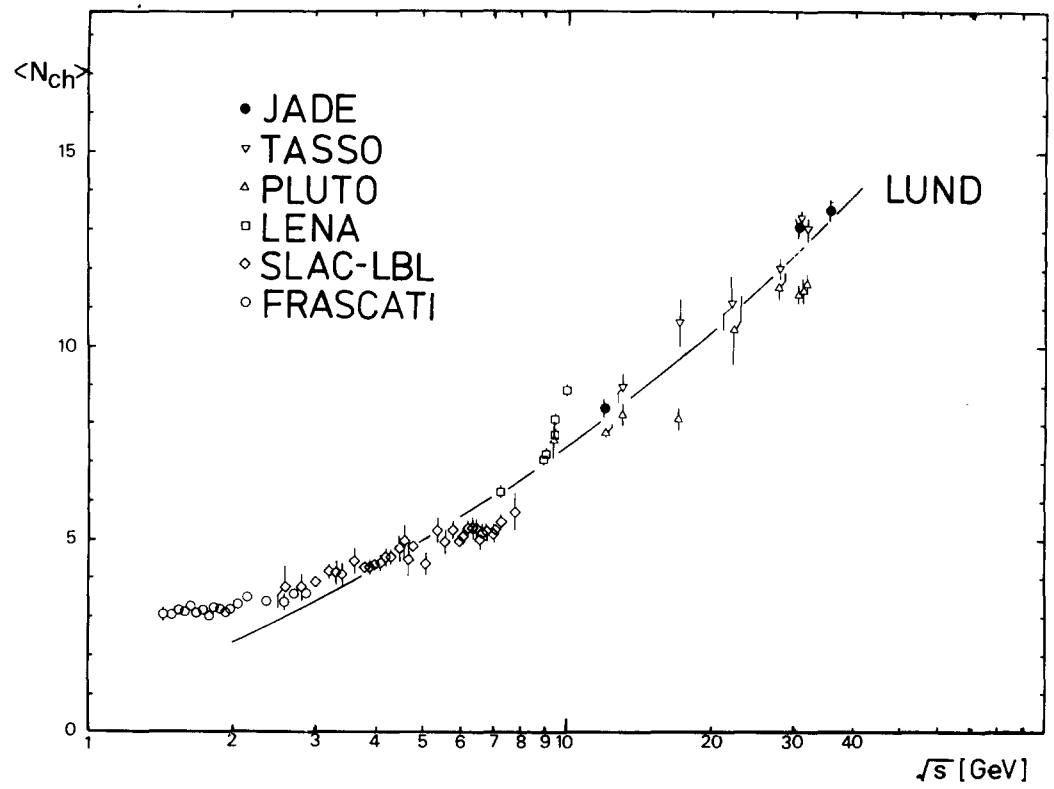

Fig. 6.2. Mean charged multiplicity as a function of $\sqrt{s}$ compared with other measurements and the Lund model.

theoretical shape of a cluster caused by a single photon. If the measured shape agreed with the expectation it was accepted (for details of the method see [139] and [140]). At $\sqrt{s} = 34$ GeV the detection efficiency for low energy photons is 50%. The efficiency drops to roughly 15% for photon energies up to ~7–8 GeV and increases again towards higher energies. This behaviour reflects the topology of hadronic events; low energy photons are relatively isolated while medium energy photons come from π^0 decays and are in regions of high particle density. At large x_γ the efficiency rises because the corresponding photons are mostly radiated off the incoming electrons and positrons and are again isolated.

The inclusive photon spectrum for photon energies $E_\gamma > 0.2$ GeV corrected for acceptance is shown in fig. 6.3 together with the expectation from the Lund model and the contribution from initial state radiation [82]. At low x_γ the Lund model alone fits the data well, while at high x_γ initial state radiation dominates. The inclusive photon spectra corrected for acceptance and initial state radiation are shown in fig. 6.4 for three centre-of-mass energies. The data show no significant deviation from scaling. This is also true for the data from CELLO [141]. A comparison with the charged pion spectrum measured by the TASSO collaboration [142] shows that the photon spectrum is softer. This is because most photons stem from π^0 decays.

The average photon multiplicities deduced from the data according to eq. (6.1) are shown in table 6.1. They are comparable to the multiplicity of charged particles. The average energy fraction carried by photons can be calculated by integrating the energy weighted spectrum. The resulting value is ~25%, almost independent of energy. The results for three energies are shown in fig. 6.5 together with

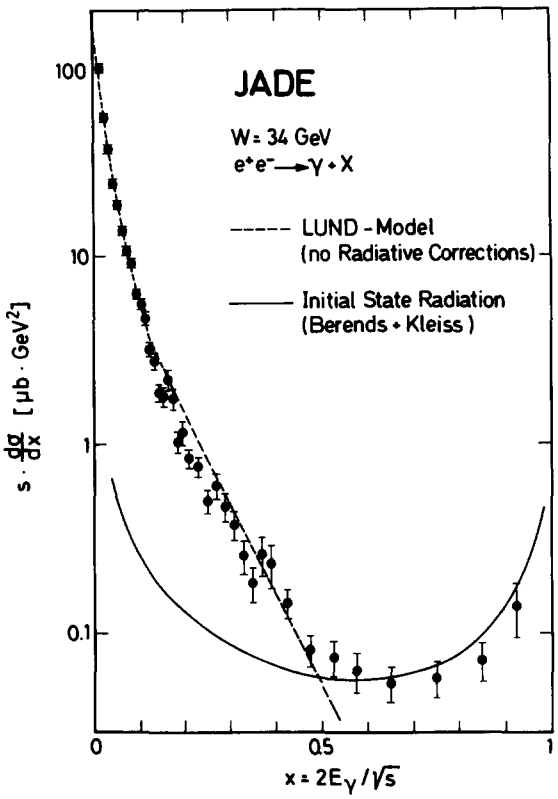

Fig. 6.3. Inclusive photon spectrum before radiative correction.

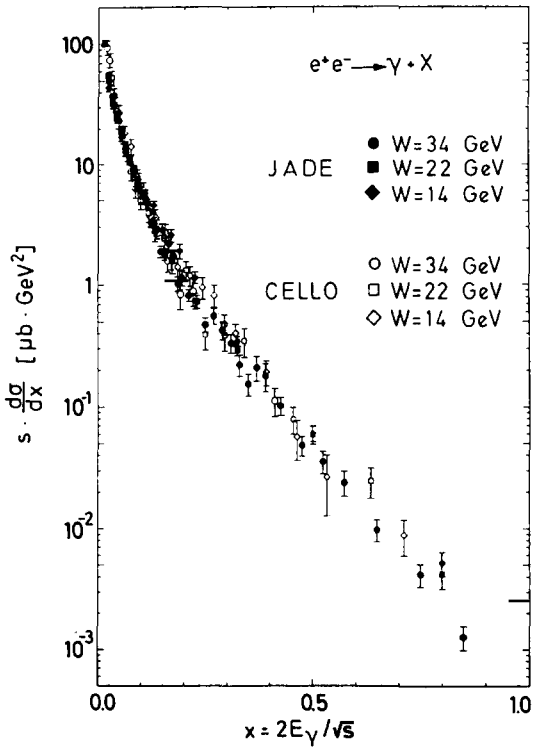

Fig. 6.4. Scaled cross-section for inclusive photon production at three centre-of-mass energies.

results from a previous measurement by JADE using a calorimetric method [143] and from other experiments [144].

The main sources of photons were examined in more detail. The data are, within errors, saturated by the decays of π^0 and η. There is at most room for one more photon per event. After removing π^0 and η decay an excess of 0.55 ± 0.11 is observed; after removing in addition photons from other hadronic decays this excess is reduced to 0.35 ± 0.11.

For the data at $\sqrt{s} = 34$ GeV, photons emitted by the quark pair in the final state were searched for at large angles with respect to the beam-line (to avoid initial state radiation) and far from the jet-axes (to avoid π^0 decays) [145]. In detail a photon of energy $2 < E_\gamma < 8$ GeV with a p_t of at least 2 GeV with respect to the jet-axis was required. The photon had to be isolated, i.e. no other particle in a cone of half opening angle 20°, and it had to be at an angle of at least 40.8° from the beam-line. The spectrum of the 279 photons passing these cuts is shown in fig. 6.6. Also shown are the expectation from hadron decays and initial state radiation. Compared with the data there is an excess of 56 ± 22 photons. Final state radiation, obtained from an adaptation to fractionally charged quarks of the $\mu^+\mu^-\gamma$ cross-sections given by Berends and Kleiss [18, 19], resulted in a contribution of 41 ± 5 events after applying all cuts and is compatible with the experimental number. The error does however not allow a definite conclusion about the presence of photon emission from quarks. An analysis of the jet angular distribution did not show a significant asymmetry as might be expected from interference of initial and

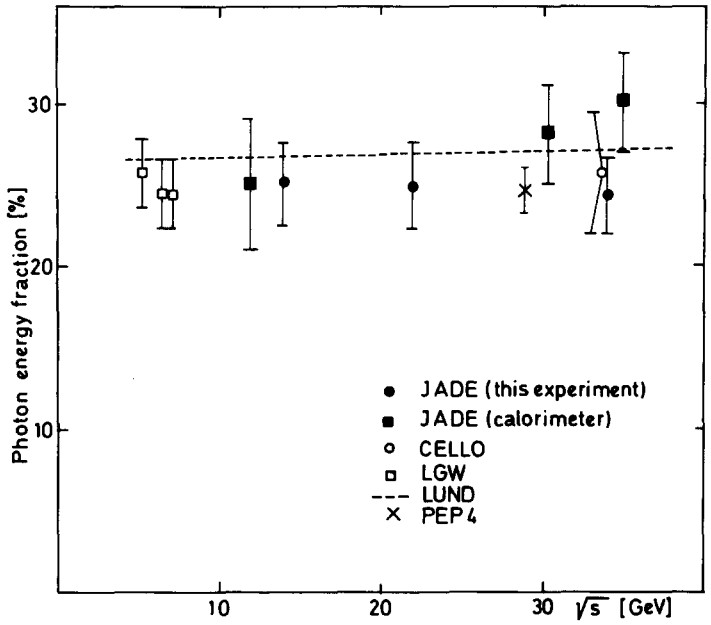

Fig. 6.5. Energy fraction carried by photons in multihadronic events.

final state radiation. MAC has done a similar analysis with higher statistics and they found an asymmetry with a significance of three standard deviations [146].

6.3.2. *Inclusive* π^0 *and* η

For the reconstruction of the π^0 invariant mass, the cut on the photon energy was relaxed to 0.1 GeV. The invariant mass of all two-photon combinations is shown in fig. 6.7. A peak near the π^0 mass is observed; it is centred at 135 ± 0.5 MeV and has a width of $\sigma = 17.1 \pm 0.6$ MeV. The π^0 yield is deduced after subtracting a background fitted by a polynomial. The detection efficiency for π^0's is limited by the cut in the photon energy for low π^0 energy and by the finite size of the lead-glass counters at high energies.

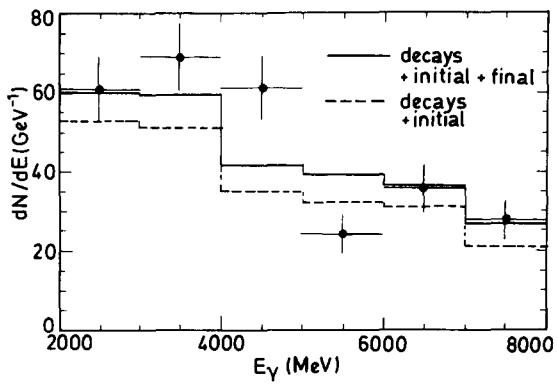

Fig. 6.6. Spectrum of photons selected to enrich quark-bremsstrahlung.

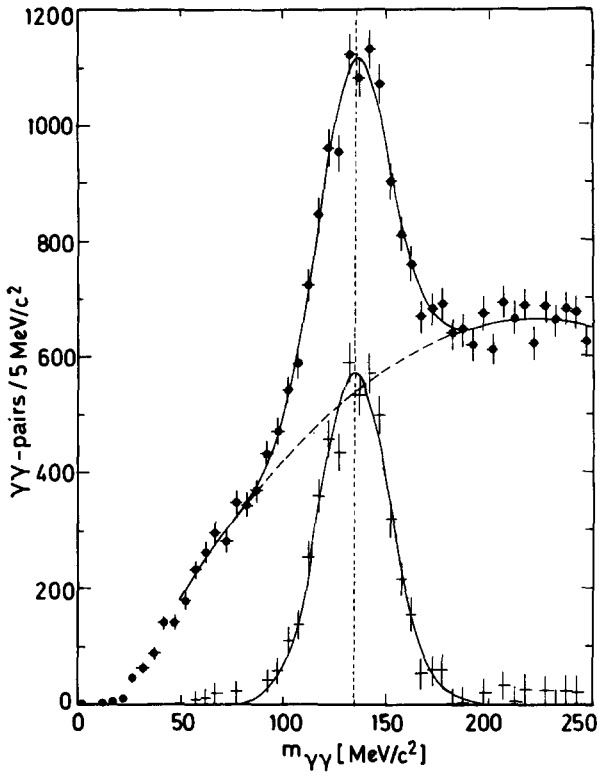

Fig. 6.7. Two-photon mass spectrum in the range of the π^0 mass with a Gaussian and a polynomial background fitted to the data. Insert: π^0 signal after background subtraction.

The scaled cross-section for π^0 production is shown in fig. 6.9 at three centre-of-mass energies together with the results from CELLO [141]. No scaling violation is observed within errors. The data at 34 GeV also show reasonable agreement with the data from other experiments [144] shown in fig. 6.10 and with the spectrum of charged pions obtained by TASSO [142] which is also indicated in the figure. The π^0 multiplicity is shown in table 6.1, it compares well with the average of the π^+ and π^- multiplicity from TASSO.

The η signal is seen in the two-photon mass spectrum (fig. 6.8) after removing photons from π^0 decay, and demanding that the sum of the two-photon energies be above 0.7 GeV and that both photons lie in the same hemisphere of the event [147]. The measured mass and width are given in table 6.1 together with the average multiplicity.

6.4. *Inclusive* K^0, $K^{*\pm}$ *and* ρ^0 *production*

The K^0, ρ^0 and K* decays were reconstructed from the following decays:

$$K_s^0 \to \pi^+\pi^-$$

$$\rho^0 \to \pi^+\pi^-$$

$$K^{*\pm} \to K_s^0\pi^\pm .$$

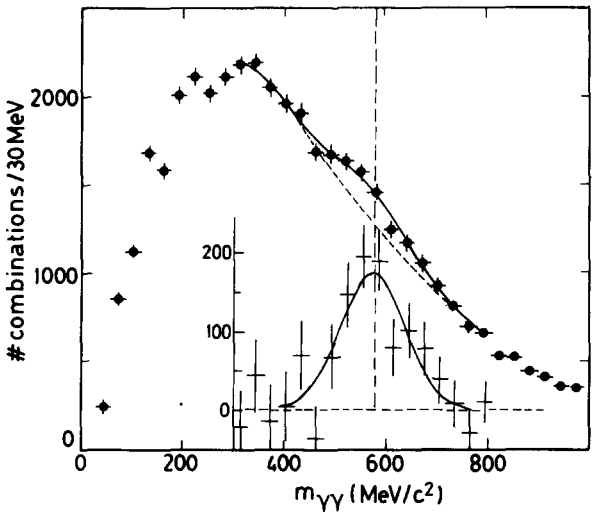

Fig. 6.8. Two-photon mass spectrum in the range of the η mass after removal of photons from π^0. Insert: η signal after background subtraction.

6.4.1. *Analysis of* K_S^0 *and determination of* γ_s

The K_S^0 was reconstructed in two different analyses with different cuts [138, 152]. Both utilized the fact that the decay-length of the K_S^0 is 2.6 cm and thus the decay vertex is at a measurable distance from the event vertex. Most of the data at high energies were reconstructed with cuts similar to those used for the Λ which will be described in the next section. The pions were not identified but all charged particles with momenta greater than 0.1 GeV were used to calculate the two-particle invariant mass. Background from e^+e^- pairs was reduced by a cut on the opening angle of the pair and its invariant mass. Combinatorial background was reduced by quality cuts on the decay vertex. The reconstructed mass peaks are shown in fig. 6.11. The residual background below the K^0 peak comes mainly from nuclear interactions and misidentified Λ decays and was estimated by analysing pion pairs of the same charge. The detection efficiency was calculated using the Lund model. The inclusive differential cross-sections were corrected for the decay branching ratio into pion pairs and multiplied by a factor of 2 to take into account K_L^0 production. The resulting spectra at four centre-of-mass energies are shown in figs. 6.12. The averaged multiplicity obtained by integrating the spectrum at 34 GeV and extrapolating into unmeasured regions is 1.5 ± 0.6 per event (table 6.1).

The following observations are made:

- The data are compatible with scaling, but in view of the errors a small deviation from scaling, as found by the TASSO Collaboration [148], cannot be excluded.
- In fig. 6.13 the data at $\sqrt{s} = 34$ GeV are compared with similar results from TASSO [148] and with results at 29 GeV from MARK II and TPC [149]. Our results agree within errors with those from TASSO and MARK II, while the TPC results lie below our results over the whole x-range.
- The average number of K^0's per event increases with centre-of-mass energy from 1.05 ± 0.14 at 14 GeV to 1.8 ± 0.14 at 44 GeV. Most of the energetic K^0's come from the fragmentation cascade, while at low centre-of-mass energies they are predominantly formed by the primary $s\bar{s}$ quarks.
- The differential cross-section at 34 GeV agrees well with the prediction of the Lund model if the relative probability to form $s\bar{s}$ pairs $\gamma_s = 0.3$ is used. γ_s was determined at $\sqrt{s}$ values between 12 and 34 GeV. No energy dependence was found and the average value is $\gamma_s = 0.27 \pm 0.03 \pm 0.05$.

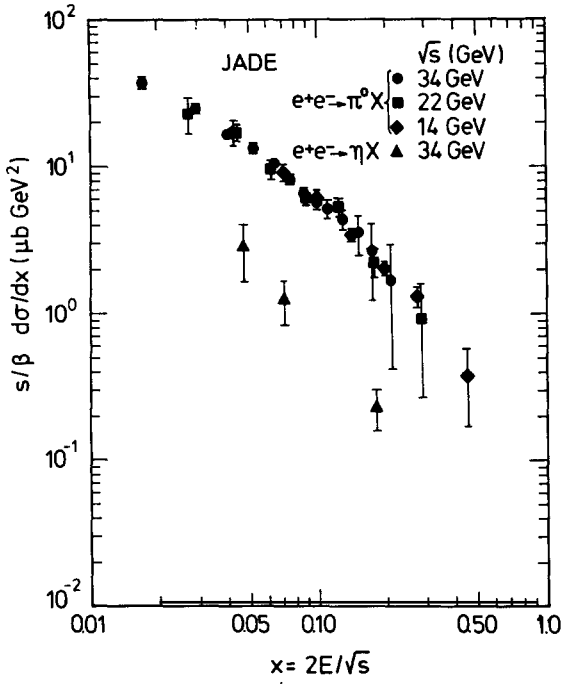

Fig. 6.9. Scaled cross-section for π^0 production at three centre-of-mass energies and for η production at 34 GeV.

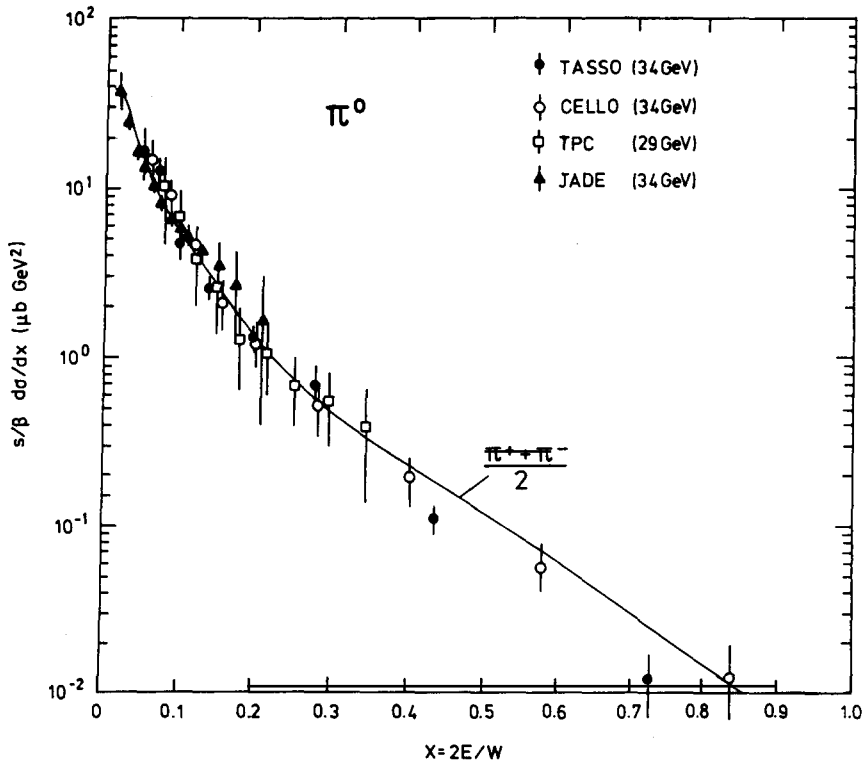

Fig. 6.10. Scaled cross-section for π^0 production at $\sqrt{s}$ = 34 GeV (JADE and TASSO) and 29 GeV (MARK II and TPC). The curve is a fit to the π^+ and π^- spectra by TASSO.

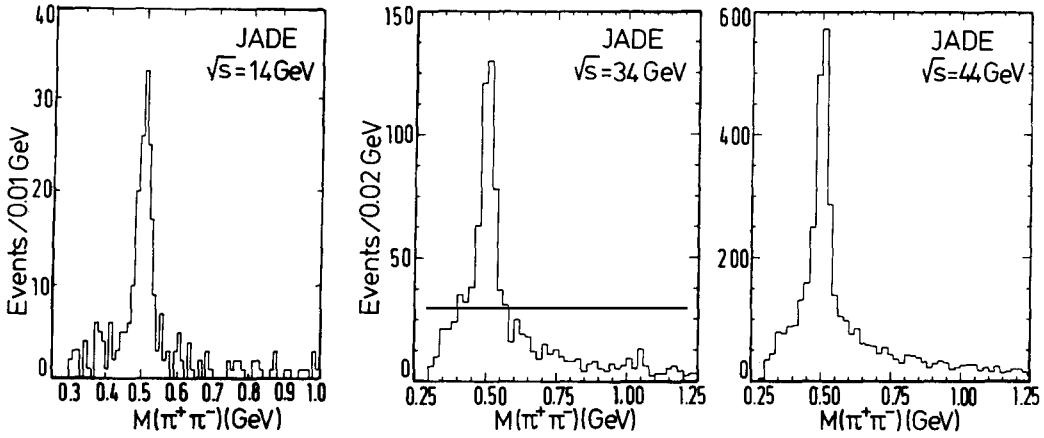

Fig. 6.11. Invariant mass of $(\pi^+\pi^-)$ states at three centre-of-mass energies after applying K^0 enrichment cuts.

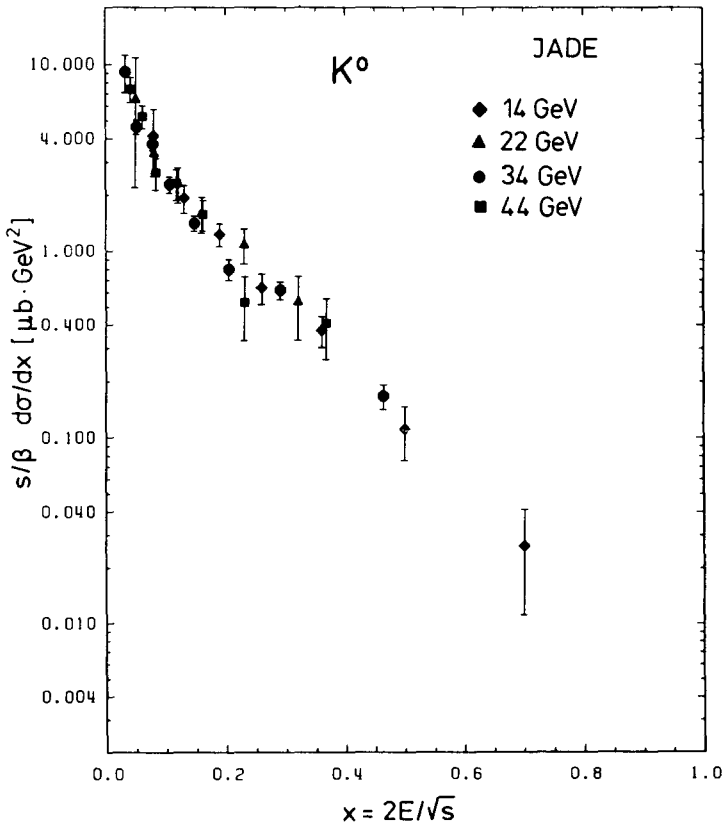

Fig. 6.12. Scaled cross-section for K^0 production at four centre-of-mass energies.

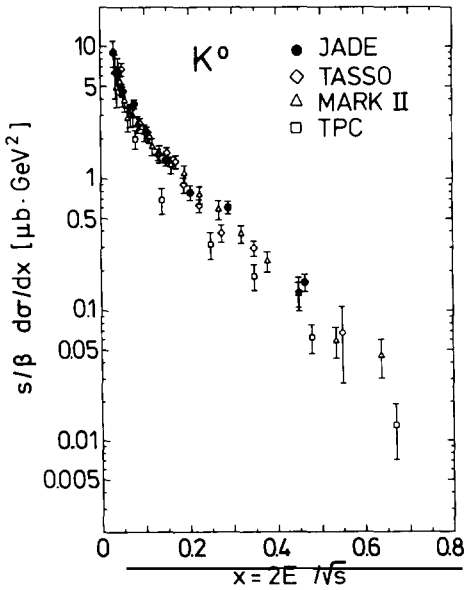

Fig. 6.13. Scaled cross-section for K^0 production at $\sqrt{s} = 34$ GeV compared with data from other experiments.

6.4.2. *Analysis of* K*

For the reconstruction of the vector meson K* ($M = 892$ MeV) a subset of the K^0_S sample at 34 GeV, corresponding to ~8200 multihadronic events, was used. The $\pi^+\pi^-$ combinations were accepted as a K^0_S candidate if they were in the mass band $0.425 < M(\pi^+\pi^-) < 0.575$ GeV. The K^0_S four-vector was obtained by a fit to the pion four-vectors constraining them to the theoretical mass value. The third pion candidate track was required to have at least 0.1 GeV and to come from the event vertex. The angle between the K^0_S and the π was required to be less than 90°. The invariant mass distribution $M(K^0_S\pi^\pm)$ is shown in fig. 6.14; it shows a prominent peak in the mass region around 900 MeV. It was fitted to the sum of a relativistic Breit–Wigner distribution and a background contribution. The K* mass was fixed at its nominal value and the nominal width was added to the detector resolution in quadrature. The background was parameterized taking into account the production threshold and the observed fall-off at high masses (dashed curve in fig. 6.14). The sum is seen to fit the data well.

The detection efficiency calculated with the Lund model was 0.083 ± 0.007. After correcting for the branching ratio of $K^* \to K^0_S\pi$ and for the unseen K^0_S decay modes, a multiplicity of $0.87 \pm 0.16 \pm 0.08$ per event is determined. The differential cross-section is shown in fig. 6.16.

6.4.3. *Analysis of* ρ^0 *and determination of r*

The reconstruction of the ρ^0 from its decay into $\pi^+\pi^-$ was more difficult than in the case of the K^0 because the decay is prompt and the combinatorial background was found to be overwhelming. After subtracting most of the combinatorial background, which was obtained from same charge pion pairs, the distribution in fig. 6.15 is observed. A ρ signal is visible above a background which, in addition to remaining combinatorial background, contains reflections from $\omega \to \pi^+\pi^-\pi^0$ and from $K^{*0} \to K^\pm\pi^\mp$ where the $K^\pm$ was assigned the pion mass. These background contributions were studied in events from the Lund model and fitted by appropriate functions (for details see [150]). The fitted sum of the resonant and non-resonant background (5 free parameters) is shown as the dashed line in fig. 6.15.

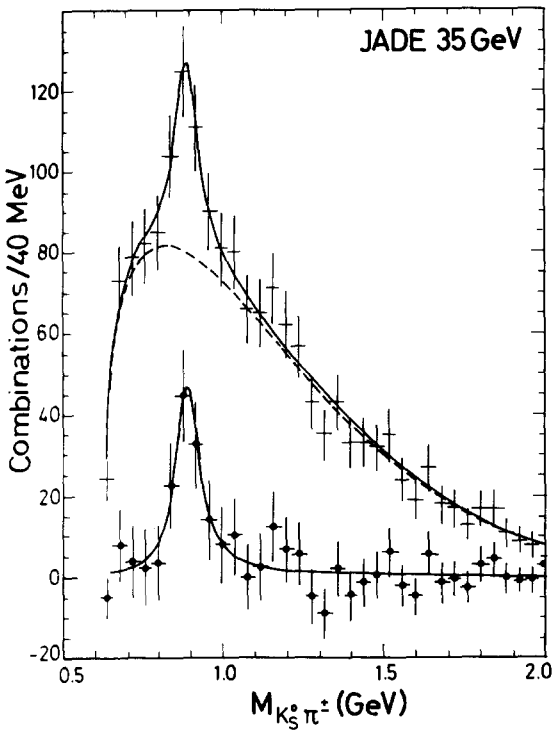

Fig. 6.14. Invariant mass spectrum $M(K^0_S\pi^\pm)$ after enrichment cuts for $K^{*\pm}$. The full curve is the result of the overall fit, the dashed curve is the fit of the background. The data with background subtracted are shown together with a resonance fit.

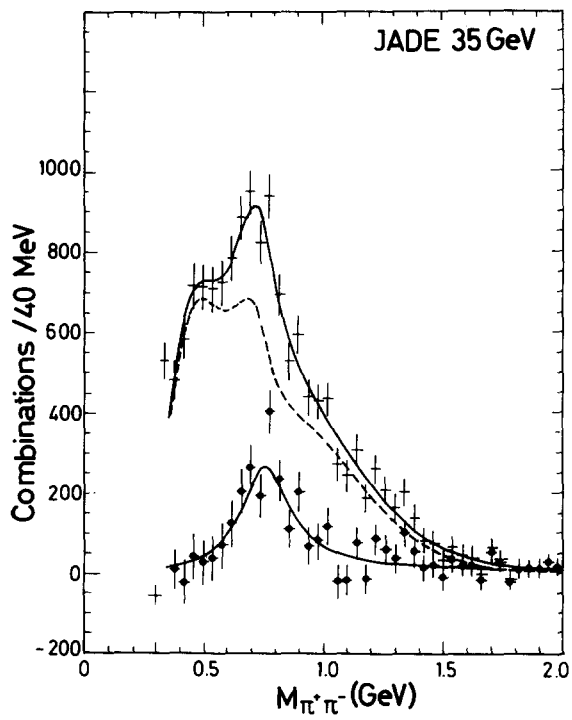

Fig. 6.15. Invariant mass spectrum $M(\pi^+\pi^-)$ after subtracting the distribution for equal charge pairs. The full curve is the result of a fit with a relativistic Breit–Wigner plus background (dashed curve) as described in the text. The data with background subtracted are shown together with a resonance fit.

According to the fit the three resonances ρ^0, ω^0 and K^{*0} each contribute roughly 20% and the remaining 40% of the data are combinatorial background. The ρ^0 signal is also shown in fig. 6.15 after background subtraction. The differential invariant cross-section was calculated in the range $0.1 < x_E < 0.7$ after correcting for efficiency ($\varepsilon = 0.31 \pm 0.01$). The result is shown in fig. 6.16 together with results from TASSO [151]. The agreement between the two experiments is good. Within errors the distributions for K* and ρ^0 agree with each other. Integrating and extrapolating into unmeasured x-regions with the help of the Lund model an average multiplicity of roughly one K* and one ρ^0 per event at $\sqrt{s} = 34$ GeV is obtained (table 6.1).

In fragmentation models the relative rate of pseudoscalar and vector particles is described by the parameter $r = \mathrm{PS}/(\mathrm{PS} + \mathrm{V})$. This parameter was determined within the Lund model by adjusting to the observed number of K*, ρ^0 and also η. In the fits the fragmentation function was varied at the same time in order to keep the charged multiplicity constant. The results are:

$r = 0.49 \pm 0.10 \pm 0.15$ from ρ^0

$r = 0.30 \pm 0.15 \pm 0.11$ from K*

$r = 0.46 \pm 0.06 \pm 0.11$ from η.

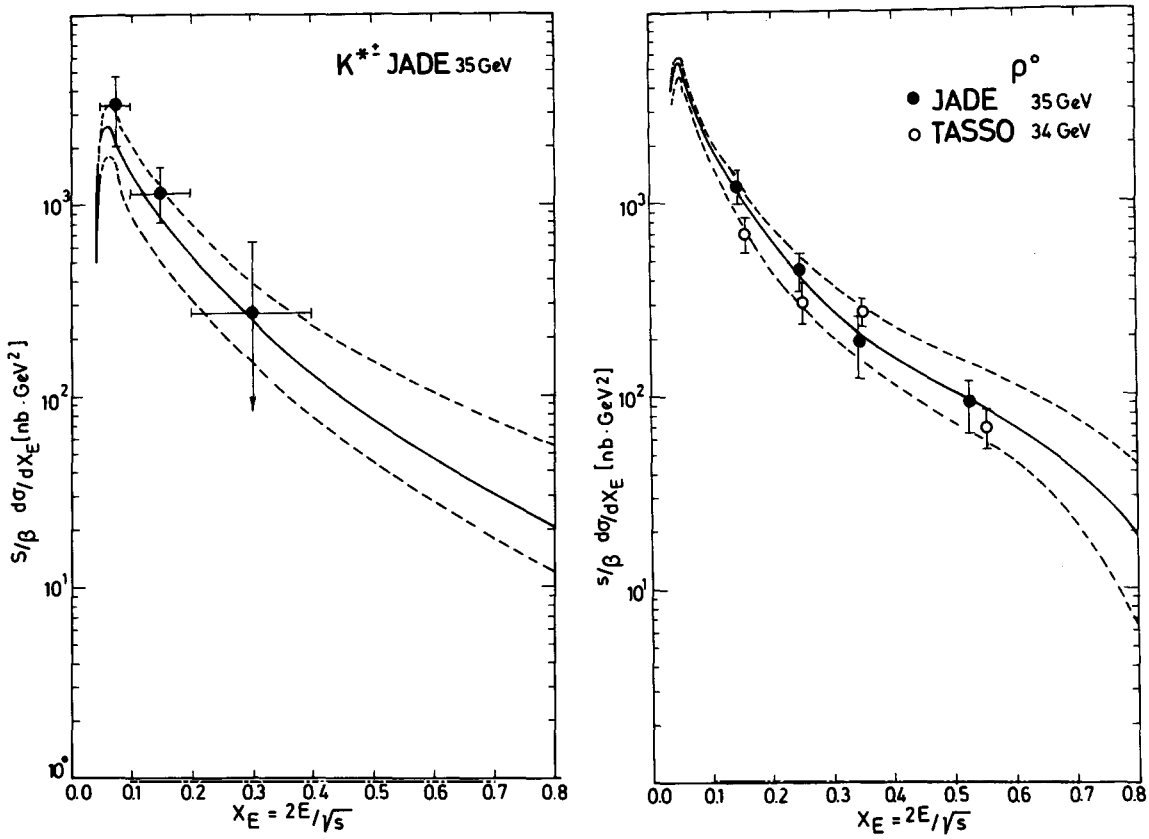

Fig. 6.16. Scaled cross-section for $K^{*\pm}$ and ρ^0 production at $\sqrt{s} = 34$ GeV compared with the Lund prediction for three sets of parameters: The full curve uses $(r, \beta, \gamma_s) = (0.49, 0.515, 0.30)$; the upper dashed curve (0.22, 0.0, 0.30); the lower dashed curve (0.72, 1.0, 0.30).

The weighted average is 0.43 ± 0.09 which is compatible with a TASSO result of $r = 0.42 \pm 0.08 \pm 0.15$ [151]. Little is known about the flavour or mass dependence of r, the large rate of D* production (section 7.1) indicates a mass dependence of r. In the early model calculations $r = 0.5$ independent of flavour was used (version 4.3 of the Lund code), while in version 5.2 of the Lund program $r = 0.25$ is used for c- and b-quarks, a value expected from spin statistics.

6.5. *Inclusive* Λ *and* Ξ^- *production*

The following decays were used for the search for the baryons Λ and Ξ^-:

$$\Lambda \to p\pi^- \qquad \Xi^- \to \Lambda\pi^-$$
$$\bar{\Lambda} \to \bar{p}\pi^+ \qquad \bar{\Xi}^+ \to \bar{\Lambda}\pi^+ .$$

For simplicity we shall in the discussions only refer to the particles and their decays, although the antiparticles were always used in addition.

Λ reconstruction

The decay-length of the Λ is ~8 cm, so it can be identified by reconstructing a secondary vertex. The reconstruction[1] of Λ was based on good tracks which had a $p_t > 0.1$ GeV with respect to the beam direction. No particle identification was used. Pairs of tracks of opposite charge were considered if the modulus of their momentum sum $|\boldsymbol{p}_\Lambda| = |\boldsymbol{p}_p + \boldsymbol{p}_\pi|$ was at least 1 GeV, where $|\boldsymbol{p}_p| > |\boldsymbol{p}_\pi|$ was defined. The angle between the tracks was required to be less than 90°. The intersection point of the tracks was calculated in the $r\varphi$-plane and is defined as the decay vertex. If the decay vertex was situated in the sensitive volume of the jet-chamber, the combinatorial background could be reduced by only allowing pairs of tracks where at most two hits had been registered on the track before the decay vertex.

However most Λ's decayed before they reached the sensitive volume of the jet-chamber. They were subjected to the following cuts:

1. The distance of the decay vertex from the beam interaction point in the $r\varphi$-plane was required to be greater than 50 mm.
2. The vector of the Λ candidate $\boldsymbol{p}_\Lambda$ was required to point to the beam interaction point V within an angle $\alpha_{r\varphi} < 3°$. This cut, which used the fact that the Λ is produced at the event vertex, was relaxed for the search of the Ξ^-.
3. The minimum distance d_π of the pion track from V was required to be greater than 3 mm. This cut took into account the decay kinematics of the Λ.
4. In studies on model events the ratio d_p/d_π was found to be centred at zero for combinatorial background, while for Λ's it was different from zero. A cut $d_p/d_\pi > 0.05$ was applied.

The invariant mass distribution for the track pairs fulfilling cuts 1–4 is shown in fig. 6.17. A Λ peak is seen at the correct mass (the value is given in table 6.1) above a background which is composed of K^0_S decays (50%) and combinatorial background. The efficiency was calculated from Lund model events, it peaks at ~38% around a Λ momentum of 3 GeV and levels off at 25% up to 10 GeV. The limit at high momenta is due to the requirement of a minimum distance of the pion from the event vertex. The life-time of the Λ was determined to be $\tau_\Lambda = (3 \pm 0.5) \times 10^{-10}$ s in good agreement with the nominal value.

The inclusive differential cross-section is shown in fig. 6.18 for three centre-of-mass energies. Scaling is observed within errors. In fig. 6.19 the data at 34 GeV are compared with measurements by other experiments [148, 153]. The agreement is good. The average Λ multiplicities calculated after integrating the differential distribution and extrapolating into x regions not measured are listed in table 6.1. The multiplicity rises with increasing centre-of-mass energy; around 34 GeV it is 0.25 per event.

Λ, $\bar{\Lambda}$ correlations

An interesting question is how the baryon number is compensated and – in the case of strange baryons – how strangeness is compensated.

In order to study correlations the selection criteria for Λ described above were improved by using the dE/dx measurement in the gas of the jet-chamber, by which the ratio of signal to background could be improved from 1:1.3 to 1:0.9. Six events were found which contained a Λ, $\bar{\Lambda}$ pair above a background of 0.5. No events were found with two Λ's or two $\bar{\Lambda}$'s. Taking into account the efficiencies and decay branching ratio this corresponds to:

$$f = \frac{\Lambda, \bar{\Lambda} \text{ pair events}}{\Lambda \text{ events}} = 0.2 \pm 0.12 .$$

[1] The Λ and Ξ^- analysis is described in detail in [152].

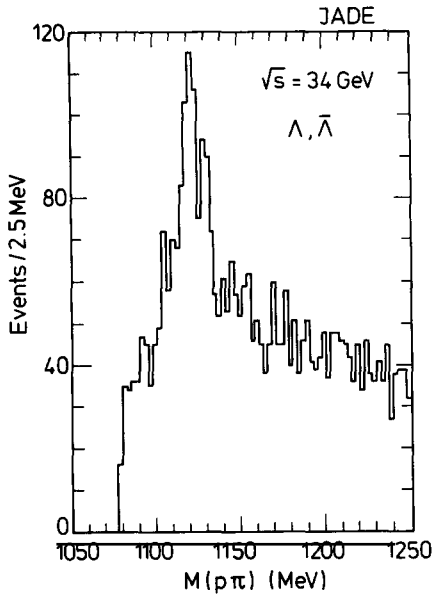

Fig. 6.17. Invariant mass of $M(p\pi^-, \bar{p}\pi^+)$ after the Λ enrichment cuts described in the text.

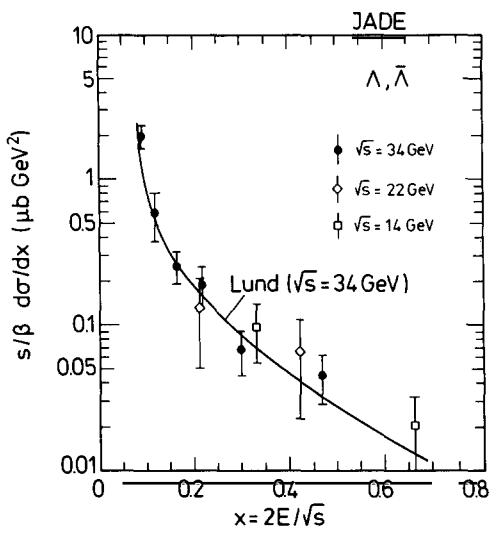

Fig. 6.18. Scaled cross-section for Λ production at three centre-of-mass energies.

If every Λ were accompanied by an $\bar{\Lambda}$ this number would be 0.5.

In 4 out of the 6 events the Λ, $\bar{\Lambda}$ pair was found in the same jet suggesting local compensation of baryon number. This could be confirmed by the study of events having an $\bar{p}$ in addition to a Λ or $\bar{\Lambda}$.[2] The antiproton was defined by cuts on the energy loss in the gas of the jet-chamber. 22 events were found which contained a Λ, $\bar{p}$ and 4 with a $\bar{\Lambda}$, $\bar{p}$ pair. In 15 of these 22 events, the Λ and the $\bar{p}$ were found in the same jet suggesting that baryon number is preferentially compensated in the same jet. This is in agreement with results from the TASSO [148] and the TPC Collaborations [153].

Ξ^- reconstruction

Λ candidates were reconstructed as described in the previous section except that cut 2 on $\alpha_{r\varphi}$ was relaxed to 10°. They were combined with an additional charged particle. Since the life-time of the Ξ^- allows the observation of a decay vertex at a distance from the beam interaction point V, a similar strategy was followed as in the search for Λ decays. Cut 4 of the Λ selection is however not applicable to Ξ^-. Instead the fact that the extrapolations of the Λ and the π track lie on different sides of the vertex V for genuine Ξ^- decays was used in an appropriate cut.

15 Ξ^- candidates were found in the mass region 1280–1360 MeV and their mass distribution is shown in fig. 6.20. The same plot for the wrong sign combinations $\Lambda\pi^+$ and $\bar{\Lambda}\pi^-$ shows no peak. The background is estimated to be 3 events. The differential cross-section for Ξ^- production is shown in fig. 6.21 in comparison with data from other experiments [154]. The mean multiplicity was found to be ~0.05 per event, a factor of 10 less than the Λ multiplicity. In the Lund model the strange baryon production is suppressed by a factor $P(su)/P(ud) \cdot P(d)/P(s) = 0.2$. From the Ξ^- rate a value of 0.5 ± 0.2 is inferred.

[2] Protons were not used because of a large background due to nuclear interactions in the material in front of the detector.

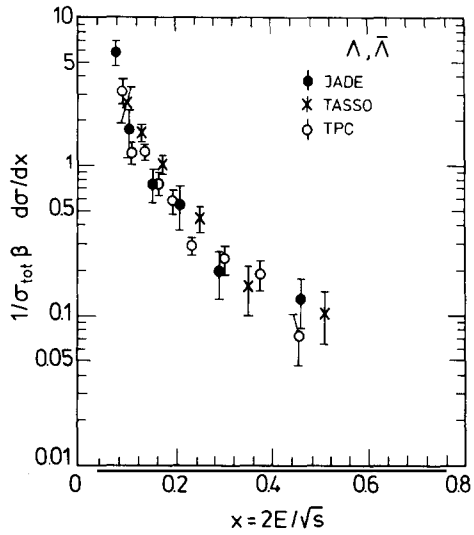

Fig. 6.19. Scaled cross-section for Λ production compared with measurements from other experiments.

6.6. η and Λ multiplicities in gluon-jets

Conjectures exist that gluon-jets may have a different particle composition compared with quark-jets. An enhanced η production was predicted by [155]. Experimentally an increased baryon yield was measured in decays of the Υ, which is dominated by three-gluon final states [156].

It is therefore interesting to investigate the yields of η and of Λ in events enriched in gluons and for events dominated by quarks. Two methods were followed: first the yields were studied as a function of the event sphericity. Events at low sphericity come mainly from $q\bar{q}$ events, while the events at higher

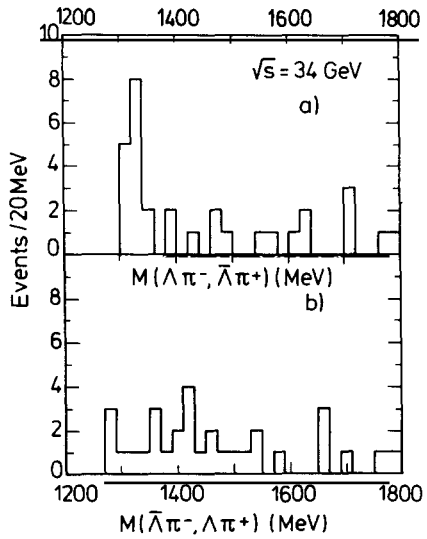

Fig. 6.20. a) Invariant mass of $M(\Lambda\pi^-, \bar{\Lambda}\pi^+)$ after Ξ^- enrichment cuts. b) Wrong charge combinations $M(\bar{\Lambda}\pi^-, \Lambda\pi^+)$.

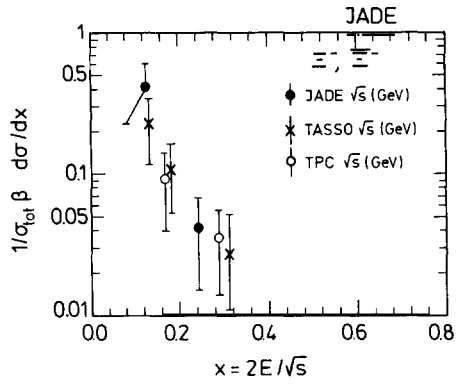

Fig. 6.21. Scaled cross-section for Ξ^- production compared with data from other experiments.

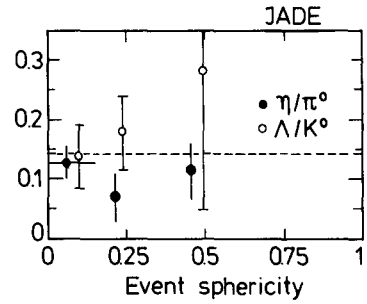

Fig. 6.22. Relative multiplicity of η with respect to π^0 and of Λ with respect to K^0 as a function of event sphericity. The dashed curve is the Lund prediction for η/π^0.

sphericity contain more events with gluon bremsstrahlung. The multiplicity of particles including η and Λ increases with sphericity, therefore the ratios $f_{\eta/\pi^0} = \eta/\pi^0$-yield and $f_{\Lambda/K^0} = \Lambda/K^0$-yield were determined. Taking into account the sphericity dependence of the detection efficiencies the results in fig. 6.22 were obtained. No statistically significant rise is observed either in f_{η/π^0} or in f_{Λ/K^0}.

A similar conclusion was reached when, in the second method, the events were subdivided according to the Q-plot into two-jet events, planar events and spherical events.

7. Properties of heavy quarks

e^+e^- interactions are well suited for studying heavy quarks because all quarks are generated in known proportions, and there is no debris from the initial particles giving rise to confusion in the final state. On the other hand, quarks are not observed directly but only after hadronisation and methods have to be devised to separate quark flavours. Flavour separation at PETRA energies was successful for the heavy quarks c and b.

One unambiguous way of flavour separation is the reconstruction of a resonant state like the D*, which tags the c-quark. Section 7.1 will be devoted to D* studies: determination of the fragmentation function of the c, rates of charged and neutral D*'s and the determination of the charge asymmetry of the c-quark.

In section 7.2 the analysis of inclusive leptons is described, which one has to rely on at PETRA to study the b-quark. Both, inclusive muons and electrons in multihadronic events have been used by the JADE Collaboration. First a description of the method developed for distinguishing leptonic c- and in particular b-decays from other lepton sources is given. Then the determination of the semi-muonic branching ratios of hadrons containing c- and b-quarks and a search for flavour changing neutral currents is described. The measurement of the charge asymmetry of b-quarks from inclusive muons and the measurement of the b life-time using inclusive electrons and muons concludes the chapter.

7.1. *Analysis of inclusive* D* *events and search for* F*

The $D^{*\pm}$ has been investigated by many experiments while the properties of the D^{*0} are less well

known. D^{*0} properties were inferred from studies of $\psi(4030)$ decays, where it was however not directly observed [162]. Experimentally the separation of charged and neutral D* events from background is possible due to the decay kinematics of the D*:[1]

$$e^+e^- \to c\bar{c} \to D^{*+} + \cdots$$
$$\hookrightarrow D^0 + \pi^+ + \cdots$$
$$e^+e^- \to c\bar{c} \to D^{*0} + \cdots$$
$$\hookrightarrow D^0 + \pi^0(\text{or } \gamma) + \cdots$$

The Q value of the D* decay is very low, ~145 MeV. This constrains the decay kinematics so that a D* signal can be clearly observed as a peak in the mass difference $\Delta M = M(D^0\pi) - M(D^0)$ or $\Delta M = M(D^0\gamma) - M(D^0)$ [157].

7.1.1. $D^{*\pm}$ *production*

The charged $D^{*\pm}$ was reconstructed from $D^0\pi^\pm$ using the following decay modes of the D^0:

$$D^0 \to K^-\pi^+$$
$$D^0 \to K^-\pi^+\pi^-\pi^+ .$$

The invariant masses $M(K^-\pi^+)$ and $M(K^-\pi^+\pi^-\pi^+)$ were reconstructed using all charged tracks with momenta $p > 1$ GeV and applying both the K and π mass hypotheses in a data sample of 23 926 multihadronic events at an average centre-of-mass energy of 34.4 GeV [158]. The mass differences $\Delta M = M(D^{*+}) - M(D^0)$ are shown in fig. 7.1 for the two D^0 decay modes. A peak is seen above a small background at low ΔM values. D* events were selected by applying the following criteria:

$$1.66 < M(D^0) < 2.06 \text{ GeV}$$
$$x = 2E_{D^*}/\sqrt{s} > 0.4$$
$$\Delta M < 0.156 \text{ GeV} .$$

The first condition selects the D^0 mass region according to the experimental resolution obtained by a Monte Carlo simulation. The peak in ΔM is only observed for $x > 0.4$. 92 events were selected in this way, 40 of which were in the $D^0 \to K^-\pi^+$ decay mode. The background from B decays was estimated to be at most 8%. The results are summarized in table 7.1. The measurement of the inclusive spectrum and the total rate will be discussed in common with the D^{*0}.

The inclusive D* events were used to study whether gluon emission has the same probability for heavy quarks as for the light ones. In an analysis of the shape of the events containing a $D^{*\pm}$ the fraction of three-jet events was determined by studying their distribution in the Q-plot: most events have a two-jet configuration, i.e. $Q_3 > 0.9$. 0.13 ± 0.04 are in the region of planar events, $Q_3 < 0.9$ and $Q_1 < 0.06$. This fraction agrees with the fraction of planar events of (0.10 ± 0.01) found in a sample of hadronic events containing a charged particle with $x > 0.4$. A comparison with Lund Monte Carlo events led to the value of α_s given in table 7.1 which is compatible with the values found by analysing all hadronic events, a result also found by TASSO [160].

[1] Henceforth only the particle decays are discussed, but in the analysis the antiparticle was included.

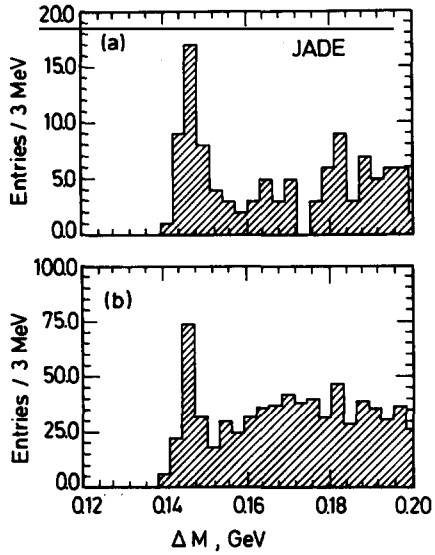

Fig. 7.1. Distribution of $\Delta M = M(D^0\pi^\pm) - M(D^0)$ for $D^{*\pm}$ decays a) where D^0 is a $(K\pi)$ system with $1.66 < M(D^0) < 2.06$ GeV; b) where D^0 is a $(K\pi\pi\pi)$ system in the same mass interval as in a).

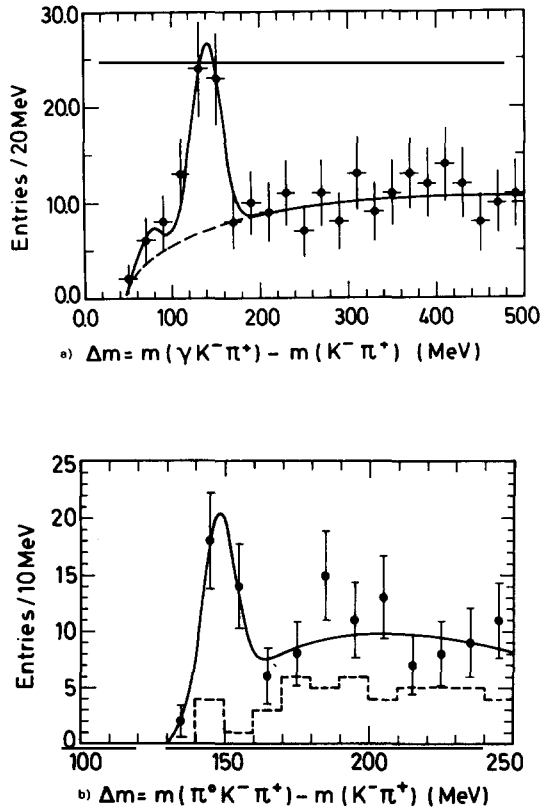

Fig. 7.2. Distribution of $\Delta M = M(D^{*0}) - M(D^0)$ for D^{*0} decays where D^0 is a $(K^-\pi^+)$ system and a) where D^{*0} is a $(\gamma K^-\pi^+)$ system after the cuts to enhance radiative D^{*0} decays; b) where D^{*0} is a $(\pi^0 K^-\pi^+)$ system.

7.1.2. D^{*0} *production*

The decay of the D^{*0} was studied by utilizing its decay into $D^0\pi^0$ and $D^0\gamma$ [161]. The D^0 decay mode was $K^-\pi^+$ and the D^0 decays were selected as above. Combinatorial background was reduced by applying a cut on the pion direction in the rest-frame of the D^0. The pion is emitted isotropically while the background is peaked parallel and antiparallel to the direction of motion of the (K, π)-system. A cut of $|\cos\theta^*(\pi)| \leq 0.8$ was imposed. In addition a photon of energy $E_\gamma > 0.4$ GeV which did not come from a π^0 decay or alternatively a π^0 of energy greater than 0.4 GeV was required. In either case all charged and neutral particles had to be in the same hemisphere. The scaled energy $x = 2E_{D^{*0}}/\sqrt{s}$ was required to be larger than 0.5. The mass difference $M(D^{*0}) - M(D^0)$ is shown for both decays in fig. 7.2. A clear enhancement is observed below 160 MeV.

The signals were fitted by a Gaussian of fixed mass and width and the background for the decay to γD^0 was parameterized. The fit is shown as the dashed line in fig. 7.2a. The background for the decay into $\pi^0 D^0$ was obtained from the analysis of a high mass sideband of the D^0; it is shown as a dashed line below the signal in fig. 7.2b.

The branching ratio for the decay $D^{*0} \to \gamma D^0$ can be calculated from the corrected numbers of the two observed decay modes assuming that they add up to 100%. The result is:

Table 7.1
Results of the D^* analysis

$D^{*\pm}$	
Production rate	$\sigma(D^{*+} + D^{*-}, x > 0.4) = 0.11 \pm 0.02 \pm 0.03$ nb
Average measured fractional energy	$\langle x \rangle = 0.64 \pm 0.05$
Average corrected fractional energy	$\langle z \rangle = 0.71 \pm 0.05$
Peterson fragmentation parameter	$\varepsilon_c = 0.04 \pm 0.015$
Forward–backward asymmetry	$A = -0.14 \pm 0.09$
Axial coupling constant	$a_e a_c = -1.0 \pm 0.6$
Fraction of planar events	0.13 ± 0.04
α_s	0.13 ± 0.08
D^{*0}	
Production rate	$\sigma(D^{*0} + \bar{D}^{*0}, x > 0.5) = 0.11 \pm 0.03$ nb
$BR(D^{*0} \to \gamma D^0)$	$0.53 \pm 0.09 \pm 0.10$

$$BR(D^{*0} \to \gamma D^0) = 0.53 \pm 0.09 \pm 0.10 .$$

The number agrees well with the previous measurement [162].

7.1.3. Inclusive spectra and total rates

The differential x distributions for the charged and the neutral D^* are shown in fig. 7.3. The distributions are vastly different from those observed when studying light mesons (see chapter 6). They peak at a value of $x \sim 0.6$ supporting the assumption that the D^* is formed by the primary c- and $\bar{c}$-quarks. This effect is due to the heavy mass of the primary quark, it has also been observed by other experiments at PEP and PETRA [163, 159, 98].

The average D^* energy measured and after corrections for photon and gluon emission are given in table 7.1 together with the parameter ε_c for the Peterson fragmentation function deduced from the $D^{*\pm}$ data.

For the determination of the absolute rates of D^* production the D^0 branching ratios, $BR(D^0 \to K\pi) = 0.054 \pm 0.004$ [164] and $BR(D^0 \to K + 3\pi) = 0.085 \pm 0.021$, given in [165] were used. The efficiency was calculated with the Lund model. The total measured D^* cross-section for $x > 0.5$ is (210 ± 64) pb compared with an expected total $c\bar{c}$ rate of ~220 pb. The contribution from b decays is expected to be on the level of a few percent. The measured cross-section thus nearly saturates the expectation, but in view of the errors enough room is left for the production of pseudoscalar charmed hadrons, which are expected to constitute 1/4 of the charm decays.

7.1.4. Charge asymmetry of the c-quark

The D^* contains the primary c-quark, except a small contribution which comes from b decays, so the electroweak couplings of the c-quark can be studied by analysing the D^* angular distribution. In order to increase statistics the mass region for the $K\pi$ system was enlarged to $1.50 < M(K^-\pi^+) < 2.06$ GeV. The region between 1.50 and 1.66 GeV is dominated by reflections of the decays:

$$D^0 \to K^-\rho^+ \to K^-\pi^+\pi^0$$

$$D^0 \to K^{*-}\pi^+ \to K^-\pi^0\pi^+$$

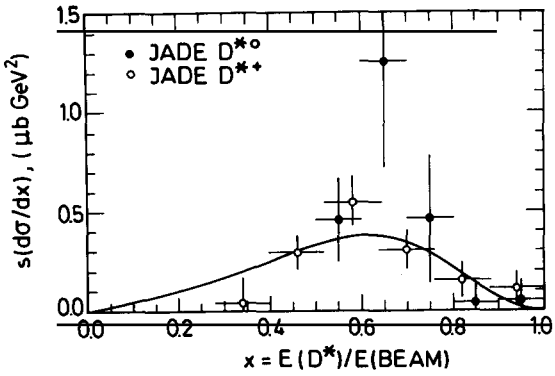

Fig. 7.3. Scaled differential cross-section $s\,d\sigma/dx$ for inclusive D* production. The curve is the Peterson fragmentation function fitted to the data.

where the π^0 remains unobserved. The angular distribution of the D* with respect to the e^- beam is shown in fig. 7.4. The fitted acceptance independent asymmetry is $A = -0.14 \pm 0.09$.

Using eq. (2.9) the axial-vector coupling of the c-quark is determined to be 1.0 ± 0.6 in good agreement with the standard model expectation. The forward–backward asymmetry of the D* has also been measured by HRS [167] at PEP and by TASSO [159, 35] at PETRA with results compatible with our measurement.

7.1.5. Search for F* *decays*

The F^{*+} (D_s^* according to the new nomenclature proposed in [164]) production and decay are similar to that of D^{*0}. The F^{*+} was searched in the established decay chain [168]:

$$F^{*+} \to \gamma F^+, \qquad F^+ \to \Phi\pi^+, \qquad \Phi \to K^+K^- .$$

The Φ candidates were reconstructed as track pairs with opposite charge assuming the K mass and selecting an invariant mass between 0.97 and 1.07 GeV. They were then combined with an additional charged particle and accepted as F^+ candidates if they had an invariant mass between $1.77 <$

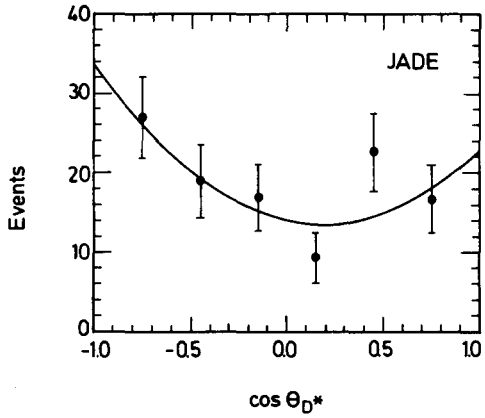

Fig. 7.4. Angular distribution of inclusive $D^{*\pm}$. The curve is a fit of the standard model prediction to the data.

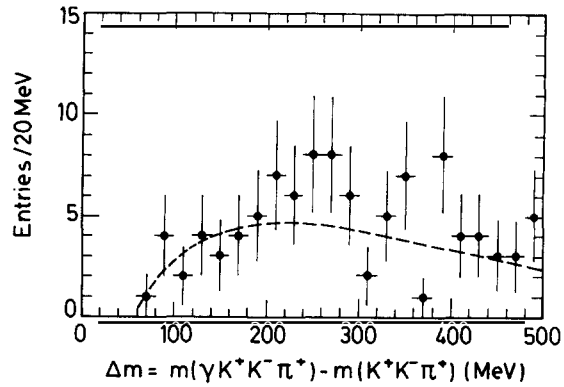

Fig. 7.5. The distribution of $\Delta M = M(\gamma K^+K^-\pi^+) - M(K^+K^-\pi^+)$ after the cuts to enhance radiative F* decays. The curve is a fit to the data of a parameterization used to parameterize the background in radiative D^{*0} decays.

$M(K^+K^-\pi^+) < 2.17$ GeV. A similar cut on the flight direction of the π^+ in the rest system of the $K^+K^-\pi^+$ system as described in the search of the D^{*0} was applied to reduce combinatorial background. Finally the F^+ candidates were combined with a photon of at least 0.4 GeV, all decay products were required to be in the same jet and the scaled $(F^+\gamma)$ energy was demanded to be at least 0.5. The mass difference for $M(\gamma K^+K^-\pi^+) - M(K^+K^-\pi^+)$ is shown in fig. 7.5. The data show no significant peak at low ΔM. Assuming a background shape similar to the one in the D^{*0} decay (dashed line in fig. 7.5) an upper limit was calculated for the F* production:

$$\sigma(F^{*+} + F^{*-}, x > 0.5) \cdot BR(F^+ \to \Phi\pi^+) < 5.4\,\text{pb (at 95\% C.L.)}.$$

7.2. *Inclusive leptons*

The analysis of inclusive leptons has been used to deduce properties of the c- and, in particular, of the b-quark. Before the discussion of the individual analysis results the common method to distinguish heavy quarks from light quarks will be given.

7.2.1. *Flavour tagging in events with inclusive leptons*

Inclusive leptons ℓ (e or μ) in multihadronic events originate from a number of processes, the main contributions are given in the following list:

C1. Direct leptons from b decays $b \to c\ell^-\bar{\nu}_\ell$;
C2. Direct leptons from c decays $c \to s\ell^+\nu_\ell$;
C3. "Background" leptons $(u, d, s) \to \text{hadrons} \to "\ell" + X$.

The background leptons "ℓ" originate – in the case of muons – from π and K decays or from punchthrough. The background for electrons is due to photon conversions and to accidental overlap of energy clusters with (non-electron) charged tracks. In addition the following sources of leptons have to be considered:

C4. Cascade decay $b \to c + \text{hadrons};\ c \to s\ell^+\nu_\ell$;
C5. "Background" b decays $b \to \text{hadrons} \to "\ell" + X$;
C6. "Background" c decays $c \to \text{hadrons} \to "\ell" + X$.

The last two event classes C5 and C6 refer to a hadronic decay of c or b where a hadron simulates a prompt muon or electron.

The leptonic b decays can be distinguished from the other event-classes due to the high mass of the b-quark, which results not only in a lepton of high transverse momentum in leptonic decays but affects also the shape of the hadronic decay products. In order to efficiently discriminate b decays from background both the p_t of the lepton and a hadron-jet related variable are analysed. The variables most effective for distinguishing decays of b-quarks from uds- and c-quarks were studied systematically in [169]. In the following we shall use:

1. The transverse jet mass $M_t = (\sqrt{s}/E_{vis}) \Sigma_N |p_t^{out}|$ where the sum runs over all charged and neutral particles in the event except the lepton.
2. The transverse momentum of the lepton p_t^ℓ.
3. The missing transverse momentum p_t^ν.

"Transverse" variables are measured relative to the sphericity axis. They are chosen because they are largely independent of the fragmentation function. p_t^{out} is the component of p_t perpendicular to the event plane. The flavour dependence is obvious for the first two variables, they depend on the momentum component transverse to the primary quark direction given to the particles in the b decay. The third variable p_t^ν, defined as the transverse component of the event's missing momentum vector, receives contributions from many sources, e.g. from undetected neutral and charged particles, from measurement errors and, for the semileptonic decays of quarks, from the neutrino. It turns out that in events with a leptonic b decay a large contribution originates from the neutrino. The contribution from the hadronisation process was found to be small.

The probability distributions $\rho(M_t, p_t^\ell, p_t^\nu)$ for the event classes C1–C6 were derived for muons from simulated Monte Carlo events. The projections on the M_t, p_t and p_t^ν axes are shown for muons from the three main contributions C1–C3 in fig. 7.7. Their average values are given in table 7.2. The distributions for b events are distinctly different from those for the other two event classes.

7.2.2. *Semimuonic branching ratio of* C- *and* B-*hadrons*

The fragmentation of b-quarks leads to the production of B-mesons or baryons which may decay muonically into the experimentally observed muons. The measured branching ratio is an average over all B-hadrons and gives the branching ratio of the b-quark only in the limit that the spectator model is valid. For the analysis hadronic events corresponding to an integrated luminosity of 70 pb^{-1} were used with an average centre-of-mass energy of $\sqrt{s} = 34.6$ GeV [171]. These data yielded 21 419 multihadronic events, from which 994 were selected as containing a penetrating track according to the "tight" selection criteria in table 7.3.

The data were compared with the predictions of the Lund Monte Carlo model, where the production ratio of the flavours is known. The fragmentation of the light quarks is described by the symmetric Lund fragmentation function eq. (5.22), while for c- and b-quark the Peterson function eq. (5.24) was used, with the parameters listed in table 5.1.

Table 7.2
Average values of the flavour discriminating variables for muon inclusive events

Variable	uds	c	b
M_t (GeV)	4.20	4.69	6.53
p_t^μ (GeV)	0.55	0.61	1.22
p_t^ν (GeV)	1.36	1.48	1.94

Table 7.3
Definition of muons: tracks of momenta greater than 1.8 GeV are required. The muon hits have to be within two standard deviations of the projected track

Criteria	Min # Abs. lengths	# of hit muon chambers	Detection efficiency	Background fraction
"loose" definition	4.8	2 hits outside magnet yoke	62%	66%
"tight" definition	5.8	all chambers traversed	48%	54%

The flavour-dependent quantities which were used to separate the c- and b-quark events were M_t as the jet related variable and the p_t of the muon. In order to determine the muonic branching ratio the Monte Carlo distributions in p_t and M_t were fitted to the data leaving the numbers of background events (punchthrough and decay were considered separately) and the numbers of c decays and b decays as free parameters. The latter two are related to the muonic branching fractions. The data are shown in fig. 7.6 together with the fitted Monte Carlo prediction which yields:

$$\mathrm{BR}(b\to\mu+\cdots)=(11.4\pm1.8\pm2.5)\%$$
$$\mathrm{BR}(c\to\mu+\cdots)=(8.9\pm1.8\pm2.5)\%\,.$$

The first error is statistical and the second one systematic. The latter is dominated by the uncertainties in the shapes of the p_t and M_t distributions and has small contributions from uncertainties in the detection efficiency of muons, in the fragmentation functions and in the background contributions. The fitted background proportion is $(45\pm4)\%$.

The measured branching ratios are in agreement with other recent measurements [172].

7.2.3. *Search for flavour-changing neutral currents*

In the standard model the b-quark is assigned to a weak isospin doublet with the t-quark and the b decays exclusively via the charged current. The absence of the t-quark in e^+e^- collisions has led to speculations [173] which have assigned the b to a singlet. A possible consequence of such models is the decay of b-quarks via neutral current which, for instance, leads to:

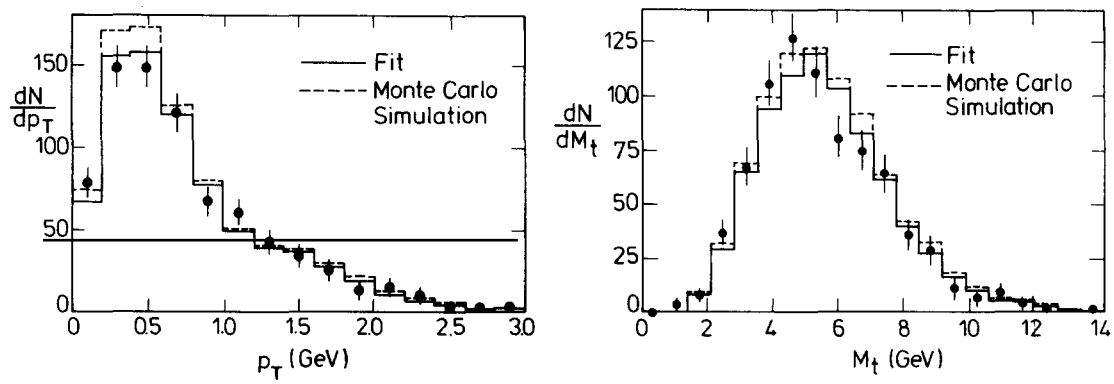

Fig. 7.6. Distributions of inclusive muons as functions of p_t^{μ} and M_t with the fits (full curve) to obtain the semimuonic branching ratio of B-hadrons. The Monte Carlo prediction is shown as the dotted histogram.

$$b \rightarrow \mu^+\mu^- + s \text{ or } d .$$

This flavour-changing neutral current (FCNC) process was searched for in hadronic events containing two muons. The data sample of inclusive muons described in the previous section was used. In addition to the first muon which was required to fulfill the "tight" cuts a second muon was required, which only had to satisfy the "loose" cuts. The events were classified according to the charge of the muons and whether they belonged to the same or to different jets:

	Charge of μ tracks			Charge of μ tracks	
Data	++	+−	Monte Carlo	++	+−
same jet	4	12	same jet	4.2 ± 0.9	14.4 ± 1.7
opposite jet	18	30	opposite jet	15.0 ± 1.7	23.3 ± 2.1

The numbers in the second table were derived from the standard Lund Monte Carlo using the Peterson fragmentation function for c and b. The decay of the B into J/Ψ was included.

Flavour-changing neutral currents would lead to muons of opposite sign in the same jet. A simulation showed that the opening angle between the same-jet dimuons produced via a FCNC mechanism would be large while ordinary background dimuons are produced with small opening angles. With the requirement that the opening angle be between 20° and 80° the number of same-jet opposite-charge dimuons was 3 and the standard model predicts 6.1 ± 1.1. This yields an upper limit on the branching ratio.

$$BR(b \rightarrow \mu^+\mu^- X) < 0.4\% \qquad \text{at } 95\% \text{ C.L.}$$

This limit is incompatible with the theoretical prediction of 2.5% based on a 5-quark model [173b]. Similar limits were also found by other experiments [174].

7.2.4. Electroweak asymmetry of b*-quarks*

The measurement of the charge asymmetry predicted by the standard model has been successful in the leptonic channels, $e^+e^- \rightarrow \mu^+\mu^-$ and $\tau^+\tau^-$, and for the c-quark using $D^{*\pm}$ decays. Here an analysis of inclusive muon data is discussed, which allows a measurement of the b asymmetry.

The data sample used corresponds to an integrated luminosity of $76\,pb^{-1}$ with an average centre-of-mass energy of $\sqrt{s} = 34.6$ GeV [170]. Multihadronic events were selected as described in section 4.2. Events with more than 5 tracks were analysed if they contained a penetrating track of more than 1.8 GeV, which satisfied the "loose" muon criteria. A few events were removed where the muon had a high probability of coming from π or K decays. In total 1729 events containing an inclusive muon were selected. The sphericity axis was used as an approximation for the quark flight direction.

The charge asymmetry is determined by comparing the numbers of quarks produced in the forward direction with those in the backward direction. Forward and backward are recognised by the charge and the direction of the decay muon. Because of this experimental technique the event category C4, the cascade decay of the b-quark, is of particular importance, since the branching ratio of $b \rightarrow c$ is large and since it results in a muon of the "wrong" sign. A negative muon at $\theta < 90°$ signals a *forward* b decay or a *backward* c decay, or if it originates from a cascade decay, also a *backward* b decay.

The separation of the event classes is achieved by using the three variables, M_t, p_t^μ and p_t^ν described

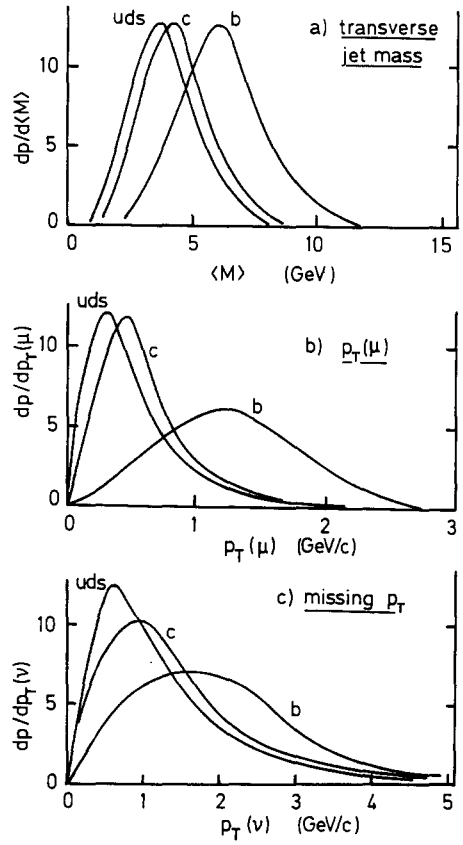

Fig. 7.7. Probability distributions for the three flavour classes, uds, c and b, as functions of M_t, p_t^{μ} and p_t^{ν}. All curves are normalised to the same area.

above. The probability distributions ρ_i for the six event classes C1–C6 defined in section 7.2.1, derived from the Lund model (version 5.2) were used:

Event class	C1 b→μ	C2 c→μ	C3 uds→"μ"	C4 b→c→μ	C5 b→"μ"	C6 c→"μ"
Prob. distr.	ρ_3	ρ_2	ρ_1	ρ_{32}	ρ_{31}	ρ_{21}

"μ" stands for a fake muon. The number of forward and backward b decays were obtained by a maximum likelihood fit to the data of the differential distributions of the forward and backward events N^F and N^B:

$$\frac{d^3N^F}{dM_t\, dp_t(\mu)\, dp_t(\nu)} = N_1\rho_1 + N_c^F\rho_2 + N_b^F\rho_3 + (\varepsilon_1 N_c^{F+B}\rho_{21} + \varepsilon_2 N_b^B\rho_{32} + \varepsilon_3 N_b^{F+B}\rho_{31})$$

$$\frac{d^3N^B}{dM_t\, dp_t(\mu)\, dp_t(\nu)} = N_1\rho_1 + N_c^B\rho_2 + N_b^B\rho_3 + (\varepsilon_1 N_c^{F+B}\rho_{21} + \varepsilon_2 N_b^F\rho_{32} + \varepsilon_3 N_b^{F+B}\rho_{31})\,.$$

The parentheses contain the background contribution and the background fractions ε_i are obtained from the Monte Carlo simulation. The results of the fits are shown with the data in fig. 7.8. The model curves are seen to describe the data well. The fitted number of b events in the forward and backward directions are $N_b^F = 114.6 \pm 12.5$ and $N_b^B = 191.3 \pm 16.2$, yielding an asymmetry of $A_b = (-25.0 \pm 6.5)\%$. Carrying out fits in smaller angular intervals yields the angular distribution shown in fig. 7.9. Assuming the shape of the angular distribution predicted by the standard model, one fits an acceptance independent asymmetry of:

$$A_b = (-22.8 \pm 6.0 \pm 2.5)\%$$

where the second error is systematic. It is due to uncertainties in the fragmentation models and the semi-muonic branching ratio of c and b quarks. A search for detector biasses yielded no significant effects.

The measured b-asymmetry can be compared with the prediction of the standard model given in eq. (2.9) for zero quark-mass. Taking into account a b mass of 5 GeV the expected value is -25.2% [77]. Comparing with the measured value one then gets:

$$a_b = -0.90 \pm 0.24 \pm 0.10$$

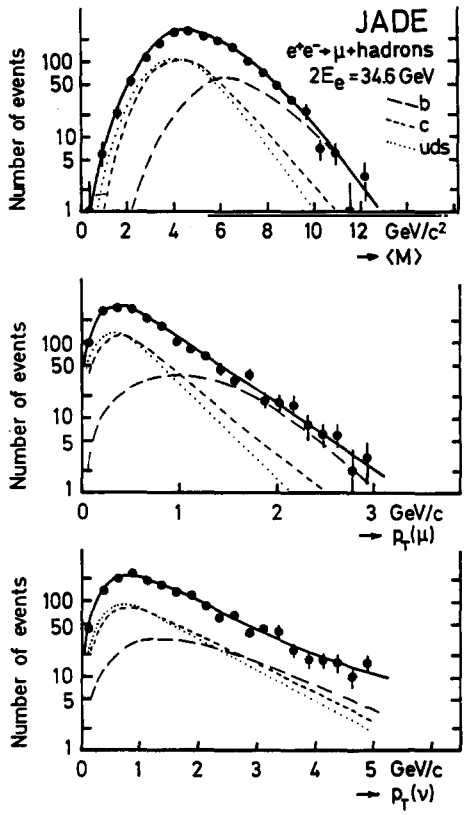

Fig. 7.8. M_t, p_t^μ and p_t^ν distributions for inclusive muons together with the uds, c and b fractions as computed by Monte Carlo.

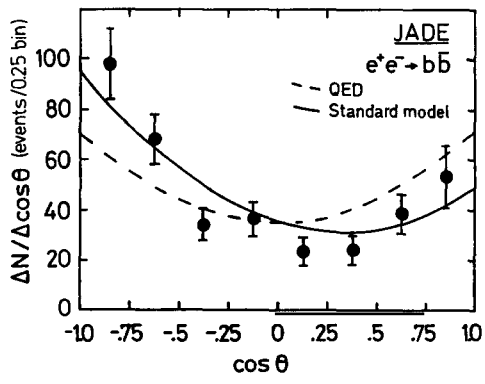

Fig. 7.9. Angular distribution of bb events. The full curve is the prediction of the standard model and the dashed curve of QED (no asymmetry).

in agreement with the standard model prediction. Similar measurements have been carried out by other experiments, the errors of the results are in general larger. A summary is given in [35].

The agreement of the measured b-asymmetry with the predicted value limits the amount of B^0–$\overline{B^0}$ mixing. If B_d^0 and B_s^0 mix with their antiparticles before decaying, the measured asymmetry would be diluted. The mixing parameter can be defined as $r = \Gamma(B^0 \to \overline{B^0} \to \mu^+)/\Gamma(B^0 \to \mu^-)$. Then

$$2Kr/(r+1) = (A_{\text{St.M.}} - A_{\text{obs}})/A_{\text{obs}} = 0.10 \pm 0.26$$

where K is the fraction of b-quarks fragmenting into B^0, assumed to be ~0.52. The upper limit obtained for r is 0.7 at 90% C.L. This limit agrees with the limit obtained by the CLEO Collaboration [175]. It is not in conflict with the UA1 findings of 100% mixing in B_s^0 [176], since the fraction of primary b-quarks fragmenting into B_s^0 is expected to be approximately 1/3.

7.2.5. Determination of the B *life-time*

In an early publication with considerably less statistics than is now available, JADE derived an upper limit on the B life-time of $\tau_B < 1.4 \times 10^{-12}$ sec [177]. This turned out to be very close to later measurements of τ_B by MAC [178], MARK II [179] and DELCO [180] at PEP and by TASSO [181] at PETRA. With the increased statistics available after the running in 1982 and improved precision of the jet-chamber due to better calibrations another determination was carried out [182].

The life-time of B-hadrons was determined by analysing in multihadronic events the displacement of the decay lepton from the average position of the event vertex. Two methods were followed:

1. A sample of B-enriched events, containing an inclusive electron or muon was selected. The impact parameter distribution of the lepton was analysed and was found to show a positive deviation from the run vertex which could be attributed to B decays.

2. The events of the hadron sample with inclusive muons were weighted to enhance those coming from B decays. Again the impact parameter distribution of the muon was found to deviate from the event vertex distribution. This weighting method was also applied to the hadrons in the event-sample and a statistically more significant result was obtained.

The flight path of B-mesons was measured in the $r\varphi$-plane using the jet-chamber (see fig. 7.10). The average vertex position (V), named the "run vertex", was determined from Bhabha events with a statistical precision of 0.04 mm. The horizontal half-width of the vertex distribution was ~0.4 mm and the vertical half-width 0.02–0.04 mm including the time variation. Well-measured tracks extrapolated to the run vertex with a resolution of 0.36 mm at the vertex.

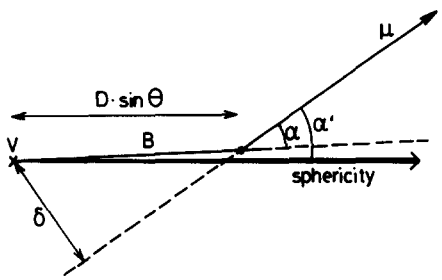

Fig. 7.10. Sketch of the decay of a B-hadron originating from the vertex V (symbols are explained in the text).

Table 7.4
Contributions to the selected event samples

Type	$b\to\ell$ (%)	$b\to c\to\ell$ (%)	$c\to\ell$ (%)	Fake leptons π, K, Λ decays (%)	Fake leptons prompt (%)	Events MC	Events data
				μ events			
Before cut 1	21	5	26	1	48	533	293
All cuts	65	6	8	1	20	114	74
				e events			
All cuts	80	8	10	0	<3		34
				hadron events			
All cuts	4	4	15	2	76		1478

The distance of the lepton candidate track from the run vertex in the $r\varphi$-plane is henceforth called the impact parameter, δ. For leptons from B decays it is related to the life-time τ_B by

$$\delta = \tau_B \beta\gamma c \sin\alpha \sin\theta$$

where βc is the velocity of the B, $\gamma = E/M$, θ is the polar angle of the B particle and α its angle in the $r\varphi$-plane with respect to the B direction. The latter is approximated by the sphericity axis.

Method 1: *Selecting an enriched sample of leptonic* B *decays*
Data corresponding to an integrated luminosity of 63 pb^{-1} at an average energy of ~34.6 GeV were used. After the standard selection cuts for multihadronic events additional cuts were applied to select inclusive muon and electron events. Muons were selected as tracks with momentum greater than 1.8 GeV fulfilling the standard "loose" muon cuts (table 7.3). Electrons were defined as tracks with momentum greater than 1.5 GeV, associated with a lead-glass cluster of an energy corresponding to 85% of the track momentum. In addition the energy loss measured in the jet-chamber had to be consistent with that of an electron, i.e. greater than 8.6 keV/cm.

The selection cuts for inclusive lepton (μ or e) events had the aim of defining a well-contained event ($\cos\theta < 0.71$ for the lepton and <0.85 for the sphericity axis) with a well-measured leptonic track. In addition the following B-enrichment cuts were applied, cuts 2 and 3 also suppress events with a pronounced three-jet structure:

1. $p_t^\ell > 0.9$ GeV, where p_t^ℓ is the transverse momentum of the lepton candidate with respect to the sphericity axis.

2. The lepton candidate is required to be isolated from other energetic tracks by requiring:

$$\sum_i p_{Li}^\ell < 2.0 \text{ GeV}$$

where p_{Li}^ℓ, is the longitudinal momentum of the ith particle with respect to the lepton. The sum runs over all particles of transverse moment less than 0.35 GeV with respect to the lepton, which lie in a cone of 25° half opening angle around it.

3. A cut which limits the width of the events by limiting the amount of transverse momentum in the event plane is applied in order to eliminate events with a pronounced three-jet structure:

$$0.20 < \left(\sum |p_t^{in}| / \sum |p|\right)_{\ell-\text{jet}} < 0.60\,; \qquad 0.10 < \left(\sum |p_t^{in}| / \sum |p|\right)_{\text{opp-jet}} < 0.45\,.$$

The sums run over all particles in a jet and p_t^{in} is the projection of the particle momentum on the Q_2 axis. The different cut values take into account the different average values of p_t^{in} in the normal jet and the jets which contains the high p_t lepton.
The effect of the B-enrichment cuts is shown in table 7.4, where the flavour composition of the events before and after the B-enrichment cuts is given, as obtained from the Monte Carlo simulation. The measured impact parameter distributions for muons and electrons are shown in fig. 7.11a and b. They show a deviation from the vertex position toward positive values, the measured deviations are:

$\langle \delta \rangle = 0.282 \pm 0.078$ mm for muons

$\langle \delta \rangle = 0.457 \pm 0.107$ mm for electrons.

The B life-time was obtained by a maximum likelihood fit of the sum of all expected contributions to the observed δ-distribution of the inclusive leptons. The only free parameter was the life-time τ_B. The probability distributions for the contributing event classes (see table 7.4) were obtained from a Monte Carlo simulation. The background was separated into decay leptons from long-lived particles like $\pi^{\pm}$, $K^{\pm}$, K^0, Λ and prompt background leptons.

The measurement error for the impact parameter was obtained by analysing prompt hadrons in multihadronic events. Their impact parameter distribution is shown in fig. 7.12. It is centred at

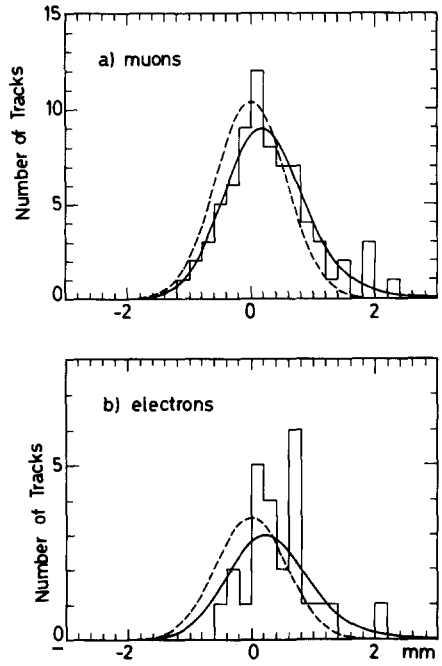

Fig. 7.11. Measured impact parameter distribution for B enriched with inclusive muons (a) and electrons (b). The full curves are fits to the data, the dashed curves show distributions symmetric around 0.

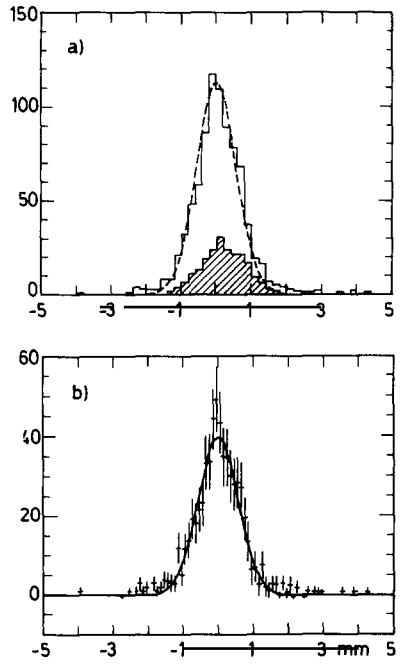

Fig. 7.12. δ-distribution for all selected hadrons before (a) and after (b) subtraction of the estimated decay contributions. The subtracted contribution is also shown in (a) as a shaded histogram. The Gaussian curves are fits with mean 0 in the range $|\delta| < 1.5$ mm.

Table 7.5
Contributions to the systematic error of the B life-time

Uncertainty of δ distribution of B→lepton decays	0.15 ps
Uncertainty of fraction of B→lepton decays	0.30 ps
Uncertainty of average C life-time: $\tau_C = 0.6 \pm 0.2$ ps	0.05 ps
Uncertainty of resolution: $\sigma_\delta = 0.570 \pm 0.075$ mm	0.15 ps
Uncertainty from π, K and Λ decays	0.10 ps
Total systematic error	0.38 ps

$\langle\delta\rangle = 0.042 \pm 0.021$ mm, a value much smaller than the signal value. After a correction for small contributions from long-lived particles it is $\langle\delta\rangle = -0.006 \pm 0.024$ mm. The resolution of 0.57 mm obtained from the hadrons is slightly larger than the value obtained from the detector simulation of 0.52 mm. The final result for the life-time from method 1 is:

$\tau_B = 1.78^{+0.55}_{-0.45}$ ps from muons

$\tau_B = 1.73^{+0.90}_{-0.67}$ ps from electrons

$\tau_B = 1.76^{+0.45}_{-0.38}$ ps combined value .

The full line in fig. 7.11 shows the fit results corresponding to these numbers, its agreement with the data is good. The estimated systematic errors are summarized in table 7.5. They amount to 0.38 ps and the largest contribution comes from the uncertainty of the B fraction in the event sample.[2]

Method 2: *A weighting algorithm for leptonic and hadronic* B *decays*
The method described here is complementary to the previous one because the dependence on the Monte Carlo simulations enters in a different way. The selected events with inclusive muons were used and were weighted according to the relative probability of their being B events. The weights were calculated using the variables p_t^μ and the event aplanarity Q_1.[3] The weight functions $P(p_t, Q_1)$ were generated by Monte Carlo simulation (Lund 5.2) and parameterized by polynomials of order 3. The weight functions were checked by applying them to the Monte Carlo events.

For each event the impact parameter δ of the muon was weighted by the weight function P and by the inverse square of the combined error from track measurement, Coulomb scattering and the beam size. The signal and background distributions were constructed by the appropriate linear combinations of weighted and unweighted histograms, they are shown in fig. 7.13a and b. The signal histogram yields $\langle\delta\rangle = (0.242 \pm 0.148)$ mm while the background histogram is symmetric with $\langle\delta\rangle = (0.047 \pm 0.084)$ mm.

This method was also applied to all hadrons in an event, although the muon was still required in order to be able to construct the weights. Due to the large mass of the b-quark, the B-hadron takes up a large fraction of the jet energy and there is little left over for the hadronisation process. Monte Carlo simulations show that 71% of all hadrons in B events originate from the decay of the B-hadron. The signal and background distributions are shown in figs. 7.14a and b. The measured average $\langle\delta\rangle =$

[2] The analysis was carried out with the Lund Monte Carlo 4.3; in the course of the analysis version 5.2 was issued. A test showed that the new version leads to statistically compatible result for τ_B.

[3] Q_1 is the smallest eigenvalue of the normalized sphericity tensor, see section 5.1 for its definition.

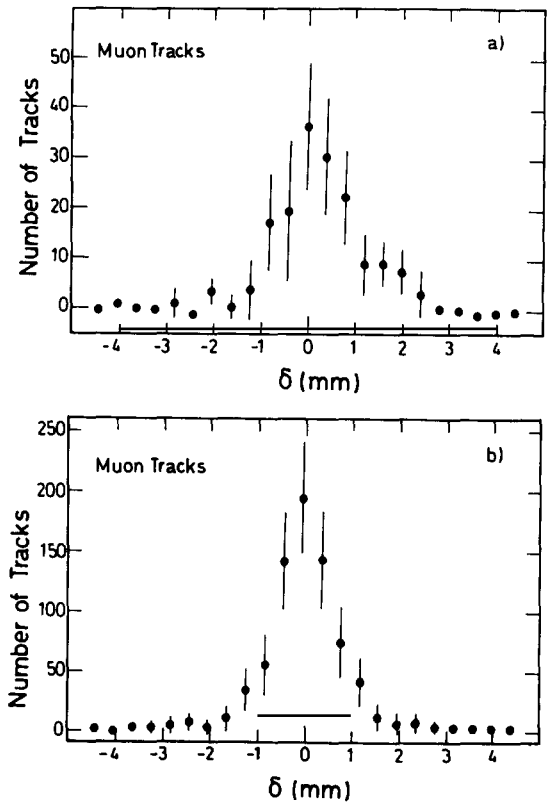

Fig. 7.13. Signal (a) and background (b) distribution for inclusive muons of the impact parameter from the weighting method.

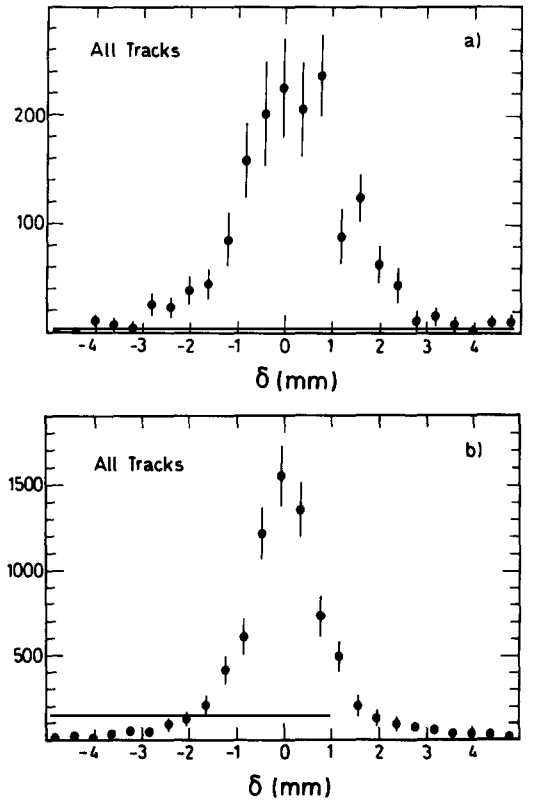

Fig. 7.14. Signal (a) and background (b) distribution of the impact parameter for all hadrons in inclusive muon events (weighting method).

0.195 ± 0.062 has to be corrected for the fraction of directly produced hadrons and also for interactions in the beam pipe. The corrected value is $\langle \delta \rangle = (0.290 \pm 0.095)$ mm, leading to a B life-time of

$$\tau_B = (1.7 \pm 0.6 \pm 0.4)\ \text{ps}$$

where the second error is due to systematic errors in the weight functions and the conversion factor for $\langle \delta \rangle$ into life-time, which has to be obtained by Monte Carlo methods. The result of method 2 confirms the more accurate value obtained using method 1.

The measurement can be used to determine the element U_{bc} from the Kobayashi–Maskawa matrix. The B life-time can be expressed as [183]:

$$\tau_B = \frac{\tau_\mu (m_\mu / m_b)^5}{2.75|U_{bc}|^2 + 7.7|U_{bu}|^2}$$

where τ_μ is the muon life-time and m_μ and m_b are the masses of the muon and b-quark. Studies of the lepton spectrum from B decays show that the element U_{bu} is small compared to U_{bc} and can be neglected [184]. One then has:

$$U_{bc} = 0.043 \pm 0.014$$

where $m_b = 5\,\text{GeV}$ was used. The error of U_{bc} is dominated by the uncertainty of the mass of the b-quark, which was estimated around 10%.

8. Search for new particles

The data obtained with the JADE detector were used to search for new particles, i.e. particles which have not been observed yet. These could be particles which would fit into the framework of the standard model, like the top quark or Higgs particles, but extensive and systematic searches were also made for particles postulated by theories that go beyond the standard model, e.g. supersymmetric or composite models.

There are two ways of searching for new particles: one is to look for deviations in a measured cross-section and exclude the production of new particles that would be observed in this particular topology. This method is used in the search for top, for example, where one examines the magnitude of the total cross-section for $e^+e^- \rightarrow$ hadrons to look for a possible contribution from the top-quark. Another method is to search for events with particular properties which the new particle is predicted to have and which "normal" events do not have. Hadronic events with missing energy, for example, could indicate the decay of supersymmetric particles. In both methods the limits are obtained by comparing the observed number of events with the predicted number. The prediction is in general obtained by simulating the production and decay using Monte Carlo methods.

None of the searches undertaken so far by the JADE Collaboration and by the other experiments at e^+e^- machines have yielded convincing evidence for new phenomena. Hence it may be more important for the future, which event topologies have been searched for new effects, rather than the particular theory which motivated the search. Therefore we include a table of the selected event samples, with a list of the cuts applied.

We shall give here an overview of the JADE results. More details can be found in the original publications. A comparison with results from other experiments can be found in the recent conference reports, e.g. [185, 186].

8.1. Search for the top-quark

The standard model assumes quarks to be in weak isospin doublets, (u, d), (c, s) and (t, b). The hunt for the missing top-quark was one of the main aims pursued as the energy of PETRA was raised gradually towards its highest value of 46.78 GeV [187, 188, 79, 84, 189]. Different methods were employed to search for the top: A new flavour would lead to an increase in R_{had}, the total hadronic cross-section normalised to the lowest order muon pair cross-section. A $\bar{t}t$ bound state is expected to show up as a narrow resonance, possibly at an energy below the threshold for open t production. The increase in R as well as the height of the resonance are determined by the charge of the new quark.

The search for a narrow resonance was carried out in three energy regions by increasing the centre-of-mass energy $W = \sqrt{s}$ in steps adjusted to the machine resolution, which is $\sigma_W = 2.2 \times 10^{-5} W^2$ GeV. The scan parameters are listed in table 8.1. The resulting R_{had} is shown in fig. 8.1. No obvious structure is visible. An upper limit on the production cross-section is obtained by fitting to the data the sum of a constant term plus a resonance of mass M_R and width $\Gamma \ll \sigma_W$:

$$R(W) = R_0 + S \exp[(W - M_R)^2 / 2\sigma_W^2] .$$

Table 8.1
Parameters and results of energy scans. The limits are at 95% C.L.

Energy range (GeV)	ΔE (MeV)	$\int L\,dt$ per energy point (nb^{-1})	Limit on $\Gamma_{ee}B_h$ (keV)	$\langle R_{had}\rangle$
29.90–31.46	20	24	<1.6	4.1 ± 0.2
33.00–36.72	20	43	<1.4	3.95 ± 0.08
39.79–46.78	30	60	<1.9	4.13 ± 0.08

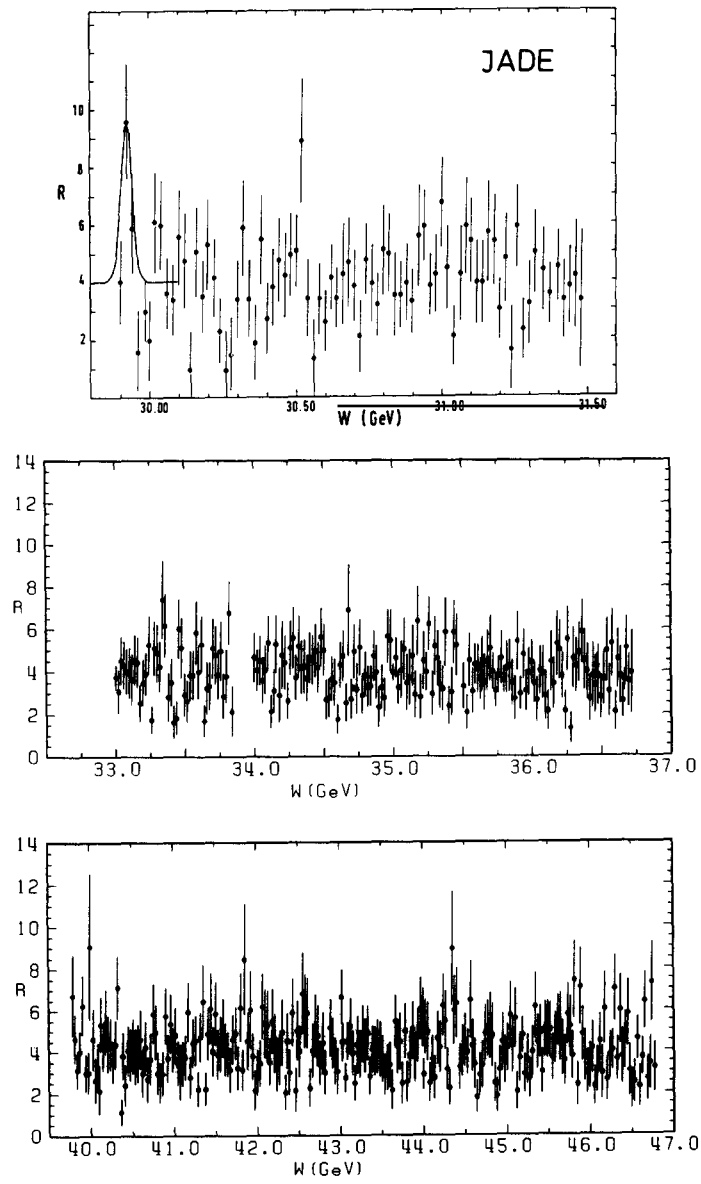

Fig. 8.1. The ratio $R_{had} = \sigma(e^+e^- \to \text{hadrons})/\sigma(e^+e^- \to \mu\mu)$ as a function of the centre-of-mass energy W for the three scan regions.

The integrated cross-section of a narrow Breit–Wigner resonance is related to the partial decay width of the resonance into two electrons and the hadronic branching fraction B_h by:

$$\Sigma = \int \sigma_R(W)\,dW = (6\pi^2/M_R^2)\cdot \Gamma_{ee}\cdot B_h\,.$$

Taking into account radiative corrections [190], one obtains at the 95% C.L. the upper limits on $\Gamma_{ee}B_h$ indicated in table 8.1. The width expected for a $t\bar{t}$ resonance is ~5 keV [191], and B_h is expected to be around 80%, so $t\bar{t}$ resonance production can be excluded. The production of a b′ of charge 1/3 can however not be excluded by this method due to its lower cross-section.

The production of a heavy quark would manifest itself also in an increased cross-section. The expected increase in R_{had} is 4/3 (1/3) for a quark of charge 2/3 (1/3). The threshold behaviour is believed to resemble a step function, due to QCD effects [77], rather than the $\beta(1-\beta^2)/2$ rise expected for the production of point-like spin 1/2 particles of velocity β. Using all data in the energy range $12 \le \sqrt{s} \le 46.78$ GeV the lower limits, at the 95% C.L., of the position of such a step-like threshold are 46.6 GeV and 43.78 GeV for charges 2/3 and 1/3 respectively.

8.2. Search for free quarks

A search for free quarks of charge 1/3 and 2/3 or other unknown particles with charges $Q = 1$, 4/3, 5/3 and 2 was carried out by examining the energy loss in the gas of the jet-chamber of observed particles. Multihadronic events and events with only two charged tracks were analysed, thus one is sensitive to stable (or sufficiently long-lived) particles with unusual ionisation losses [192].

The data from the extended multihadronic data set described in section 4.2 were used, i.e. multihadronic data which still contain a large fraction of two-photon interactions and some beam-gas contamination. In order to obtain a good measurement of dE/dx, tracks coming from the beam interaction point were selected which had at least 24 hits and which had a reduced momentum $p/Q > 0.2$ GeV.

The specific ionisation loss dE/dx was calculated for these tracks (truncated mean, see chapter 1) and compared with the expectations for the known particles. The expectations were parameterized following [193]. Data and expectations are shown in fig. 8.2 for positive particles as an example. Particles were considered as candidates for exotics if their ionisation was greater than 22 keV/cm or more than five standard deviations above that of known particles (the limits for positive particles are also indicated in fig. 8.2). 6 such highly ionising candidates were found, one with positive and five with negative charge. The five negative particles could be explained by track reconstruction errors. The positive candidate was an α particle which had by chance passed close to the interaction point. Particles with an abnormally low ionisation were accepted if their ionisation was more than six standard deviations below that of known particles. No candidate was found.

Limits on the production cross-sections were obtained by normalising to the integrated luminosity. The limits at the 90% C.L. for the normalised cross-sections $R_Q = \sigma(e^+e^- \to q\bar{q}X)/\sigma_0$, where σ_0 is the lowest order QED cross-section for muon pairs, are shown in fig. 8.3 for particles of charge 2/3, 1/3, 1 and 4/3. The limits for charges 5/3 and 2 are not shown, they are similar to those of charge 4/3. The momentum spectra were assumed to follow an exponential law. The limits for flat momentum spectra are similar. The upper limits for quarks of charges 2/3 and 1/3 are $\sim 10^{-2}$ for masses below 17 GeV.

A similar search was made for the exclusive pair-production of particles with fractional charge,

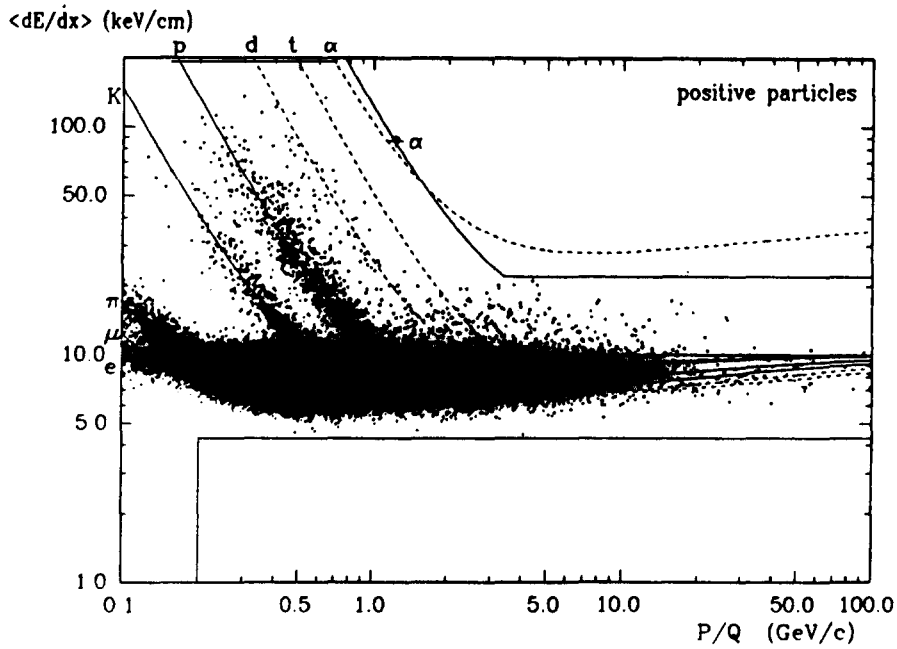

Fig. 8.2. dE/dx as a function of reduced particle momentum P/Q, where Q is the charge, for positive particles. The straight lines indicate the cuts used for the search of exotic particles.

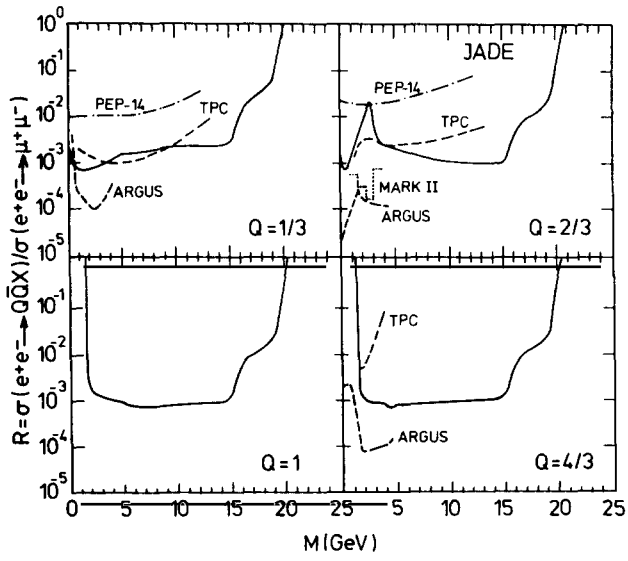

Fig. 8.3. Lower limit at 90% C.L. for the inclusive production of quarks and particles with charges 1 and 4/3 for a momentum spectrum $E\,d^3\sigma/dp^3 \sim \sigma_{tot}\exp(-3.5E)$.

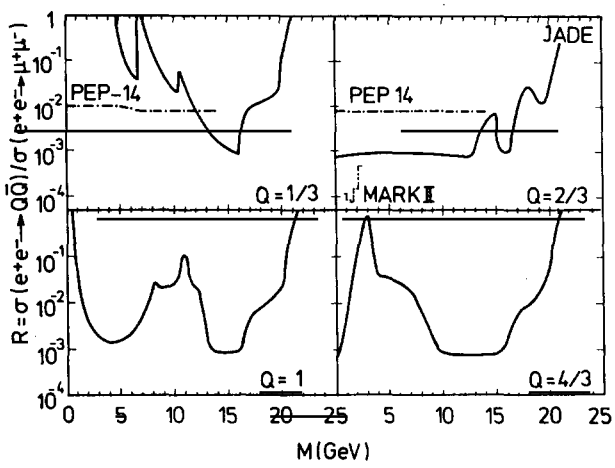

Fig. 8.4. Lower limit at 90% C.L. for the pair production of quarks and stable particle of charges 1 and 4/3.

$e^+e^- \to q\bar{q}$. The result is shown in fig. 8.4. The limits obtained by other experiments [194] are also shown in figs. 8.3 and 8.4.

8.3. Search for a heavy sequential lepton

The number of quark and lepton families could be larger than the presently known three. The present limit – derived from measurements at the $p\bar{p}$ collider – is ~10 at 90% C.L. if the neutrinos are light. The combined limit of e^+e^- experiments is 5 [196]. If a new heavy lepton existed, with a sufficiently low mass, it would be produced at PETRA. The cross-section for $e^+e^- \to L^+L^-$ is:

$$\sigma_{L^+L^-} = \sigma_0 \cdot \beta(3-\beta^2)/2 \qquad \text{where} \qquad \sigma_0 = 4\pi\alpha^2/3s \tag{8.29}$$

and β is the velocity of the lepton L. The decay would proceed via $W^\pm$ into the known leptons and quarks:

$$L \to \nu_L + W \qquad \text{and} \qquad W \to \underbrace{(ud), (cs)}_{\times 3}, (e\nu), (\mu\nu), (\tau\nu)\,.$$

The decay branching ratios were computed according to [75, 197], they are only independent of the lepton mass if $m_L > 14$ GeV. Due to the colour factor 3 the hadronic decays will dominate, about 45% of the L^+L^- pairs are expected to decay into two-hadron jets which are acoplanar because of the missing neutrinos. The other topology would be a lepton (e, μ or τ) accompanied by a jet (~15% per lepton species), while purely leptonic decays would be rare.

JADE has obtained limits on the production of heavy leptons L in three ways, for small and large masses and for a stable L [199]. Large L-masses – $m_L \gtrsim 14$ GeV – were excluded by searching for acoplanar jet events with a visible energy smaller than the centre-of-mass energy. Comparison with a Monte Carlo simulation of L production and decay led to a mass limit of $M_L > 22.7$ GeV at 95% C.L.

Masses below ~14 GeV were excluded by searching for acoplanar τ-like events, one isolated track opposite to a jet. Heavy leptons with masses from the τ mass up to 14 GeV could be excluded at the 95% C.L.

The third possibility considered was that the heavy leptons be stable. This would be the case if the associated neutrino ν_L were heavier than the lepton itself. Such a stable heavy lepton would be detected by its specific energy loss in the gas of the jet-chamber. The limits in fig. 8.4 for charge 1 are thus applicable and yield a limit of $M_L > 21.1$ GeV at 95% C.L.

Similar limits on the production of heavy leptons have also been obtained by MARK J [39, 198] and somewhat lower values were found by PLUTO and TASSO [200]. UA1 has given a lower mass limit of 41 GeV [196].

8.4. Search for a charged Higgs

In the standard model in its minimal version, the Higgs mechanism, invoked for the symmetry breaking, requires the existence of one Higgs doublet. As a consequence only one physical Higgs particle is expected; it is neutral and its coupling to e^+e^- is very small. In non-minimal theories, however, a richer Higgs structure could lead to the existence of charged Higgs particles $H^\pm$ [201] which could be pair-produced in e^+e^- annihilations. The charged Higgs would decay rapidly into heavy fermion pairs, either ($\tau\nu$) or (cs) or (cb). Experimentally the most promising signatures are acoplanar τ-pairs or acoplanar τ-jet events.

It turns out that this signature is also characteristic for other scalars, for example the scalar τ, technipions, or heavy axions [202]. The cross-section for the production of a pair of scalar particles is given in eq. (8.30); it is a factor 4 smaller than that for the production of fermions pairs, but the angular distribution ($\sim\sin^2\theta$) leads to a better acceptance than the $1+\cos^2\theta$ of fermions.

For the τ-pair search the selected τ sample was used (section 2.3.2). Additional cuts were applied in order to reduce contributions from radiative τ events: it was required that there be no isolated photon of more than 500 MeV and that the sum of the momenta of the tracks for each τ was larger than 2 GeV. The acoplanarity distribution of these events is shown in fig. 8.5 for $\sqrt{s} > 40$ GeV.

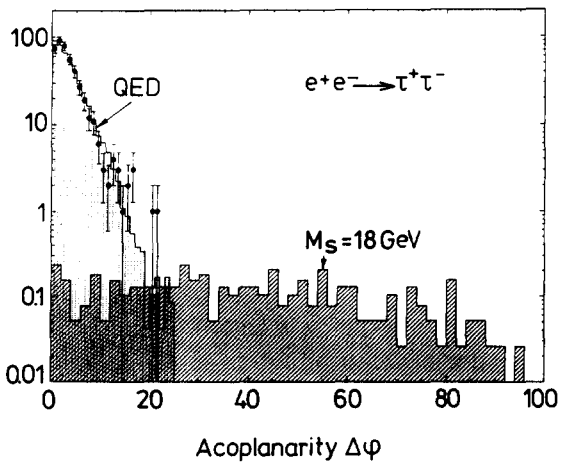

Fig. 8.5. Acoplanarity distribution for $e^+e^- \to \tau^+\tau^-$. The hatched histogram corresponds to the distribution for a scalar particle of 18 GeV.

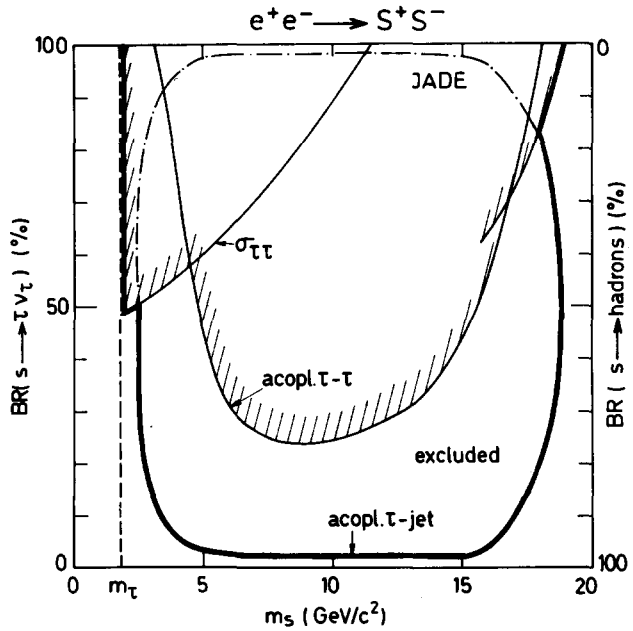

Fig. 8.6. Lower limits at 95% C.L. for the production of a charged scalar S decaying into τ's or hadrons.

The simulated acoplanarity distribution of the decay of scalar particles shows a different behaviour. As an example the distribution for $M(S) = 18$ GeV is superimposed on the data in fig. 8.5. By comparing the expected number of events above $\Delta\varphi > 30°$ to the observed number (0), an upper limit can be computed for the branching fraction $BR(S^{\pm} \to \tau\nu)$ as a function of the mass of the S. It is shown in fig. 8.6.

At low masses ($m(S) < 5$ GeV) the limit can be improved by using the total production cross-section for $e^+e^- \to \tau^+\tau^-$ (see fig. 8.6).

Limits were also set by searching for events which have a τ decay opposite to a hadron jet. The acoplanar event sample of one track opposite to a jet was used for this search (table 8.2). The resulting limits are also shown in fig. 8.6, where the branching ratios $BR(S \to \tau\nu)$ and $BR(S \to \text{hadrons} + \nu)$ were assumed to add up to 1 as expected.

As can be seen in the figure, the production of a scalar particle which decays into τ + massless particle or jet + massless particle can be excluded at the 95% C.L. in the range from the τ mass up to ~18 GeV [216]. Scalar particles have been searched for also by other experiments at PEP and PETRA recently. A summary of upper limits can be found in [185].

8.5. Search for a neutral Higgs: Monojets

Single jets with high transverse energy were observed by the UA1 Collaboration in events with large missing momentum [208]. A possible theoretical explanation for these was given by Glashow and Manohar [209] who suggested that they could be due to Z^0 decay into two neutral Higgs particles, h_1^0

Table 8.2
List of cuts for the search of new particles

Hadronic data sets
Selection from extended multihadronic data set
2 hemispheres are defined by a plane vertical to the thrust (th) axis
E_{vis} = visible energy; α = acollinearity, φ = azimuthal angle

Data set	Limits for	$\int L\,dt$	Track cuts	$E_{vis}/\sqrt{s}$	$\Delta\alpha$ or $\Delta\varphi$	Others
Lepton low mass	L	94	4–8; 1 track isolated by 90° and with $p > 2$ GeV; $\cos\theta$ (isol. tr.) < 0.77; E_{LG} (isol. tr.) $< 0.35\sqrt{s}$	>0.33; $p_{bal} < 0.4$		
Jet opposite to one track (acoplanar)[1]	L, $S^{\pm}$	94	N_{track} (one hemisph.) = 1; $\lvert\cos\theta_{th}\rvert < 0.65$	0.4–1	$\Delta\varphi > 40°(1 + \lvert\cos\theta_{th}\rvert)$	
Acopl. jets	$\tilde{q}$, $\tilde{Z}$, $\tilde{\chi}^{\pm}$, h_2^0	88	N_{track} (one hemisph.) $\neq 1$; $\lvert\cos\theta_{th}\rvert < 0.65$	0.4–1	$\Delta\varphi > 40°(1 + \lvert\cos\theta_{th}\rvert)$	
Single jet	$\tilde{Z}$	88	$\lvert\cos\theta_{th}\rvert < 0.65$; 0 tracks in backward hemisph.	$E_{back} < 1$ GeV		p_t(miss) > 7 GeV; cuts against escaping tracks
Spherical events	$\tilde{q}$, $\tilde{\chi}^{\pm}$	94	$\lvert\cos\theta_{th}\rvert > 0.65$	$E_{vis} > \sqrt{s}/2$	$S' > 0.7$ [2]	

[1] Acoplanarity between two unit vectors $\boldsymbol{u}_1$ and $\boldsymbol{u}_2$ is defined as ($\boldsymbol{z}$ is the unit vector pointing in the direction of the e^+-beam):

$$\cos\theta_{acop} = -(\boldsymbol{u}_1 \times \boldsymbol{z}) \cdot (\boldsymbol{u}_2 \times \boldsymbol{z}) / (|\boldsymbol{u}_1 \times \boldsymbol{z}| \cdot |\boldsymbol{u}_2 \times \boldsymbol{z}|) .$$

[2] Modified sphericity S': $S' = (3/2)(1 - Q_3')$, where Q_3' is the largest eigenvalue of the modified momentum tensor:

$$T'_{\alpha\beta} = \sum (p_{i\alpha} p_{i\beta} / |\boldsymbol{p}_i|) \Big/ \sum |\boldsymbol{p}_i| \quad (\alpha, \beta = x, y, z) .$$

The sums run over charged and neutral particles.

and h_2^0. One of the two is postulated to be long-lived and escapes the detector, while the other one is observed as an energetic jet. If the mass of the heavier one (we assume it to be h_2^0) is within the reach of PETRA, the process should be observable as the decay of a virtual Z^0 in fig. 8.7a. The cross-section comes out to be ~0.6 pb at $\sqrt{s} \sim 45$ GeV, if the masses are neglected [210]. The h_2^0 decay would either be directly into fermion pairs (fig. 8.7b) or into the lighter h_1^0 and fermion pairs (fig. 8.7c). The relative branching ratio is unknown. For our analysis [211] we used a fixed mass of 0.2 GeV for h_1^0, as it can only be long-lived at low masses, and kept $M(h_2^0)$ and the relative branching fraction r as free parameters, where $r = \Gamma(h_2^0 \to f\bar{f}) / \{\Gamma(h_2^0 \to f\bar{f}) + \Gamma(h_2^0 \to h_1^0 f\bar{f})\}$. The decay of h_2^0 leads to single-jet events if the h_2^0 mass is small, for larger masses the event topology will be two acoplanar jets (the selection criteria are in table 8.2). For masses below 2 GeV a special selection for low-multiplicity events was made. Comparing the data with the event simulation led to limits which exclude h_2^0 masses between 1 and 21 GeV almost independent of r, fig. 8.8.

Limits were also computed in a more model-independent way leaving the partial width ξ of $Z^0 \to h_1^0 h_2^0$ free (which is fixed in the Glashow–Manohar model) and also for the supersymmetric version of the model [210, 212]. These limits involve more parameters but lead to similar results [211].

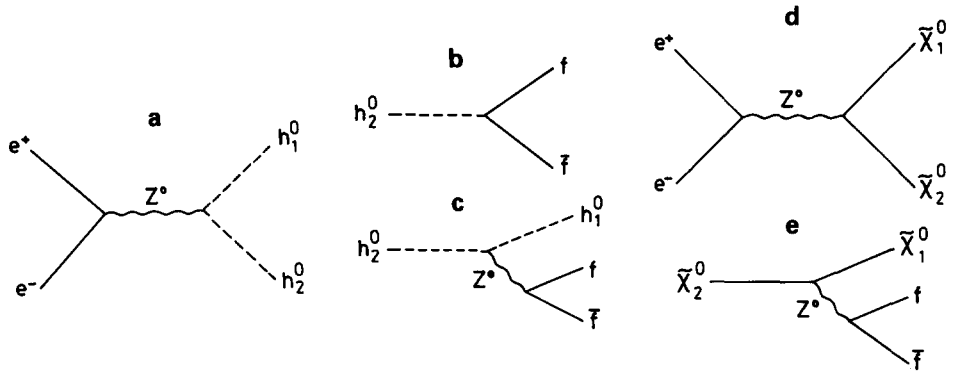

Fig. 8.7. Diagrams for pair production of two neutral Higgs (a) or Higgsino (d) and their decays (b, c and e).

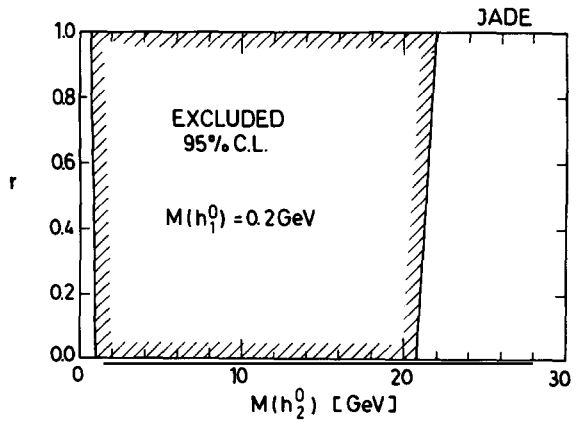

Fig. 8.8. Limits for the production of a neutral Higgs in the Glashow–Manohar model: Excluded region in the r–$M(h_2^0)$ plane at 95% C.L.

8.6. Search for supersymmetric particles

Although the standard model has been found to be very successful in describing present experimental results there are certain problems connected with it. Alternatives or extensions to the standard model have been looked for, among them supersymmetric theories. Supersymmetric theories are attractive because they provide solutions for some of the fundamental problems of the standard model. Furthermore gravity can be unified with the electroweak and strong forces in such theories.

In supersymmetric theories [205, 206] fermions and bosons are linked by a common symmetry, every particle has a supersymmetric partner, a "sparticle". Since the fermions and bosons already existing did not fit into this pattern of "particle" and "sparticle", new particles had to be postulated, partners of the usual particles which differ from them by half a unit of spin. The couplings of these new particles are well defined and therefore production cross-sections can be calculated. However the mass predictions of the different models depend on the symmetry breaking mechanism, which is not well defined. It is not even clear which is the lightest particle, candidates are the partners of the neutral gauge bosons, e.g. the photino ($\tilde{\gamma}$) or the partner of the neutrino, the sneutrino ($\tilde{\nu}$), possibly a gravitino or, in globally broken theories, a Goldstino. Due to these uncertainties in the mass scale, experimental searches for the supersymmetric partners of particles have to take into account many decay possibilities in order to acquire some degree of model independence.

Particles and sparticles are assigned opposite "R parity". Throughout the searches conservation of R parity is assumed, i.e. the supersymmetric particles are produced in pairs and the lightest supersymmetric particle is stable and it will always be at the end of a decay chain. It should also be noted that there is a supersymmetric partner for each chiral state of a particle, and these two need not have the same mass.

So far no experiment has found a superpartner of any particle, although searches have been performed in many reactions at almost all accelerators. In this chapter we will describe JADE's contribution to the search, which consists in ruling out the existence of $\tilde{\gamma}$, $\tilde{e}$, $\tilde{\mu}$, $\tilde{\tau}$, $\tilde{q}$, $\tilde{H}$, $\tilde{Z}$, $\tilde{W}$ in wide mass ranges. The searches have been described in detail in separate publications (except for the search for $\tilde{q}$) and we shall try to emphasize the idea behind the search rather than describe and justify the cuts in detail. These are, however, included in tables 8.2 and 8.3 for completeness. For a summary of the world data on searches for supersymmetric particles we refer to reports in recent conferences, e.g. S. Komamiya [185].

8.6.1. Scalar leptons

The production of selectron pairs, $\tilde{e}\bar{\tilde{e}}$, can proceed via the diagrams of fig. 8.9; for $\tilde{\mu}$ and $\tilde{\tau}$ only the first diagram contributes. In the $\tilde{\gamma}$ exchange diagram, the $\tilde{\gamma}$ can in general mix with a $\tilde{Z}$. This was not taken into account, implying $M(\tilde{Z}) \gg M(\tilde{\gamma})$. The differential cross-section for the production of a pair of

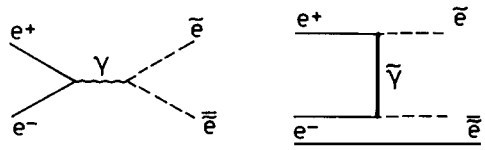

Fig. 8.9. Diagrams contributing to $e^+e^- \to \tilde{e}\bar{\tilde{e}}$.

Table 8.3
List of cuts for the search of new particles

Leptonic data sets						
Data set	Limits on	$\int L\,dt$	Track cuts	Energy and cluster cuts	$\Delta\alpha$ or $\Delta\varphi$	Others
Acopl. e^+e^-	$\tilde{e}, \tilde{\gamma}, \tilde{Z}, \tilde{\chi}^{\pm}$	87.2	2–10 tracks, connected to big clusters; no track outside 10° of clusters	2 clusters with $E > \sqrt{s}/8$; $\lvert\cos\theta\rvert < 0.75$; residual energy < 1 GeV	$\Delta\alpha > 10°$; $\Delta\varphi > 40°$	$\lvert$Miss. mass$^2\rvert > 70$ GeV^2 or $\lvert\cos\theta$ (miss. mom.)$\rvert < 0.7$; reject escaping photons[1]
Acopl. $\mu^+\mu^-$	$\tilde{\mu}, \tilde{\gamma}, \tilde{Z}, \tilde{\chi}^{\pm}$	52.5	$=2$; $p_1 > 3.5$ GeV, $p_2 > 0.2$ GeV; one identified as muon	En. behind both tracks < 2.5 GeV; No additional γ above 0.5 GeV	$20 < \Delta\varphi < 150°$	$p_{\text{miss. mom}}$ in fid. region; p_t of miss. mom. > 4 GeV
Acopl. $\gamma\gamma$	$\tilde{\gamma}^u, \tilde{e}$	79.1	No tracks	2 photons $E > 0.125\sqrt{s}$; $\lvert\cos\theta_\gamma\rvert < 0.76$; Residual energy < 0.5 GeV	$\Delta\varphi > 10°$	
Copl. $\gamma\gamma$ of reduced energy	$\tilde{\gamma}^u, \tilde{e}$	79.1	No tracks	2 photons $E > 0.125\sqrt{s}$; $\lvert\cos\theta_\gamma\rvert < 0.76$; residual energy < 0.5 GeV; $E_\gamma(1)\cdot E_\gamma(2) \le 0.15\,s$	$\Delta\alpha < 10°$	Reject cosmic rays[2]; missing energy $< 0.1\sqrt{s}$ or $\lvert\cos\theta$ (miss. mom.)$\rvert < 0.78$
$\mu^+\mu^-\gamma\gamma$	$\tilde{\mu}, \tilde{\gamma}^u$	94.9	Exactly 2 with $p > 1$ GeV consistent with muons; angles $(\mu\gamma) > 15°$; one track has an angle >60° to vector sum of $\mu^+\mu^-\gamma\gamma$	2 photons $E_1 > 1$ GeV, $E_2 > 0.5$ GeV; no additional γ above 0.5 GeV; energy behind each track ≤ 1.25 GeV		$0.25 \le E_{vis}/\sqrt{s} \le 0.8$; p_t of miss. mom. > 3.5 GeV
Single electron	$\tilde{e}, \tilde{\gamma}, \tilde{Z}$	72.8	1–10, $p > 0.2$ GeV, one connected to big cluster; no track outside 10° of cluster; $p_t = E_\gamma \sin\theta_\gamma > 0.325\sqrt{s}$	The biggest cluster has $E > 0.125\sqrt{s}$; $\lvert\cos\theta_{cls}\rvert < 0.70$; residual energy < 1 GeV		$\lvert\varphi - 90°(270°)\rvert > 25°$; no muon-hits opposite to electron
Single photons	$\tilde{e}, \tilde{\gamma}^u$	46.2	No tracks	The biggest cluster has $E_\gamma \sin\theta_\gamma > 0.2\sqrt{s}$; $\lvert\cos\theta_\gamma\rvert < 0.70$; residual energy < 500 MeV		Reject cosmic rays[2]

[1] Rejection of escaping photons: Photons that went through cracks in the lead-glass often leave signals in the first layers of the muon chambers.

[2] Rejection of cosmic rays: Cosmic rays which do not pass through the jet-chamber can be recognised by the muon filter, the cluster shape in the lead-glass and by the TOF measurement in the lead-glass.

Table 8.4
Limits at 95% C.L. for the production of scalar leptons and photinos

Stable massless $\tilde{\gamma}$			
	$m_{\tilde{\ell}}$ excluded with 95% C.L.		
Production/Decay	$m_{\tilde{\ell}_L} \neq m_{\tilde{\ell}_R}$	$m_{\tilde{\ell}_L} = m_{\tilde{\ell}_R}$	Signature
$e^+e^- \to \tilde{e}\tilde{e}$ $\tilde{e} \to e\tilde{\gamma}$	<21.8	<22	acoplanar e^+e^-
$e^+e^- \to \gamma\tilde{\gamma}\tilde{\gamma}$	<15.5	<11	single photon
$e^+e^- \to (e)\tilde{e}\tilde{\gamma}$	<25		single electron
$e^+e^- \to \tilde{\mu}\tilde{\mu}$ $\tilde{\mu} \to \mu\tilde{\gamma}$	<20.3	<21.0	acoplanar muons
$e^+e^- \to \tilde{\gamma}\tilde{\gamma}$ $\tilde{\gamma} \to \tau\gamma$	<18.0		acoplanar taus
stable sleptons	<20		Bhabha, μ pair cross-section; heavy pairs
	Massive $\tilde{\gamma} \to \gamma\tilde{G}$		
$e^+e^- \to \tilde{\mu}\tilde{\mu}$ $\tilde{\mu} \to \mu\tilde{\gamma}$	<19 (for $m_{\tilde{\gamma}} = 0$)		$\mu^+\mu^-\gamma\gamma$ + miss. energy $\tilde{\gamma}$ short-lived
$e^+e^- \to \tilde{\gamma}\tilde{\gamma}$	$0.08 < m_{\tilde{\gamma}} < 18$ $d = (100\,\mathrm{GeV})^2$, $m_{\tilde{e}} = 40$		acoplanar photons almost coplanar photons
	$m_{\tilde{e}} < 100$ for $m_{\tilde{\gamma}} \lesssim 15$		one photon

sleptons, $\tilde{\ell}\bar{\tilde{\ell}}$, is given by [203]:

$$\frac{d\sigma}{d(\cos\theta)} = \frac{\pi\alpha^2}{8s}\beta^3\sin^2\theta\left[1+\left[1-\frac{4K}{1-2\beta\cos\theta+\beta^2+\mu^2}\right]^2\right], \qquad K = \begin{cases} 0 \text{ for } \tilde{\mu}, \tilde{\tau} \\ 1 \text{ for } \tilde{e} \end{cases} \tag{8.30}$$

where $\mu = 2M(\tilde{\gamma})/\sqrt{s}$ and β is the velocity of the $\tilde{\ell}$. The cross-section refers to the case, in which only one $\tilde{e}$, the $\tilde{e}_L$ or the $\tilde{e}_R$, are in the available mass range. For the mass degenerate case additional terms have to be added taking into account the production of $\tilde{e}_R\bar{\tilde{e}}_L$ and of $\tilde{e}_L\bar{\tilde{e}}_R$ [203c].

For the experimental search of scalar leptons it is relevant whether the mass of the photino $M(\tilde{\gamma})$ is larger or smaller than the mass of the slepton. In the first case the scalar lepton could be the lightest supersymmetric particle and thus be stable. If the photino mass is lower than the slepton mass the slepton will decay into a photino, which can be either stable or again decay into photon and gravitino or Goldstino. We shall not consider weak decays of sleptons, which might be important if the electromagnetic decay into lepton and photino is forbidden. A summary of limits for sleptons is given in table 8.4.

Stable scalar leptons, $\tilde{e}$, $\tilde{\mu}$ or $\tilde{\tau}$

If any of the scalar leptons should turn out to be stable or very long-lived, its signature in the detector would be either that of an electron or of a muon, depending on its mass. For very light masses, of the order of the electron mass, electromagnetic showering is possible and the process would contribute to Bhabha scattering. Therefore this case can be excluded since the measured Bhabha cross-section agrees with the QED expectation.

If the $\tilde{\ell}$ is not as light as an electron but has a mass of the order of the muon mass, it would be experimentally indistinguishable from muons and would contribute to the muon pair data. The measured differential cross-section for μ pairs, which is in agreement with expectations led to the limits

$M(\tilde{e}) > 9.4$ GeV and $M(\tilde{\mu}) > 13$ GeV, the difference being due to the different cross-sections (eq. 8.30).

For still larger masses the standard muon-pair sample is no longer relevant because it was obtained using the fact that muons travel at the speed of light. A special selection allowing for slow muon-like particles was made using TOF and dE/dx information. The resulting limits are shown as curves (C) in fig. 8.10a and b for selectrons and in 8.13 for smuons. Both the partners of electrons and muons or taus, have masses above ~20 GeV at 95% C.L. if they are stable.

Unstable selectrons, stable photino

$e^+e^- \to \tilde{e}\bar{\tilde{e}}$. If the mass of the $\tilde{e}$ is larger than the photino mass it will decay into $e + \tilde{\gamma}$. In this section the photino will be assumed to be stable; limits on unstable photinos will be discussed later. The cross-section for photino interactions with matter is negligibly small. Thus the signature of the events is an acoplanar electron-pair and missing energy. The cuts to select such events are given in table 8.3. The main background comes from $e^+e^-\gamma$ and $e^+e^-\gamma\gamma$ final states where the photons are lost in the beam pipe. The acoplanarity distribution of these background processes is however peaked at 0° in contrast to the expectation from $\tilde{e}\bar{\tilde{e}}$ decays. The limit at 95% C.L. is shown in fig. 8.10a as the curve labelled (A) for the case that only one selectron, $\tilde{e}_L$ or $\tilde{e}_R$, is in the available mass range. The results for the mass-degenerate case are shown in fig. 8.10b.

$e^+e^- \to \gamma\tilde{\gamma}\tilde{\gamma}$. Another method of looking for selectrons is an indirect one, whereby the combination of small selectron photino masses can be excluded. The reaction $e^+e^- \to \gamma\tilde{\gamma}\tilde{\gamma}$ goes via $\tilde{e}$ exchange as shown in fig. 8.11. For the case of a stable photino the event signature is a single photon. The selection cuts for this process can be found in table 8.3. Its cross-section has been derived in [204]. The resulting limit at 95% C.L. is shown in fig. 8.10 as curve B.

$e^+e^- \to e\tilde{e}\tilde{\gamma} \to e + \cdots$. For low photino-masses the limit on the selectron mass can be pushed beyond the beam energy by searching for it in the processes shown in fig. 8.12, namely radiation of a single photon by one of the initial electrons and production of $\tilde{e}\tilde{\gamma}$ after its re-absorption. The electron which has radiated the photon usually stays in the beam pipe and only the decay electron of the $\tilde{e}$ is visible. All candidates for single-electron events (details of the selection in table 8.3) were found to have a

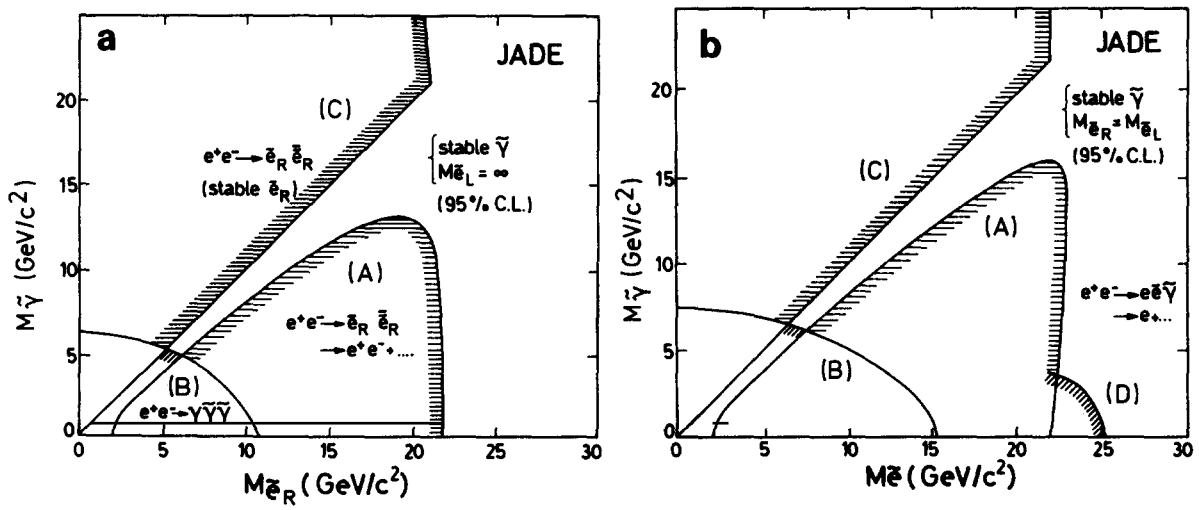

Fig. 8.10. Lower limits at 95% C.L. for the production of supersymmetric partners of electrons assuming (a) $m(\tilde{e}_L) \gg m(\tilde{e}_R)$; (b) $m(\tilde{e}_L) = m(\tilde{e}_R)$. See text for explanation of curves.

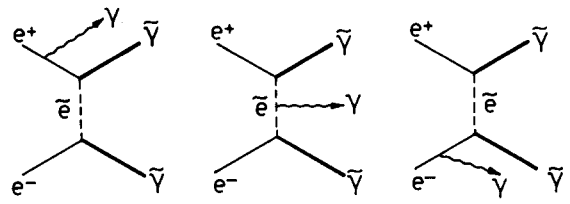

Fig. 8.11. Diagrams contributing to $e^+e^- \to \gamma\tilde{\gamma}\tilde{\gamma}$.

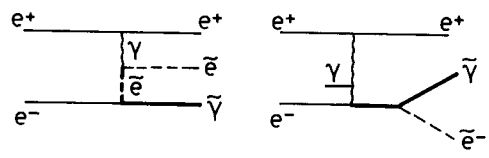

Fig. 8.12. Diagrams contributing to $e^+e^- \to e + \cdots$.

$p_T < 0.65$ GeV with respect to the beam direction and could be explained as remnants of $e^+e^-\gamma$ final states where the photon and one of the electrons escapes detection. The expected p_T distribution for decays of high-mass selectrons extends to higher values. The cross-section was calculated according to [213] and the resulting limit at 95% C.L. excludes selectron masses up to 25 GeV (curve D in fig. 8.10).

Unstable smuons

Stable photinos: $e^+e^- \to \tilde{\mu}\tilde{\mu} \to \mu^+\mu^- + \tilde{\gamma}\tilde{\gamma}$. Here we shall again assume that only one smuon lies within the available energy range. If the $\tilde{\mu}$ decays into $\mu + \tilde{\gamma}$ and the photino is stable and non-interacting the experimental signature is an acoplanar muon pair and missing energy. The main background, as in the search for acoplanar electrons, comes from two-photon scattering and $\mu^+\mu^-\gamma$ and $\mu^+\mu^-\gamma\gamma$ final states where the photons escape detection. The $\mu^+\mu^-\gamma$ and $\mu^+\mu^-\gamma\gamma$ events were removed by requiring the missing momentum vector of the event to be within the fiducial range of the detector; the two-photon process $e^+e^- \to e^+e^-\mu^+\mu^-$ was removed by requiring the missing transverse momentum to be large (table 8.3).

The production and decay was simulated using Monte Carlo methods, taking into account initial state radiation [82]. The mass range which can be excluded is shown in fig. 8.13 as curve A. This

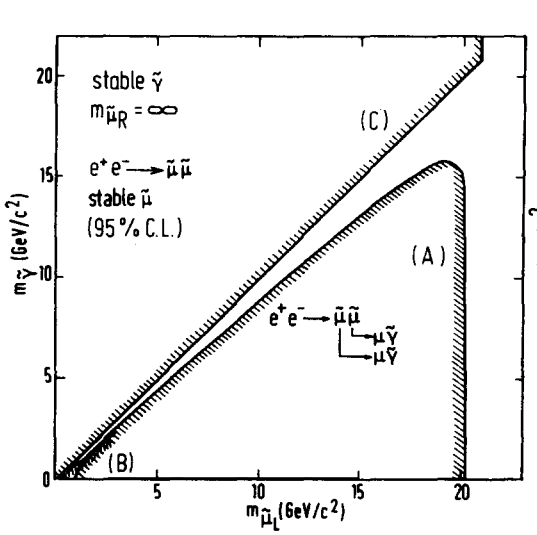

Fig. 8.13. Lower limits at 95% C.L. for the production of supersymmetric partners of muons assuming $m(\tilde{\mu}_L) \gg m(\tilde{\mu}_R)$ and assuming a decay into stable photinos.

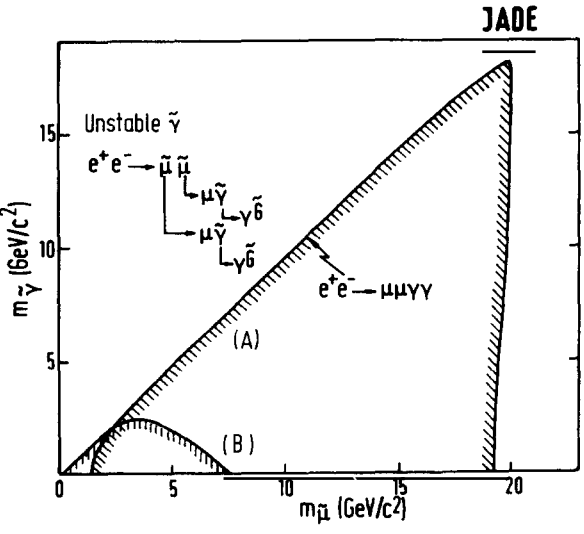

Fig. 8.14. Lower limits at 95% C.L. for the production of the supersymmetric partners of muons assuming a decay into unstable photinos.

method fails at small $\tilde{\mu}$ masses. These were excluded by a detailed investigation of the acoplanarity distribution of muon pairs at low values of acoplanarity. The limit at 95% C.L. is also shown in fig. 8.13 (curve B).

Unstable photino. An unstable massive $\tilde{\gamma}$ will decay: $\tilde{\gamma} \rightarrow \gamma\tilde{G}$, where $\tilde{G}$ is a gravitino or goldstino which is assumed to have a negligible mass and to be non-interacting. Pair production of smuons will then lead to a final state:

$$e^+e^- \rightarrow \tilde{\mu}\tilde{\mu} \rightarrow \mu\mu\gamma\gamma\tilde{G}\tilde{G}$$

where only the two muons and the two photons are observable. Thus the event selection was based on the $\mu^+\mu^-\gamma\gamma$ events similar to those which have already been used for QED tests. In contrast to QED events, however, a large missing transverse momentum was required and a visible energy below the centre-of-mass energy (for details see table 8.3). In this way the background from 2-photon processes and $\mu^+\mu^-\gamma\gamma$ final states could be removed. The mass limits derived at 95% C.L. are shown in fig. 8.14, curve A.

Due to the requirement that the photons have to be separated from the muons this search becomes ineffective for low $\tilde{\mu}$ masses. For this case muons with overlapping photons were searched for in Bhabha events with reduced shower energy. No such events were found, leading to the limit displayed as curve B in fig. 8.14.

Unstable massive photino

In the previous section, the analysis of $\tilde{\mu} \rightarrow \mu + \tilde{\gamma}$ with subsequent decay of the photino, the photino life-time was assumed to be so short that it will decay in the detector, i.e. $\gamma\tau \leq$ a few ns. This need not be the case. The life-time of a massive photino is given by [214].

$$\tau = 8\pi d^2/m_{\tilde{\gamma}}^5$$

where d is the scale parameter of supersymmetry breaking and has the dimension of $(\text{mass})^2$.

The cross-section for pair production of photinos via the exchange of a selectron, is given by [215]:

$$\frac{d\sigma}{dx} = \tfrac{1}{4}\pi\alpha^2 s\beta^3 \frac{k^2(1+x^2) - s(2k - m_{\tilde{\gamma}}^2 - s/4)x^2 + s^2\beta^2x^4/4}{(k^2 - s^2\beta^2x^2/4)^2}$$

where $k = M(\tilde{e})^2 - M(\tilde{\gamma})^2 + s/2$, β is the velocity of the photino and $x = \cos\theta_{\tilde{\gamma}}$. This cross-section is for the exchange of one $\tilde{e}$, if both selectrons can contribute it has to be multiplied by 2.

Three event signatures have been studied to derive limits on the photino mass:

1. Heavy photinos will have a short life-time and will appear as acoplanar photon pairs in the detector.

2. Light photinos with a life-time short enough that both can decay in the detector, $\gamma\tau$ of a few ns, will lead to nearly coplanar photon pairs which have, however, less energy than the beam energy and their energy will in general be unbalanced.

3. Light photinos which have such a long life-time that in most cases only one has a chance to decay in the detector, i.e. $\gamma\tau$ of the order of a few ns, will lead to events with one photon and missing transverse momentum.

The main background encountered in the search for such events (details are again in table 8.3) was

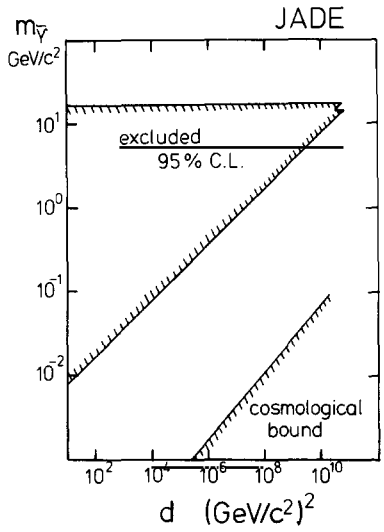

Fig. 8.15. Limits at 95% C.L. for the production of unstable massive photinos as a function of the scale parameter d ($M(\tilde{e}) = 40$ GeV).

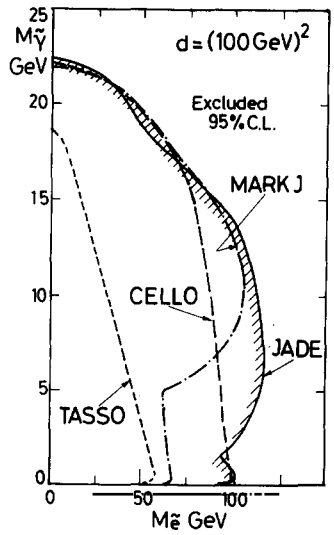

Fig. 8.16. Excluded region in the $M(\tilde{\gamma})$, $M(\tilde{e})$ plane for unstable $\tilde{\gamma}$ for JADE and other experiments ($d = 100\,\text{GeV}^2$ assumed).

from $e^+e^- \to \gamma\gamma\gamma$. The mass limits were computed assuming mass degeneracy for $\tilde{e}_L$ and $\tilde{e}_R$. For $M(\tilde{e}) = 40$ GeV the limits obtained for the photino mass as a function of the scale parameter d are shown in fig. 8.15. Also shown is a limit from cosmological studies [214]. For fixed $d = (100\,\text{GeV})^2$ the limits are shown in the $m_{\tilde{\gamma}}$, $m_{\tilde{e}}$ plane (fig. 8.16). Note that photino masses near 0 cannot be excluded since the detection efficiency drops to 0.

8.6.2. Scalar quarks

The supersymmetric partners of the quark are scalar colour triplets. As in the case of the leptons there are two squarks for each quark flavour, the partners of the left-handed and the right-handed quarks. Squarks can be pair-produced via a photon or Z^0 with a cross-section essentially as in (8.30). A factor $3Q_{\tilde{q}}^2$ takes into account colour and electrical charge:

$$d\sigma/d\Omega = (3\alpha^2/8s)Q^2\beta^3 \sin^2\theta\,. \tag{8.31}$$

The $\tilde{q}$ has the following decay possibilities, if they are kinematically allowed:

1. Decay by *strong* interaction into $\tilde{q} \to q\tilde{g}$ and subsequent decay of $\tilde{g} \to q'\bar{q}'\tilde{\gamma}$ (fig. 8.17b);
2. Decay by *electromagnetic* interaction $\tilde{q} \to q\tilde{\gamma}$ (fig. 8.17c);
3. Decay by *weak* interaction $\tilde{q} \to \ell q'\tilde{\nu}$ via $\tilde{W}$, where the ℓ can be either e, μ or τ (fig. 8.17d) or $\tilde{q} \to \nu\tilde{\nu}q$ via $\tilde{Z}$ (fig. 8.17e);
4. $\tilde{q}$ is *stable* or very long-lived.

The above list is ordered according to the importance of the decay: if the gluino is so light that the strong decay 1. is possible, this will be the dominant decay. If the gluino is heavier than the $\tilde{q}$ the electromagnetic decay 2. will dominate. Only if the gluino and photino are heavier than the $\tilde{q}$ will the weak decays 3. play a role. Finally the $\tilde{q}$ could be stable if all the above decay modes are forbidden. The two-body decays $\tilde{q} \to q'\tilde{W}$ or $q'\tilde{Z}$ can be excluded because of the mass limits on the $\tilde{W}$ and $\tilde{Z}$ which will be discussed in the next section.

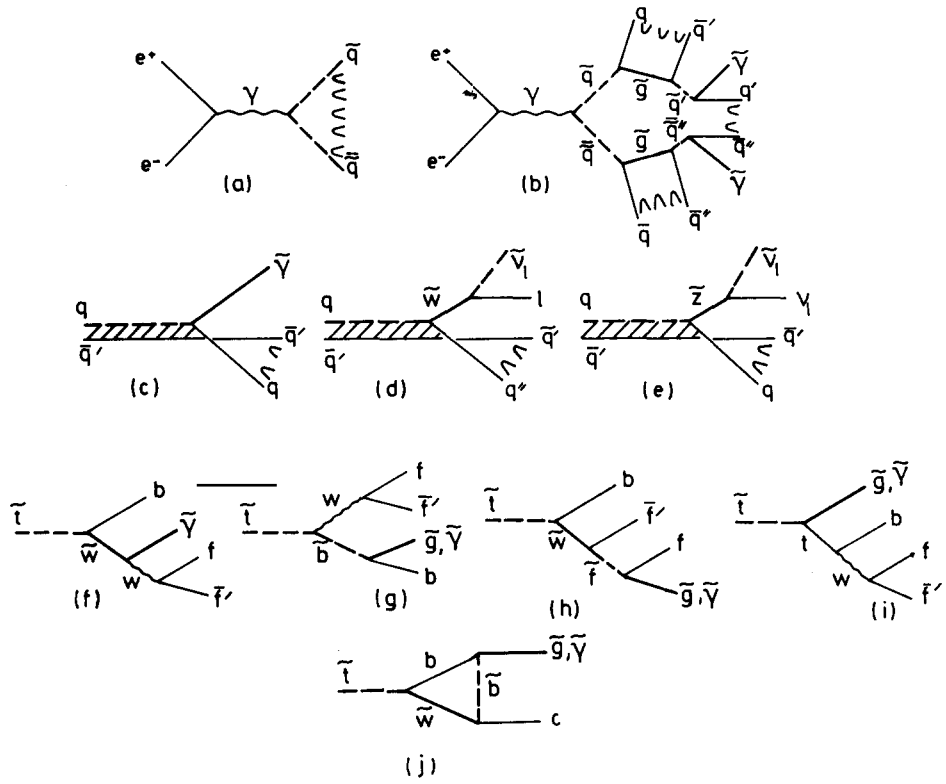

Fig. 8.17. Diagrams contributing to production and decay of scalar quarks $\tilde{q}$.

JADE has investigated all four $\tilde{q}$-decay possibilities. The production and decay were simulated for charge 2/3 squarks with Monte Carlo techniques. For the fragmentation of quarks the Lund string model was used. In the decay $\tilde{q} \rightarrow q\tilde{g}$ the fragmentation was assumed to take place after the decay of the scalar particles, although the time scales of decay and fragmentation may be comparable. The limits obtained will however be conservative because, due to this assumption, the photinos at the end of the $\tilde{q}$ decay-chain carry away more energy. The photino was assumed to be stable and its mass was assumed to be $M(\tilde{\gamma}) = \frac{1}{6}M(\tilde{g})$.

On the other hand, in the decay $\tilde{q} \rightarrow q\tilde{\gamma}$ and the weak decays of the $\tilde{q}$, fragmentation was assumed to occur before the decay. The fragmentation of squarks was parameterized in analogy with the normal quarks: the $\tilde{q}$ picks up a $\overline{q'}$ from the sea and forms an R-hadron. R-baryon formation was neglected. The fragmentation function was parameterized in the form proposed by Peterson et al. [100] in analogy to c- and b-quarks.[1] In the rest frame of the R-hadron the $\tilde{q}$ decays into $q\tilde{\gamma}$ and strings between q and the spectator q' are fragmented (fig. 8.17c).

In the case of stable or long-lived scalar quarks stable R-hadrons are formed which can be charged or neutral. The relative probability of charged and neutral R-hadron production is unknown and was treated as a free parameter η. If one or two charged R-hadrons are formed in the final state they would, due to their high mass, show higher ionization losses in the gas of the jet-chamber than ordinary

[1] The parameter ε was scaled with the square of the masses: $\varepsilon_{\tilde{q}} = \varepsilon_c(M_c/M_{\tilde{q}})^2$.

hadrons. If only neutral R-hadrons are produced the event would have a large missing transverse momentum. As a result, stable scalar quarks can be excluded up to ~19 GeV nearly independent of η.

The event signatures expected for the four decay modes are given in table 8.5 together with the data from which the mass limit was derived. The range of excluded squark masses is given for equal left and right masses (cross-section multiplied by 2) and also for the case that only one $\tilde{q}$ is within the experimental reach. (The detailed selection cuts for the event samples used are summarized in table 8.2.)

The above limits were derived for the scalar partners of the known "low mass" quarks. The top-quark has a mass $M(t) > 23$ GeV (section 8.1); nevertheless there are models where one of its scalar partners could be the lightest scalar quark [217]. The decay $\tilde{t} \to t\tilde{\gamma}$ or $t\tilde{g}$ is then not possible, the $\tilde{t}$ would decay via processes of higher order as in fig. 8.17f–j. Recent studies [218] have shown that fig. 8.17j: $\tilde{t} \to c\tilde{\gamma}$ or $c\tilde{g}$ will dominate if the $\tilde{W}$ mass is not much higher than 100 GeV. The probabilities for observation will be similar to those for the decays $\tilde{u} \to u\tilde{\gamma}$ or $u\tilde{g}$ and mass limits can be obtained. These are also given in table 8.5.

8.6.3. Gauginos

The supersymmetric partners of the gauge bosons and of the Higgs have spin 1/2 and the appropriate charge states can in general mix. There will be a charged supersymmetric gaugino – the chargino $\tilde{\chi}^{\pm}$ – which is the mass eigenstate of the mixture of $\tilde{W}^{\pm}$ and $H^{\pm}$, and a neutral supersymmetric state – the neutralino – which is the mass eigenstate of the mixture of $\tilde{\gamma}$, $\tilde{Z}$ and H^0. In some models the mass of the gauginos is predicted to be below that of the W- and Z-bosons [219] which made a search at PETRA energies worth while.

Table 8.5
Excluded mass regions for $\tilde{q}$ with 95% C.L. by JADE, assuming charge 2/3. The parameter η is the production probability for charged stable R-hadrons in the fragmentation of a stable $\tilde{q}$

	$m_{\tilde{q}}$ excluded with 95% C.L.			
Decay	$m_{\tilde{q}_L} = m_{\tilde{q}_R}$	$m_{\tilde{q}_L} \ll m_{\tilde{q}_R}$	Conditions	Signature
$\tilde{q} \to q\tilde{g}$	<19.2 GeV	11.3–17.8 GeV	$m_{\tilde{g}} = 3$ GeV $m_{\tilde{\gamma}} = 0.5$ GeV	
	<20.0 GeV		$m_{\tilde{g}} = 10$ GeV $m_{\tilde{\gamma}} = 1.7$ GeV	spherical events R-measurement
$\tilde{t} \to c\tilde{g}$		12–17.7 GeV	$m_{\tilde{g}} = 3$ GeV $m_{\tilde{\gamma}} = 0.5$ GeV	
$\tilde{q} \to q\tilde{\gamma}$	<21.4 GeV	3.2–21.0 GeV	$m_{\tilde{\gamma}} < 10$ GeV	
$\tilde{t} \to c\tilde{\gamma}$		3.8–20.0 GeV	$m_{\tilde{\gamma}} = 0$ GeV	acoplanar jets R-measurement
		11.2–20 GeV	$m_{\tilde{\gamma}} = 10$ GeV	
$\tilde{q} \to q'\tilde{\nu}\ell$ $\tilde{q} \to q\tilde{\nu}\nu$	<20.8 GeV	5.6–20.0 GeV	$m_{\tilde{Z}} = m_{\tilde{W}} \approx m_W$ $m_{\tilde{\nu}} = 1.0$ GeV	acoplanar jets R-measurement
stable $\tilde{q}$	<19.0 GeV	2.0–19.0 GeV	$\eta = 0.5$	events with heavy stable particles
	<15.0 GeV	2.0–15.0 GeV	$0 \le \eta \le 1$	events with large missing p_t

Search for zinos

A possible production process for zinos is via fig. 8.18a, namely $e^+e^- \to \tilde{Z}\tilde{\gamma}$ with the exchange of a selectron. Since the photino mass is believed to be small the threshold for this process is probably lower than that for $\tilde{Z}$-pair production. The cross-section was calculated by Reya [220]; we used the assumption that $M(\tilde{e}_L) = M(\tilde{e}_R)$, in which case the cross-section for small $\tilde{Z}$ and $\tilde{\gamma}$ masses is in the range of 0.1–40 pb if the selectron mass is below ~100 GeV. The $\tilde{Z}$ decays into a fermion pair plus $\tilde{\gamma}$ (fig. 8.18b–d) or into $q\bar{q}\tilde{g}$ (fig. 8.18e). The latter decay could be dominant if all $\tilde{\ell}$ and $\tilde{q}$ masses turn out to be similar. The decay matrix element was calculated by Reiter et al. [221]. For the fragmentation of quarks the Lund string model was used with parameters which were optimized for QCD studies (section 5.2). We have studied the following decay modes:

1. $\tilde{Z} \to e^+e^-\tilde{\gamma}$, fig. 8.18b: The acoplanar e^+e^- sample was used to obtain limits at high $\tilde{Z}$ masses and the single electron sample for low masses. The mass limits were extracted with $M(\tilde{Z})$, $M(\tilde{e})$ and $M(\tilde{\gamma})$ as free parameters. In principal the branching fraction into $e^+e^-\tilde{\gamma}$ can be calculated but it depends on the masses of all decay particles, therefore the branching ratio was taken to be a free parameter as well. The limits for three values of the branching ratio and for two photino masses are shown in fig. 8.19a in the $M(\tilde{Z})$, $M(\tilde{e})$ plane. For small photino masses and branching ratios above 10% $\tilde{Z}$ masses below ~28 GeV are ruled out, if the $\tilde{e}$ mass is less than ~40 GeV.

2. $\tilde{Z} \to \mu^+\mu^-\tilde{\gamma}$, fig. 8.18c: The mass limits were obtained using the acoplanar muon sample. They are shown in fig. 8.19b.

3. $\tilde{Z} \to q\bar{q}\tilde{\gamma}$ or $q\bar{q}\tilde{g}$, fig. 8.18d, e: For low $\tilde{Z}$-masses one expects an event topology which has a single jet opposite to missing energy, because the $q\bar{q}$ from the $\tilde{Z}$ decay merge into one jet. For higher $\tilde{Z}$ masses the two jets will separate but due to the unobserved photinos the event will be acoplanar. The limits were obtained from two event-samples, the single-jet events and the acoplanar jet-sample. The limits are shown in fig. 8.19c for $q\bar{q}\tilde{\gamma}$ and in fig. 8.19d for $q\bar{q}\tilde{g}$.

Due to the complicated decay possibilities of the $\tilde{Z}$ there are several free parameters involved in calculating production limits. Making additional assumptions one can be more specific. If, for example, one makes assumptions about the masses of the supersymmetric particles, one can calculate the decay branching ratios of the $\tilde{Z}$. We calculated limits for two sets of assumptions:

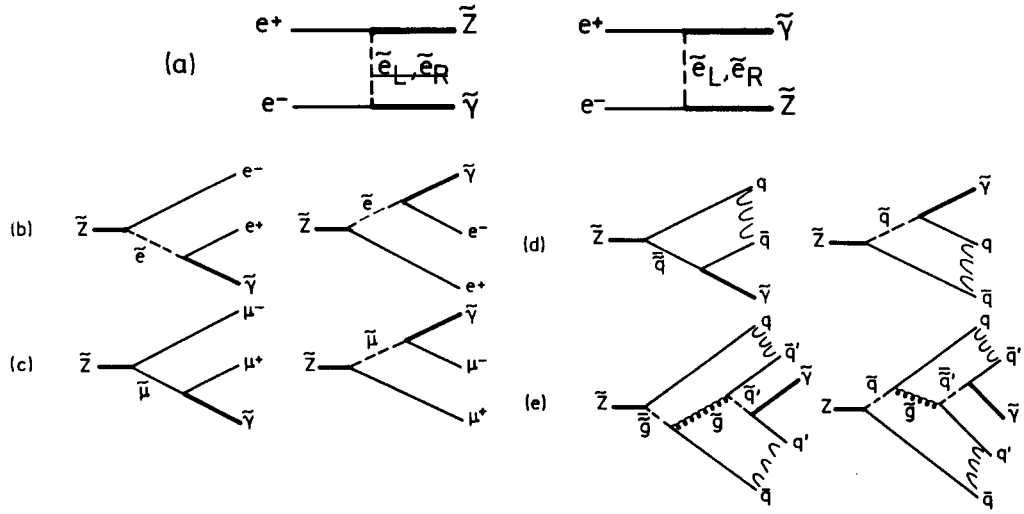

Fig. 8.18. Diagrams contributing to production and decay of $\tilde{Z}$.

1. $M(\tilde{\ell}) = M(\tilde{\nu}) = M(\tilde{g})$; $M(\tilde{\gamma}) = 0$ and $M(\tilde{g}) > M(\tilde{Z})$. The latter condition suppresses the decay into $q\bar{q}\tilde{g}$. The resulting limits are shown in fig. 8.19e.

2. $M(\tilde{g}) = 3$ GeV: in this case the $q\bar{q}\tilde{g}$ channel dominates and the limit is shown in fig. 8.19f.

In such well-defined scenarios, zino masses up to ~30 GeV can be excluded if $\tilde{e}$ masses are not larger than 50 GeV.

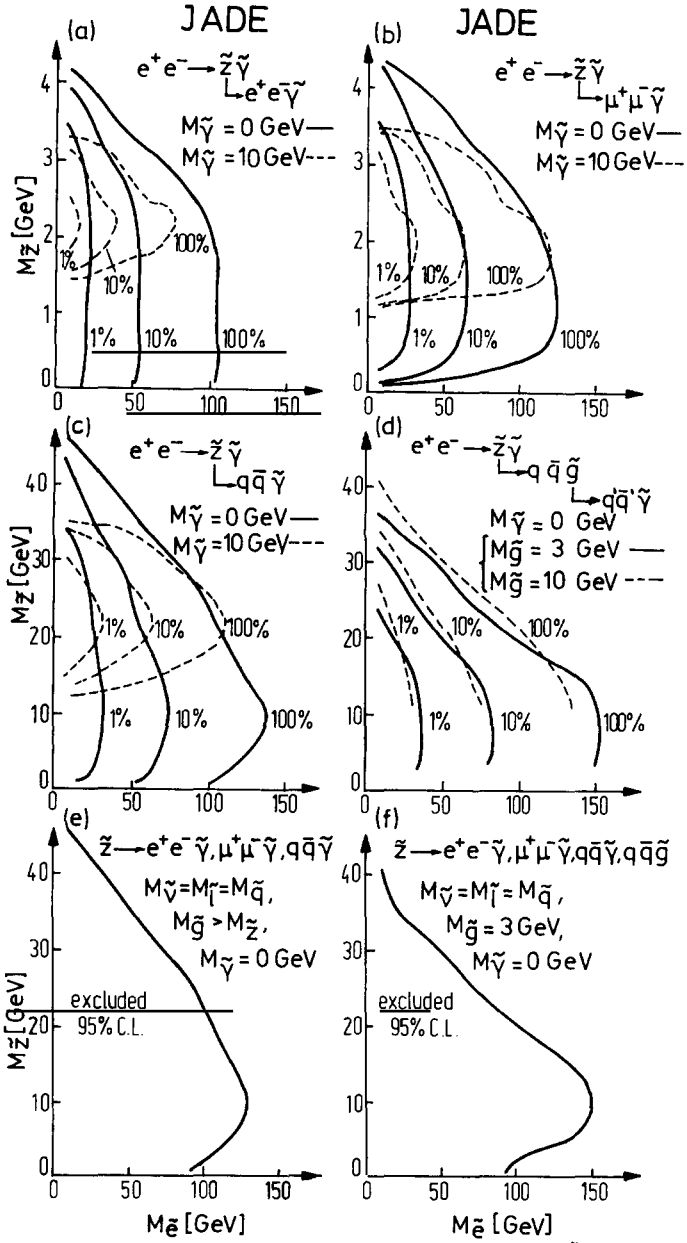

Fig. 8.19. Lower limits at 95% C.L. for the production of the supersymmetric partner of the Z-boson, $\tilde{Z}$. (a) Limits for $\tilde{Z}$ decay into electrons; (b) for $\tilde{Z}$ decay into muons; (c) for $\tilde{Z}$ decay into quark pairs and photino; (d) for $\tilde{Z}$ decay into quark pairs and gluino. In (a), (b) and (c) two mass hypotheses for the photino were made, in (d) two hypotheses for the gluino mass. The percentages near the limiting curves give the $\tilde{Z}$ decay branching ratio into the channel considered. (e) $\tilde{Z}$ limits for definite mass assumptions: $M(\tilde{\ell}) = M(\tilde{\nu}) = M(\tilde{q})$; $M(\tilde{\gamma}) = 0$ and $M(\tilde{g}) > M(\tilde{Z})$; (f) $M(\tilde{g}) = 3$ GeV.

Charginos

Charginos can be produced via e^+e^- annihilation into $\tilde{\chi}^\pm$ pairs (fig. 8.20a) and the cross-section is similar to that for muon pairs. Exchange of a scalar neutrino, fig. 8.20b, will give a large contribution only for a small $\tilde{\nu}$-mass. This was not taken into account and thus the calculated limits will be somewhat pessimistic. Single production of a chargino in the process $e^+e^- \to e\tilde{\chi}^\pm\tilde{\nu}$ (fig. 8.20c) was also investigated [222]. The limits were however covered by those from pair production.

There are many possible decay modes of charginos depending on the masses of the other supersymmetric particles. The decay matrix elements were obtained by modifying those calculated for $\tilde{Z}$ and $\tilde{q}$ decay. For the leptonic decay modes three-body phase space was used as an alternative. The limits were always derived with the lowest value of the cross-section. The fragmentation of the quarks in the final states was done using the Lund string model. We have investigated the following decays:

1. $\tilde{\chi}^\pm \to q_1\bar{q}_2\tilde{\gamma}$ or $\ell\bar{\nu}\tilde{\gamma}$. These decays are described by fig. 8.20 (e), (f), (g), (h), and proceed via W, slepton or squark exchange. They will take place if both the $\tilde{\nu}$ and the $\tilde{g}$ are heavier than the $\tilde{\chi}^\pm$. They lead to leptonic or hadronic final states and the branching ratios depend on the masses of the exchanged scalar particles and are treated as unknown parameters. Due to the photino and neutrino in the final state, the events are characterized by large missing energy and momentum.

Limits were derived using the following event-samples: Acoplanar e^+e^-, $\mu^+\mu^-$, $\tau^+\tau^-$-pairs and acoplanar jets (selection cuts in tables 8.2 and 8.3). For the hadronic decay modes the measurement of the total hadronic cross-section was used in addition. The limits on the leptonic and hadronic branching ratios as a function of the chargino mass are shown in fig. 8.21 for several photino-masses. The resulting lower limit is of the order of 23–24 GeV. But low chargino masses can only be excluded for light photinos.

2. $\tilde{\chi}^\pm \to q\bar{q}\tilde{g}$ with subsequent $\tilde{g} \to q\bar{q}\tilde{\gamma}$. These decays (fig. 8.20i) lead to hadronic states and the events can look like normal hadronic events or, near production threshold, they can be more spherical. Limits were thus derived from the total cross-section measurement, which yields $M(\tilde{\chi}^\pm) > 16.5$ GeV for $M(\tilde{g}) = 3$ GeV and $M(\tilde{g}) = 0.5$ GeV. The spherical event sample excluded charginos between 12 and 22.4 GeV. The combined upper limits are largely insensitive to the gluino mass and exclude chargino masses up to 22.4 GeV (fig. 8.21).

3. $\tilde{\chi}^\pm \to \ell\tilde{\nu}$. For light sneutrinos this two-body decay will dominate and the final state will contain two acoplanar leptons. We have again used the acoplanar electron, muon and tau event-sample to obtain the limits in fig. 8.22. For small $\tilde{\nu}$-masses the lower limit of the $\tilde{\chi}^\pm$ mass is ~22.5 GeV.

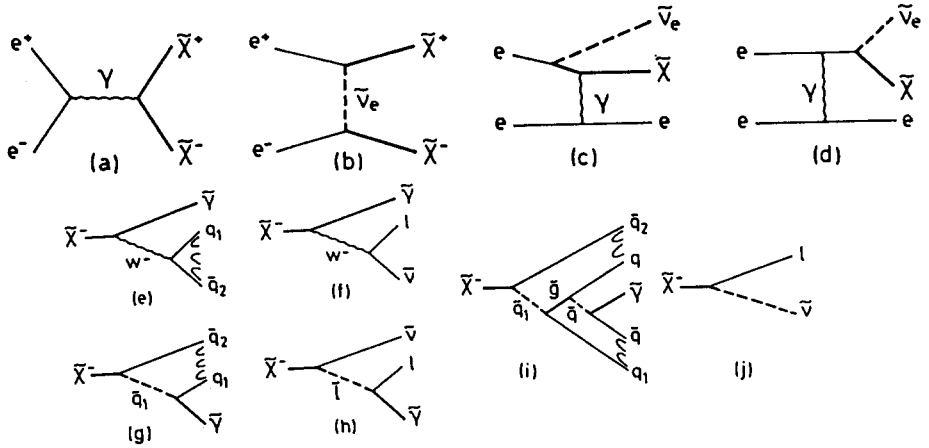

Fig. 8.20. Diagrams contributing to production and decay of $\tilde{\chi}^\pm$.

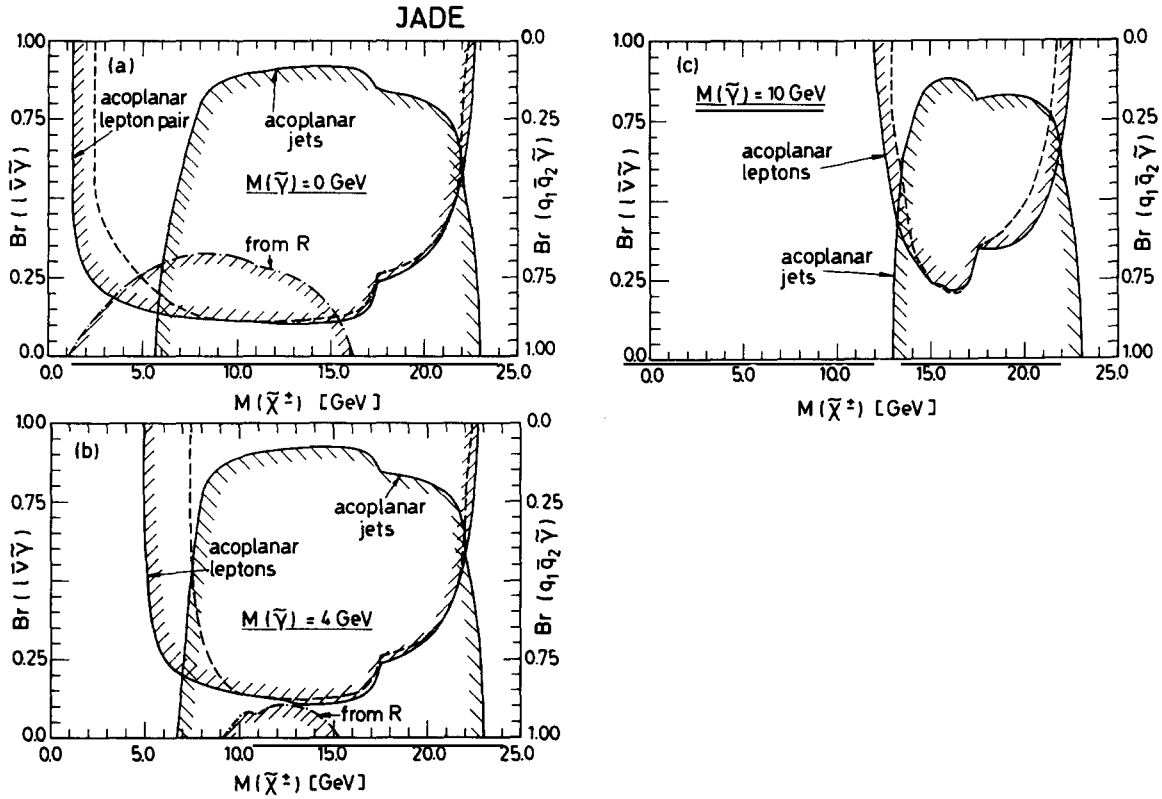

Fig. 8.21. Excluded chargino mass as a function of BR($\ell\tilde{\nu}\tilde{\gamma}$) and BR($q_1q_2\tilde{\gamma}$) at 95% C.L. for three photino-masses.

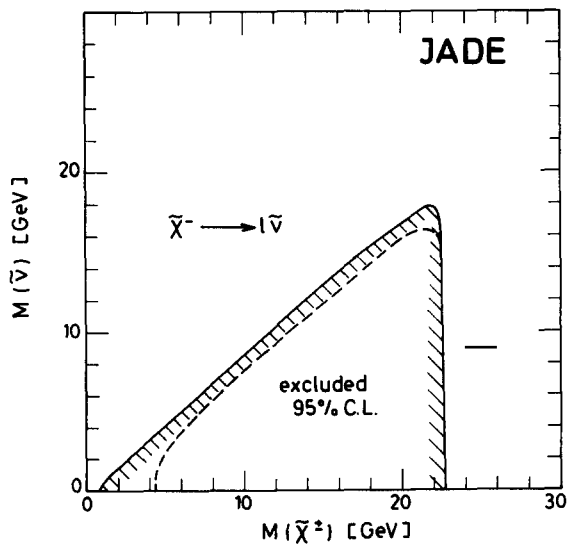

Fig. 8.22. Excluded region in the $M(\tilde{\chi}^{\pm})$, $M(\tilde{\nu})$ plane at 95% C.L. for $\tilde{\chi}^{\pm}$ decay into $\ell\tilde{\nu}$.

4. Stable $\tilde{\chi}^{\pm}$. If charginos are stable they have the same signature as stable sleptons. The mass limit of 21.1 GeV was derived along the same lines as described in the search for stable sleptons (section 8.6.1).

8.7. Limits on compositeness

The proliferation of "fundamental" particles encountered in the standard model, up to now there are 5 left-handed and 5 right-handed quarks with 3 colours, 6 leptons, at least 3 of them in both chiralities, 4 gauge bosons in the electroweak sector, 8 gluons in the QCD sector, etc., has initiated speculations about possible substructure which would simplify this picture [223]. At present this is pure speculation since no statistically significant deviation of a cross-section from the prediction of the standard model has been measured. JADE has obtained limits on possible substructure (1) by direct searches for excited states of leptons; (2) by looking for colour-octet leptons and for leptoquarks; (3) by looking for deviations from the electroweak prediction in measured leptonic and hadronic cross-sections.

8.7.1. Search for excited leptons

Excited states of leptons ℓ^*, where ℓ^* can be e^*, μ^* or τ^*, could be produced singly or in pairs (fig. 8.23). An e^* could manifest itself also in the process $e^+e^- \to \gamma\gamma$ where e^* exchange could lead to deviations from QED. In the latter case the mass limit for the e^* is given by the cut-off parameter Λ_+ for $e^+e^- \to \gamma\gamma$ in table 2.2. The approximate relation is $M^2/\lambda^2 = \Lambda_+^2$ and the upper limit deduced is shown in fig. 8.24. The cross-section for single production is given by [21, 224]:

$$\frac{d\sigma}{dt} = -\frac{2\pi\alpha^2\lambda^2}{M^2 s^2}\left[\frac{t^2 + (t-M^2)^2}{s} + \frac{s^2 + (s-M^2)^2}{t}\right] \tag{8.32}$$

where M is the mass of the excited lepton and λ is a coupling constant which describes the $\gamma\ell^*\ell$ coupling; $\lambda = 1$ if the coupling is QED-like. Pair production of excited leptons is usually parameterized by introducing a form-factor F_{ℓ^*}, which describes the $\gamma\ell^*\ell^*$ coupling, in the cross-section.

The ℓ^* decays into $\ell + \gamma$. The life-time is expected to be short and both decay products can be observed in the detector; thus one can search for a mass peak. In the case of the τ, where the τ momentum cannot be measured due to the missing neutrino, the photon energy was used as a discriminating property. The photon energy from the decay of a massive τ^* is monochromatic in the τ rest-frame and still shows a narrow peak in the laboratory frame.

The event samples for $e^+e^-\gamma$, $e^+e^-\gamma\gamma$, $\mu^+\mu^-\gamma$, $\mu^+\mu^-\gamma\gamma$, $\tau^+\tau^-\gamma$ and $\tau^+\tau^-\gamma\gamma$, described in section 2.5,

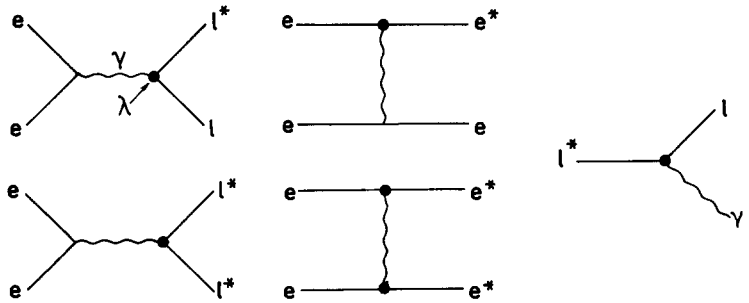

Fig. 8.23. Diagrams contributing to production and decay of excited leptons.

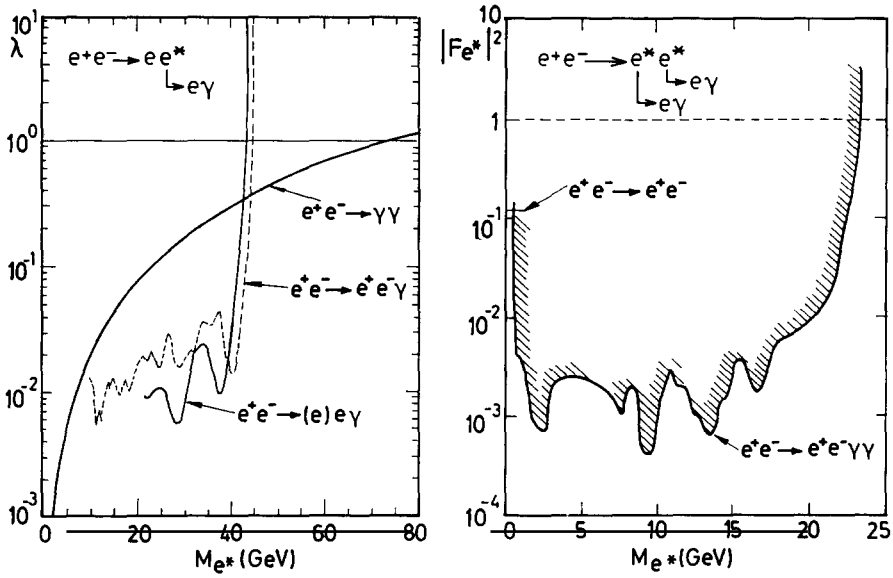

Fig. 8.24. Limits at 95% C.L. for excited electrons which decay into electron and photon.

were used to obtain mass limits. For $e^+e^-\gamma$ both event samples were used, that in which all three particles were observed and that in which one electron was allowed to escape down the beam pipe.

The resulting mass limits at the 95% C.L. are shown in figs. 8.24, 8.25 and 8.26 as a function of the coupling constant λ for single production of ℓ^*. If $\lambda = 1$ the limits are $M(e^*) < 70$ GeV, $M(\mu^*) < 35$ GeV and $M(\tau^*) < 40$ GeV. For pair production the limits have been obtained as a function of the form-factor. If it is 1 the limits are ~22 GeV for all three excited leptons.

8.7.2. Search for coloured leptons

Subconstituents of leptons could have colour [226], and some models predict the existence of coloured leptons ℓ_8 in addition to the normal colourless leptons. If a colour-octet electron e_8 existed the reaction $e^+e^- \to 2$ gluons would be possible via the exchange of such an e_8 and the events would look

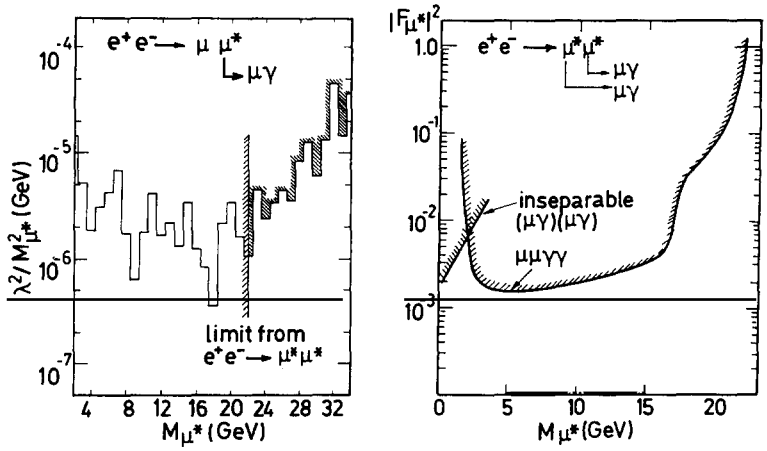

Fig. 8.25. Limits at 95% C.L. for excited muons which decay into muon and photon.

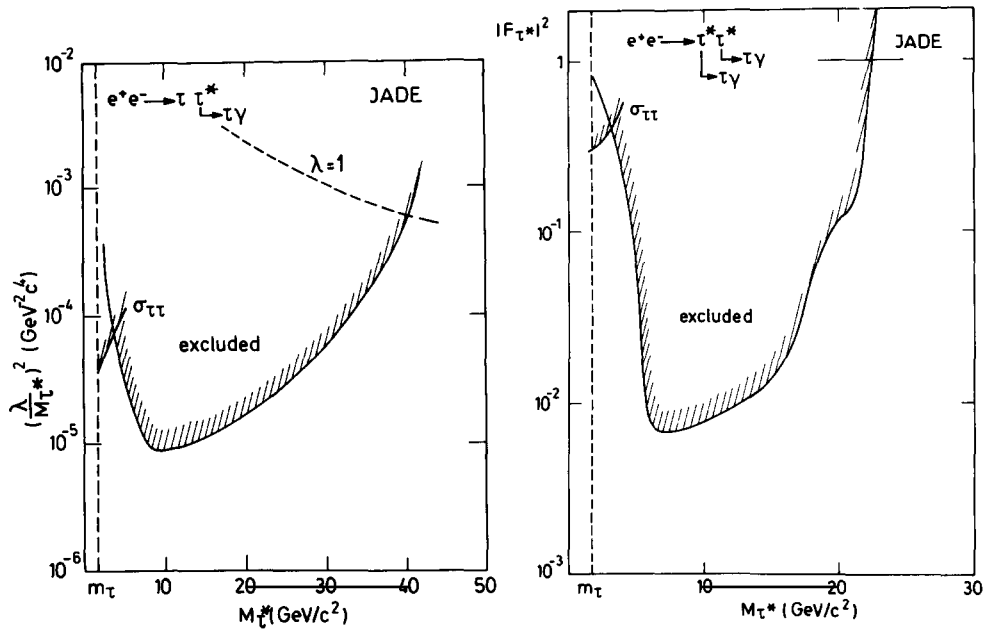

Fig. 8.26. Limits at 95% C.L. for excited taus which decay into tau and photon.

like ordinary multihadronic events. The cross-section, in analogy to $e^+e^- \to \gamma\gamma$, is given by [227]:

$$\sigma = (8/\pi)\lambda^4(s^2/M^6)$$

where λ is the coupling strength. The limit on an s-dependent excess of events in the total cross-section for multihadrons led to the limit:

$$M_{e_8} > 173\lambda^{2/3}\ \text{GeV}.$$

For $\lambda = 1$, a colour-octet electron can thus be excluded up to twice the mass of the W.

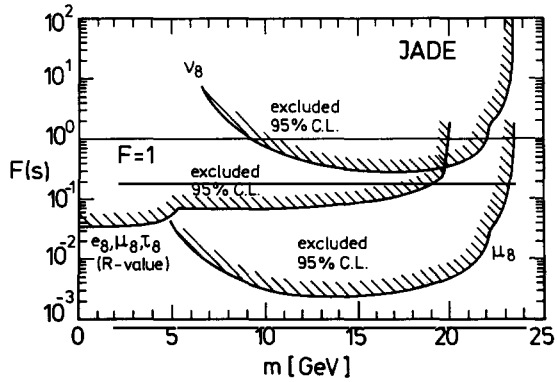

Fig. 8.27. Lower limits on the production of coloured muons and neutrinos.

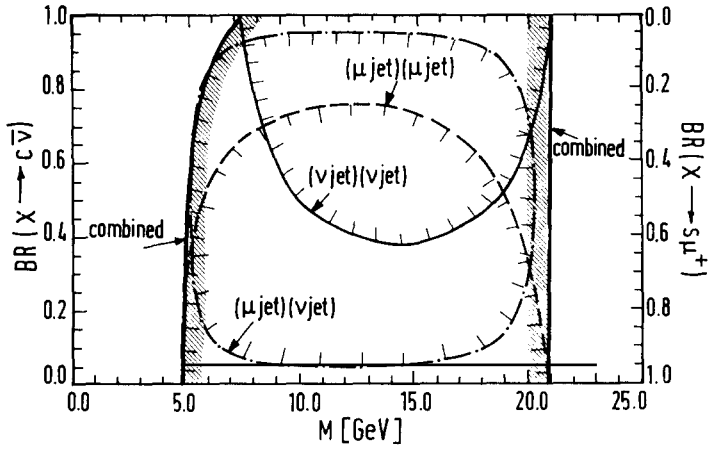

Fig. 8.28. Limits on the production of a second generation leptoquark χ of charge 2/3 decaying into $\mu\bar{s}$ or $\nu_\mu\bar{c}$.

The decay of colour-octet muons via μg leads to events containing two muons and two hadron-jets; the decay of a colour-octet neutrino into νg leads to acoplanar jets. The production cross-sections are a factor 8 larger than those for ordinary μ- or ν-pairs. In general a form-factor $F(s)$ has to be introduced taking into account the compositeness. The limits obtained by comparing the appropriate event-samples to the cross-sections are shown in fig. 8.27. Charged coloured leptons which are produced in pairs also contribute to the total hadronic cross-section. The limit derived is also shown in fig. 8.27.

8.7.3. Search for leptoquarks

The search for leptoquarks was motivated more by experiment than by theory, although leptoquarks would be expected in many composite models. The CELLO group at PETRA found an event containing two energetic muons and two energetic jets [228]; the invariant masses of the (μ jet) systems were of the order of 20 GeV. The probability that this event could be explained by ordinary reactions was very small. The probability of the event being due to "background" has increased to the level of a percent since the publication, as CELLO has accumulated more than a factor of four more luminosity at high energies without finding another such event. The decay of a neutral heavy lepton was not very probable as an explanation for this event in view of the measured jet-masses. A natural explanation would be the decay of a heavy leptoquark into a muon and a quark [229].

Assuming that such a leptoquark exists and that it mixes only with one family, in our case (c, s, μ, ν_μ) the possible decays are: $\mu\bar{s}$ or $\nu_\mu\bar{c}$. Thus three event-configurations could be expected and JADE has looked for all three:

$\mu^+\mu^-$ jet jet: Two muons with momenta above 3 GeV were sought in the multihadronic data set, one of the muons had to have a transverse momentum with respect to the thrust axis larger than 3 GeV. One candidate event was observed, which is however not as spectacular as the CELLO event.

$\nu\mu$ jet jet: One muon with a momentum above 5 GeV was demanded in the multihadronic event-sample. An additional cut in the visible energy and in the acollinearity of the event took account of the escaping neutrino: $E_{vis} < \sqrt{s}/2$ and $\Delta\varphi > 40°(1 + 0.5|\cos\theta_{th}|)$. Again one event survived the cuts; it could be due to a $D^\pm$ decay with a long-lived unobserved K_L^0 or to a partially observed QED event: $e^+e^- \to q\bar{q}\mu^+\mu^-$.

$\nu\nu$ jet jet: The events will consist of two acoplanar jets and the selection cuts in table 8.2 were used. No event survived the cuts.

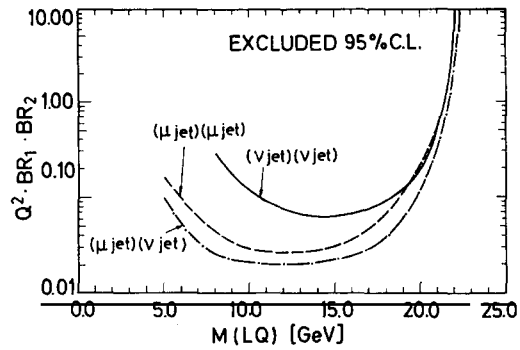

Fig. 8.29. Lower limits on the mass of leptoquarks of charge Q, pair produced in e^+e^- annihilation and decaying into quark and muon or neutrino. $BR_{1,2}$ are the decay branching ratios of the leptoquarks.

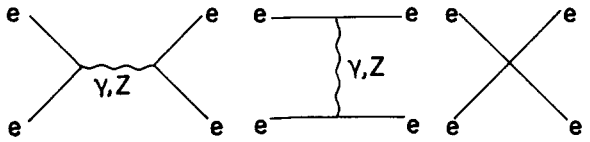

Fig. 8.30. Diagrams of $e^+e^- \to e^+e^-$ in the standard model and additional contract term.

In calculating the mass limits the event candidates found were taken into account; no background subtraction was attempted. The production cross-section for charged coloured spinless particles was given in eq. (8.31). In the simulation of events the leptoquarks were assumed to fragment like heavy quarks and to decay afterwards. The limits for a leptoquark of charge 2/3 that decays exclusively into particles of the second generation are shown in fig. 8.28. The combined limit is $M(\text{leptoquark}) > 20.8\,\text{GeV}$ or $M(\text{leptoquark}) < 5\,\text{GeV}$. The CELLO event has muon-jet invariant masses of $19.4 \pm 1.3\,\text{GeV}$ and $22.2 \pm 1.6\,\text{GeV}$, just at the border of our limits.

In fig. 8.29 limits for a more general case are shown, namely for leptoquarks of charge Q decaying into $q\mu$ or $q\nu$ where q can be any quark.

8.7.4. Limits on a mass scale for preons

As we have seen in section 2.2.2, deviations from QED are traditionally parameterized with cut-off parameters Λ which can be related to the size of the "fundamental" particles taking part in the interaction. The limits for these cut-off parameters Λ, which were measured to be around 200–300 GeV, are mainly determined – apart from the experimental errors – by the s-dependence of the hypothetical deviation from QED or the standard model.

Eichten et al. [225] have suggested a parameterization of deviations due to substructure. They assume the standard model to be correct but assume that in addition to the photon and Z^0 exchange there exist contact terms which are brought about by the preons contained in the particles (see fig. 8.30). These additional diagrams would lead to an additional term in the interaction Lagrangian:

$$L_{\text{eff}} = \frac{g^2}{2\Lambda_{\pm}^{\text{comp}}} [\eta_{\text{LL}} j_{\text{L}} \cdot j_{\text{L}} + \eta_{\text{RR}} j_{\text{R}} \cdot j_{\text{R}} + 2\eta_{\text{RL}} j_{\text{R}} \cdot j_{\text{L}}] .$$

The parameter Λ^{comp} gives the compositeness mass scale; the sign in the subscript of Λ^{comp} indicates the overall sign of the resulting additional term in the standard cross-section. Λ^{comp} is defined such that the coupling constant $g^2/4\pi = 1$, which corresponds to a strong coupling. The additional interaction does not necessarily conserve parity, therefore the left- and right-handed currents j_{L} and j_{R} appear separately. Depending on the type of modification expected the η's assume values of 0 or ± 1:

Table 8.6
Compositeness mass scale: Lower limits of Λ^{comp} at 95% C.L. in TeV

	LL, RR		AA		VV	
	Λ_+^{comp}	Λ_-^{comp}	Λ_+^{comp}	Λ_-^{comp}	Λ_+^{comp}	Λ_-^{comp}
e^+e^-	1.1	1.4	2.4	2.3	2.5	3.1
$\mu^+\mu^-$	4.4	2.1	7.5	2.8	5.8	4.8
$\tau^+\tau^-$	2.2	3.2	2.7	5.7	4.1	5.7

Interaction	η_{LL}	η_{RR}	η_{LR}
Left-handed (LL)	1	0	0
Right-handed (RR)	0	1	0
Vector (VV)	1	1	1
Axial-vector (AA)	1	1	−1

Limits for the cut-off parameters have been determined for $e^+e^- \to e^+e^-$, $\mu^+\mu^-$ and $\tau^+\tau^-$. They are listed in table 8.6; the values are all larger than 1 TeV. The magnitude is of course related to the assumption of a large coupling constant $g^2/4\pi = 1$. In the case of $\mu^+\mu^-$ and $\tau^+\tau^-$ final states the contact interactions will only exist if electrons and muons or taus have common subconstituents.

8.7.5. Unusual hadronic events containing isolated muons

In the course of the searches for new particles the "normal" events were examined in detail and "unusual" events were searched for. The only unusual events found in the JADE detector which could not be explained satisfactorily – as being due to a standard process or as a new phenomenon – were low thrust hadronic events containing an isolated muon. They were found at the highest PETRA energies, which might indicate that they are due to some new physics. This fact on the other hand led to the persisting doubts about the events; the background due to synchrotron radiation and off-momentum particles at the highest running energies was high and the muon filter was particularly affected.

The events were found in the multihadronic data above 46.3 GeV, where the MARK J group had reported an excess of events of low thrust with isolated muons [230]. 1.7 pb^{-1} were accumulated above 46.3 GeV with the JADE detector. In addition to the standard cuts for multihadronic events a muon was required which fulfilled the loose cuts defined in table 7.3. A distribution of the event thrust (the muon track was included in the calculation) and $|\cos\delta|$, where δ is the angle between muon and thrust axis is shown in fig. 8.31. The distribution is shown for energies above $\sqrt{s} = 46.3$ GeV and for a lower energy region which serves as a reference. The signal region which is also indicated in the figure, was defined in analogy to the MARK J analysis: $T < 0.8$ and $|\cos\delta| < 0.7$. In this region 5 events are observed above 46.3 GeV while the expectation from the lower energy data is 0.56 ± 0.18. The expectation is in agreement with Monte Carlo computations based on five flavours. The s-dependence of the observed cross-section in the signal region is shown in fig. 8.32. The point at the highest energy shows an excess compared to lower energies. This effect is in agreement with the data from MARK J which are also shown. The probability of such an excess was calculated to be 0.35%.

Several checks were performed to investigate further the origin of the events. Since the five muons do not belong to the sample of best identified muons, the probability that they are caused by background was carefully examined. The studies led to a background estimate of typically one event. A similar analysis was carried out for inclusive electrons, which were searched for in a region of polar

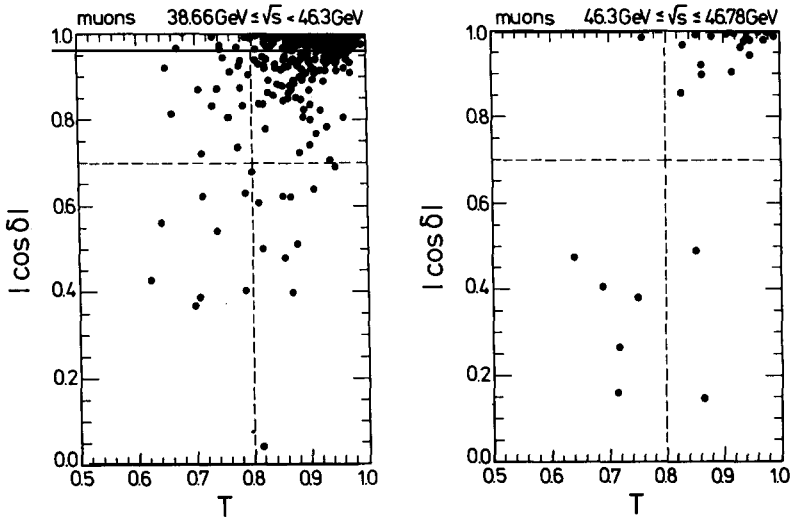

Fig. 8.31. $|\cos\delta|$ versus thrust T for hadronic events with an inclusive muon. δ is the angle of the muon with respect to the thrust axis.

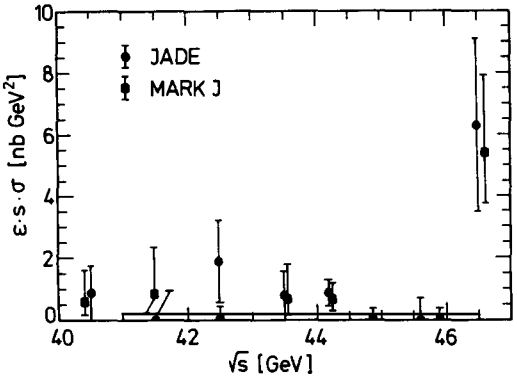

Fig. 8.32. The observed cross-section for muon-inclusive hadronic events in the signal region ($T < 0.8$ and $|\cos\delta| < 0.7$) as a function of $\sqrt{s}$.

angle $|\cos\theta| < 0.76$. No event was observed although the detection efficiency is similar to that for muons.

Since there are no plans to run PETRA again at these high energies, it must be left to other detectors at future accelerators to decide, whether these events are merely background or genuinely indicate the on-set of some new physics.

Summary

The JADE detector has been operated successfully for more than five years at the e^+e^- storage ring PETRA and has collected data in the energy range $12 \leq \sqrt{s} \leq 46.78$ GeV.

Tests of the Glashow–Salam–Weinberg model of electroweak interactions were carried out using leptonic and hadronic final states. The charge asymmetry due to γ–Z^0 interference predicted by this

model was confirmed in the processes $e^+e^- \to \mu^+\mu^-$, $\tau^+\tau^-$, $c\bar{c}$ and $b\bar{b}$. The muon data gave the most precise results but the precision of the τ results was almost as good, since reconstruction of τ-leptons is possible with high efficiency in the JADE detector, resulting in a low-background (~5%) event sample. The muon and tau asymmetries were measured up to the highest energy $\sqrt{s} = 46.78$ GeV. The angular distributions and the total rates were well described by the GSW model with a Z mass of 93 GeV and including radiative corrections.

The charge asymmetry of $e^+e^- \to c\bar{c}$ was measured by reconstructing the $D^{*\pm}$ resonance. A technique for flavour separation in multihadronic events with inclusive muons was developed which allowed determination of the b asymmetry. Both analyses were carried out at an average centre-of-mass energy of $\sqrt{s} \sim 34$ GeV. The axial–vector coupling constants determined from the measured asymmetries are:

$$a_e a_\mu = 1.21 \pm 0.14$$
$$a_e a_\tau = 0.76 \pm 0.18$$
$$a_e a_c = -1.0 \pm 0.6$$
$$a_e a_b = 0.9 \pm 0.3 .$$

The weak mixing angle $\sin^2 \theta_W$ was determined from the processes with leptonic final states and also in an analysis of the total hadronic cross-section. The total hadronic cross-section receives, in addition to the electroweak correction, a non-negligible contribution from QCD effects. The mixing angle was determined in a simultaneous fit of $\sin^2 \theta_W$ and α_s. The results are, assuming $M_Z = (93 \pm 2)$ GeV:

$$\sin^2 \theta_W = 0.20^{+0.03}_{-0.02} \pm 0.01 \quad \text{from } e^+e^-, \mu^+\mu^-, \tau^+\tau^- \text{ combined}$$
$$\sin^2 \theta_W = 0.23^{+0.03}_{-0.04} \quad \text{from } R_{had} .$$

In Bhabha scattering Z^0-exchange effects are expected to be small and this was confirmed by the data, which agreed with QED up to the highest PETRA energies. The measurement was sensitive to contributions of order α^3. The normalisation error was typically 3%, while electroweak effects are expected to be <0.5%.

Tests of QED were also carried out in $e^+e^- \to \gamma\gamma$ where the weak neutral current does not contribute in lowest order. Furthermore the higher order processes $e^+e^- \to \ell^+\ell^-\gamma$ and $\ell^+\ell^-\gamma\gamma$ where $\ell = e, \mu, \tau$ and $e^+e^- \to \gamma\gamma\gamma$ and $\gamma\gamma\gamma\gamma$ and two-photon scattering were measured in $e^+e^- \to e^+e^-e^+e^-$ and $e^+e^-\mu^+\mu^-$. The data agreed with the QED predictions to order α^3 and α^4 respectively. The accuracy is in most cases limited by the statistical errors (except in $e^+e^- \to \gamma\gamma$ and $e^+e^- \to e^+e^-\gamma$).

The decay branching ratios of the τ into one, three and five charged particles plus neutrals and into electrons, muons and pions plus neutrinos were determined:

$$BR_1 = (86.1 \pm 0.5 \pm 0.9)\% \qquad BR_e = (17.0 \pm 0.7 \pm 0.9)\%$$
$$BR_3 = (13.6 \pm 0.5 \pm 0.8)\% \qquad BR_\mu = (18.8 \pm 0.8 \pm 0.7)\%$$
$$BR_5 = (\ 0.3 \pm 0.1 \pm 0.2)\% \qquad BR_\pi = (11.8 \pm 0.6 \pm 1.1)\% .$$

The results are in agreement with theoretical calculations.

The tests of the hadronic sector of the standard model turned out to be very complex mainly because of the lack of a quantitative theory of hadronisation but also because of problems in perturbative QCD. The picture of hadronic processes given by perturbative QCD, $e^+e^- \to q\bar{q}$ plus one or more gluons, was confirmed by demonstrating the existence of three- and four-jet events. For a more detailed comparison of event shapes and rates fragmentation models had to be used. Thus the ability of the existing fragmentation models to describe the data had to be investigated.

In an analysis of three-jet events differences were found between gluons and quarks in the distribution of transverse momentum with respect to the jet-axis, in the angular distribution of particle multiplicity and energy flow. In addition a systematic deviation of the event shape of three-jet events from the expectations based on independent behaviour of the three partons in the fragmentation process was discovered. This latter effect is in the literature known as the "string effect" since it – and also the differences between quarks and gluons – is well described by a model based on a QCD matrix element and a string model for fragmentation. A different type of model which was also found to give a good description of the data was based on a leading log approximation of QCD. It was however found that this type of model reproduced the structure of $q\bar{q}g$ events only if soft gluon interference effects were taken into account, e.g. as in the Webber model. Models based on QCD matrix elements and subsequent independent fragmentation of partons did not yield satisfactory agreement with the data.

A comparison of experimental jet-multiplicities with the predictions of $O(\alpha_s^2)$ QCD + Lund model seems to indicate a fundamental problem; the predicted proportion of spherical events is too small. Spherical events are mainly due to four-parton events. To achieve agreement with the data either α_s has to be increased, which leads to contradictions with the rate of three-jet events, or a small proportion (~2%) of five-parton events has to be added artificially suggesting the importance of higher order QCD effects. Since fragmentation effects were shown to be excluded as a source of these discrepancies, the problem lies with the QCD matrix elements. The Webber model, which is based on a leading log summation and thus includes all orders, reproduces the rate of spherical events better; but this model has problems in reproducing the rate of three-jet events correctly.

The determination of the strong coupling constant α_s is affected by these theoretical problems. It was attempted several times as the understanding of the theory advanced. In principle the total hadronic cross-section yields a measurement of α_s which is independent of detailed knowledge about fragmentation – except in the acceptance calculation. However due to the systematic experimental normalisation error the resulting precision in α_s is limited. In the simultaneous fit of the weak mixing angle and of α_s mentioned above a value of $\alpha_s = 0.19^{+0.06}_{-0.07}$ (at $\sqrt{s} \sim 34$ GeV) was deduced.

A second method of determining α_s which is also independent of fragmentation models was an analysis of parameters deduced from the event shape, which can be calculated exactly in $O(\alpha_s^2)$ QCD (using the ERT matrix element). The data contain contributions from fragmentation in addition to those from QCD, but the two contributions have a different energy dependence. Thus limits on α_s are obtained by analysing the s-dependence of the data. A value of $\alpha_s = 0.12 \pm 0.02$ was found by this method, which is not fragmentation model dependent but assumes that the $O(\alpha_s^2)$ QCD matrix element gives a correct description of the data.

The third means of determining α_s is the analysis of energy–energy correlations. The asymmetry was evaluated in terms of $O(\alpha_s^2)$ QCD in two different ways. Firstly fragmentation effects, which were shown to be small, were neglected, yielding $\alpha_s = 0.12 \pm 0.01$. Secondly the Lund model was included in the analysis (together with the GKS matrix element). This led to a value of $\alpha_s = 0.16 \pm 0.02$.

All results for α_s are affected by missing higher orders in the QCD matrix elements. The QCD scale

parameter corresponding to the α_s values found lies between 50 and 500 MeV. The uncertainty is mainly due to a lack of theoretical understanding.

A different approach to studying hadronic final states was pursued in the analysis of inclusive production of particular particle species. In addition to γ, π^0, K^0, η, ρ^0, $K^{*\pm}$, Λ, Ξ^- and D^* the production of charged particles without further identification was studied. In the case of unidentified charged particles, photons, neutral pions, kaons and Λ's the energy dependence of the inclusive spectra was examined. The accuracy of the data did not in general suffice to establish scaling violations. The multiplicity distributions of charged particles were better described by the Lund model than by models with independent fragmentation. Fragmentation parameters for the production of strange mesons and baryons and for the relative probability of vector meson production were determined.

Analysis of the D^* yielded information on the mechanisms of heavy quark production. The fragmentation spectrum is hard and can be described by the Peterson function with $\varepsilon_c = 0.05$. The rate of gluon emission in $c\bar{c}$ events was found to be compatible with the overall probability of gluon emission.

The properties of heavy quarks were further analysed by studying their decay muons and – in the B life-time determination – also their decay electrons. The b fragmentation function was found to be harder than that for the c. The muonic branching ratios were determined:

$$BR(b \to \mu + \cdots) = (11.4 \pm 1.8 \pm 2.5)\%$$
$$BR(c \to \mu + \cdots) = (8.9 \pm 1.8 \pm 2.5)\% .$$

The limit on flavour-changing neutral currents deduced from the rate of di-muons is:

$$BR(b \to \mu^+\mu^- X) < 0.4\% \qquad \text{at } 95\% \text{ C.L.}$$

The life-time of B-hadrons, determined by measuring the impact parameter, is:

$$\tau_B = 1.8^{+0.5}_{-0.4} \pm 0.4 \text{ ps} .$$

Since all investigations were carried out at energies which reach up to the highest energies available in e^+e^- collisions one was always aware of the possibility of "new physics". The searches for deviations from the standard model cross-sections greater than the experimental errors were all negative. Limits for QED cut-off parameters of the order of 200–300 GeV were determined for leptons and hadrons. Searches for specific particles led to mass limits for the top-quark, for free quarks, new massive leptons and charged and neutral (non-minimal) Higgs. Searches for supersymmetric partners of photons, electrons, muons, taus, quarks, W and Z bosons were undertaken in a systematic way, trying to avoid dependence on specific models. Searches for excited leptons, leptoquarks, colour-octet leptons were also negative and gave no indication of compositeness. The limit on the compositeness scale parameter, assuming a contact interaction, is of the order of a TeV.

In the course of these searches the following event-types were analysed and found to be consistent with standard expectations: acoplanar leptons and photons, single leptons and photons, an acoplanar configuration of a lepton and a jet, acoplanar jets, single jets, events with isolated leptons and jets, spherical hadronic events, events containing tracks of unexpected ionisation properties.

Acknowledgements

I should like to thank all Prof. G. Weber who encouraged me to undertake this report. Secondly I thank all my colleagues in the JADE Collaboration who discussed details of their analysis efforts with me. I gratefully acknowledge discussions with colleagues from other groups working at PETRA and PEP and with members of the theory group in Hamburg. Finally, I want to thank the people who critically read the manuscript. Thanks are also due to Dr. K. Schilling from the DESY computer centre, who patiently helped me in my struggles with the text processing system, and to Miss H. Evers from the drawing office.

References

[1] The list of past and present (indicated by an *) members of the JADE Collaboration:
W. Bartel*, L. Becker*, T. Canzler, D. Cords, P. Dittmann, R. Eichler, R. Felst*, D. Haidt*, H. Junge, S. Kawabata, G. Knies*, H. Krehbiel*, P. Laurikainen*, R. Meinke*, B. Naroska*, L.H. O'Neill, J. Olsson*, E. Pietarienen, D. Schmidt*, P. Steffen*, H. Wenninger, W.L. Yen, M. Zachara, Y. Zhang
Deutsches Elektronen-Synchrotron DESY, Hamburg, Germany;
G. Dietrich, E. Elsen*, J. Hagemann*, G. Heinzelmann*, M. Helm, H. Kado*, K. Kawagoe, C. Kleinwort*, M. Kuhlen*, N. Magnussen*, K. Meier, A. Petersen, R. Ramcke*, U. Schneekloth*, P. Warming*, G. Weber*
II. Institut für Experimentalphysik der Universität Hamburg, Germany;
K. Ambrus*, S. Bethke*, A. Dieckmann*, H. Drumm, J. Heintze*, K.H. Hellenbrand*, R. Heuer, S. Komamiya*, J. von Krogh*, P. Lennert*, H. Matsumura*, H. Rieseberg*, H. v.d. Schmitt*, L. Smolik*, J. Spitzer*, A. Wagner*, M. Zimmer*
Physikalisches Institut der Universität Heidelberg, Germany;
A. Bell, C. Bowdery*, D.C. Darvill*, A. Finch*, F. Foster*, G. Hughes*, T. Nozaki, J. Nye*, I. Walker*, H. Wriedt
University of Lancaster, England;
J. Allison*, J. Armitage, J. Baines, A.H. Ball, G. Bamford, R. Barlow*, J. Chrin*, I.P. Duerdoth*, I. Glendinning, T. Greenshaw*, J.F. Hassard, B.T. King, F.K. Loebinger*, A.A. Macbeth*, H.E. Mills*, P.G. Murphy*, H. Prosper, P. Rowe, K. Stephens*
University of Manchester, England;
R.G. Glasser*, P. Hill*, B. Sechi-Zorn, J.A. Skard*, S.R. Wagner, G.T. Zorn*
University of Maryland, College Park, USA;
S.L. Cartwright*, D. Clarke*, M.C. Goddard, R. Hedgecock*, R. Marshall*, R.P. Middleton*, G.F. Pearce, J.B. Whittaker
Rutherford Appleton Laboratory, Chilton, UK;
M. Imori, J. Kanzaki, T. Kawamoto*, T. Kobayashi*, M. Koshiba, T. Mashimo, M. Minowa*, M. Nozaki, S. Odaka, S. Orito, A. Sato, T. Suda, H. Takeda*, T. Takeshita*, Y. Totsuka, Y. Watanabe, S. Yamada*, C. Yanagisawa
ICEPP Univ. of Tokyo, Japan.

[2] A survey of all PETRA experiments and references for the detectors are given in S.L. Wu, Phys. Reports 107 (1984) 59.

[3] G.A. Voss, Contribution to the 1979 Particle Accelerator Conf. held in San Francisco, IEEE Transact. on Nucl. Science NS-26, p. 2970;
D. Degele, Contribution to the 11th Int. Conf. on High Energy Accelerators held in Geneva, Switzerland, ed. W.S. Newman, p. 16;
J. Rossbach, Contribution to the 1981 Particle Accelerator Conf. held in Washington, IEEE Transact. on Nucl. Science NS-28, p. 2025.

[4] JADE Coll., W. Bartel et al., Phys. Lett. B107 (1981) 163; B113 (1982) 190; B121 (1983) 203; Z. Phys. C24 (1984) 231; Phys. Lett. B160 (1985) 421; B174 (1986) 350.

[5] H. Drumm et al., in: Wire Chamber Conf., eds. W. Bartl and M. Regler (North-Holland Publishing Comp., 1980) p. 333;
J. Heintze, Nucl. Instr. Meth. 196 (1982) 293;

[6] J. Olsson et al., Nucl. Instr. Meth. 176 (1980) 403.

[7] J. Allison et al., Nucl. Instr. Meth. A238 (1985) 220 and 230,

[8] D. Cords et al., Nucl. Instr. Meth. A245 (1986) 137.

[9] H.E. Mills, Nucl. Instr. Meth. A247 (1986) 525.

[10] S.L. Glashow, Nucl. Phys. 22 (1961) 579; Rev. Mod. Phys. 52 (1980) 539;
A. Salam, Phys. Rev. 127 (1962) 331; Rev. Mod. Phys. 52 (1980) 525;
S. Weinberg, Phys. Rev. Lett. 19 (1967) 1264; Rev. Mod. Phys. 52 (1980) 515.

[11] R. Budny, Phys. Lett. B45 (1973) 340; B55 (1975) 227.

[12] Particle Data Book, C.G. Wohl et al., Rev. Mod. Phys. 56 (1984).
[13] UA1 Coll., G. Arnison et al., Phys. Lett. B126 (1983) 398; B129 (1983) 273;
UA2 Coll., P. Bagnaia et al., Z. Phys. C24 (1984) 1.
[14] A. Sirlin and W.J. Marciano, Nucl. Phys. B189 (1981) 442;
W.J. Marciano, in Cornell Conf. 1983[3].
[15] MAC Coll., E. Fernandez et al., SLAC-PUB 4005 (1986);
HRS Coll., M. Derrick et al., Phys. Lett. B166 (1986) 463.
[16] JADE Coll., W. Bartel et al., Phys. Lett. B92 (1980) 206.
[17] JADE Coll., W. Bartel et al., Z. Phys. C19 (1983) 197.
[18] F.A. Berends et al., Nucl. Phys. B57 (1973) 381; B61 (1973) 414; B68 (1974) 541; B186 (1981) 22; B206 (1982) 61.
[19] F.A. Berends et al., Nucl. Phys. B63 (1973) 381; B177 (1981) 237.
[20] F.A. Berends and G.J. Komen, Phys. Lett. B63 (1976) 432.
[21] A. Litke, Harvard University PHD thesis (1970), unpublished.
[22] S.D. Drell, Ann. Phys. 4 (1958) 75.
[23] L. Criegee and G. Knies, Phys. Reports 83 (1982) 151.
[24] CELLO Coll., H.J. Behrend et al., Phys. Lett. B103 (1981) 148.
[25] PLUTO Coll., Ch. Berger et al., Z. Phys. C27 (1985) 341;
H. Kaptiza, thesis Un. Hamburg (1985) unpublished.
[26] TASSO Coll., M. Althoff et al., Z. Phys. C22 (1984) 13.
[27] JADE Coll., W. Bartel et al., Phys. Lett. B108 (1982) 140.
[28] CELLO Coll., H.J. Behrend et al., Z. Phys. C14 (1982) 283;
MARK J Coll., B. Adeva et al., Phys. Rev. Lett. 48 (1982) 1701;
TASSO Coll., R. Brandelik et al., Phys. Lett. B110 (1982) 173.
[29] JADE Coll., W. Bartel et al., Z. Phys. C26 (1985) 507.
[30] JADE Coll., W. Bartel et al., Phys. Lett. B161 (1985) 188;
U. Schneekloth, DESY Intern. Report F22-85-01 (1985) (in German).
[31] JADE Coll., W. Bartel et al., Z. Phys. C30 (1986) 371.
[32] J. Smith, J.A.M. Vermaseren, G. Grammer, Phys. Rev. D15 (1977) 3280;
J.A.M. Vermaseren, Proc. Int. Workshop on $\gamma\gamma$ collisions, Amiens, France (1980), eds. G. Cochard and P. Kessler, p. 35.
[33] F.A. Berends, R. Kleiss and S. Jadach, Nucl. Phys. B202 (1982) 63.
[34] S. Jadach and Z. Was, Acta Phys. Pol. B15 (1984) 1151.
[35] A summary of recent results can be found in:
B. Naroska, Physics in Collisions 5, Autun, France (1985), ed. L. Montanet, p. 287.
[36] CELLO Coll., H.J. Behrend et al., Z. Phys. C16 (1983) 301; and contributed paper to the Bari[5] and Kyoto[6] conferences, 1985.
[37] CELLO Coll., H.J. Behrend et al., Phys. Lett. B114 (1982) 282.
[38] MARK J Coll., B. Adeva et al., Phys. Rev. Lett. 55 (1985) 665.
[39] MARK J Coll., B. Adeva et al., Phys. Reports 109 (1984) 131.
[40] PLUTO Coll., Ch. Berger et al., Z. Phys. C28 (1985) 1.
[41] PLUTO Coll., Ch. Berger et al., Z. Phys. C21 (1983) 53; C27 (1985) 341.
[42] TASSO Coll., M. Althoff et al., Z. Phys. C26 (1985) 521.
[43] HRS Coll., D. Bender et al., Phys. Rev. D30 (1984) 515;
M. Derrick et al., Phys. Rev. D31 (1985) 2352.
[44] HRS Coll., K.K. Gan et al., Phys. Lett. B153 (1985) 116.
[45] MAC Coll., W. Ash et al., Phys. Rev. Lett. 55 (1985) 1831.
[46] MAC Coll., E. Fernandez et al., Phys. Rev. Lett. 54 (1985) 1620.
[47] MARK II Coll., N.E. Levi et al., Phys. Rev. Lett. 51 (1983) 1941.
[48] A. Boehm, Un. Aachen preprint PITHA 84/11 (1984).
[49] W. Wetzel, Nucl. Phys. B227 (1983) 1; Preprint Heidelberg 1983, At $s = 1195\,\mathrm{GeV}^2$ $\Delta A = +0.6\%$ and at $s = 1853\,\mathrm{GeV}^2$ $\Delta A = +1.1\%$ were used.
[50] M. Boehm and W. Hollik, Nucl. Phys. B204 (1982) 45; Z. Phys. C23 (1984) 31;
R.W. Brown, K. Decker, E.A. Paschos, Phys. Rev. Lett. 52 (1984) 1192.
[51] W. Hollik, DESY preprint 86-047 (1986).
[52] W. Krenz, Aachen preprint PITHA 84/42 (1984), submitted to Nucl. Phys. B.
[53] CHARM Coll., F. Bergsma et al., Phys. Lett. 147B (1984) 481;
L.A. Ahrens et al., Phys. Rev. Lett. 54 (1984) 18.
[54] B. Naroska, Proc. XXIst Reconcontre de Moriond, Les Arcs, 1986, to be published and DESY 86-051.
[55] H. Abramovicz et al., Phys. Rev. Lett. 57 (1986) 298;
CHARM Coll., J.V. Allaby et al., CERN EP-86-094 (1986), Phys. Lett. B177 (1986) 446. (In both cases $m_c = 1.5\,\mathrm{GeV}$ was used.)

[56] D.H. Saxon, in: Physics in Collisions 4, ed. A. Seiden (UC Santa Cruz, 1984) p. 295.
[57] JADE Coll., W. Bartel et al., Z. Phys. C24 (1984) 223.
[58] JADE Coll., W. Bartel et al., DESY preprint 86-023 (1986) to be published.
[59] JADE Coll., W. Bartel et al., Z. Phys. C30 (1986) 545.
[60] CALKUL Coll., F.A. Berends et al., Nucl. Phys. B264 (1986) 243; B239 (1984) 395; B228 (1983) 537; Leuven Cath. Un. preprint KUL-TFF-84-017 (to be published).
[61] F.A. Berends, P.H. Daverveldt and R. Kleiss, Nucl. Phys. B253 (1985) 421.
[62] H. Terazawa, Rev. Mod. Phys. 45 (1973) 615;
A. Cuur and P. Kessler, Orsay Report 1985 LAL 85-01.
[63] CELLO Coll., H.-J. Behrend et al., Phys. Lett. B158 (1985) 536.
[64] MARK J Coll., DESY preprint 85-073 (1985).
[65] CELLO Coll., H.-J. Behrend et al., DESY preprint 84-103 (1984).
[66] M.L. Perl, Ann. Rev. Nucl. Part. Sci. 30 (1980) 299.
[67] E.H. Thorndike, Contr. to Kyoto Conf. 1985[6], p. 406.
[68] K.K. Gan, Purdue University preprint PU-85-539 (1985).
[69] T.N. Truong, Phys. Rev. D30 (1984) 1509.
[70] F.J. Gilman and S.H. Rhie, Phys. Rev. D31 (1985) 1066.
[71] JADE Coll., W. Bartel et al., DESY preprint 86-091 (1986) to be published.
[72] MARK II Coll., C.A. Blocker et al., Phys. Rev. Lett. 49 (1982) 1369;
CELLO Coll., H.J. Behrend et al., Z. Phys. C23 (1984) 103;
TPC Coll., H. Aihara et al., Phys. Rev. D30 (1984) 2436;
TASSO Coll., M. Althoff et al., Z. Phys. C26 (1985) 521;
MAC Coll., E. Fernandez et al., Phys. Rev. Lett. 54 (1985) 1624;
HRS Coll., M. Derrick et al., ANL-HEP-PR-85-05 (1985);
HRS Coll., I. Beltrami et al., Phys. Rev. Lett. 54 (1985) 1775.
[73] DELCO Coll., G.B. Mills et al., Phys. Rev. Lett. 52 (1984) 1944.
[74] MARK II Coll., C.A. Blocker et al., Phys. Lett. B109 (1982) 119;
CELLO Coll., H.J. Behrend et al., Phys. Lett. B127 (1983) 270;
MARK III Coll., R.M. Baltrusaitis et al., Phys. Rev. Lett. 55 (1985) 1842;
MAC Coll., W.W. Ash et al., Phys. Rev. Lett. 55 (1985) 2118.
[75] See e.g., Y.S. Tsai, Phys. Rev. D4 (1971) 2821.
[76] V. Lüth, in: Physics in Collisions 5, Autun, France (1985), ed. L. Montanet, p. 191.
[77] J. Jersak, E. Laerman and P.M. Zerwas, Phys. Lett. B98 (1981) 363.
[78] JADE Coll., W. Bartel et al., Phys. Lett. B129 (1983) 145.
[79] JADE Coll., W. Bartel et al., Phys. Lett. B160 (1985) 337.
[80] MAC Coll., E. Fernandez et al., Phys. Rev. D31 (1985) 1537.
[81] J.H. Field, Nucl. Phys. B168 (1980) 477.
[82] F.A. Berends and R. Kleiss, Nucl. Phys. B178 (1981) 141.
[83] MARK J Coll., B. Adeva et al., Phys. Rev. Lett. 53 (1984) 134; MIT Techn. Rep. 146 (1986).
[84] TASSO Coll. M. Althoff et al., Phys. Lett. B138 (1984) 441; Z. Phys. C22 (1984) 307.
[85] JADE Coll., W. Bartel et al., Phys. Lett. B91 (1980) 142.
[86] MARK J Coll., D.P. Barber et al., Phys. Rev. Lett. 43 (1979) 830;
PLUTO Coll., Ch. Berger et al., Phys. Lett. B86 (1979) 418;
TASSO Coll., R. Brandelik et al., Phys. Lett. B86 (1979) 243.
[87] R.D. Field and R.P. Feynman, Nucl. Phys. B136 (1978) 1.
[88] P. Hoyer et al., Nucl. Phys. B161 (1979) 349.
[89] A. Ali et al., Phys. Lett. B93 (1980) 155;
A. Ali, Phys. Lett. B110 (1982) 67.
[90] G. Altarelli and G. Parisi, Nucl. Phys. B126 (1977) 298.
[91] B. Anderson et al., Z. Phys. C1 (1978) 105;
B. Anderson and G. Gustafson, Z. Phys. C3 (1980) 223;
B. Anderson, G. Gustafson and T. Sjöstrand, Phys. Lett. B94 (1980) 211;
B. Andersson, G. Gustafson, G. Ingelman and T. Sjöstrand, Phys. Reports 97 (1983) 33.
[92] T. Sjöstrand, Comput. Phys. Commun. 27 (1982) 243; 28 (1983) 229.
[93] T. Sjöstrand, Comput. Phys. Commun. 39 (1986) 347.
[94] G.C. Fox and S. Wolfram, Nucl. Phys. B168 (1980) 285.
[95] R.D. Field and S. Wolfram, Nucl. Phys. B213 (1983) 65;
T.D. Gottschalk, Nucl. Phys. B214 (1983) 201.

[96] G. Marchesini and B.R. Webber, Nucl. Phys. B238 (1984) 1;
B.R. Webber, Nucl. Phys. B238 (1984) 492.
[97] A.H. Mueller, Phys. Lett. B104 (1981) 161;
B.I. Ermolaev and V.S. Fadin, JETP Lett. 33 (1981) 269;
Yu.L. Dokshitzer, V.S. Fadin and V.A. Khoze, Phys. Lett. B115 (1982) 242; Z. Phys. C18 (1983) 37.
[98] S. Bethke, Z. Phys. C29 (1985) 175.
[99] DELCO Coll., D.E. Koop et al., Phys. Rev. Lett. 52 (1983) 970.
[100] C. Peterson et al., Phys. Rev. D27 (1983) 105.
[101] S. Brandt and H. Dahmen, Z. Phys. C1 (1979) 61;
S.L. Wu and G.L. Zobernig, Z. Phys. C2 (1979) 107.
[102] Ya.I. Asimov et al., Leningrad preprint 1051, April 1985.
[103] JADE Coll., W. Bartel et al., Phys. Lett. B123 (1983) 460; B134 (1984) 275;
Z. Phys. C21 (1983) 37; Phys. Lett. B157 (1985) 340.
[104] A. Petersen, DESY internal preprint F22-84-02 unpublished (in German).
[105] H. Aihara et al., Z. Phys. C28 (1985) 31.
[106] TASSO Coll., M. Althoff et al., Z. Phys. C29 (1985) 29.
[107] Summaries can be found in:
T.F. Walsh, Talk given at the Brighton Conf.[2], p. 545;
G. Altarelli, Talk given at the Bari Conf.[5], p. 729.
[108] CELLO Coll., H.J. Behrend et al., Phys. Lett. B138 (1984) 311.
[109] JADE Coll., W. Bartel et al., Z. Phys. C25 (1984) 231.
[110] PLUTO Coll., Ch. Berger et al., Z. Phys. C28 (1985) 365.
[111] MARK J Coll., B. Adeva et al., Phys. Rev. Lett. 54 (1985) 1750.
[112] TASSO Coll., M. Althoff et al., Z. Phys. C26 (1984) 157.
[113] F. Barreiro, Inv. Talk at XVIth Symp. on Multiparticle Dynamics Tel Aviv 1985, proceedings to be published, DESY preprint 85-086.
[114] E. Fernandez et al., Phys. Rev. D31 (1985) 2724.
[115] T. Sjöstrand, Z. Phys. C26 (1984) 93.
[116] K. Fabricius, G. Kramer, G. Schierholz and I. Schmitt, Z. Phys. C11 (1982) 315.
[117] F. Gutbrod, G. Kramer and G. Schierholz, Z. Phys. C21 (1984) 235.
[118] R.K. Ellis, D.A. Ross and A.E. Terrano, Nucl. Phys. B178 (1981) 421.
[119] J.A.M. Vermaseren, K.J.F. Gaemers and S.J. Oldham, Nucl. Phys. B187 (1981) 301.
[120] T.D. Gottschalk, Phys. Lett. B109 (1982) 331.
[121] T.D. Gottschalk and M.P. Shatz, Phys. Lett. B150 (1985) 451.
[122] S. Yamada, Contr. to the Madison Conf. 1980[1].
[123] JADE Coll., W. Bartel et al., Phys. Lett. B119 (1982) 239.
[124] Yu. Dokshitzer, D.I. D'yankonov and S.I. Troyan, Phys. Lett. B78 (1978) 290;
C. Basham, L. Brown, S. Ellis and S. Love, Phys. Rev. Lett. 41 (1978) 1585; Phys. Rev. D19 (1979) 2018.
[125] D.G. Richards, W.J. Stirling and S.D. Ellis, Phys. Lett. B119 (1982) 193.
[126] A. Ali and F. Barreiro, Phys. Lett. B118 (1982) 155.
[127] S.D. Ellis, Phys. Lett. B117 (1982) 333.
[128] JADE Coll., Contr. to Berkeley Conf. 1986.[7]
[129] R.D. Field, Contr. to Cornell Conf. 1983.[3]
[130] PLUTO Coll., Ch. Berger et al., Phys. Lett. B99 (1981) 292 and Z. Phys. C12 (1982) 297.
[131] D.G. Richards, W.J. Stirling and S.D. Ellis, Nucl. Phys. B229 (1983) 317.
[132] L. Clavelli and D. Wyler, Phys. Lett. B103 (1981) 383.
[133] See for example: R. Voss, Talk at "The Quark Structure of Matter", Strasbourg-Karlsruhe, 1985 and CERN-EP/85-204.
[134] JADE Coll., W. Bartel et al., Phys. Lett. B115 (1982) 338.
[135] A. DeRujula, J. Ellis, E.G. Floratos and M.K. Gaillard, Nucl. Phys. B138 (1978) 387.
[136] O. Nachtmann et al., Z. Phys. C14 (1982) 47.
[137] JADE Coll., W. Bartel et al., DESY preprint 86-086 (1986) to be published.
[138] JADE Coll., W. Bartel et al., Z. Phys. C20 (1983) 187.
[139] JADE Coll., W. Bartel et al., Z. Phys. C28 (1985) 343.
[140] K.-H. Meier, DESY Internal Report F11-84-01 (1984) (in German).
[141] CELLO Coll., H.J. Behrend et al., Z. Phys. C20 (1983) 207.
[142] TASSO Coll., R. Brandelik et al., Phys. Lett. B113 (1982) 98;
TASSO Coll., M. Althoff et al., Z. Phys. C17 (1983) 5.
[143] JADE Coll., W. Bartel et al., Z. Phys. C9 (1981) 315.
[144] TASSO Coll., W. Braunschweig et al., DESY preprint 86-078 to be published;
CELLO Coll., H.J. Behrend et al., Z. Phys. C20 (1983) 207;
PEP 4/TPC Coll., H. Aihara et al., Z. Phys. C27 (1985) 187.

[145] E. Laerman et al., Nucl. Phys. B207 (1982) 205.
[146] MAC Coll., E. Fernandez et al., Phys. Rev. Lett. 54 (1985) 95.
[147] JADE Coll., W. Bartel et al., Phys. Lett. B130 (1983) 454.
[148] TASSO Coll., M. Althoff et al., Z. Phys. C27 (1985) 27.
[149] MARK II Coll., H. Schellman et al., Phys. Rev. D31 (1985) 3013;
TPC Coll., H. Aihara et al., Phys. Rev. Lett. 53 (1984) 2378.
[150] JADE Coll., W. Bartel et al., Phys. Lett. B145 (1984) 441.
[151] TASSO Coll., R. Brandelik et al., Phys. Lett. B117 (1982) 135.
[152] G. Dietrich, thesis Univ. Hamburg (1985) (in German).
[153] TPC Coll., H. Aihara et al., Phys. Rev. Lett. 54 (1985) 274.
[154] TASSO Coll., M. Althoff et al., Phys. Lett. B130 (1983) 340;
K. Maruyama (TPC Coll.), XIXth Rencontre de Moriond (1984).
[155] C. Peterson and R.F. Walsh, Phys. Lett. B91 (1980) 455.
[156] DASP Coll., R. Brandelik et al., Nucl. Phys. B148 (1979) 189;
DASP Coll., H. Albrecht et al., Phys. Lett. B102 (1981) 291;
CLEO Coll., M.S. Alam et al., Phys. Rev. Lett. 53 (1984) 24;
ARGUS Coll., Contr. to Berkeley Conf. 1986.[7]
[157] D. Nussinov, Phys. Rev. Lett. 35 (1976) 1672;
G.J. Feldman et al., Phys. Rev. Lett. 38 (1977) 1313.
[158] JADE Coll., W. Bartel et al., Phys. Lett. B146 (1984) 121.
[159] TASSO Coll., M. Althoff et al., Phys. Lett. B126 (1983) 493; B135 (1984) 243;
C. Youngman, Proc. XIXth Rencontre de Moriond, ed. Tran Thanh Van (1984) p. 173.
[160] TASSO Coll., M. Althoff et al., Phys. Lett. B138 (1984) 317.
[161] JADE Coll., W. Bartel et al., Phys. Lett. B161 (1985) 197.
[162] MARK I Coll., G. Goldhaber et al., Phys. Lett. B69 (1977) 503;
Crystal Ball Coll., H.F.W. Sadrozinski, Contr. to the Madison Conf. 1980,[1] p. 681.
[163] A summary is given in the contribution by H. Yamamoto in the Kyoto Conf.[6];
J.M. Yelton et al., Phys. Rev. Lett. 49 (1982) 430;
HRS Coll., S. Ahlen et al., Phys. Rev. Lett. 51 (1983) 1147;
DELCO Coll., H. Yamamoto, Phys. Rev. Lett. 54 (1985) 522.
[164] Particle Data Group, Phys. Lett. B170 (1986).
[165] G. Trilling, Phys. Reports 75 (1981) 57.
[166] MARK III Coll., R.M.. Baltrusaitis, Phys. Rev. Lett. 56 (1986) 2140.
[167] HRS Coll., M. Derrick et al., Phys. Rev. Lett. 53 (1984) 1971; Phys. Lett. B146 (1984) 261.
[168] ARGUS Coll., H. Albrecht et al., Phys. Lett. B146 (1984) 111;
ARGUS Coll., H. Albrecht et al., Phys. Lett. B153 (1985) 343;
CLEO Coll., A. Chen et al., Phys. Rev. Lett. 51 (1983) 634;
TASSO Coll., M. Althoff et al., Phys. Lett. B136 (1984) 130.
[169] R. Marshall, Z. Phys. C26 (1984) 291.
[170] JADE Coll., W. Bartel et al., Phys. Lett. B146 (1984) 437.
[171] JADE Coll., W. Bartel et al., Phys. Lett. B163 (1985) 277.
[172] S. Stone, Cornell Conf. 1983,[3] p. 203 (summary);
CELLO Coll., H.J. Behrend et al., Z. Phys. C19 (1983) 291;
CELLO Coll., K. Chadwick et al., Phys. Rev. D27 (1983) 475;
CUSB Coll., G. Levman et al., Phys. Lett. B141 (1984) 271;
MAC Coll., E. Fernandez et al., Phys. Rev. Lett. 50 (1983) 2054;
MARK J Coll., B. Adeva et al., Phys. Rev. Lett. 51 (1983) 443;
MARK II Coll., M.E. Nelson et al., Phys. Rev. Lett. 50 (1983) 1542;
TASSO Coll., M. Althoff et al., Z. Phys. C22 (1984) 219.
[173] a) V. Barger, W.Y. Keung and R.J.N. Philips, Phys. Rev. D24 (1981) 1328;
b) H. Georgi and S.L. Glashow, Nucl. Phys. B167 (1980) 173;
c) G.L. Kane and M.E. Peskin, Nucl. Phys. B195 (1982) 29.
[174] P. Avery et al., Phys. Rev. Lett. 53 (1984) 1309;
E.H. Thorndike, Ann. Rev. Nucl. Part. Sci. 35 (1985) 195 and references.
[175] T. Schaad et al., Phys. Lett. B160 (1985) 188.
[176] UA1 Coll., G. Arnison et al., Phys. Lett. B155 (1985) 442.
[177] JADE Coll., W. Bartel et al., Phys. Lett. B114 (1982) 71.
[178] MAC Coll., E. Fernandez et al., Phys. Rev. Lett. 51 (1983) 1022.
[179] MARK II Coll., N.S. Lockyer et al., Phys. Rev. Lett. 51 (1983) 1316.
[180] DELCO Coll., D.E. Klem et al., Phys. Rev. Lett. 53 (1984) 1873.

[181] TASSO Coll., M. Althoff et al., Phys. Lett. B149 (1984) 524.
[182] JADE Coll., W. Bartel et al., Z. Phys. C31 (1986) 349.
[183] M.K. Gaillard and L. Maiani, Proc. 1979 Cargèse Summer Institute on Quarks and Leptons, eds. M. Levy et al. (Plenum Press, New York, 1979) p. 443.
[184] A. Chen et al., Phys. Rev. Lett. 52 (1984) 1084.
[185] S. Komamiya, Contr. to the Kyoto Conf. 1985,[6] p. 612.
[186] S. Yamada, Contr. to Cornell Conf. 1983,[3] p. 525; Reviews in Leipzig Conf. 1984[4] by S. Yamada, p. 72; U. Becker and S. Yamada, p. 198; P. Schacht, p. 196; D.H. Miller, p. 200; R. Prepost, p. 204.
[187] JADE Coll., W. Bartel et al., Phys. Lett. B91 (1980) 152.
[188] JADE Coll., W. Bartel et al., Phys. Lett. B100 (1981) 364.
[189] CELLO Coll., H.J. Behrend et al., Phys. Lett. B144 (1984) 297;
MARK J Coll., B. Adeva et al., Phys. Lett. B152 (1985) 439.
[190] J.D. Jackson and D.L. Scharre, Nucl. Instr. Methods 128 (1975) 13.
[191] D.R. Yennie, Phys. Rev. Lett. 34 (1975) 239;
F.E. Close, D.M. Scott and D. Sievers, Phys. Lett. B62 (1976) 213;
M. Krammer, H. Krasemann and S. Ono, preprint DESY 80-25 (1980) unpublished.
[192] K. Ambrus, thesis Un. Heidelberg, unpublished (in German).
[193] L. Landau, J. Phys. USSR 8 (1944) 201;
P.M. Sternheimer and R.F. Peierls, Phys. Rev. B3 (1971) 3681.
[194] A. Marini et al., Phys. Rev. Lett. 48 (1982) 1649;
J.M. Weiss et al., Phys. Lett. B101 (1981) 439;
M.C. Ross et al., Phys. Lett. B118 (1982) 199;
H. Aihara et al., Phys. Rev. Lett. 52 (1984) 168, 2332;
H. Albrecht et al., Phys. Lett. B156 (1985) 134.
[195] L. DiLella, Review Talk given at the Bari Conference 1985;[5]
S.J. Wimpenny (UA1) and B. DeLotto (UA2), Proc. XXIst Rencontre de Moriond, Les Arcs, 1986, to be published.
[196] M. Davier, Review Talk given at Berkeley Conf. 1986.[7]
[197] Y.S. Tsai, SLAC-PUB- 2450 (1979).
[198] A. Böhm, Proc. XXth Rencontre de Moriond, Les Arcs, vol. 2 (1985) p. 141.
[199] JADE Coll., W. Bartel et al., Phys. Lett. B123 (1983) 353.
[200] PLUTO Coll., Phys. Lett. B99 (1981) 489;
TASSO Coll., Phys. Lett. B99 (1981) 163.
[201] E. Golowich and T.C. Yang, Phys. Lett. B80 (1979) 245;
L.N. Chang and J.E. Kim, Phys. Lett. B81 (1979) 233;
H.E. Haber, G.L. Kane and T. Sterling, Nucl. Phys. B161 (1979) 493.
[202] S.-H.H. Tye, Phys. Rev. Lett. 47 (1981) 1035.
[203] a) G.R. Farrar and P. Fayet, Phys. Lett. B89 (1980) 191;
b) M. Glück and E. Reya, Phys. Lett. B130 (1983) 423;
c) T. Kobayashi and M. Kuroda, Phys. Lett. B134 (1984) 271.
[204] T. Kobayashi and M. Kuroda, Phys. Lett. B139 (1984) 208;
J.D. Ware and M.E. Machacek, Phys. Lett. B142 (1984) 301.
[205] J. Wess and B. Zumino, Nucl. Phys. B70 (1974) 39; Phys. Lett. B49 (1974) 52;
A. Salam and B. Strathdee, Phys. Rev. D11 (1975) 1521.
[206] P. Fayet and S. Ferrara, Phys. Reports 32C (1977) 249.
[207] J. von Krogh, Proc. XXth Rencontre de Moriond, Les Arcs, vol. 1 (1985) p. 567.
[208] UA1 Collab., G. Arnison et al., Phys. Lett. B139 (1984) 115.
[209] S.L. Glashow and A. Manohar, Phys. Rev. Lett. 54 (1985) 526.
[210] H. Baer, K. Hagiwara and S. Komamiya, Phys. Lett. B156 (1985) 117;
G. Pocsik and G. Zsigmond, Z. Phys. C10 (1981) 367.
[211] JADE Coll., W. Bartel et al., Phys. Lett. B155 (1985) 288.
[212] J. Ellis, J.S. Hagelin, D.V. Nanopoulos and M. Srednicki, Phys. Lett. B127 (1983) 233;
J. Ellis, J.M. Frere, J.S. Hagelin, G.L. Kane and S.T. Petcov, Phys. Lett. B132 (1983) 436.
[213] M.K. Gaillard, L. Hall and L. Hinchliffe, Phys. Lett. B116 (1982) 279.
[214] N. Cabibbo et al., Phys. Lett. B105 (1981) 155;
H. Goldberg, Phys. Rev. Lett. 50 (1983) 1419.
[215] J. Ellis and J.S. Hagelin, Phys. Lett. B122 (1983) 303.
[216] JADE Coll., W. Bartel et al., Z. Phys. C31 (1986) 359.
[217] C. Cremmer, P. Fayet and L. Grirardello, Phys. Lett. B122 (1983) 41.

[218] I.I. Bigi and S. Rudaz, Phys. Lett. B153 (1984) 335.
[219] S. Weinberg, Phys. Rev. Lett. 50 (1983) 387;
P. Fayet, Phys. Lett. B125 (1983) 178; B133 (1983) 363.
[220] E. Reya, Un. Dortmund preprint, DO-TH 83/17 (1983).
[221] O. Nachtmann and A. Reiter (Un. of Heidelberg) private communication.
[222] G. Eilam and E. Reya, Phys. Lett. B145 (1984) 425; B148 (1984) 502.
[223] Recent reviews are in: M.E. Peskin in Kyoto Conf.[6];
R.D. Peccei, Proc. 4th Topical Workshop on Proton Antiproton Collider Physics, Bern 1984, p. 483;
H. Terazawa, in: Leipzig Conf. vol. 1 (1984)[4] p. 63;
H. Fritzsch, Lectures given at the Int. School on Subnuclear Physics, Erice, MP1-PAE/PTH, vol. 85/84 (1984);
W. Buchmüller, CERN TH-4189 (1985).
[224] H. Terazawa et al., Phys. Lett. B112 (1984) 387.
[225] E.J. Eichten, K.D. Lane and M.E. Peskin, Phys. Rev. Lett. 50 (1983) 811.
[226] H. Fritzsch and G. Mandelbaum, Phys. Lett. B102 (1981) 319.
[227] B. Schrempp and F. Schrempp, private communication.
[228] CELLO Coll., H.J. Behrend et al., Phys. Lett. B141 (1984) 145.
[229] R.N. Mohapatra, G. Segrè and L. Wolfenstein, Phys. Lett. B145 (1984) 433;
B. Schrempp and F. Schrempp, Phys. Lett. B153 (1985) 101.
[230] A. Böhm, Proc. XXth Rencontre de Moriond, Les Arcs, Vol. 1 (1985) p. 559;
MARK J Coll., B. Adeva et al., MIT technical report 146, January 1986.

[1] 20th Int. Conf. on High Energy Particle Physics, Madison, Wisconsin (1980).
[2] Int. Europhysics Conf. on High Energy Physics, Brighton, UK, July 1983 (Rutherford Appleton Laboratory).
[3] 1983 Int. Symp. on Lepton and Photon Interactions at High Energies, eds. D.G. Cassel and D.L. Kreinick (Cornell University, 1983) p. 80.
[4] 22nd Int. Conf. on High Energy Physics, Leipzig 1984, eds. A. Meyer and E. Wieczorek.
[5] Int. Europhysics Conf. on High Energy Physics, Bari, Italy, July 1985, eds. L. Nitti and G. Preparata.
[6] 1985 Int. Symp. on Lepton and Photon Interactions at High Energies, Kyoto, Japan, August 1985, eds. M. Konuma and K. Takahashi.
[7] 23rd Int. Conf. on High Energy Physics, Berkeley (USA), August 1986, to be published.